Universität Augsburg
Mathematisch-Naturwissenschaftlich-
Technische Fakultät

On New Silicate-Analogous Host Structures For Phosphors

Dissertation zur Erlangung des Doktorgrades (Dr. rer. nat.)
an der Mathematisch-Naturwissenschaftlich-Technischen Fakultät
der Universität Augsburg

vorgelegt von

Katharina Förg

Universität Augsburg
Institut für Physik
Lehrstuhl für Festkörperchemie

Augsburg 2016

Erstgutachter:	Prof. Dr. H. A. Höppe
Zweitgutachter:	Prof. Dr. A. Reller
Tag der mündlichen Prüfung:	04.05.2016

Acknowledgement

First of all I would like to thank Prof. Dr. Henning Höppe for giving me the opportunity to work in his group, for offering me this very interesting and promising research topic and for the continuous friendly and helpful support during the last years. I am very grateful for the freedom in research to develop and follow my own ideas. I learned a lot during this time and used the experience for my personal development.

I am very thankful to Prof. Dr. Armin Reller for being available as co-referee of this thesis.

For the financial support during the last year of my thesis I am indebted to the Frauenbüro of the Universität Augsburg for receiving the doctoral fellowship *Chancengleichheit für Frauen in Forschung und Lehre*.

Special thanks go to my working group colleagues Dr. Karolina Kazmierczak, Stephan Jantz, Peter Gross, Arno Kirchhain and Martin Schäfer (especially for the required, but nevertheless very creative "Kronkorken-Feuerauffangschale" and the miraculous transformation of juice into vodka) for fruitful discussions and their helpfulness. I am extremely grateful to Stephan who never hesitated to invest an unpredictable amount of time for the solution of any LaTeX problem and for proof-reading this thesis.

For carrying out numerous EDX-measurements I would like to thank Silke Weigel.

For spending plenty of time and supporting me during several *Rietveld* analyses, the contact mediation for the magnetic measurements, the entertaining coffee breaks and fruitful discussions I would like to thank Dr. Stefan Riegg.

To actual and former members of the Chair of Solid State Chemistry I am thankful for creating a pleasant working atmosphere, for the numerous and time-independent "Bier um 4" and the phenomenal time during the pub quizzes. I am very grateful to my former colleagues Dr. Annina Steinbach and Dr. Sebastian Tränkle. They helped me in my initial days to familiarise at the Chair of Solid State Chemistry and cared about me not to miss a lunch or coffee break.

In particular, I want to thank Annina and Rebekka with whom it was possible to have serious or entertaining conversations at any time of the day, which made

everyday life a lot more comfortable. At this point I would like to apologize for any inconvenience we caused in the hallway in the meantime. Both of them supported me in particular at the beginning and end of my dissertation in terms of convivial rounds with sparkling wine (@ Rebekka) and for always being understanding and available when needed. Thanks to Annina, I had the honour to receive *Hydrothermia* as my superhero name to be able to participate (but rarely win against her as *Acid Girl*) in the "d'accord" game. Thanks also to her, I quickly became introduced to the delight of "Mensa-Chai-Tea" ☕, a passion, which I dutifully passed on to Rebekka at the right time.

A special thank goes to my bachelor and research students Florian Funcke, Anatoli Manski and Stefanie Junger.

I thank Prof. Dr. Jörg Hähner for being my mentor during my participation in the UniMento program, giving me ideas, suggestions and support beyond the program during our meetings and numerous sushi sessions and for the best "Feuerzangenbowle" at his Christmas parties (thanks also to Uwe Jänen!).

Many thanks go to my friends, who were there for me, celebrated 90ies parties and made my life full of diversity in the spare time.

Last but not least, I am deeply grateful to my family and my partner Stephan, who always supported and encouraged me, gave me assurance during this thesis and had an open ear for my problems. Thanks for your patience!

Contents

Abbreviations

°	Degree	FWHM	Full Width at Half Maximum
°C	Degree Celsius	g	Gram
/	Per	*g*	*Landé* Factor
%	Percent	GooF	Goodness of Fit
Ø	Average	h	Hour
λ	Wavelength	*hs*	*high-spin*
λ_{Exc}	Excitation Wavelength	Hz	Hertz
λ_{Em}	Emission Wavelength	IRE	Internal Reflection Element
θ	Theta	IR	Infrared
Δ	Difference	K	Kelvin
ν	Stretching Vibration	kJ	Kilojoule
δ	Bending Vibration	kV	Kilovolt
∞	Infinite	kW	Kilowatt
$\sphericalangle$	Angle	lB	Loop-branched
Å	Ångstrom	LED	Light-Emitting Diode
A	Acceptor	LFS	Ligand Field Splitting
ATR	Attenuated Total Reflectance	LMCT	Ligand-to-Metal-Charge-Transfer
a.u.	Arbitrary Units	*Ln*	Lanthanide
B_{Δ}	BO_3 Unit	*ls*	*low-spin*
$B_{\square}$	BO_4 Unit	LT	Low Temperature
BBU	Basic Building Unit	m	Metre
C	*Curie* Constant	mA	Milliampere
cB	Cyclo-branched	MAPLE	Madelung Part of Lattice Energy
cm	Centimetre Constant	max.	Maximum
CN	Coordination Number	mg	Milligram
D	Donor	min	Minute
EDX	Energy-Dispersive X-Ray Spectroscopy	min.	Minimum
		ml	Millilitre
e.g.	For Example	mm	Millimetre
et al.	Et alii	μ_{eff}	Effective Magnetic Moment
FBU	Fundamental Building Unit	µm	Micrometre
FT	*Fourier*-Transform	μ_B	*Bohr* Magneton

mol	Mol	mmol	Millimol
nm	Nanometre	s	Second
no.	Number	SQUID	Superconducting Quantum
oB	Open-branched		Interference Device
Oe	Ørsted	T	Transmission
olB	Open-loop-branched	TG	Thermogravimetry
pm	Picometre	uB	Unbranched
PTFE	Polytetrafluoroethylene	UV	Ultraviolet
R	Reflectance	Vis	Visible
RE	Rare-Earth	wt%	Weight Percent
RT	Room Temperature	Z	Formula Units Per Unit Cell

1 Introduction

Almost every day, one can follow the worldwide discussed climate conflict in the media. Two different sources for the generation of energy are used predominantly: fossil fuel power plants, which promote the greenhouse effect by producing countless amounts of CO_2, and nuclear power plants, which can lead to unpredictable damage to nature and human life as horribly demonstrated by the nuclear disaster of Fukushima in 2011. In-between, both have been heavily criticised. Hence, more and more voices have been raised for a turnaround in energy policy until the German federal government changed sides towards a green policy and proclaimed a rapid nuclear energy phase-out. However, each change in such an order of magnitude raises new problems and questions. Which form of energy should replace the atomic energy or even how could energy be used more efficiently?

Nowadays a large amount of energy is consumed for lighting. In the early 20th century highly efficient mercury discharge lamps were used for the first time. Low-pressure mercury discharge lamps are widely used in fluorescent lamps and comprise besides gaseous mercury also argon, which simplifies the ignition of the mercury plasma. Emission lines are almost exclusively in the UV region at 185, 254 and 365 nm. To produce white light phosphors were developed, which could be excited effectively at 254 nm, and which emitted blue, green and red light. Thus, lamps with any colour could be produced depending on the phosphor mixture on the inner tube wall [1–3]. As mercury represents a toxic component in discharge lamps, another solution was searched to do without. This trend was also supported by politics and in 2013 the German federal government signed the *Minamata Convention on Mercury* to reduce the worldwide spread of mercury.

An alternative light source reveal Xenon high-pressure discharge lamps exhibiting emission lines in the vacuum-UV region at 147 and 172 nm. However, this means a fundamental cut in terms of energy efficiency, due to the increased energy loss between excitation and emission [4]. A further problem represents the insufficient photostability of conventional phosphors.

Since the invention of the blue GaN light-emitting diode (LED) by *Nakamura et al.* in 1994 [5], III-V semiconductors have entered everyday life. They possess band gaps

from the UV to the visible spectral region (e.g. series between AlGaN and InGaN), and by applying a current light emission is induced [4, 5]. In the meantime, the whole colour spectrum and the emission of white light can be achieved by adding blue, green and red diodes. Another possibility represents the combination of different phosphors, which convert for example invisible UV radiation into visible light [3]. Thus, their application area could be extended and reaches now from displays and remote controls to lighting comprising advantages, such as high quantum efficiency, long service life and no toxicity [4, 6].

Due to the increasing demand on light sources, more efficient and economical LEDs have to be developed. Several combinational concepts by adding phosphors lead to the emission of white light. The combination of a blue LED chip with a yellow emitting phosphor, e.g. YAG:Ce^{3+}, produces a long-lived white-light-emitting diode (Figure 1.1 a), exhibiting one disadvantage: the emitted light appears cold, due to the missing red portion. The *C*olour *R*endering *I*ndex (CRI), which reflects the ability to display the colours of an irradiated object in a natural way, is rather low. The sun, as a blackbody, possesses a CRI value of 100 by definition [3, 4]. Two further combinational concepts for the generation of white light exist. A blue chip is covered with a green and red emitting phosphor (Figure 1.1 b). The mixing of the transmitted part of the blue light with the converted green and red light results in a white light, which may appear warmer due to the participating red portion. The third, more complex concept is the combination of three different phosphors on a UV emitting chip, emitting in the blue, green and red spectral region (Figure 1.1 c). The advantage is the possibility of tuning the colour by adjusting each single phosphor. Thus, a wider colour spectrum and a better CRI can be achieved [3, 4, 7].

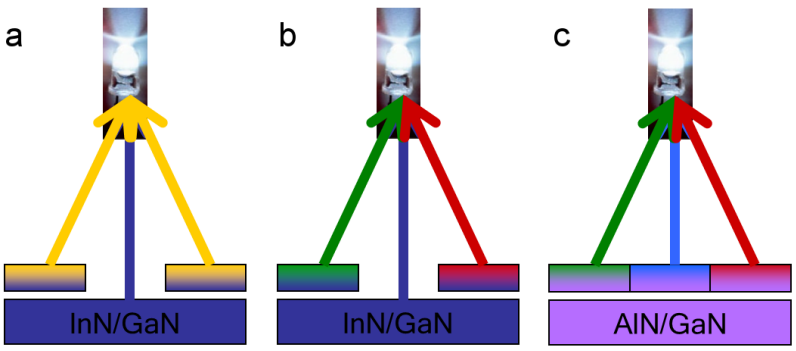

Figure 1.1: White light generation by combining a
a) blue LED chip covered with a yellow phosphor,
b) blue LED chip covered with a green and red phosphor,
c) UV LED chip covered with a blue, green and red phosphor [4].

In contrast to discharge lamps, the excitation wavelength increases from 254 nm to

300–450 nm and thus the energy loss decreases [4, 7]. Most of these diodes exhibit phosphors containing rare-earth ions as activators, which are not as rarely present on earth as one could suspect by their name [8]. Nevertheless, the availability of rare-earth elements and thus their price strongly depends on economical and particularly political relationships. Rare-earth ions satisfy the requirements for optical applications in the visible region. Due to the strong shielding of the $4f$ states by outer orbitals, interactions with the ligands are relatively weak. As a consequence, rare-earth ions possess nearly constant and rarely influenceable energy levels. Rapid processes between absorption, internal relaxation and emission avoid an undesired afterglow. Very efficient f–d transitions can be observed, if $4f$ and $5d$ orbitals are involved, revealing high transition rates and short lifetimes, e.g. in Ce^{3+} and Eu^{2+} [3, 4, 9, 10]. Nevertheless, the interaction between host lattice and activator defines the properties of a phosphor, which have to be adjusted according to the respective purpose. Important key parameters are besides the CRI and stability towards radiation the efficiency, quantum yield, resistance towards ageing, decay time and sufficient absorption at the emission wavelength of the emitting diode [3].

The particular focus in this thesis was the synthesis and characterisation of novel robust compounds, which should be synthesised as crystalline solids to investigate their structures via single-crystal and powder X-ray diffractometry. Moreover, attention was paid to their corresponding optical and thermal properties. Due to their structural variety and thermal stability, borates and phosphates represent interesting compound classes. For this purpose, novel representatives should be doped with ions, which are important for optical applications. Condensed borophosphate compounds should be synthesised with new stable structures as potential host lattices. Further formal substitution leads to the new compound class of the borosulphates, a representative of which should be synthesised to investigate its suitability as potential luminescent material.

This thesis is structured according to compound classes. Firstly, borates and phosphates will be treated followed by their formal condensation product, the borophosphates. Finally, the compound class of borosulphates concludes this work.

2 Preparative Methods

In this chapter the preparative methods used for this work are introduced. Depending on the compound, samples were synthesised either via solid-state or hydrothermal synthesis.

The commercially available starting materials, the sources of supply, as well as the purity, are listed in Table 2.1. All chemicals were used without further purification.

Table 2.1: Starting Materials

Compound	Formula	Supplier	Purity
Hydrogen peroxide	H_2O_2	Merck	30 %
Ammonium dihydrogenphosphate	$NH_4H_2PO_4$	Merck	>99.99 %
Boric acid	H_3BO_3	Merck	>99.5 %
Boron oxide	B_2O_3	Sigma Aldrich	99 %
Cerium(III) nitrate hexahydrate	$Ce(NO_3)_3{\cdot}6H_2O$	Merck	extra pure
Chromium(III) chloride hexahydrate	$CrCl_3{\cdot}6H_2O$	Fluka	>98 %
Diammonium hydrogenphosphate	$(NH_4)_2HPO_4$	Merck	>99 %
Dysprosium(III) oxide	Dy_2O_3	Kristallhandel Kelpin	99.99 %
Europium(III) nitrate pentahydrate	$Eu(NO_3)_3{\cdot}5H_2O$	Sigma-Aldrich	99.9 %
Europium(III) oxide	Eu_2O_3	Sigma Aldrich	99.9 %
Holmium(III) oxide	Ho_2O_3	Auer-Remy K.-G.	99.9 %
Manganese(II) chloride	$MnCl_2$	Fluka	>99 %
Phosphoric acid	H_3PO_4	Fluka	>85 %
Phosphorous acid	H_3PO_3	Riedel-de Haën	>98 %
Potassium hydrogensulfate	$KHSO_4$	Aldrich	>98 %
Terbium(III/IV) oxide	Tb_4O_7	Chempur	99.9 %
Terbium(III) nitrite pentahydrate	$Tb(NO_3)_3{\cdot}5H_2O$	Sigma-Aldrich	99.9 %
Strontium carbonate	$SrCO_3$	Riedel-de Haën	>96 %

2.1 Solid-State Synthesis

Solid-state synthesis represents one of the oldest methods of preparing solid materials at higher temperatures, with at least one reactant in the solid state. Due to slow diffusion rates in solids, high temperatures are necessary for considerable reaction rates. Approximately two thirds of the melting temperature of one reactant are sufficient for ion diffusion through the crystal lattice. At this point one could question the advantages of solid-state reactions. They are obvious if you look at the huge availability of starting compounds and low costs for the powder production on a large scale [11].

Grinding is an important step in solid-state synthesis to maximize the surface and the contact area and thus to improve the reaction rate. Furthermore, starting materials are selected according to a certain reactivity, e.g. temperature of decomposition. High temperatures allow higher diffusion rates but also claim special demands on the crucible material. It may neither react with the starting materials nor decompose at high temperatures. Common containers are made of platinum, silica or corundum [11].

Next to numerous advantages, a number of disadvantages also exists. As solid-state reactions lead to thermodynamically stable products, undesirable or side products may be formed. Additionally, homogeneity due to slow diffusion processes is hard to achieve. *In-situ* monitoring via high-temperature X-ray powder diffraction is possible. Since only small quantities can be measured to achieve homogeneity and reproducibility is rarely given going to larger amounts, usually X-ray powder diffraction is carried out periodically after cooling to room temperature. Reaction temperatures have to be considered with respect to a better diffusion rate at higher temperatures on the one hand and possible volatilization processes of one or more of the starting materials on the other hand [11].

Starting materials, such as carbonate, oxide, phosphate and sulphate powders (Table 2.1) were thoroughly ground in an agate mortar and transferred into an alumina boat (Friatec, Mannheim) or a silica glass crucible (Häberle, Lonsee-Ettlenschieß). Reactions in air were carried out in muffle furnaces (Nabertherm, Lilienthal) in a temperature range of 500–1000 °C. Reactions in a nitrogen or *forming gas* (90 % N_2, 10 % H_2) flow (40–250 ml min^{-1}), such as dotations with Eu^{2+}, were conducted in a tube furnace (Gero, Neuhausen) with corundum or silica working tubes (Friatec, Mannheim) in the same temperature range as mentioned above.

By using this synthesis method, phosphates and borosulphates could be obtained (Chapters 6 and 8).

2.2 Hydrothermal Synthesis

Many inorganic compounds are unstable under rather rough solid-state synthesis conditions, such as high temperatures. In contrast, hydrothermal syntheses are an imitation of geological processes in nature, where solids are obtained from a liquid phase under moderate conditions. Hydrothermal processes are defined as heterogeneous reactions that take place in an aqueous medium above a temperature of 100 °C and a pressure of 1 bar [11, 12]. Water satisfies two duties. Next to being the solvent it is also the pressure-transmitting medium [11]. Advantages of hydrothermal conditions are obvious; while only gentle temperatures (100–300 °C) are needed, hardly soluble compounds can go into solution or form a flux which subsequently accelerates the reaction rate. Additionally, products with a high crystallinity can be obtained. Pressure tuning can be achieved by using different temperatures, solvents or filling degrees [11, 12].

Figure 2.1: *Teflon* autoclave.

For this work, *Teflon* (PTFE) autoclaves with inlay containers (Bola, Grünsfeld) with a total volume of 10 ml (Figure 2.1) or silica ampoules made of enclosed silica pipettes were used. The maximum operating temperature was 220 °C using a drying cabinet VENTI-Line (VWR, Darmstadt). The exchangeable perfluoralkoxy and polyfluorethylen rupture membranes of the *Teflon* autoclaves burst at a maximum pressure of 25 bar. The starting materials were weighed, homogenised by grinding in an agate mortar and transferred into the *Teflon* autoclave or silica ampoule. A few milliliters of water or phosphoric acid were added for a filling degree of 50–70 % (*Teflon* autoclave) and 20–30 % (silica ampoule). The silica ampoules were enclosed using a *Bunsen* burner. The water of crystallization of certain starting materials

served as additional solvent during the reaction process.

By using synthesis methods in sealed-off systems with elevated moderate pressure ternary or higher oxidic compounds, such as borophosphates [13] and borates [14, 15], are easily accessible.

3 Analytical Methods

In this chapter the applied analytical methods are introduced. Herein the investigation of the crystal structures and the spectroscopic properties of the synthesised compounds are in the focus. First of all, synthesised solid samples are investigated via X-ray powder diffraction. If the sample reveals a certain degree of crystallinity and no conformance with the powder database occurs, single-crystal X-ray diffraction is applied. After the solution and refinement of the crystal structure, further refinement of the atomic and structural parameters can be performed via *Rietveld* analysis. The presence of certain structural characteristics can be proofed by investigating the spectroscopic properties, such as the behaviour in the IR or UV-Vis region. Furthermore, magnetic and thermal properties of the synthesised materials are investigated.

3.1 X-Ray Diffraction

Investigating crystalline solids via X-ray powder diffraction is a standard method. All crystalline compounds possess a three-dimensional periodical lattice. Thus it is sufficient to know the crystal system and the dimensions of the unit cell, its smallest unit. The wavelengths of Cu ($\lambda_{\text{Cu-}K_\alpha} = 1.54178\,\text{Å}$) and Mo radiation ($\lambda_{\text{Mo-K}_\alpha} = 0.71069\,\text{Å}$) are in the same range as typical lattice plane distances. Therefore interference is attended if a crystal is exposed therein. The obtained diffraction patterns correspond to projections of the crystal lattice in reciprocal space. By using the *Bragg* equation (Equation 3.1), which is also illustrated in Figure 3.1, this phenomenon can be described.

$$n\,\lambda = 2\,d\,sin\theta \tag{3.1}$$

Equation 3.1: *Bragg* equation; n: order of interference, λ: wavelength, d: distance between lattice planes, θ: *Bragg* angle.

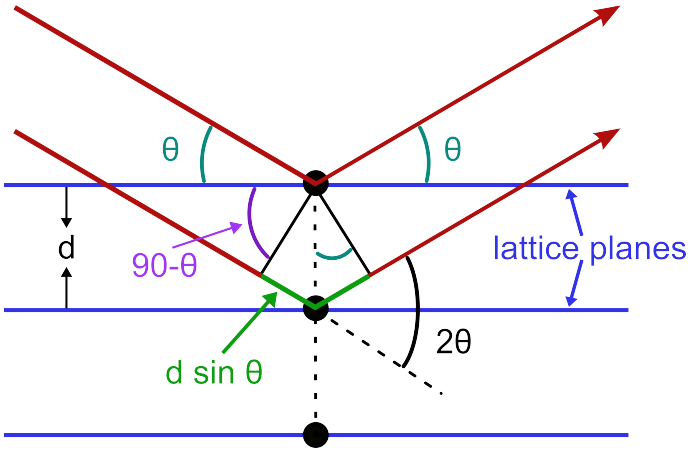

Figure 3.1: Diffraction of X-rays on lattice planes and derivative for the *Bragg* equation.

Positive interference can be observed only if the *Bragg* equation is satisfied. Otherwise phase shifted waves will extinguish. X-rays interact with the electron shell of the atoms. According to their scattering capability atoms can be distinguished [16–18].

As source for X-radiation serve generators with X-ray tubes. A focussed electron beam is directed in high vacuum to an anode, consisting of a highly pure metal (e.g. Mo, Cu, Ag). Due to an energy release of up to 3 kW the anode is being water-cooled on the rear side. The formation of X-radiation is subject to two different processes. On the one hand kinetic energy of the electrons is partially converted into *bremsstrahlung*, when the electron beam is deflected by the electric fields of the metal ions, whereby a continuous energy distribution results. On the other hand radiation of distinct energies is emitted, when the kinetic energy of the electrons is completely converted into X-radiation (Figure 3.2) [16]. This characteristic X-radiation arises if an electron is knocked out of its shell (e.g. K-shell) and the atom becomes ionised. The instable state relaxes by filling this hole with an electron from an energetically higher shell (e.g. L-shell) and emitting an X-ray photon with a distinct wavelength. The splitting in the L-shell leads to the presence of three states ($S=\frac{1}{2}$, $L=1$, $J=\{\frac{1}{2}, \frac{3}{2}\}$ and $S=\frac{1}{2}$, $L=0$, $J=\frac{1}{2}$), explaining with respect to the selection rules ($\Delta L=\pm 1$) the presence of a doublet ($K_{\alpha 1}$ and $K_{\alpha 2}$) [16].

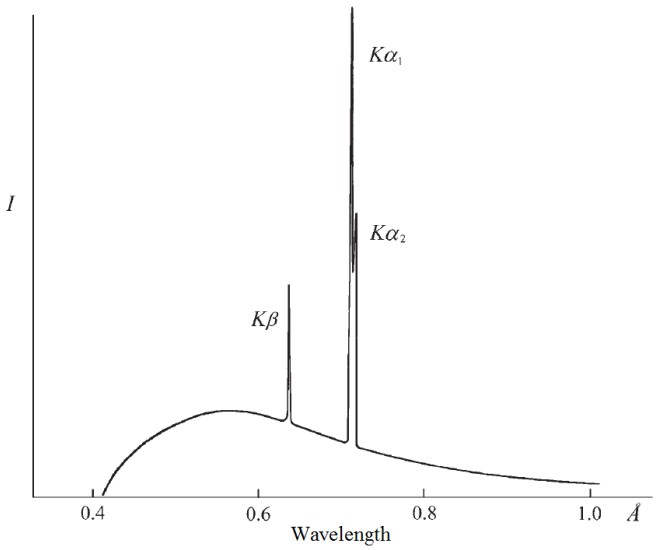

Figure 3.2: Spectral distribution of a Mo X-ray tube [16].

In the following sections X-ray powder diffraction and single-crystal X-ray diffraction are introduced.

3.1.1 X-Ray Powder Diffraction

The most common method applied for qualitative and quantitative (Chapter 3.1.3) investigation of crystalline powders is X-ray powder diffraction. Information about composition and phase purity of a sample can be obtained. Using this method the radiation of the X-ray source filtered by a monochromator is scattered and partially reflected at the planes of the crystal lattice of the powder sample. By grinding the powder sample in a mortar, random oriented crystallites are gained and lead to a higher amount of lattice planes in diffraction position [17, 18]. In contrast to single-crystal X-ray diffraction (Chapter 3.1.2), a two-dimensional diffraction pattern is obtained, in which the intensity of the diffracted radiation is recorded and plotted against the diffraction angle 2θ.

Using a powder diffractometer with a *Bragg*-Brentano setup (Figure 3.3) the parafocussed divergent incident beam is reflected from the surface of the flat rotating sample and converges at a fixed radius from the sample position. Source and detector move simultaneously by -θ and θ, whereas the sample is fixed in the horizontal position. Slit apertures are used to control the divergence of the beam. Wavelengths other than Cu-$K_{\alpha 1,2}$ are filtered by a secondary monochromator. The automatically varying entrance slit (Meteor 1D linear detector) improves intensities at higher angles. At fixed slit, the window of focus decreases with increasing 2θ angles, which leads to lower intensities due to stronger absorption processes and an additional

larger penetration depth of the X-rays [18, 19]. The penetration depth depends on the absorption, the type of material and the incident angle [18]. This setup was also used for *Rietveld* analysis (Chapter 3.1.3).

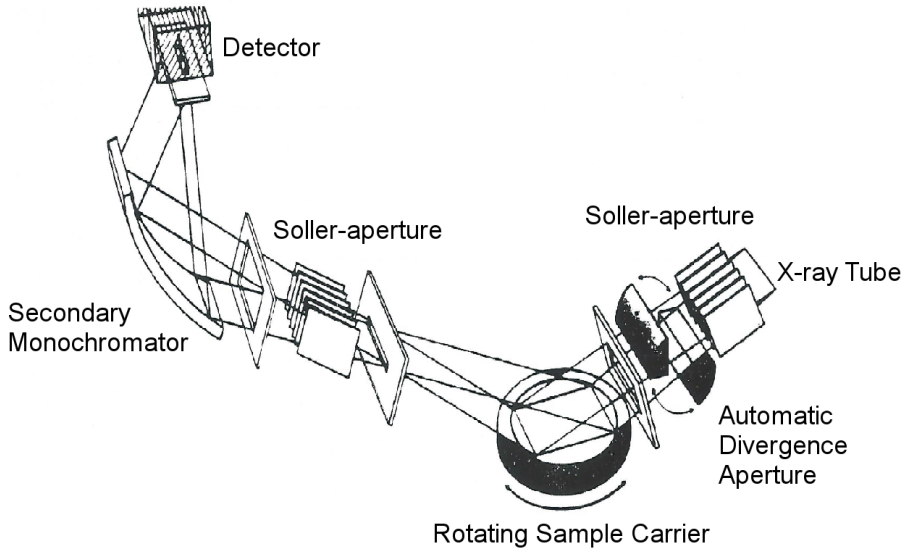

Figure 3.3: *Bragg*-Brentano diffractometer setup with flat sample [17].

Using a powder diffractometer with transmission geometry (*Debye-Scherrer* setup) the divergent beam from the X-ray source is not exactly focussed on the sample, but beyond onto the 2θ measuring circle of the detector (Figure 3.4). A better statistical distribution of lattice planes is obtained by spinning the ground sample around its axis. This results in high diffraction intensities due to more crystallites being in diffraction position and fulfilling *Bragg's* equation [18, 19].

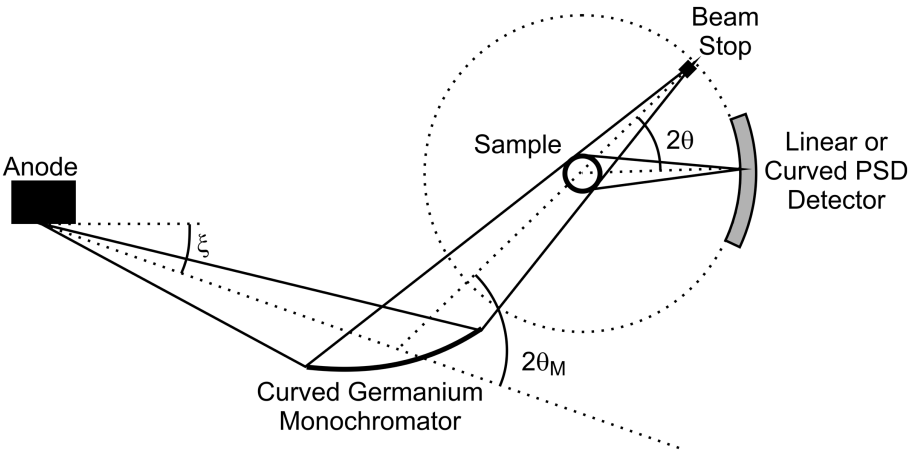

Figure 3.4: *Debye-Scherrer* diffractometer setup with capillary sample [19].

Diffraction measurements were either performed on a Seifert XRD T/T 3003 (Meteor 1D linear detector) reflection powder diffractometer or on a Bruker D8 Advance

(1D-LynxEye detector) transmission powder diffractometer. Both radiation sources were X-ray tubes with a copper anode providing Cu-$K_{\alpha 1,2}$ radiation and were working at an acceleration voltage of 40 kV and an emission current of 40 mA. Usually measurements were carried out in the range of 5–140 °2θ with a step size of 0.2 °.

Using the Seifert XRD T/T 3003 reflection powder diffractometer the homogenised samples were prepared on a stainless steel sample holder and flattened using a glass plate.
For measurements with the Bruker D8 Advance transmission powder diffractometer the homogenised samples were transferred into soda lime glass (measurements at room temperature) or quartz glass (measurements at elevated temperatures) marktubes (Hilgenberg, Malsfeld) with an outer diameter of 0.3 mm and mounted on a goniometer head.

3.1.2 Single-Crystal X-Ray Diffraction

Single-crystal X-ray diffraction is used to get a three-dimensional picture of the arrangement of the atoms in the crystal lattice. This can be achieved by measuring the intensities of the recorded reflections in the reciprocal space. Equal to powder diffraction X-ray radiation can be used and the *Bragg* equation has to be fulfilled to observe diffraction.

After checking the crystal quality by exposing the selected crystal to the X-ray beam for 30–100 seconds, the unit cell parameters were determined in a first short run. With this information an appropriate strategy for the complete measurement can be obtained using the APEX2 software suite (Bruker AXS, Karlsruhe). Depending on the crystal symmetry this process can take between several hours and days. The lower the symmetry, the more crystallographic information is needed for a satisfactory structure solution and refinement. The multi-scan absorption correction was performed with the program SADABS [20]. Crystal structures were solved by direct methods and refined in a least squares algorithm using the programs SHELXS-97 and SHELXTL-97 [21, 22]. All non-hydrogen atoms were refined with anisotropic displacement parameters. Hydrogen atoms were localised via Difference-*Fourier*-Synthesis and their positions were refined isotropically. To prove the quality of the structure model, residual values R are calculated [16, 18]. A distinction is made between the conventional $R1$-value (Equation 3.2) and the weighted $wR2$-value (Equation 3.3). $R1$ describes the deviation between the observed (F_o) and calculated (F_c) structure factor. In contrast, $wR2$ considers the weighting factor w and uses the least squares method refining with F_o^2 and F_c^2. Due to the squaring down in Equation 3.3, $wR2$ reacts more sensitively to small errors in the structure model.

$$R1 = \frac{\sum_{hkl} \| F_o | - | F_c \|}{\sum_{hkl} | F_o |} \tag{3.2}$$

$$wR2 = \sqrt{\frac{\sum_{hkl} w(F_o^2 - F_c^2)^2}{\sum_{hkl} w(F_o^2)^2}} \tag{3.3}$$

Equations 3.2 and 3.3: Definitions of $R1$ and $wR2$; w: weighting factor, F_o: observed structure factor, F_c: calculated structure factor [16].

For a satisfying structure refinement $R1$ and $wR2$ should be well below 5 % and 10 %, respectively. Next to the structure model those values are also dependent on the quality of the measurement and structural restraints, e.g. electron distribution and displacement factors [16].

Another distinguishing mark is the goodness of fit (Equation 3.4) whose value should be around unity if structure and weighting scheme are correct [16]. If more parameters are applied than reflections are observed, no value for S can be obtained, which leads to the assumption that the chosen structure model is wrong.

$$S = \sqrt{\frac{\sum_{hkl} w \| F_o | - | F_c \|^2}{m - n}} \tag{3.4}$$

Equation 3.4: Goodness of fit S; w: weighting factor, F_o: observed structure factor, F_c: calculated structure factor, m: number of reflections, n: number of parameters [16].

Adequate crystals were preselected using a SZX2-ILLT 8–56-x light optical microscope (Olympus, Hamburg) with a polarisation filter and picked up on a *MicroMount* (MiTeGen, Ithaka). Measurements were carried out either on a D8 Venture single-crystal diffractometer (Bruker, Karlsruhe) equipped with a Kappa four-circle goniometer, a PHOTON 100 CMOS detector and both a Cu and Mo radiation source or on an IPDS II (Stoe & Cie, Darmstadt) equipped with an Imaging Plate Diffraction system.

All representations of crystal structures were generated using the programs Diamond [23] and POV-Ray [24].

3.1.3 Rietveld Analysis

Rietveld analysis is used for the refinement of crystal structures from powder data using a known structure model and for quantitative phase analysis on multi-phase systems. In both cases the reflection intensities of the structure data are calculated and fitted (pattern-fitting structure refinement) to the corresponding powder data [17].

Due to rapid improvement of computer techniques the number of crystal structures solved from powder data increased. For a successful refinement the starting structure model has to be close to the final solution otherwise no satisfying refinement can be applied. The positions of the atom layers are shifted by a least squares algorithm until the difference between the measured and calculated diffraction pattern is minimised [17, 18, 25, 26]. Parameters are divided into local and global parameters. Whereas global parameters are applied to all phases in a mixture, local parameters vary for all phases. In the first step the lattice constants, the form of reflections and the background are refined. Afterwards, phase and atomic parameters are refined, which is in the classical meaning the *Rietveld* analysis [17]. There exist several values for the progress and quality of the refinement. The goodness of fit χ^2 (Equation 3.5) is minimised during the refinement process:

$$\chi^2 = \sum_i w_i \left(y_{i(\mathrm{obs})} - y_{i(\mathrm{cal})}\right)^2 \tag{3.5}$$

Equation 3.5: Goodness of fit χ^2; w_i: weighting factor, $y_{i(\mathrm{obs})}$: observed intensities, $y_{i(\mathrm{cal})}$: calculated intensities [17, 27].

The value of the weighting factor w_i corresponds to the inverse measured intensities $y_{i(\mathrm{obs})}$ ($w_i = 1/y_{i(\mathrm{obs})}$). A difference plot between the measured and calculated powder pattern gives an overview of the refinement's progress. A measure for the quality of the refinement are the residual values R, such as the profile residual R_{P}, and the weighted profile residual R_{wP} (Equations 3.6 and 3.7).

$$R_{\mathrm{P}} = \frac{\sum_i \mid y_{i(\mathrm{obs})} - y_{i(\mathrm{cal})} \mid}{\sum_i y_{i(\mathrm{obs})}} \tag{3.6}$$

$$R_{\mathrm{wP}} = \sqrt{\frac{\sum_i w_i \mid y_{i(\mathrm{obs})} - y_{i(\mathrm{cal})} \mid^2}{\sum_i w_i y_{i(\mathrm{obs})}}} \tag{3.7}$$

Equations 3.6 and 3.7: Definitions of residual values R_{P} and R_{wP}; w_i: weighting factor, $y_{i(\mathrm{obs})}$: observed intensities, $y_{i(\mathrm{cal})}$: calculated intensities [17, 18].

In general, the lower the R-values the better the refinement's quality. Acceptable values for R_{wP} are below 10 % and are close to unity for χ^2. These values are not absolute values as they depend on the instrumentation and the parameters of the measurement. Only if all aspects, such as R-values and difference plot, physical parameters and standard deviations, are proofed plausible, can one rely on the correctness of the refinement [17, 18].

According to *Hill* and *Howard* a close relationship exists between the scale factor s_i and the weight proportion W_i of the phase i in a sample with several phases j (Equation 3.8)[18].

$$W_i = \frac{s_i \rho_i V_i}{\sum_j s_j \rho_j V_j} \tag{3.8}$$

Equation 3.8: Definition of the weight proportion W_i; $s_{i/j}$: scale factor of i/j, $\rho_{i/j}$: density of i/j, $V_{i/j}$: volume of the unit cells of i/j [18].

Several conditions have to be fulfilled for a quantitative phase analysis. All crystal structures and the occupation numbers of the crystallographic sites have to be known. Textures, such as preferred orientation, have to be corrected, refining the corresponding factors.

Rietveld refinements were carried out with the FullProf program suite and the WINPlotR graphical user interface [27]. The graphical presentation of the data was performed using the program OriginPro [28].

3.1.4 Energy-Dispersive X-Ray Spectroscopy

For investigation of the elemental composition of the synthesised compounds, energy-dispersive X-ray spectroscopy (EDX) measurements were carried out. A beam of X-radiation hits the surface of a sample and stimulates the generation of a primary electron, which is removed from the shell, creating an electron hole. As this state is unstable, an electron with higher energy from an outer shell fills the hole and releases the excess energy as an X-ray photon. This energy is element specific as it increases with the nuclear charge. The spectrometer can detect X-radiation of any element. Exact assignments for light elements, e.g. hydrogen, carbon or oxygen, are not possible due to overlapping of the emission lines [29, 30].

EDX measurements were carried out on a XL-30 Field Emission ESEM (FEI/Philips, Hillsboro/Columbus, USA) spectrometer, which was equipped with an EDX detector. Evaluation of the data was performed using the software Genesis Spectrum [31].

3.2 MAPLE Concept

Madelung factors play an important role in the calculation of lattice energies (E_L) (following the Born-Haber cycle) and enthalpies of formation in ionic compounds. Thereby long range orders can be considered from so-called *MAPLE* (= *Ma*delung *P*art of *L*attice *E*nergy) values.

Nevertheless, next to ionic interactions (E_M), other effects such as the polarization energy E_{Pol}, repulsion energy E_{Rep} and covalent energy E_{Cov} have to be considered as well. In general, the correction term E_{Corr} is added to balance the difference between experimental and calculated lattice energies (Equation 3.9) [32, 33].

$$E_L = E_M + E_{Pol} + E_{Rep} + E_{Cov} + E_{Corr} \tag{3.9}$$

Equation 3.9: Lattice energy E_L; E_M: *Madelung* part of the lattice energy; E_{Pol}: polarization energy, E_{Rep}: repulsion energy, E_{Cov}: covalent energy, E_{Corr}: correction term [32, 33].

By calculating the *Madelung* energy E_M the *Coulomb* energy E_C forms a large part (Equation 3.10), which considers the potential energy between a cation and anion in a particular distance d_0.

$$E_C = \frac{z^+ z^- e^2}{4\pi\epsilon_0 d_0} \tag{3.10}$$

Equation 3.10: *Coulomb* energy E_C; z^+: charge of cation, z^-: charge of anion, e: elementary charge, ϵ_0: dielectric constant in vacuum, d_0: distance cation–anion [34].

To complete the equation for the *Madelung* energy the term of the *Coulomb* energy is extended by the *Avogadro* constant N_A and the *Madelung* factor A (Equation 3.11) [32]. In contrast to the coordination number, where only electrostatic interactions to the closest neighbours count, the *Madelung* factor A considers the sum of all attractive and repulsive interactions in the crystal lattice.

$$E_M = N_A \frac{z^+ z^- e^2}{4\pi\epsilon_0 d_0} A \tag{3.11}$$

Equation 3.11: *Madelung* energy E_M; N_A: *Avogadro* constant, z^+: charge of cation, z^-: charge of anion, e: elementary charge, ϵ_0: dielectric constant in vacuum, d_0: distance cation–anion, A: *Madelung* factor [34].

The *Madelung* factor A depends on the ions charge and structure type. It can be calculated by summing up partial *Madelung* factors of simple binary compounds for any arbitrary structure type, which makes them useful for structure discussions [32–34].

3.3 Deviation of Tetrahedra

In 1996 *Balić-Žunić* and *Makovicky* [35] first published a numerical method to determine the centroid coordinates in a defined polyhedron. This method based on least-squares fitting of a circumscribed sphere of the polyhedron. Using this information, amongst others, the degree of sphericity and the displacement of the central atom from the centroid can be calculated, depending on the coordination number. Using this method the regularity of the coordination of the central atom and the regularity of the ligand distribution in the polyhedron are discussed in a universal procedure [35]. Two years later they had developed a new global measure of the distortion of coordination polyhedra. An extended scheme is presented, which focuses on the ligand distribution in the polyhedron. They postulate that each polyhedron type with the maximum possible volume can be considered as an ideal one. Thus, all platonic polyhedra possess the maximum volume for their type of polyhedron. The comparison of the volume of the circumscribed sphere (V_r) of a real polyhedron

to that of the corresponding ideal polyhedron (V_i) V_r/V_i gives a suitable measure for polyhedral distortion. The distortion percentage can be calculated by the following equation (Equation 3.12) [36].

$$\nu(\%) = (V_i - V_r)/V_i \cdot 100 \tag{3.12}$$

Equation 3.12: Distortion percentage $\nu(\%)$; V_i: volume of ideal polyhedron, V_r: volume of real polyhedron [36].

Next to a quantitative measure of polyhedral distortion, the volume discrepancy can be also used as a measure of deviation of the chosen polyhedron model [36]. Exhibiting a deviation $< 1\,\%$ tetrahedra are classified as regular.

3.4 Spectroscopic Methods

Spectroscopic methods represent an important part of modern analytics. All spectra have in common that the detected intensity of the corresponding measurement is plotted against the wavelengths or wavenumbers of any spectral range. The electromagnetic spectrum extends over a large range of wavelengths, starting in the short-wave region of the cosmic radiation ($\lambda = 10^{-15}\,\mathrm{m}$, $f = 10^{23}\,\mathrm{Hz}$) reaching to the long-wave region of alternating current ($\lambda = 10^{6}\,\mathrm{m}$, $f = 10^{3}\,\mathrm{Hz}$) (Figure 3.5). In-between the areas of γ-rays, X-rays, UV-Vis, IR, microwaves and radio frequencies are located [37].

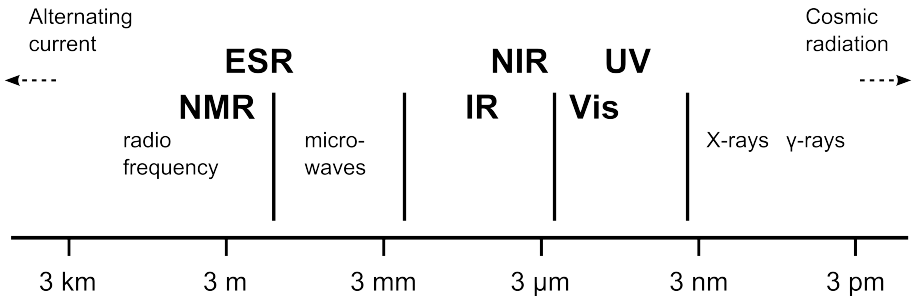

Figure 3.5: Survey of the electromagnetic spectrum.

All analytical methods using electromagnetic radiation in this wavelength scale have the interaction of radiation with mater in common. Following the energetic relation $E = h\nu$ the energy of a photon E with the frequency ν is linked via *Planck's* constant h. The speed of light c devided by the wavelength λ gives the frequency ν (Equation 3.13).

$$\nu = \frac{c}{\lambda} \tag{3.13}$$

Equation 3.13: Frequency ν; c: speed of light, λ: wavelength [37].

Following *Bohr*'s frequency condition $\Delta E = h\nu$, a molecule with its discrete energy levels can absorb energy, only if ΔE is an even multiple of *Planck's* constant h. In contrast, an energetic continuum could not give any information, but h divides energy levels into characteristic units [37].

3.4.1 Infrared Spectroscopy

The infrared (IR) region of the electromagnetic spectrum ranges between 1000 and $10{\cdot}10^6$ nm (10000–10 cm^{-1}). Spectra are depicted in the intensity of the transmission as a function against the wavenumber $\tilde{\nu}$ in cm^{-1} (Equation 3.14) with decreasing energy from left to right. The intensities of absorption are usually illustrated inversely as transmission T in % [37].

$$\tilde{\nu} = \frac{1}{\lambda} \tag{3.14}$$

Equation 3.14: Wavenumber $\tilde{\nu}$; λ: wavelength [37].

Exposure of molecules to infrared radiation leads to absorption in molecules, which either possess an alterable or inducible dipole moment, and results in vibrations (12800–200 cm^{-1}) and rotations ($< 200\,cm^{-1}$), respectively. Due to characteristic absorption bands at certain wavenumbers in the IR spectrum, functional groups can be assigned and conclusions about the chemical environment of the compound can be made. Intensities are characterised as strong, medium and weak [37, 38].

By now all mid-infrared instruments for analytical applications are *Fourier* transform infrared (FT-IR) spectrometer using a *Michelson* interferometer (Figure 3.6).

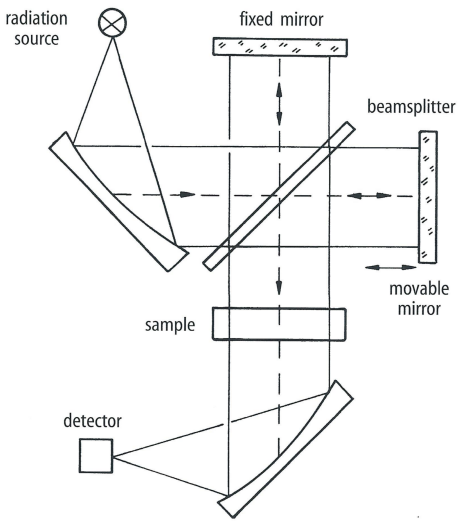

Figure 3.6: Schematic diagram of a *Fourier* transform spectrometer with a *Michelson* interferometer [38].

The incident beam is split by a semi-permeable beamsplitter into two partial beams. Whereas one beam is reflected on a fixed mirror, the second beam is reflected on a movable mirror. At the semi-permeable beamsplitter the partial beams are recombined and interfere. The optical pathlength of the right interferometer arm can be changed by shifting the movable mirror and a phase difference between both beams, hence, a change of the interference amplitude, can be induced. In an interferogram, the intensity signal from the detector is depicted as a function of the change of the optical pathlength. By using a *Fourier* transformation (FT) the interferogram can be converted into a spectrum. A lower detector noise, due to more sensitive detectors, a better signal-to-noise ratio and a lower expenditure of time are the major advantages of FT-IR spectrometers [38].

Solids that are either too thick or too strongly absorbing for standard transmission spectroscopy are investigated via attenuated total reflectance (ATR) technique (Figure 3.7) which uses the total reflection of light at the interface between two media of different refractive indices. The refractive index n_1 is higher than the refractive index of the sample n_2. Due to reflection and refraction laws the angle θ has to exceed the critical angle θ_c for total internal reflection (Equation 3.15). Exhibiting a very small depth of penetration d_p an evanescent wave extends in the less dense medium beyond the reflecting interface and interacts with this medium. In this case the sample was placed in contact with a diamond as internal reflection element (IRE) where the light is totally reflected. The interaction of the evanescent wave with the external less dense medium is detected [37, 38].

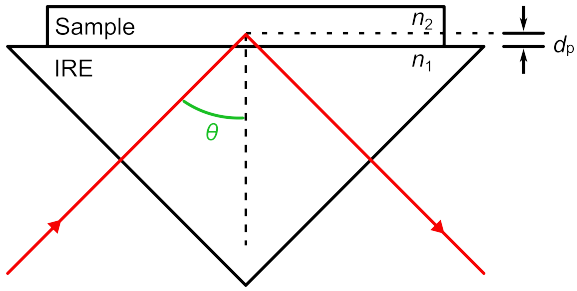

Figure 3.7: Schematic representation of a total internal reflection with n_1 : refractive index of the internal reflection element (IRE), n_2 : refractive index of the sample with $n_2 < n_1$; θ : angle of incidence, d_p : depth of penetration.

$$\theta_c = sin^{-1}\frac{n_2}{n_1} \tag{3.15}$$

Equation 3.15: Critical angle θ_c; n_1: refractive index of the internal reflection element (IRE), n_2: refractive index of the sample [37].

IR spectra were recorded on an EQUINOX 55 FT-IR spectrometer with a Platinum ATR unit (Bruker AXS, Karlsruhe) in the range of 4000–400 cm^{-1}. Before the investigation of a sample, a background measurement was carried out. The determined interferogram results from the difference between the measurement of the sample and the background. Evaluation of the data was performed using the programs OPUS [39] and OriginPro [28].

3.4.2 UV-Vis Spectroscopy

In general, UV-Vis spectra are recorded in a wavelength range of 200–800 nm (50000–12500 cm^{-1}) (Figure 3.8).

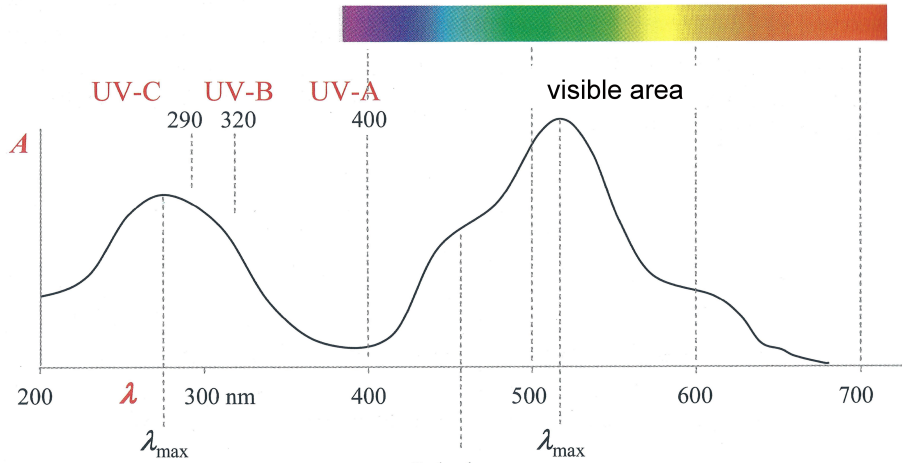

Figure 3.8: Schematic spectrum in the UV-Vis region [37].

In contrast to the excitation of bonds in the IR region, absorption of energy in the UV-Vis range leads to excitation of valence electrons, which are of lower energy compared to the electrons of inner shells. Accordingly they are responsible for the binding situation and thus are characteristic for the structure. Therefore structural information can be gained by UV-Vis spectroscopy. Processes that occur between absorption and emission of photons are represented in the *Jablonski* diagram (Figure 3.9) [37, 40].

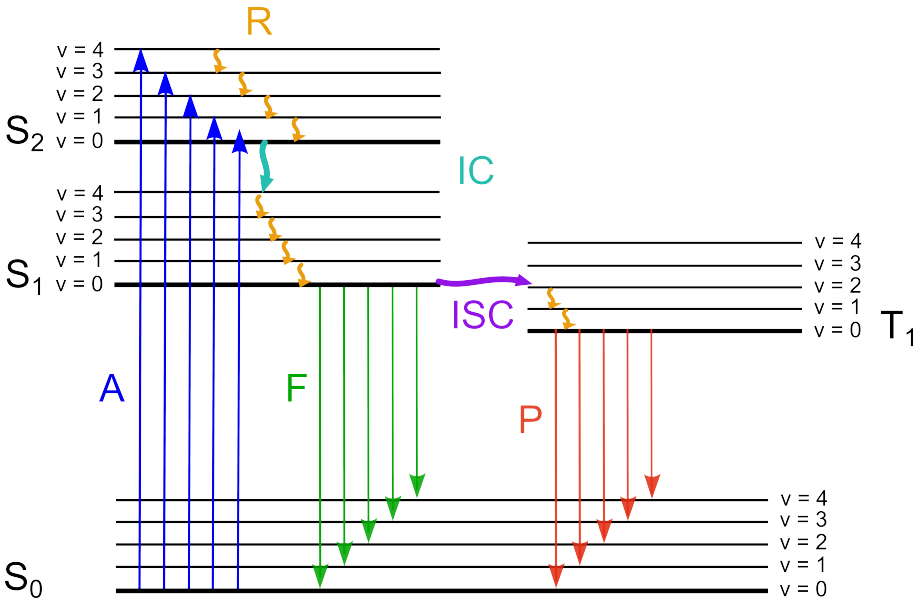

Figure 3.9: *Jablonski* diagram.

Photons possessing a distinct energy $E = h\nu$ can be absorbed (A) and are excited from the singlet ground state S_0 (antiparallel spin arrangement) into an energetically higher state S_n ($n = 1,2,3,...$). Excitation from the ground state S_0 occurs with conservation of the antiparallel orientation of the spins with a multiplicity M ($M = 2S+1$) of 1 and a total electron quantum number $S = 0$. In contrast, triplet states T_n ($n = 1,2,3,...$) differ from the singlet state S_n in the total electron quantum number of $S = 1$ and therefore also in the multiplicity of $M = 3$ due to parallel unpaired spins. ΔE between ground and excited state determines the absorbed energy and thus the corresponding wavelength of the absorption maximum. In addition to each electronic state, there are a large number of vibrational states ν_n ($\nu = 0,\ 1,\ 2,...$) and a number of rotational states (omitted for reasons of clarity). This fact explains the observation of absorption bands instead of absorption lines [37].

Next to intensive allowed transitions exist quantum-mechanical forbidden transitions, based on spectroscopic selection rules, which show much lower absorption intensities. Two rules have to be fulfilled:
The *LaPorte* prohibition indicates that in complexes with an inversion centre transitions are forbidden between states with the same parity ($g \rightarrow g$ and $u \rightarrow u$) and are thus low in intensity ($\Delta L = \pm 1$).
The spin prohibition indicates that transitions with a change of the total spin S of the complex are also forbidden ($\Delta S = 0$) [8, 37, 41, 42].
In UV-Vis spectroscopy relaxation occurs fast and energy is released radiationless (R) as vibrational, rotational and translational energy either within one excited state or between two states as internal conversion (IC) (Figure 3.9) [37]. Further relaxation processes, e.g. radiationless intersystem crossing (ISC), fluorescence (F) and phosphorescence (P), including emission of radiation, will be illustrated in Chapter 3.4.3.

For the quantitative interpretation of spectra of transition metal compounds *Tanabe-Sugano* diagrams are used [43], which take into consideration both weak and strong field ligands. For each electronic configuration such diagrams exist. Both the energy E and the field strength Δ are expressed as reduced dimensions E/B and Δ/B by the *Racah* parameter B. The *Racah* parameter B of free ions always deviates from the *Racah* parameter B' of ions in complexes. Due to the delocalisation of electrons in the orbitals of the central ion and its ligands the so-called *nephelauxetic* effect occurs. Thus, the electronic repulsion of the electrons and B' decreases. The ratio of B' to B is called the nephelauxetic ratio β (Equation 3.16) [42].
Both ligands and metal ions can be arranged in a nephelauxetic order (Table 3.1). With increasing oxidation ability of the metal and increasing polarisability and reduction ability of the ligand β increases.

$$\beta = B'/B \tag{3.16}$$

Equation 3.16: Nephelauxetic ratio β; B': *Racah* parameter of ions in complexes, B: *Racah* parameter of free ions [42].

Table 3.1: Nephelauxetic order of selected metals and ligands

Metals
$Mn^{2+} < V^{2+} < Mo^{2+} < Cr^{3+} < Fe^{3+} < Co^{3+} < Mn^{4+} < Pt^{4+}$
Ligands
$F^- < H_2O < NH_3 < Cl^- < CN^- < Br^- < I^- < S^{2-}$

In a *Tanabe-Sugano* diagram the ground state is always represented by the abscissa and all energies of the excited states are shown relatively to the ground state. The ratios of all observed transition energies to the first transition are calculated and marked in the diagram by sliding along the abscissa until the ratio is found. Δ/B is obtained. At this position E/B for all transitions can be marked and B' can be calculated. The average value corresponds to B' of the metal ion in the complex. Subsequently the size of the ligand field splitting Δ can be calculated.

Measurements were carried out in the range of 200–800 nm using a Cary 300 Scan UV-Vis spectrometer (Varian, Santa Clara, USA) and the software Varian UV Scan Application [44]. Spectra are depicted in reflection intensities R in % as a function against the wavelength in nm. The received data were plotted using the software OriginPro [28].

3.4.3 Fluorescence Spectroscopy

Via fluorescence spectroscopy, compounds exhibiting luminescence by exposing them to short-wavelength radiation in the UV-Vis region (200–800 nm) are investigated. This phenomenon either occurs as fluorescence or as phosphorescence. The latter includes emission of light with low emission rates in the range of milliseconds to seconds (10^3–$10^0\,s^{-1}$) after excitation. Due to the excited electron having the same spin orientation as the ground state electron, emission from the triplet excited state is spin-forbidden ($\Delta S \neq 0$) and results in slow emission rates. Intersystem crossing (ISC) is the transition between the singlet and triplet state (Figure 3.9). As this phenomenon will not be part of further discussions, more details can be found in the corresponding literature [37, 40].

Fluorescence represents a phenomenon with fast emission rates of photons ($10^8\,s^{-1}$) after excitation. In contrast to phosphorescence, fluorescence occurs as allowed emission of a photon if an electron returns from the excited singlet state S_n ($n = 1,2,3,...$) to the ground state S_0 with no change of the total spin S ($\Delta S = 0$) [37, 40]. Usually excitation to a higher vibrational level of S_2 or S_3 occurs, and within $10^{-12}\,s$ or less, relaxation takes place to the lowest vibrational level of S_1 via IC [37, 40]. This relaxation process is faster than fluorescence emission, which occurs therefore normally from the lowest vibrational level of S_1. Emission to the electronic ground state first occurs to a higher excited vibrational ground state of S_0 before thermal equilibrium is reached within $10^{-12}\,s$. Due to different radiationless relaxation processes, e.g. IC and R, the wavelength of emitted photons is in the visible range and is usually larger than the wavelength of the absorbed photons. This wavelength difference is called *Stokes*-shift [40] In contrast to this are upconversion (anti-*Stokes*) phosphors, which convert several low-energy photons into one high-energy photon [4].

Conventional inorganic phosphors consist of a host structure with a small amount of doped activator ions of about 10 mol-% or less. Activator ions can be divided into two groups.
The involved energetic states of trivalent lanthanide ions Ln^{3+} interact only weakly with the host lattice. Due to strong shielding of the $5s^2$ and $5p^6$ orbitals, crystal field splitting is very small, and weak $4f$–$4f$ transitions occur leading to the characteristic line emission [3, 9, 10]. Since they are parity forbidden they only become allowed by admixture of states of the opposite parity. The energy levels of free trivalent lanthanide ions up to $42000\,cm^{-1}$ investigated by *Dieke* and *Crosswhite* are shown in Figure 3.10 [45, 46].

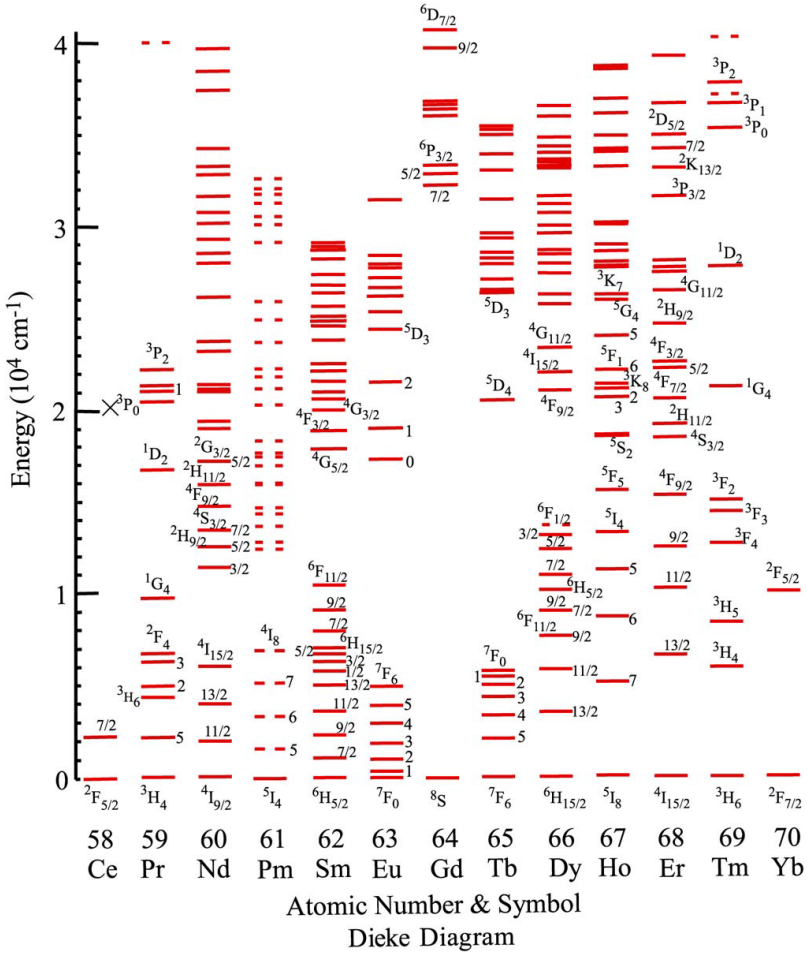

Figure 3.10: *Dieke* diagram for free Ln^{3+} ions [46].

Using this diagram for analysis of $4f$–$4f$ transitions is a helpful tool to assign the corresponding transitions. Many transitions between the depicted energy levels are in the visible range (12500–25000 cm^{-1}), which makes them very useful for optical applications. In the meantime optical materials working in the UV or VUV spectral region are demanded. Lanthanide ions would be well suited due to a large number of energy levels in this region (Figure 3.10) [45, 46].
A strong interaction between activators and host lattice occurs in ions exhibiting electrons in d orbitals, e.g. in Mn^{2+}, Eu^{2+} and Ce^{3+}, as well as in s^2 ions, such as Pb^{2+} and Sb^{3+} or in complex anions, e.g. MoO_4^{2-} or WO_4^{2-}. Due to parity allowed interconfigurational $4f^n \rightarrow 4f^{n-1}5d$ transitions or charge transfer (CT) from complex anions to the activator ion, broad absorption and emission bands occur, respectively [3, 9].

Excitation and emission spectra were recorded at room temperature on a Fluoromax-4 spectrofluorometer with a Xe plasma lamp (Horiba Scientific, Unterhaching) using the software FluorEssence [47]. The received data were plotted using the software OriginPro [28].

3.4.3.1 Luminescence of Ce^{3+}

Ce^{3+} is one representative as typical f–d emitter. These transitions are allowed and thus relatively fast. A very prominent example of a yellow broad band phosphor is $Y_3Al_5O_{12}$:Ce^{3+} (YAG:Ce). [3, 4, 9, 48–50]. In combination with a blue light emitting diode (LED) based on GaN [5] white light can be produced with efficiencies comparable to halogen lamps [3, 4, 9, 49, 50]. Other Ce containing phosphors are (Ce,Tb)$MgAl_{11}O_{19}$, $LaPO_4$:Ce and $SrAl_{12}O_{19}$:Ce [3, 4, 9, 49, 51]. In the ground state the term symbol of Ce^{3+} is $^2F_{5/2}$ with the electronic configuration [Xe] $4f^1\,5d^0\,6s^0$. The excitation and emission wavelengths strongly depend from the ligand field splitting of the $5d$ orbitals. Stronger interaction of the ligands lead to a stronger ligand field splitting and the emission is shifted to longer wavelengths of the electromagnetic spectrum. Depending on the chemical surrounding emissions can be shifted between 510 and 280 nm [3].

Common are phosphors, which are co-doped with Tb^{3+}, e.g. $MgAl_{11}O_{19}$:Ce^{3+},Tb^{3+}, $LaPO_4$:Ce^{3+},Tb^{3+} and $GdMgB_5O_{10}$:Ce^{3+},Tb^{3+}. Ce^{3+} as sensitizer is a helpful tool to intensify the desired emission of Tb^{3+}. Excitation and emission occur on different optical centres. Due to the overlap of the emission wavelength of Ce^{3+} with the excitation wavelength of Tb^{3+}, excited Ce^{3+} transfers its energy towards the Tb^{3+} centres, where intensified green emission occurs [3, 9, 49].

3.4.3.2 Luminescence of Eu^{3+}

Eu^{3+} ([Xe]$4f^6$) is a typical f–f line emitter in the red spectral region and therefore has applications in illumination and display technology [4, 50–52]. Next to the more stable oxidation state +III, europium also occurs as Eu^{2+} [8], which will be discussed in Chapter 3.4.3.3. In the ground state the term symbol of Eu^{3+} is $^7F_0$. By absorption of distinct energies of electromagnetic radiation, excitation to ^5D_J, ^5L_J and ^5H_J levels is possible [45, 46, 53]. As mentioned before, radiationless relaxation processes occur to the lowest vibrational level $^5D_0$, which are followed by emission in the visible range to the electronic ground states ^7F_J. The originally spin and parity forbidden transitions, which become allowed by admixture of states of the opposite parity lead to the well known emissions from $^5D_0$ to the ^7F_J levels ($J = 0$, 1, 2, 3, 4) in the red region of the visible spectrum at around 580, 590, 620, 650 and 695 nm, respectively. In comparison, the $^5D_0 \rightarrow {}^7F_5$ and $^5D_0 \rightarrow {}^7F_6$ transitions are of very weak intensity in the near infrared region at around 750 and 810 nm [53].

Investigations of *Blasse et al.* exhibited varying intensity ratios of the main transitions $^5D_0 \rightarrow {}^7F_1$ and $^5D_0 \rightarrow {}^7F_2$. In compounds with Eu^{3+} in a strict centre of symmetry the $^5D_0 \rightarrow {}^7F_1$ transition dominates as it is insensitive to the site symmetry [54]. As

electric dipole transitions are strictly forbidden, this transition must be due to a magnetic dipole transition. In contrast, if Eu^{3+} occupies a site with no centre of symmetry, the dominant electric dipole transition is $^5D_0 \rightarrow {}^7F_2$ due to admixture of states of the opposite parity. Transitions with $\Delta J = 2$, 4 or 6 are now allowed and are called hypersensitive. Usually small deviations from inversion symmetry occur and lead to $^5D_0 \rightarrow {}^7F_1$ and $^5D_0 \rightarrow {}^7F_2$ transitions of similar intensity [55, 56]. As $4f$ electrons are well shielded, there is only a small influence of the crystal field on the ion in the host lattice with a crystal field splitting of the energy levels of about $100\,cm^{-1}$. Therefore only a small shift in the emission wavelength can be achieved by varying the corresponding ligands [10].

Eu^{3+} containing red phosphors found their application in the illumination sector. Initially they were only present in high pressure mercury discharge lamps, e.g. $Y(V,B,P)O_4:Eu^{3+}$ [3, 49]. Later application was in low pressure mercury discharge lamps (fluorescent lamps), so-called Color 80 lamps, e.g. $Y_2O_3:Eu^{3+}$, using the tri-color concept, where three narrow band emitters with emission maxima at around 450, 540 and 610 nm are combined [3, 49, 57].

3.4.3.3 Luminescence of Eu^{2+}

Due to its parity allowed broad f–d transitions in the visible range, Eu^{2+} has been established as an efficient absorber and emitter in compounds used as phosphors for high quality fluorescent lamps (e.g. $BaMgAl_{10}O_{17}:Eu^{2+}$ (BAM) [9], $Sr_4Al_{14}O_{25}:Eu^{2+}$ and $Sr_5(PO_4)_3Cl:Eu^{2+}$ [49]). Further compounds such as $Ba_2Si_5N_8:Eu^{2+}$ [49, 58], $Sr_2Si_5N_8:Eu^{2+}$ and $Eu_2Si_2O_2N_2:Eu^{2+}$ [58, 59] reveal great potential for optical applications. Doping of compounds containing Sr^{2+}, Ca^{2+} or Ba^{2+} ions with divalent europium is suitable due to their similar ionic radii ($r_{Eu^{2+}} = 1.17\,pm$, $r_{Ca^{2+}} = 1.00\,pm$, $r_{Sr^{2+}} = 1.18\,pm$, $r_{Ba^{2+}} = 1.35\,pm$) [60, 61]. In the ground state the term symbol of Eu^{2+} is $^8S_{7/2}$ with the electronic configuration $[Xe]\,4f^7\,5d^0\,6s^0$. The coordination sphere has a strong influence on the ligand field splitting of the $5d$ orbitals. The stronger the interaction of the ligands with Eu^{2+} the larger is the ligand field splitting of the $5d$ orbitals. Thus the lower $5d$ orbitals approach the $4f$ orbitals and the excitation of an electron into the lower $5d$ levels is shifted to the visible region of the electromagnetic spectrum. Emissions of Eu^{2+} containing compounds can range from the UV ($BaFBr:Eu^{2+}$ [62]), to the blue ($BaMgAl_{10}O_{17}:Eu^{2+}$ (BAM), $\lambda_{max} = 453\,nm$ [9, 63]) and green ($Eu_2Si_2O_2N_2:Eu^{2+}$, $\lambda_{max} = 575\,nm$ [58, 59]) up to the red ($Ba_2Si_5N_8:Eu^{2+}$, $\lambda_{max} = 610\,nm$ [58, 59]) region of the visible spectrum. This reveals a great opportunity for tuning emission maxima by varying the type of ligands.

3.4.3.4 Luminescence of Tb^{3+}

As most of the ternary lanthanides Tb^{3+} ([Xe]$4f^8$) is a typical f–f line emitter in the green-yellow spectral region [9, 49]. In the ground state the term symbol of Tb^{3+} is $^7F_6$ [45, 46, 64]. Excitation occurs in the UV region and via radiationless relaxation processes the system relaxes into the lowest vibrational level $^5D_4$ followed by emission to the electronic ground states ^7F_J. The well known emissions from $^5D_4$ to the $^7F_6$, $^7F_5$, $^7F_4$ and $^7F_3$ level occur in the green-yellow region of the visible spectrum at around 490, 543, 583 and 617 nm, respectively. The transitions from $^5D_4$ to $^7F_2$, $^7F_1$ and $^7F_0$ are very weak in the orange-red region at around 645, 664 and 674 nm, respectively. [64].

In the past Tb^{3+} has been studied for phosphor and laser applications [65] and is used in the meantime in conversion phosphors for high quality fluorescent lamps [9, 66].

3.4.3.5 Luminescence of Dy^{3+}

The energy level diagram of the f–f line emitter Dy^{3+} ([Xe]$4f^9$) was well investigated by *Carnall et al.*. In the ground state it adopts the term symbol $^6H_{15/2}$. Excitation occurs in the UV region and due to internal relaxation processes all visible emissions occur from the lowest vibrational level $^6F_{9/2}$ to the $^6H_{15/2}$, $^6H_{13/2}$ and $^6H_{11/2}$ electronic ground states as white emission [67]. Additionally, a weak emission at 450 nm can be observed, which can be assigned to the $^4F_{7/2}\rightarrow{}^6H_{13/2}$ transition. Next to a hypersensitive transition in the near infrared region at around 1300 nm [67–69], Dy^{3+} also exhibits a hypersensitive transition in the yellow region at around 570 nm, which can be assigned to the $^4F_{9/2}\rightarrow{}^6H_{13/2}$ transition [54, 70]. As discussed in Chapter 3.4.3.2 the hypersensitive transition of the corresponding Ln^{3+} ion strongly depends on its site symmetry. If the surrounding of Dy^{3+} reveals a high symmetry, the electric dipole transition is forbidden and therefore rather weak compared to the $^4F_{9/2}\rightarrow{}^6H_{15/2}$ transition. If the surrounding of Dy^{3+} is of low symmetry, the $^4F_{9/2}\rightarrow{}^6H_{13/2}$ transition is more intense.

Dy^{3+} is used in metal halide lamps. In addition to mercury, metal halogenides, e.g. NaI, LnI_3 (Ln = Dy, Ho, Tm), are added. Iodine containing compounds posses the advantage of bringing hardly vaporizable metals into the gas phase at a moderate temperature, where they can dissociate partially and generate line emission [50, 52].

3.4.3.6 Optical Properties of Ho^{3+}

The energy level diagram of the f–f line emitter Ho^{3+} ($[Xe]4f^{10}$) was also well investigated by *Carnall et al.*. In the ground state it adopts the term symbol $^5I_8$ [67]. Due to the large number of neighboring energy levels in pure Ho^{3+} compounds, efficient fluorescence extinction via reabsorption occurs [71]. Hence only absorption and reflection spectra for investigation of optical properties can be measured, respectively.

Holmium compounds comprise an optical phenomenon called the *alexandrite effect*, named after the mineral alexandrite, $BeAl_{2-x}Cr_xO_4$, which is a variety of chrysoberyl. Depending on the incident light source, the observed body colour changes from green in sunlight to reddish purple in artificial light [72–74]. In contrast to holmium compounds, Cr^{3+} containing compounds are subject to a strong influence of the ligands on the $3d$ orbitals of the Cr^{3+} ions. Replacing Al^{3+} partially by Cr^{3+} ions leads to crystal field splitting and due to the different spectral composition of artificial and daylight the *alexandrite effect* occurs. In Ho^{3+} containing compounds only $4f$–$4f$ transitions occur, which are nearly independent on the surrounding ligand field. The typical absorption bands occur in the UV-Vis region. Exposed to sunlight, holmium containing compounds absorb more radiation with blue content and the reflected light appears yellow. In contrast, artificial light (e.g. Color 80 lamps) exhibits narrowband emissions in the blue, green and red region of the visible spectrum. The green emission is absorbed by the holmium compound and the reflected light appears pink. Exactly at the wavelengths of the blue and red emission bands of the artificial light no absorption of the holmium compound occurs.

It is well known that Ho^{3+} ions doped in a host lattice can lead to short-wave laser emission in the µm range [75–79]. Due to the large number of electronic levels transitions occur in the visible and in the infrared region of the spectrum [79].

3.5 Magnetic Properties

The investigation of magnetic properties was used to confirm the corresponding oxidation states of the metals and thus the stoichiometric composition of the synthesised compounds. Depending on the presence of centres with magnetic moments, compounds can show different magnetic behaviour. Diamagnetism is a phenomenon that occurs in every material, as closed electron shells are always present to a certain degree, but can be rather weak, if other magnetic properties are present as well. In

contrast, paramagnetism occurs, if unpaired electrons in the valance shells of isolated centers are present. They are sensitive to external magnetic fields and lead to cooperative effects below specific phase transition temperatures, such as *ferromagnetism*, where magnetic moments align parallel to each other, or *antiferromagnetism*, where antiparallel arrangement of the magnetic moments occurs. A third common possibility, *ferrimagnetism*, shows partial compensation of the magnetic moments due to different absolute values.

The susceptibility χ is the dimensionless but temperature dependent proportionality factor in the ratio of the magnetisation $\vec{M}$ (sum of atomic magnetic moments μ per volume) of a compound to the external magnetic field $\vec{H}$ (Equation 3.17). In a paramagnet the magnetisation $\vec{M}$ and the magnetic field $\vec{H}$ are proportional, whereas in a diamagnetic material they are in inverse proportion [80].

$$\vec{M} = \chi \vec{H} \tag{3.17}$$

Equation 3.17: Magnetisation $\vec{M}$; χ: susceptibility, $\vec{H}$: magnetic field [80].

In materials with centers of unpaired electrons magnetic dipoles are oriented randomly and thus no directional magnetisation exists. Applying an external magnetic field leads to orientation of the magnetic moments parallel to the magnetic field in dependency on the present temperature. Due to the macroscopic magnetisation parallel to the magnetic field, positive susceptibility values χ_{mol} are observed, which increase with decreasing temperature (*Curie* paramagnetism) according to *Curie's* law (Equation 3.18) [80].

$$\chi_{\mathrm{mol}} = \frac{C}{T} = \mu_0 \frac{N_{\mathrm{A}} \mu^2}{3 k_{\mathrm{B}} T} \tag{3.18}$$

Equation 3.18: *Curie's* law: χ_{mol}: susceptibility, C: *Curie* constant, T: temperature, μ_0: vacuum permeability, N_{A}: *Avogadro* constant, μ: atomic magnetic moment, k_{B}: *Boltzmann* constant [80].

The *Curie* constant C is a characteristic parameter for a material and can be depicted as gradient, when the reciprocal susceptibility χ^{-1} is plotted against the temperature T. *Curie's* law is invalid below a critical temperature and above a critical magnetic field due to saturation magnetisation.

In general, the susceptibility χ_{mol} of a paramagnetic material is described by the *Curie-Weiss* law (Equation 3.19), where cooperative effects between adjacent centers are included [80].

$$\chi_{\mathrm{mol}} = \frac{C}{T - \Theta} \tag{3.19}$$

Equation 3.19: *Curie-Weiss* law; χ_{mol}: susceptibility, C: *Curie* constant, T: temperature, Θ: parameter for temperature correction [80].

Equation 3.18 is solved for μ_{eff} in *Bohr* magnetons μ_{B} per magnetic ion by replacing μ (Equation 3.20) and insertion of the values of the constants. For investigation of the magnetic properties of a material the obtained values for μ_{eff} are compared with theoretical values.

$$\mu_{\mathrm{eff}} = \sqrt{\frac{3k_{\mathrm{B}}C}{\mu_0 N_{\mathrm{A}}}} \approx \sqrt{4\pi C} \cdot 0.79773 \tag{3.20}$$

Equation 3.20: Effective magnetic moment μ_{eff}; k_{B}: *Boltzmann* constant, C: *Curie* constant, μ_0: vacuum permeability, N_{A}: *Avogadro* constant, μ_{B}: *Bohr* magneton [80].

The theoretical value of μ_{eff} can be calculated on the basis of the electron configuration with respect to the quantum numbers S (total spin) and L (total orbital angular momentum)(Equation 3.21). The weak influence of the LS (*Russell-Saunders*) coupling leads to the total momentum J.

$$\mu_{\mathrm{eff}} = g\sqrt{J(J+1)}\mu_{\mathrm{B}} \tag{3.21}$$

Equation 3.21: Effective magnetic moment μ_{eff}; g: *Landé* factor, J: total momentum, μ_{B}: *Bohr* magneton [80].

The *Landé* factor g considers the contributions of spin and angular momentum (Equation 3.22). A term symbol ${}^{2S+1}L_J$ with $2S+1$ as the multiplicity describes the *Russell-Saunders* term. For the determination of S and L a scheme found in the literature is used [80].

$$g = 1 + \frac{J(J+1) + S(S+1) - L(L+1)}{2J(J+1)} \tag{3.22}$$

Equation 3.22: *Landé* factor g; J: total momentum, S: total spin, L: total orbital angular momentum [80].

This approximation works very well for rare-earth ions taking into account that the well shielded f electrons are responsible for the magnetic properties. Interactions

with the crystal lattice are negligible and rare-earth ions can thus be treated as free ions.

Due to strong interactions between $3d$ metal ions and ligands, no approximation for isolated ions can be applied. Instead the approach depends on the strength of the surrounding ligand field. Generally one can presume that the angular momentum is rather small compared to a strong ligand field and the effective magnetic moment μ_{eff} simplifies to the "spin-only" scenario (Equation 3.23).

$$\mu_{\text{eff}} = 2\sqrt{S(S+1)}\mu_{\text{B}} \tag{3.23}$$

Equation 3.23: Effective magnetic moment μ_{eff}; S: total spin, μ_{B}: *Bohr* magneton [80].

The temperature dependent magnetic susceptibility data were recorded on a MPMS-XL superconducting quantum-interference device (SQUID) magnetometer (Quantum Design Inc., San Diego, USA) in a magnetic field of 1000 Oe and in a temperature range of $1.8\,\text{K} < \text{T} < 400\,\text{K}$.

3.6 Thermogravimetric Properties

To study the thermal stability of the synthesised compounds, thermogravimetric measurements were carried out. A small amount of the sample (15–30 mg) was filled in a special alumina crucible and was heated with a constant heating rate to a certain temperature. Depending on temperature and time, mass loss was observed. Possible occurring processes are vaporization, sublimation, desorption, decomposition and oxidation.

Thermogravimetric measurements were carried out on a STA-409 PC thermal analyzer (Netzsch, Selb) in the temperature range of 22–1350 °C in nitrogen or forming gas (H_2/N_2) flow (70 mL min^{-1}) with a heating rate of 5–10 °C/min. The maximum temperature was held for 15 min before the cooling process to room temperature started. The data were recorded with the software Netzsch STA [81] and was plotted using the software OriginPro [28].

4 Compound Classes

4.1 Borates

Borates, the salts of the boric acid, reveal a large variety in structure and composition. Due to the possible coordination of three or four oxygen atoms in planar $B\Phi_3$ or tetrahedral $B\Phi_4$ ($\Phi = O$, OH) units (Figure 4.1), they provide an even more manifold structural diversity than silicates [8, 82, 83].

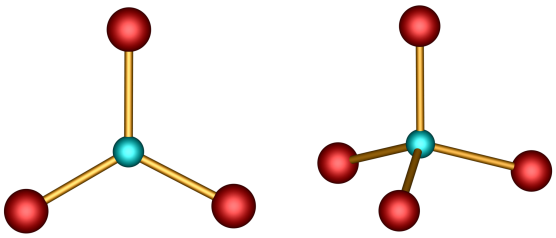

Figure 4.1: Trigonal planar $B\Phi_3$ and tetrahedral $B\Phi_4$ ($\Phi = O$, OH) groups; boron turquoise, oxygen red.

Besides isolated units condensation ranges from isle, chain and layer to three-dimensional network structures. Whereas in monoborates $B\Phi_3$ units are predominantly represented, in oligoborates $B\Phi_3$ triangles and $B\Phi_4$ tetrahedra coexist. In nature almost all borates are hydrated possessing both hydroxyl groups and crystal water. Polyborates reveal besides condensed isle borates (e.g. $Li_2B_4O_7$ [84]) a number of high-pressure modifications, which exhibit networks of corner- and edge-sharing BO_4 groups, (e.g. $Dy_4B_6O_{15}$ [85]) [8, 83].

Condensed polyborates, which occur both in minerals and in synthetic inorganic compounds, are characterised topologically by so-called FBBs (*F*undamental *B*uilding *B*locks) and their structural units [82, 83]. According to *Hawthorne* [86–89] the FBB represents a cluster of coordination polyhedra as a representative oligomeric fragment, which is repeated to form usually a complex structural anionic unit. Charge compensation is achieved by the presence of large low-valence interstitial cations. Such classifications are important to simplify the comparison of crystal structures enabling an additional insight on the bond topology. First attempts were made by *Christ* and *Clark*, whose classification is based on three principal criteria:

(1) the number of boron atoms n, (2) the number i of $B\Phi_3$ triangles Δ and j of $B\Phi_4$ tetrahedra $\square$ in the FBB and (3) the mode of polymerisation between the FBBs. They proposed the notation $n : i\Delta + j\square$ for each FBB [82, 90]. By then only borates exhibiting small FBBs with a maximum of six borate atoms were reported. Later borates containing larger and more complex FBBs were solved and the nomenclature of *Christ* and *Clark* could not distinguish clearly between FBBs. *Burns et al.* thus proposed to include information on the connectivity of the polyhedra. Investigations showed that borates strongly tend to form rings. Therefore the descriptor needs, besides the information of (1), (2) and (3) (as above), (4) the presence of rings <> and (5) their connectivity (−, =, ≡) within the FBB (Figure 4.2) [82, 83]. In this work the descriptor proposed by *Burns et al.* for borates is used [82, 91].

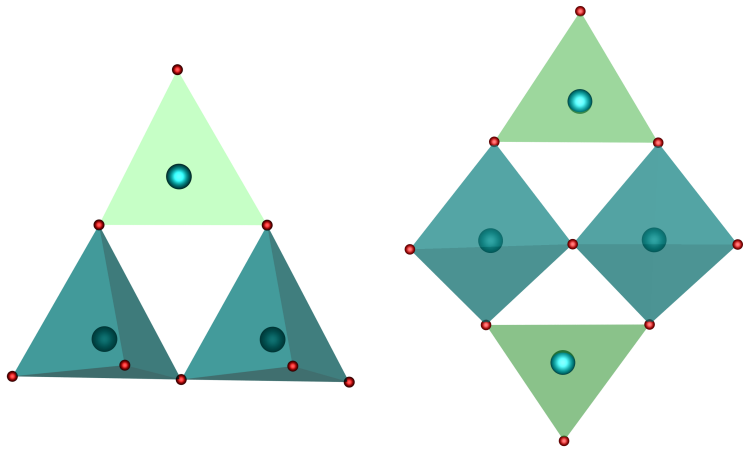

Figure 4.2: Examples of borate polyhedra as three-membered ring (Δ2□:<1Δ2□>, left) and two three-membered rings, that have two borate tetrahedra in common (2Δ2□:<Δ2□>=<Δ2□>, right); $B\Phi_3$ light green, $B\Phi_4$ turquoise (Φ = O, OH) [82].

4.2 Phosphates

Analogously to the borates, phosphates represent the salts of the phosphoric acid and its derivatives. In contrast, phosphorus is predominantly coordinated four-fold. Via a heating process over 200 and 300 °C the diphosphoric and oligophosphoric acids are built, respectively. Further heating leads besides the formation of cyclic metaphosphoric acids $(P_nO_{3n})^{n-}$ also to branched iso- or ultraphosphoric acids ($(P_{(2m+n)}O_{(5m+3n)})^{n-}$ or $(P_{(n+2)}O_{(3n+5)})^{n-}$) (Figure 4.3) [8, 92].

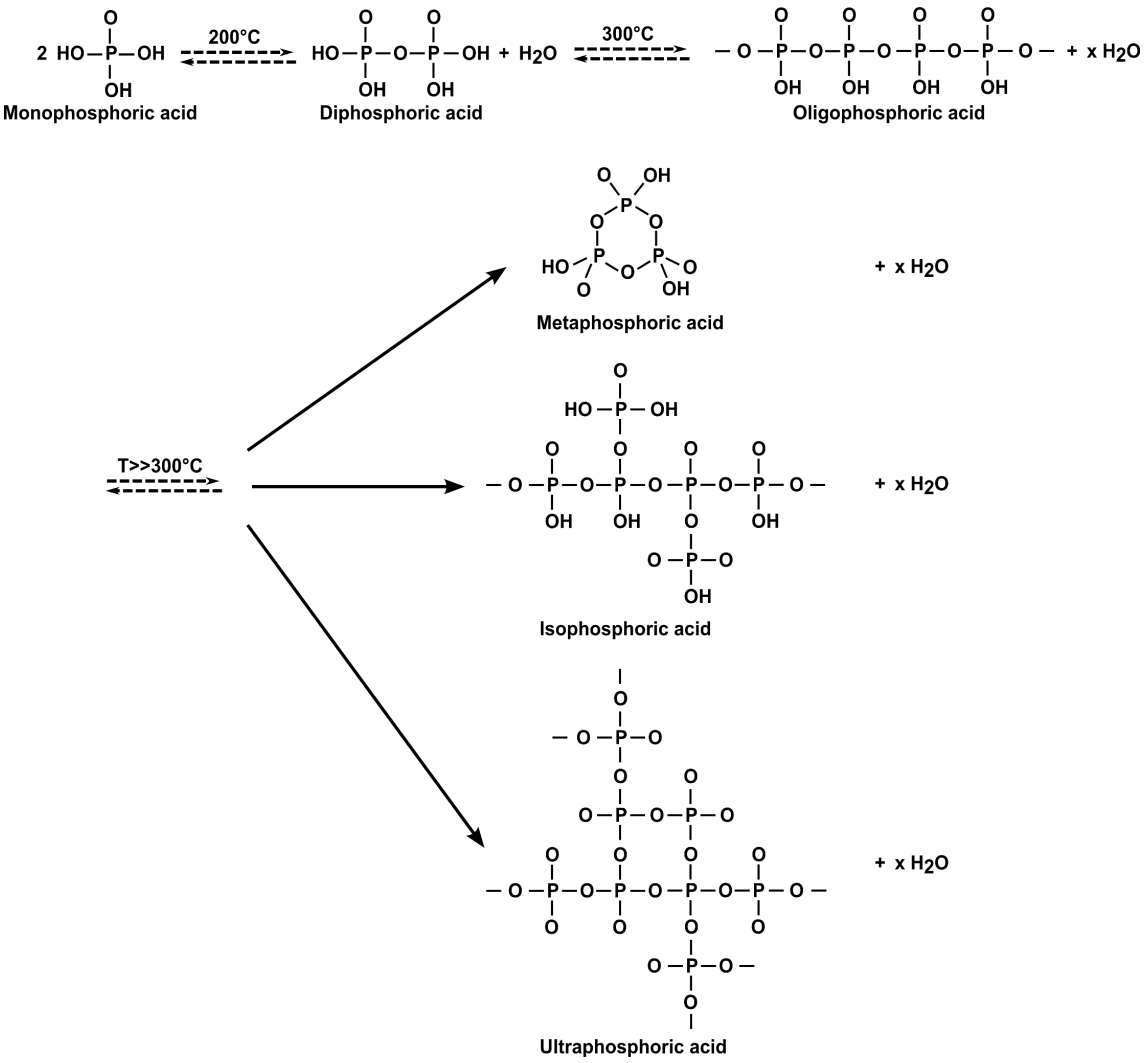

Figure 4.3: Condensation scheme of phosphoric acid.

The nomenclature of condensed phosphates gives the information of the number of phosphate atoms, e.g. for $n = 2$, $P_2O_7^{4-}$ ≙ diphosphate anion. For very large n the formula tends to $(P_nO_{3n})^{n-}$ as an infinite chain and is thus called a polyphosphate [92]. In contrast to the nomenclature of borates introduced by *Burns* and *Grice* [82, 83], no structural information is given.

Condensed trivalent phosphates reveal a great structural variety. Next to cyclic $[P_3O_9]^{3-}$ units (e.g. in $Ce(P_3O_9)\cdot 3H_2O$ [93], $MNa_3(P_3O_9)_2\cdot 9H_2O$ (M = Bi [94], Er [95], Y [96]), $RE(P_3O_9)\cdot 5H_2O$ (RE = Pr, Nd) [97]) also $[P_4O_{12}]^{4-}$ rings (e.g. in $Ba_2(P_4O_{12})\cdot 3.5H_2O$ [98], $Lu_4(P_4O_{12})_3$ [99], $M_2P_4O_{12}$ (M = Mg, Mn, Fe, Co, Ni, Cu [100, 101])) exist. Ultraphosphates with the general sum formula MP_5O_{14} (M = trivalent cation) tend to build polymorphs in four different structure types: SmP_5O_{14} (Type I) [102], HoP_5O_{14} (Type II) [103], HoP_5O_{14} (Type III) [104] and CeP_5O_{14} (Type IV) [105]. Lanthanide polyphosphates, which attracted interest due to their properties as efficient laser materials or phosphors, include besides the sum formula $Ln(PO_3)_3$ also lanthanide hydrogen-polyphosphates $Ln[H(PO_3)_4]$. A large

number of mixed trivalent monovalent cation polyphosphates ($M^{III}M^{I}(PO_3)_4$) is known exhibiting seven different structure types (Table 4.1) [92].

Table 4.1: Distribution of the seven structure types among the mixed trivalent monovalent cation polyphosphates $M^{III}M^{I}(PO_3)_4$ [92]

Type	M^{I}/M^{III}
I	Li/La–Lu
II	Na/Bi, La–Er
	Ag/Nd
III	K/Bi, La–Er
IV	K/Er–Lu
	NH_4/Bi
	Rb/Ce, Nd–Lu
	Cs/La, Pr–Er
	Tl/Nd
V	K/Tm–Lu
VI	Rb/La, Pr–Er
	Cs/La–Er
VII	K/Er
	NH_4/Y

Tetraphosphates as one representative of oligophosphates include already quite a number of compounds, whereas many of them form cyclophosphates. Up to now divalent cation tetraphosphates are only known of strontium ($Sr_3P_4O_{13}$ [106]) and barium (LT-$Ba_3P_4O_{13}$ [107, 108] and $Ba_3P_4O_{13}$ [107, 109]).

In 1986 *Millet et al.* determined the unit cell parameters of LT-$Ba_3P_4O_{13}$ ($a = 5.757$ Å, $b = 7.243$ Å, $c = 8.104$ Å, $\alpha = 82.75$ °, $\beta = 73.94$° and $\gamma = 70.71$°) and HT-$Ba_3P_4O_{13}$ ($a = 7.107$ Å, $b = 13.883$ Å, $c = 19.219$ Å) by indexing the corresponding powder diffractograms. The temperature of transformation of the two polymorphs was determined to occur at 870 °± 10 °C [107].

A few years later in 1991 *Gatehouse* and *Platts* took up this issue and investigated the structure of LT-$Ba_3P_4O_{13}$ crystallising in the triclinic space group $P\bar{1}$ with unit cell parameters of $a = 5.691(5)$ Å, $b = 7.238(7)$ Å, $c = 8.006(5)$ Å, $\alpha = 83.65(5)$ °, $\beta = 75.95(8)$° and $\gamma = 70.49(7)$° [108]. These values fit very well to those determined by *Millet et al.*.

In 2002 *Bennazha et al.* reported the single-crystal structure of LT-$Ba_3P_4O_{13}$, which was synthesised at 900 °C [109]. According to *Millet et al.* the temperature of transformation occurs at 870 °± 10 °C [107]. Thus, the discussed single-crystal structure should represent HT-$Ba_3P_4O_{13}$. It crystallises in the triclinic space

group $P\bar{1}$ with unit cell dimensions of $a = 7.557(1)$ Å, $b = 8.618(1)$ Å, $c = 10.582(1)$ Å, $\alpha = 108.26(1)$ °, $\beta = 104.50(1)$° and $\gamma = 102.37(1)$°. In contrast to LT-$Ba_3P_4O_{13}$ by *Gatehouse* and *Platts* (V =301.4 Å^3) this unit cell exhibits a doubled volume (V =600.65(12) Å^3). The comparison with the determined unit cell parameters of HT-$Ba_3P_4O_{13}$ by *Millet et al.* reveals a distant resemblance as halfed b and c axes, but no obvious relationship. For the data collection a small θ range between 6.2–12.8° was measured and the ratio of the R values ($R1 = 0.032$, $wR2 = 0.099$) is rather 1:3 instead of 1:2, which could indicate that the determination of the cell parameters might not be correct. For a clear determination the HT-structure of $Ba_3P_4O_{13}$ should be revised.
Strontium or barium tetraphosphates doped with Eu^{3+} or Eu^{2+} were characterised for potential applications as luminescent materials [110, 111].

4.3 Borophosphates

Borophosphates combine both structural properties of borates and phosphates and are furthermore in many cases isoelectronic to silicates [13, 112, 113]. Although nomenclature following *IUPAC* (*I*nternational *U*nion of *P*ure and *A*pplied *C*hemistry) would name such compounds as "phosphatoborates", "borophosphates" has been used generally in literature and is also used in this work. Compared to other compounds their history is rather young. *Bauer* first reported in 1965/1966 the synthesis and X-ray powder diffraction pattern of the isostructural phases $M^{II}[BPO_5]$ (M^{II} = Ca, Sr, Ba) [114, 115]. Finally the crystal structures of $M^{II}[BPO_5]$ (M^{II} = Ca, Sr) were solved by *Kniep et al.* in 1994 [112]. Within a few years the number of borophosphate compounds increased strongly and a first attempt to order borophosphate compounds according to their structures followed in 1998 by *Kniep et al.* [116]. In general, the authors distinguished between anhydrous and hydrated borophosphates. By then the number of hydrated borophosphates was already way larger than of anhydrous compounds. In 2007 *Ewald* and *Kniep* [13] represented a very detailed review of a systematic classification of borophosphates distinguishing first of all between tetrahedral and mixed coordinated partial structures, followed by the B:P ratio of the so-called BBUs (*B*asic *B*uilding *U*nits) and FBUs (*F*undamental *B*uilding *U*nit) as representative oligomeric fragments, the dimensionality (e.g. chains, layers, networks) and the degree of protonation (O:OH). It was observed that certain B:P ratios appear predominantly and some connection patterns are found more frequently. The classification of borophosphates is overtaken analogously from (alumo)silicates introduced by *Liebau* [113] and from borate chemistry [82, 83]. BBUs represent the simplest un- or open-branched oligomers

of which the more complex FBUs can be created. In general, borophosphate compounds are referred to as M_xO_y–B_2O_3–P_2O_5(–H_2O) (M = main group/transition metal) compounds, which can also incorporate organic molecules/cations. Boron and phosphorus are exclusively coordinated by oxygen and hydroxyl groups. Phosphorus always adopts the coordination $P\Phi_4$ (Φ = O, OH), while boron can be coordinated in a trigonal planar $B\Phi_3$ or tetrahedral $B\Phi_4$ manner. One structural feature – the B–O–P linkage – all borophosphates have in common. Until now no P–O–P linking has been observed. According to *Pauling's* fourth rule concerning the nature of contiguous polyhedra, cations possessing a high charge and a low coordination sphere do not tend to share these polyhedra with one another [117]. A similar phenomenon occurs in alumosilicates, where according to *Loewenstein* Al–O–Al linkages of tetrahedra are rarely observed [118]. According to the notation introduced for borates by *Burns* and *Grice* [82, 83] the descriptor of the BBU/FBU in borophosphates also reveals two strings of the type A:B. A gives the number of participating polyhedra and B includes the structural information of the connection. The symbols used in descriptors are presented in Table 4.2 and subsequently some examples for FBUs are shown in Figure 4.4 [13].

Table 4.2: Selected symbols used in descriptors [13]

Symbol	Description
□	tetrahedron
Δ	trigonal planar
<...>	ring motif
[...]	branching polyhedron
|	separator for branches
–, =, ≡	structural motifs share 1, 2, 3 common polyhedra

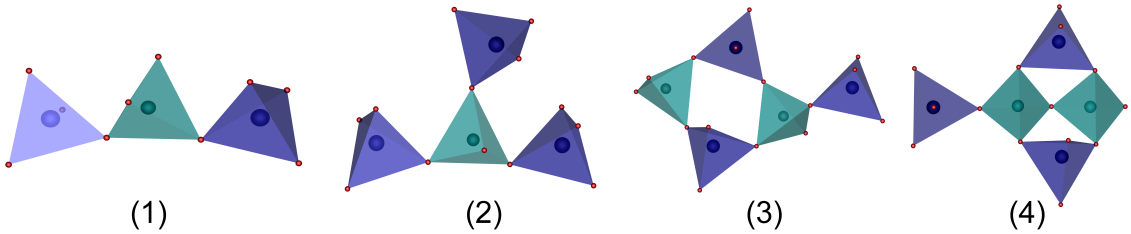

Figure 4.4: Examples of FBUs in borophosphates;
(1) 3□:3□ (uB trimer), (2) 4□:[□]□|□|□| (oB trimer), (3) 5□:<4□>□ (oB ring), (4) 5□:<3□>=<3□>□ (olB ring); phosphate tetrahedra blue, borate tetrahedra turquoise.

Due to the analogy in silicates, certain terms for the description of borophosphate anions were taken over [113] (Table 4.3).

Table 4.3: Selected terms for the description of borophosphate anions according to the concept for silicates [13, 113]

Term	Description
Branchedness	$B =$ uB, oB, cB, lB, olB, ...
	(unbranched, open-, cyclo-, loop, open-loop-branched)
Dimensionality	$D =$ 0, 1, 2, 3
	(oligomer or ring, chain, layer, network)
Multiplicity	$M =$ 1, 2, 3, ...
	(single, double, triple, ...)
Periodicity	$P =$ 1, 2, 3, ...
	(einer, zweier, dreier, ...)

The parameter branchedness B describes the connection pattern of complex anions. In Figure 4.5 a selection of different types of branching in chain borophosphates is presented [13, 113].

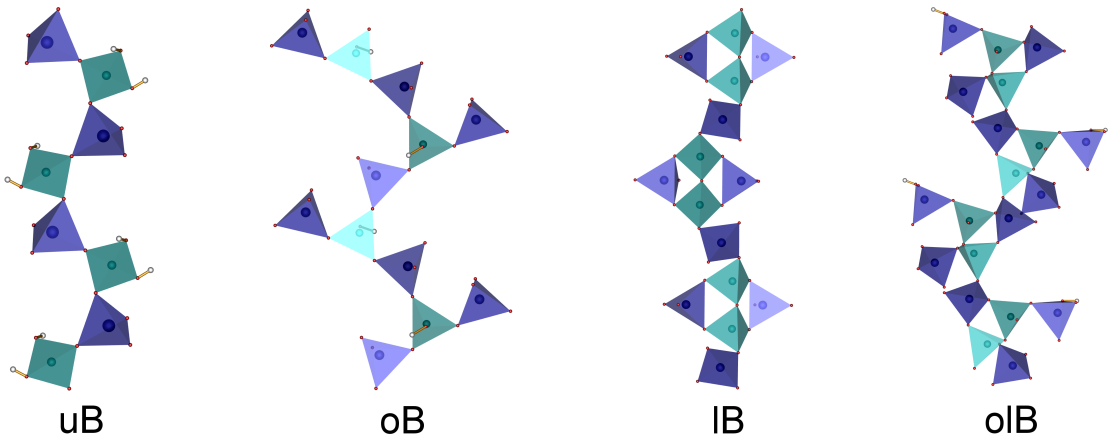

Figure 4.5: Different types of branching in borophosphates; uB (unbranched), oB (open-branched), lB (loop-branched), olB (open-loop-branched); phosphate tetrahedra blue, borate tetrahedra turquoise.

The dimensionality D indicates the extent of the spatial extension of the sequence to either oligomers, rings ($D = 0$), chains ($D = 1$), layers ($D = 2$) or networks ($D = 3$). The multiplicity M gives the number of identical assembled anions which are connected to multiple anions in the same dimensionality. The number of polyhedra in the repetitive unit of the linear part of the chain is defined as the periodicity P [13, 113].

BPO_4 is the simplest representative in the borophosphate family, which exhibits an isostructural relationship to the polymorphic modifications of SiO_2 [8, 119].

Borophosphates reveal a manifold structural chemistry and a great variety of connection patterns which leads to a large field of possible applications, e.g. as magnetic

materials (e.g. $(NH_4)_{0.4}Fe(II)_{0.55}Fe(III)_{0.5}(H_2O)_2[BP_2O_8]{\cdot}0.6H_2O$ [120], $M^{II}[BPO_4(OH)_2]$ (M^{II} = Mn, Fe, Co) [121], $(NH_4)_2Mn(II)[B_2P_3O_{11}(OH)_2]Cl$ [122]), as possible storage materials with framework structures (e.g. $(NH_4)Fe(III)[BP_2O_8]$ [120], $Na[ZnBP_2O_8]$ [123], $(C_4N_3H_{16})[Zn_3B_3P_6O_{24}]{\cdot}H_2O$ [124]) or as luminescent materials (e.g. $(Ba,Sr)_{1-x}Eu_yBPO_5$ ($0{\leq}x{\leq}0.5$, $0.003{\leq}y{\leq}0.15$) [125], $CaBPO_5$:*RE* (*RE* = Ce^{3+}, Sm^{3+}, Eu^{2+}, Eu^{3+}, Tb^{3+}, Dy^{3+}) [126], $Sr_6[B(PO_4)_4PO_4]:Eu^{2+}$ [127] and $KMn[BP_2O_7(OH_2)]$ [128]).

In contrast, borate-phosphates possess isolated BΦ_3, BΦ_4 and PΦ_4 (Φ = O, OH) units and are not classified as borophosphates [13].

4.4 Borosulphates

In contrast to borophosphates, borosulphates exhibit B–O–S linkage and represent an even younger compound class. In 2012 the crystal structure of the first borosulphate $K_5[B(SO_4)_4]$ was published by *Höppe et al.* [129], which will be presented in this work. Since then a great variety in structure and composition developed. The nomenclature is overtaken directly from borophosphates [13]. Sulphates do not show a strong tendency to build S–O–S linkage as oligoanions following *Pauling's* fourth rule [8, 117]. Nevertheless, examples of oligosulphates are already known [130–133]. Up to now borosulphate compounds exist with B:S ratios of 1:1, 1:2, 1:3, 1:4 and 2:3. $B_2S_2O_9$ with a B:S ratio of 1:1 was synthesised by *Logemann* and *Wickleder* and is the simplest representative in the borosulphate family. It comprises an uB sechser-single ring 6□:<6□> as FBU. The uB vierer-double layer shows phyllosilicate topology (Figure 4.6) [134].

Borosulphates possessing B:S ratios between 1:2 and 1:4 are up to now compounds with exclusively monovalent cations with one exception, which will also be discussed. All compounds with a B:S ratio of 1:2 have in common the $[B(SO_4)_2]^-$ anion, which adopts one typ of FBU: the uB trimer 3□:3□ in $A^I[B(SO_4)_2]$ ($A^I = H_3O$ [135], Li [136], Na, K, NH_4 [137]), which forms a lB vierer-single chain for $A^I = H_3O$, Na, K, NH_4 and an oB sechser network in $Li[B(SO_4)_2]$, respectively (Figure 4.7).

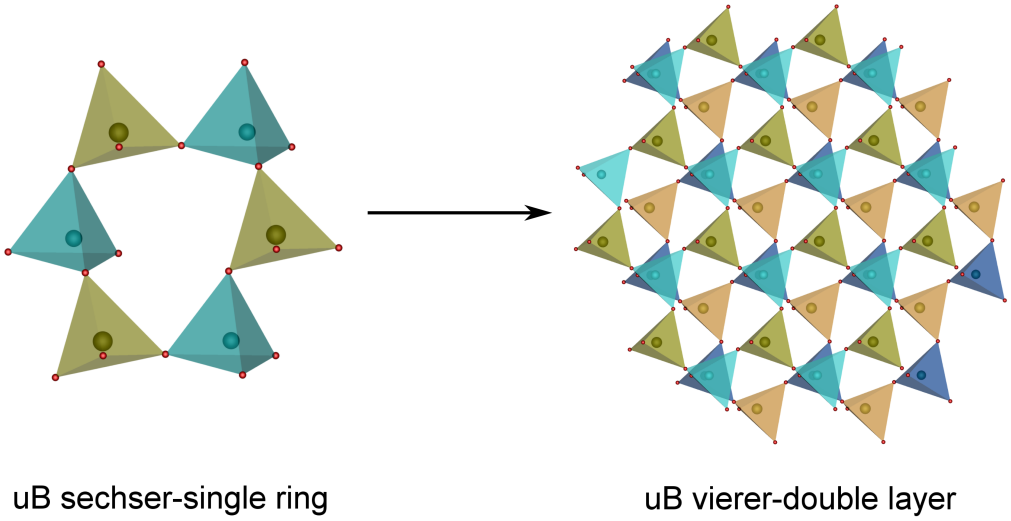

Figure 4.6: uB sechser-single ring 6□:<6□> as FBU (left), which forms an uB vierer-double layer (right); sulphate tetrahedra yellow (top layer) and orange (bottom layer), borate tetrahedra turquoise (top layer) and blue (bottom layer).

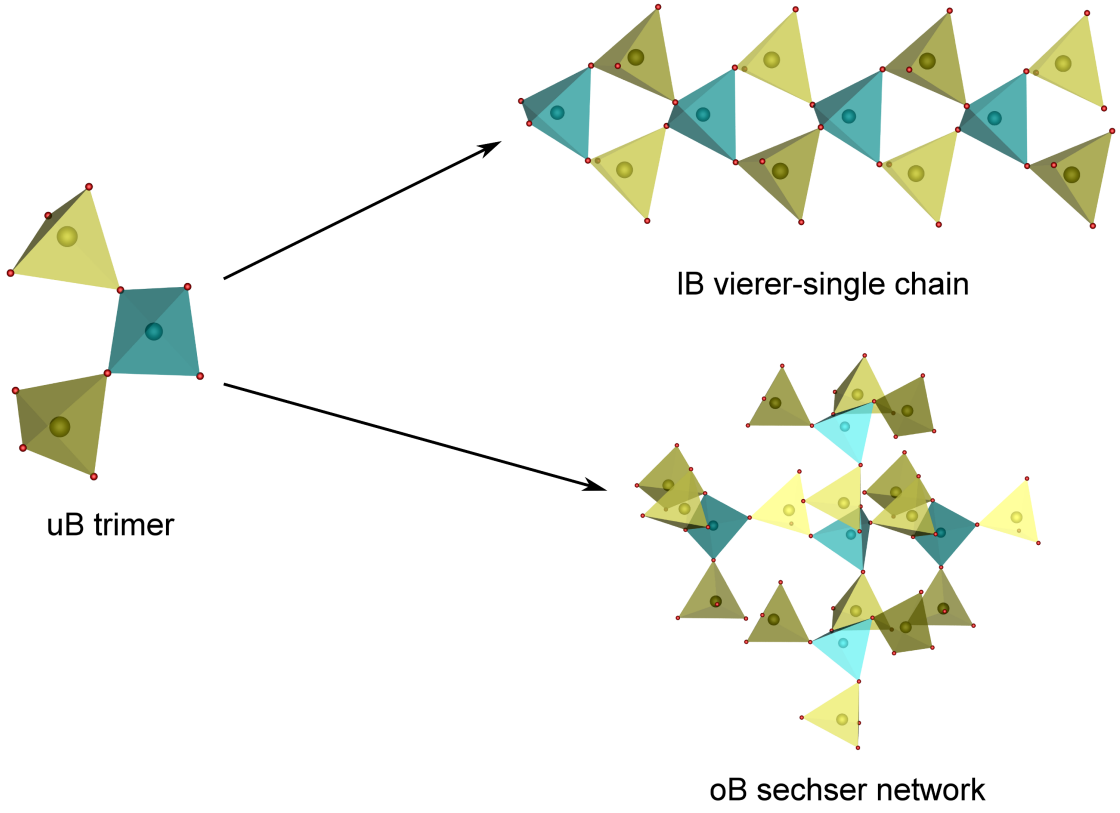

Figure 4.7: FBU with a B:S ratio of 1:2: uB trimer 3□:3□ forming a lB vierer-single chain (top) and an oB sechser network (bottom), respectively; sulphate tetrahedra yellow, borate tetrahedra turquoise.

Borosulphate compounds with a B:S ratio of 1:3 reveal three different FBUs. Whereas the FBU of $A^I_3[B(SO_4)_3]$ (A^I = K, Rb) [136] represents an oB tetramer 4□:[□]□|□|□| and forms an oB vierer-single chain, the FBU of $A^I[B(SO_4)(S_2O_7)]$ (A^I = H, Cs) exhibits an oB dreier-single ring 4□:<3□>□, which forms a cB vierer-single chain (Figure 4.8). $Gd[B(SO_4)_3]$ [138, 139] possesses an oB vierer-single ring 8□:□|□<4□>□|□ as FBU, which is present in the structure as oligomer.

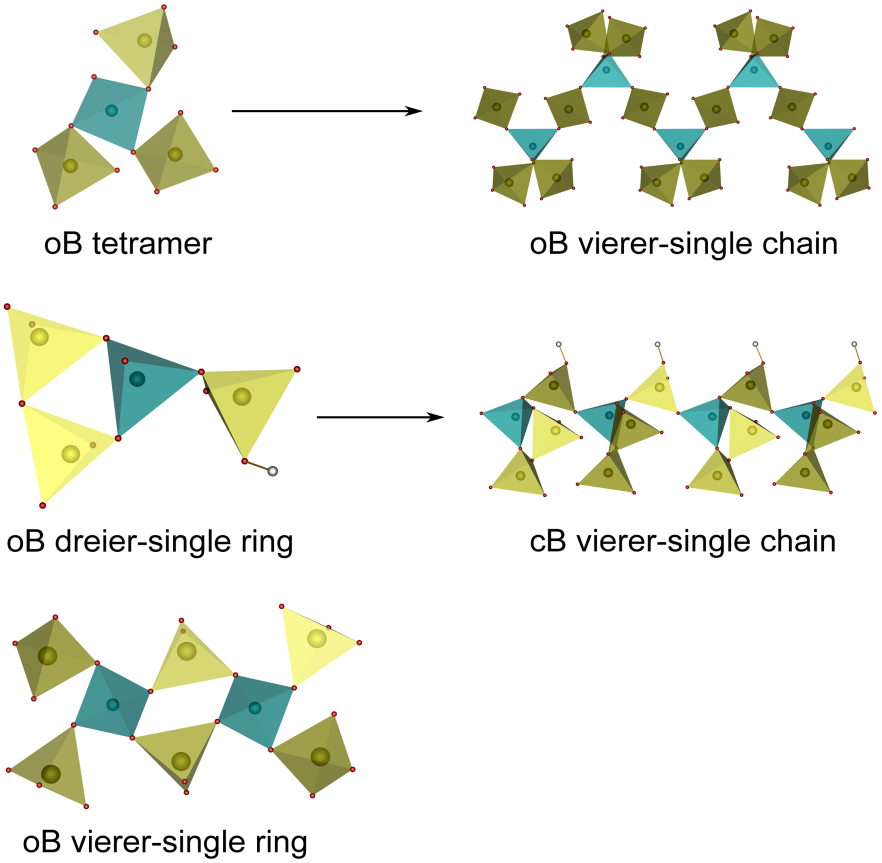

Figure 4.8: FBUs with a B:S ratio of 1:3: oB tetramer 4□:[□]□|□|□| forming an oB vierer-single chain (top), an oB dreier-single ring 4□:<3□>□ forming an cB vierer-single chain (middle) and an oB vierer-single ring 8□:□|□<4□>□|□ (bottom); sulphate tetrahedra yellow, borate tetrahedra turquoise.

Borosulphates with a B:S ratio of 1:4 show the largest number of representatives up to now exhibiting two different FBUs. An oB pentamer 5□:[□]□|□|□|□| as FBU is present in $A^I_5[B(SO_4)_4]$ (A^I = Li [137], Na-I, Na-II [136], K [129]) and in $K_4[HB(SO_4)_4]$ [140], which exists in the structure as oligomer. A further structure type possessing a disulphate unit is represented in $A^I[B(S_2O_7)_2]$ (A^I = Li [136], Na, K, NH_4 [137]) revealing a lB dreier-single ring 5□:<3□>–<3□>, which exists in the structure as oligomer (Figure 4.9).

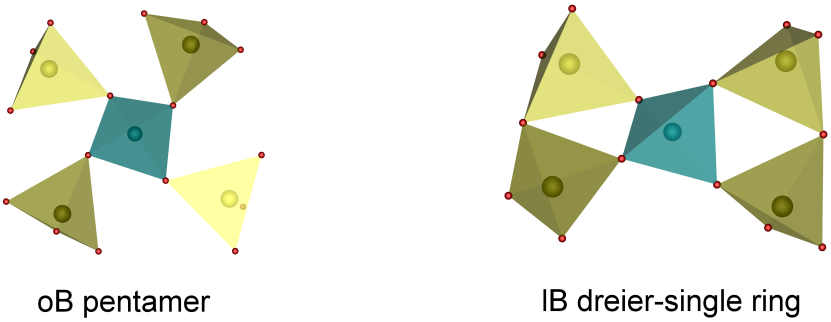

Figure 4.9: FBUs with a B:S ratio of 1:4: oB pentamer 5□:[□]□|□|□|□| (left) and lB dreier-single ring 5□:<3□>–<3□> (right); sulphate tetrahedra yellow, borate tetrahedra turquoise.

So far $Ba[B_2S_3O_{13}]$ [140] is the only alkaline earth borosulphate whose crystal structure is solved. The B:S ratio of 2:3 is also found for B:P in borophosphates [122, 141–144]. The well-known oB dreier-single ring 5□:□<3□>□ as FBU builds a lB zweier-double chain (Figure 4.10).

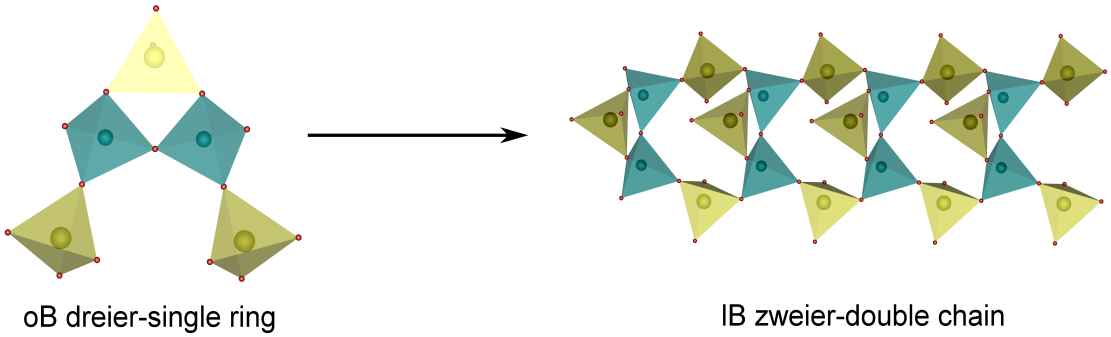

Figure 4.10: FBU with a B:S ratio of 2:3: oB dreier-single ring 5□:□<3□>□ (left) forming a lB zweier-double chain (right); sulphate tetrahedra yellow, borate tetrahedra turquoise.

Although up to now borosulphates exhibit a few cations from the group of the alkaline, alkaline-earth and lanthanide metals, they represent an interesting class of compounds due to the already existing structural variety.

5 The Borate $Cs_2[B_{10}O_{14}(OH)_4]\cdot H_2O$

The heavy alkaline pentaborate hydrates already attracted attention more than 40 years ago. In 1966 besides investigations of borate anhydrides *Kocher* published results about investigations in the systems Rb_2O-B_2O_3-H_2O and Cs_2O-B_2O_3-H_2O. Different hydrated pentaborates were studied via thermogravimetry. The caesium pentaborate heptahydrate (Cs_2O-$5B_2O_3$-$7H_2O$) revealed a thermal stability up to 60 °C. The thermal investigation under pressure confirmed the existence of further two hydrated pentaborates, Cs_2O-$5B_2O_3$-$8H_2O$ and Cs_2O-$5B_2O_3$-$2H_2O$, respectively. According to *Kocher* the phase diagram of the system caesium pentaborate-water is still incomplete [145]. A few years later *Benhassaine* pursued the investigations on the hydrated pentaborates of rubidium and caesium [146]. He reported of three novel compositions in the ternary system: α-caesium pentaborate octahydrate (α-Cs_2O-$5B_2O_3$-$8H_2O$), caesium pentaborate tetrahydrate (Cs_2O-$5B_2O_3$-$4H_2O$) and caesium pentaborate trihydrate (Cs_2O-$5B_2O_3$-$3H_2O$). He described the thermal decomposition of the novel compounds, which loose one water molecule after the other in defined steps. A graphical presentation was not included. Furthermore, he claimed that Cs_2O-$5B_2O_3$-$3H_2O$ is "identical" to Tl_2O-$5B_2O_3$-$3H_2O$ investigated by *Touboul* [147]. Up to now no structural investigations were performed. The title compound $Cs_2[B_{10}O_{14}(OH)_4]\cdot H_2O$ could be abbreviated as Cs_2O-$5B_2O_3$-$3H_2O$ and thus could be the compound described by *Benhassaine* in 1972. Therefore, besides the crystal structure and optical properties also the thermal properties of $Cs_2[B_{10}O_{14}(OH)_4]\cdot H_2O$ are investigated.

5.1 Synthesis

$Cs_2[B_{10}O_{14}(OH)_4]\cdot H_2O$ was synthesised under hydrothermal conditions. A mixture of 152.7 mg (0.4687 mmol) Cs_2CO_3 and 347.2 mg (5.615 mmol) H_3BO_3 was ground in an agate mortar, transferred into a 10 mL Teflon autoclave and kept at 195 °C. After seven days a colourless solid was obtained. The product was washed with hot water, filtered off and dried in air overnight.

$Cs_2[B_{10}O_{14}(OH)_4]\cdot H_2O$ was doped with 5.0 mol% Eu^{3+} by substituting the corresponding amount of Cs_2CO_3 by 5.0 mol% (10.03 mg) $Eu(NO_3)_3\cdot 5H_2O$.

5.2 X-Ray Powder Diffraction

The phase purity of the polycrystalline sample was checked by X-ray powder diffraction. Via a *Rietveld* analysis (Figure 5.1) the structure of $Cs_2[B_{10}O_{14}(OH)_4]\cdot H_2O$ was refined using the structure data of $Rb_2[B_{10}O_{14}(OH)_4]\cdot H_2O$ [15] as starting model. In their publication *Belokoneva et al.* determined half of the moiety formula as sum formula ($Rb[B_5O_7(OH)_2]\cdot 0.5H_2O$) with $Z = 4$ instead of 2. The refinement was carried out in the range between 5–140 °2θ. Initially, zero point, scale factor and lattice parameters were refined. Subsequently the background was fit manually by linear interpolation and the reflection peak shape was fitted using the pseudo-Voigt function. Additionally, four different asymmetry factors were refined. The atomic coordinates of the starting model were refined individually. Temperature factors (B_{iso}), site occupancies and the hydrogen atoms present in this structure were not included in the refinement. Due to the dimensions of the unit cell and the measuring method preferred orientation was considered as well.

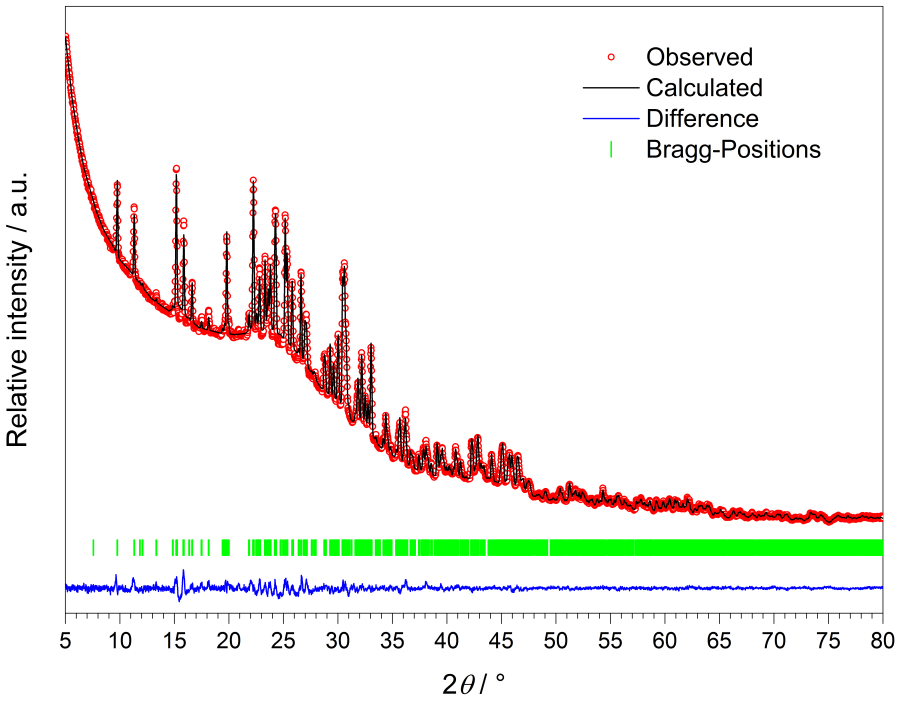

Figure 5.1: X-ray powder diffraction pattern and result of the *Rietveld* refinement for $Cs_2[B_{10}O_{14}(OH)_4]\cdot H_2O$.

$Cs_2[B_{10}O_{14}(OH)_4]\cdot H_2O$ crystallises isotypically to $Rb_2[B_{10}O_{14}(OH)_4]\cdot H_2O$ in the triclinic space group $P\bar{1}$ with the lattice parameters $a = 7.8038(2)$ Å, $b = 9.1840(2)$ Å,

$c = 12.3403(3)$ Å, $\alpha = 98.979(2)°$, $\beta = 106.345(1)°$ and $\gamma = 91.081(2)°$. The structure was refined to very good residuals of $R_p = 0.013$, $R_{wp} = 0.018$ and $\chi^2 = 3.28$. Besides the Gaussian peak width parameters, the asymmetry and preferred orientation parameters are also in a good range (Table 5.1). The refined atomic coordinates, isotropic displacement factors (B_{iso}), selected interatomic distances and angles and hydrogen bonds are summarised in Tables 5.2 to 5.4. The *Rietveld* analysis revealed a phase pure sample of $Cs_2[B_{10}O_{14}(OH)_4]\cdot H_2O$. Via EDX spectroscopy the presence of caesium was proved.

Table 5.1: *Rietveld* refinement parameters of $Cs_2[B_{10}O_{14}(OH)_4]\cdot H_2O$; standard deviations in brackets

Sum formula	$Cs_2[B_{10}O_{14}(OH)_4]\cdot H_2O$
Molar weight / g·mol^{-1}	683.96
Crystal system	triclinic
Space group	$P\bar{1}$ (no. 2)
Colour	colourless
a / Å	7.8038(2)
b / Å	9.1841(3)
c / Å	12.3403(3)
α / °	98.979(2)
β / °	106.345(2)
γ / °	91.081(2)
Volume / Å^3	836.44(4)
Z	2
Calculated density D_x / g·cm^{-3}	2.716
Radiation	Cu-K_α
Wavelength λ / Å	1.5406
Diffractometer	Bruker D8 Advance
Theta range / °	$5.00 \leq 2\theta \leq 140.00$
Step width / °	0.02 2θ
Data points	7055
No. of atoms	37
Zero point	0.0190(6)
Scale factor	0.0015(0)
Profile function	pseudo-Voigt
Gaussian peak width parameters / U | V | W	0.078(3) | -0.027(1) | 0.012(0)
Asymmetry parameters	0.0078(27), 0.0069(0), 0.0224(0), 0.0068(0)
Preferred orientation parameters	0.9672(22), 0.0821(0)
Refined parameters	111
R_p	0.013
R_{wp}	0.018
χ^2	3.28

Table 5.2: Refined atomic coordinates and isotropic displacement parameters B_{iso} / Å^2 of $Cs_2[B_{10}O_{14}(OH)_4]\cdot H_2O$; standard deviations in brackets

Atom	x	y	z	B_{iso}
Cs1	0.4920(4)	0.0576(3)	0.2541(3)	0.70
Cs2	–0.1007(4)	0.7064(3)	0.2096(2)	0.70
B1	–0.0034(72)	0.1407(58)	0.2659(47)	1.00
B2	0.4028(75)	0.6621(61)	0.2680(44)	1.00
B3	0.8163(70)	0.0517(53)	0.0602(46)	1.00
B4	0.0417(62)	0.2492(53)	0.1006(43)	1.00
B5	0.2251(74)	0.4819(58)	0.1143(44)	1.00
B6	0.4277(67)	0.6734(54)	0.0815(47)	1.00
B7	0.1626(68)	0.0404(56)	0.4275(44)	1.00
B8	–0.0006(71)	0.2507(54)	0.4619(45)	1.00
B9	0.5810(70)	0.6450(55)	0.4732(46)	1.00
B10	0.3650(71)	0.8277(56)	0.4412(45)	1.00
$O_{br}1$	–0.0552(30)	0.2346(23)	0.3536(22)	1.00
$O_{br}2$	0.1117(28)	0.1449(27)	0.5151(20)	1.00
$O_{br}3$	0.1246(32)	0.0472(25)	0.3232(21)	1.00
$O_{br}4$	0.8685(34)	0.0423(24)	0.1788(21)	1.00
$O_{br}5$	–0.0994(31)	0.1576(26)	0.0253(21)	1.00
$O_{br}6$	0.1025(30)	0.2490(24)	0.2279(20)	1.00
$O_{br}7$	0.1270(29)	0.3579(25)	0.0650(18)	1.00
$O_{br}8$	0.2928(34)	0.5461(26)	0.0349(20)	1.00
$O_{br}9$	0.4789(30)	0.7246(25)	0.1960(23)	1.00
$O_{br}10$	0.2693(34)	0.5348(29)	0.2152(21)	1.00
$O_{br}11$	0.5618(30)	0.6086(26)	0.3563(19)	1.00
$O_{br}12$	0.4866(34)	0.7570(25)	0.5116(19)	1.00
$O_{br}13$	0.3171(32)	0.7871(27)	0.3199(20)	1.00
$O_{br}14$	0.2953(32)	–0.0601(26)	0.4925(19)	1.00
O_H1	–0.0492(28)	0.3562(26)	0.5520(19)	1.00
O_H2	0.6949(31)	0.9298(24)	0.0302(19)	1.00
O_H3	0.4800(29)	0.7214(23)	0.0081(18)	1.00
O_H4	0.7217(31)	0.5725(24)	0.5550(18)	1.00
O_W	0.6430(27)	0.3687(25)	0.2334(22)	1.00
H1	0.8550	0.3851	0.5452	1.00
H2	0.3688	0.1008	0.0101	1.00
H3	0.5622	0.3041	0.1016	1.00
H4	0.2655	0.3619	0.3930	1.00
H5	0.7314	0.4336	0.2292	1.00
H6	0.7187	0.2980	0.2869	1.00

O_{br} = bridging oxygen atom; O_H = hydroxyl group, O_W = oxygen of water molecule

Table 5.3: Selected interatomic distances / Å and angles / ° in $Cs_2[B_{10}O_{14}(OH)_4]\cdot H_2O$; standard deviations in brackets

B_Δ–O_{br}	1.34(7)–1.41(6)
$B_\square$–O_{br}	1.43(5)–1.54(5)
B–O_H	1.39(7)–1.42(6)
Cs–O	2.80(2)–4.00(3)
B_Δ–O_{br}–B_Δ	116(7)–131(7)
$B_\square$–O_{br}–B_Δ	119(7)–136(7)
O_{br}–$B_\square$–O_{br}	105(4)–113(4)
O–B_Δ–O	114(5)–126(4)

$B_\Delta = BO_3$; $B_\square = BO_4$

Table 5.4: Distances / Å and angles / ° of the hydrogen bonds in $Cs_2[B_{10}O_{14}(OH)_4]\cdot H_2O$; *D*: Donor, *A*: Acceptor

D–*H*	*A*	*d*(*D*–*H*)	*d*(*H*–*A*)	∢(*DHA*)	*d*(*D*–*A*)
O_H1–H1	O_H4	0.78	2.04	143	2.70
O_H2–H2	O_H3	0.69	2.01	149	2.62
O_H3–H3	O_W	1.09	1.58	168	2.66
O_H4–H4	O_{br}6	0.79	2.16	149	2.87
O_H4–H4	O_{br}12	0.79	2.35	93	2.52
O_W–H6	O_{br}1	1.07	1.87	147	2.83

5.3 Crystal Structure Description

$Cs_2[B_{10}O_{14}(OH)_4]\cdot H_2O$ crystallises in the triclinic space group $P\bar{1}$ with two formula units per unit cell. All atoms are located on the general *Wyckoff* position $2i$. The anionic partial structure of $Cs_2[B_{10}O_{14}(OH)_4]\cdot H_2O$ comprises parallel zig-zag chains (Figure 5.2 top) of corner-sharing borate tetrahedra, borate triangles and hydroxoborate triangles (Figure 5.2 bottom).

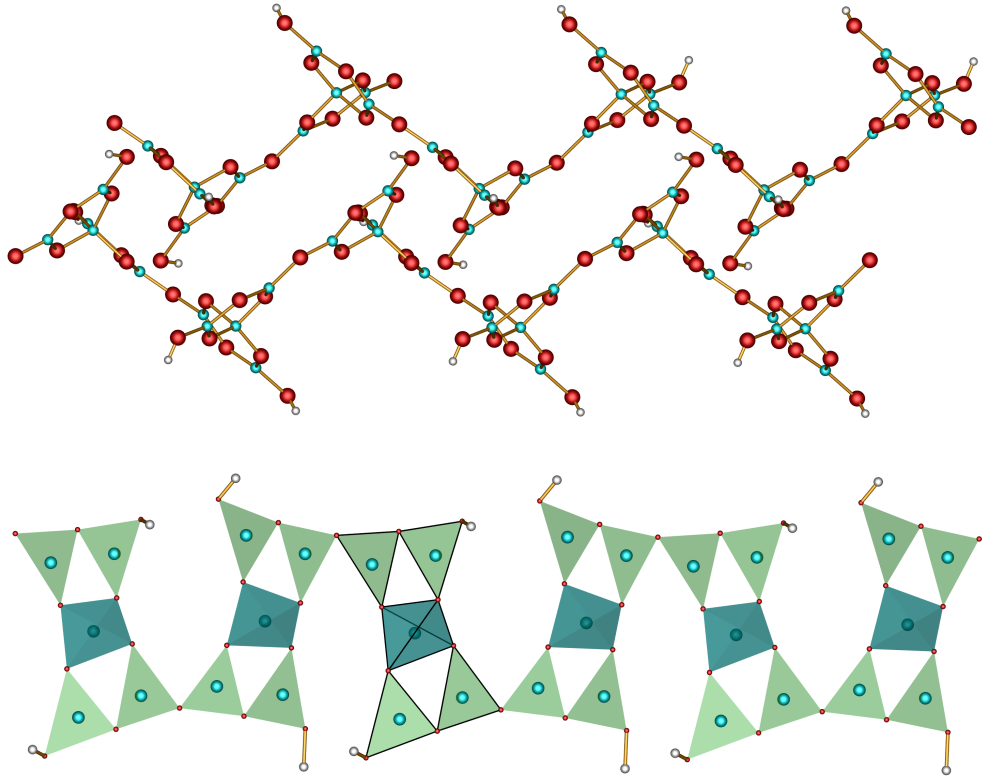

Figure 5.2: Top: Parallel lB sechser-single chains along [010]; boron turquoise, oxygen red, hydrogen white. Bottom: Highlighted FBU in a lB sechser-single chain in $Cs_2[B_{10}O_{14}(OH)_4]\cdot H_2O$; borate tetrahedra turquoise, borate triangles green, hydrogen white.

The polyanion is constructed by pentameric $^{1}_{\infty}[B_5\Phi_9]$ (Φ = O, OH) units (Figure 5.2 bottom) exhibiting an O:OH ratio of 14:4. The lB sechser-single chains contain a lB pentamer as FBU formed by four BΦ_3 triangles and one BΦ_4 tetrahedra (Figure 5.3), illustrated with the descriptor 4Δ□:<2Δ□>–<2Δ□> [13, 82, 83, 113].

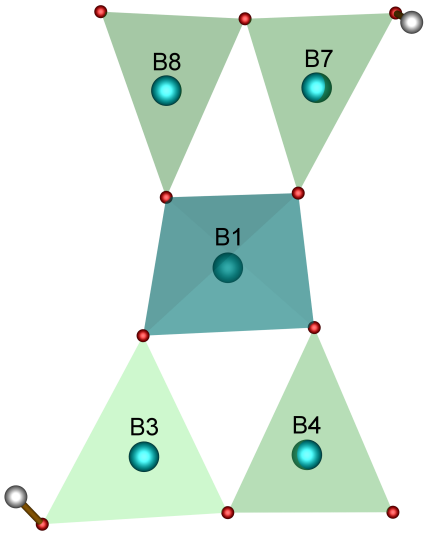

Figure 5.3: FBU as a lB pentamer 4Δ□:<2Δ□>–<2Δ□> in $Cs_2[B_{10}O_{14}(OH)_4]\cdot H_2O$; borate tetrahedra turquoise, borate triangles green, hydrogen white.

The boron atoms are coordinated both trigonally planar and tetrahedrally forming BO_3, BO_3H and BO_4 units. $B_{\square}$–O_{br} bond lengths range between 1.44 and 1.55 Å, whereas B_{Δ}–O_{br} bond lengths lie between 1.35 and 1.42 Å. B–O_H distances are between 1.40 and 1.43 Å. The increase of bond lengths from B–O_H<B_{Δ}–O_{br}<$B_{\square}$–O_{br} corresponds to data found in other monovalent pentaborates [15, 148, 149]. B–O–B angles range between 114 and 132°, whereas O–B–O angles lie between 105 and 113° (Ø = 110°). Selected bond lengths and angles of $Cs_2[B_{10}O_{14}(OH)_4]\cdot H_2O$ are listed in Table 5.3.

An appropriate method for the calculation of deviation of tetrahedra from ideal symmetry was introduced by *Balić-Žunić* and *Makovicky* [35, 36]. The two crystallographically different borate tetrahedra feature the values −2.10 % (B1) and −1.70 % (B2). Exhibiting a deviation of only slightly more than 1 %, tetrahedra can be classified as nearly regular. In general, structure solutions received from X-ray powder diffractometry including a *Rietveld* refinement do not reveal atomic coordinates as exactly as from single-crystal X-ray diffractometry. Thus, the relatively small degree of deviation can be neglected.

In $Cs_2[B_{10}O_{14}(OH)_4]\cdot H_2O$ the two caesium atoms are coordinated irregularly by ten and fourteen oxygen atoms (Figure 5.4). Next to several bridging oxygen atoms and one hydroxyl group both caesium atoms are coordinated by one water molecule, which is unique in the unit cell. The Cs–O bond lengths range between 2.80–4.00 Å (Table 5.3). These values agree with the sum of the ionic radii of Cs^+, which are 3.16 Å (CN = 10) and 3.3 Å (CN = 14), respectively [60]. Nevertheless, the difference between the observed values compared to the theoretical distances can

be explained by the insufficient accuracy of the atomic positions from powder data. The coordination numbers were also confirmed by MAPLE calculations (Chapter 5.4).

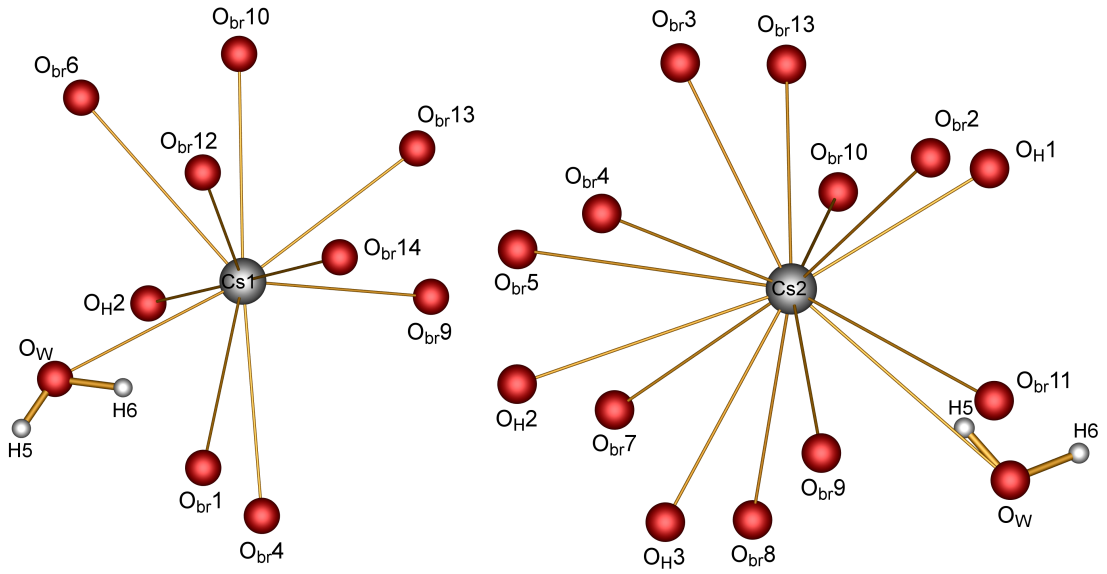

Figure 5.4: Coordination spheres of caesium in $Cs_2[B_{10}O_{14}(OH)_4]\cdot H_2O$.

According to *Steiner* [150] hydrogen bonds between 1.5 and 2.2 Å can be classified as moderately strong, whereas hydrogen bonds larger than 2.20 Å can be assigned as weak. In Figure 5.5 all moderately strong (dotted orange) and weak (dotted violet) hydrogen bonds are depicted, existing between bridging and protonated oxygen atoms and the water molecule (Table 5.4). Similar values for hydrogen bonds were also found in other alkaline pentaborate hydrates [14, 15, 148, 149, 151].

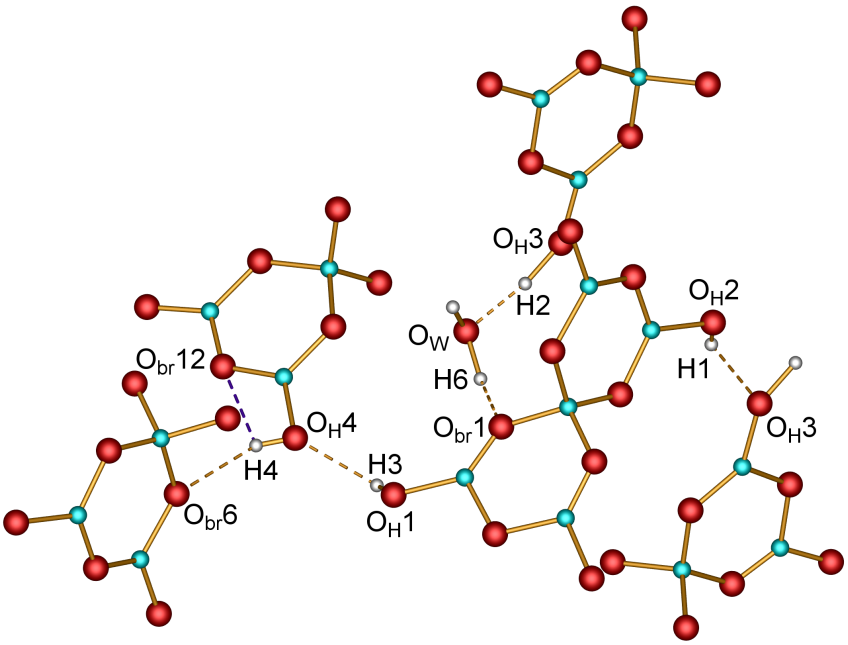

Figure 5.5: Moderately strong (dotted orange) and weak (dotted violet) hydrogen bonds in $Cs_2[B_{10}O_{14}(OH)_4]\cdot H_2O$.

5.4 Electrostatic Calculations

The coordination number of caesium (Table 12.1) and the electrostatic consistency of the structure model were proved by calculations based on the MAPLE concept (= *Ma*delung *P*art of *L*attice *E*nergy) [32, 33, 152]. A structure model is electrostatically consistent if the sum of MAPLE values of chemically similar compounds deviates from the MAPLE value of the compound of interest by less than 1 %. According to the calculations, the structure model of $Cs_2[B_{10}O_{14}(OH)_4]\cdot H_2O$ thus shows electrostatic consistency, as presented in Table 5.5.

Table 5.5: MAPLE calculations for $Cs_2[B_{10}O_{14}(OH)_4]\cdot H_2O$ [32, 33, 152]

$Cs_2[B_{10}O_{14}(OH)_4]\cdot H_2O$	Cs_2O [153] + 5 B_2O_3 [154] + 3 H_2O [155]
MAPLE = 126976 kJ·mol^{-1}	MAPLE = 127199 kJ·mol^{-1}
Δ = -0.2 %	

5.5 Spectroscopic Properties

5.5.1 IR Spectroscopy

The infrared spectrum of $Cs_2[B_{10}O_{14}(OH)_4]\cdot H_2O$ was recorded between 4000 and 400 cm^{-1} and is shown in Figure 5.6. The positions of the bands and the corresponding assignments are given in Table 5.6.

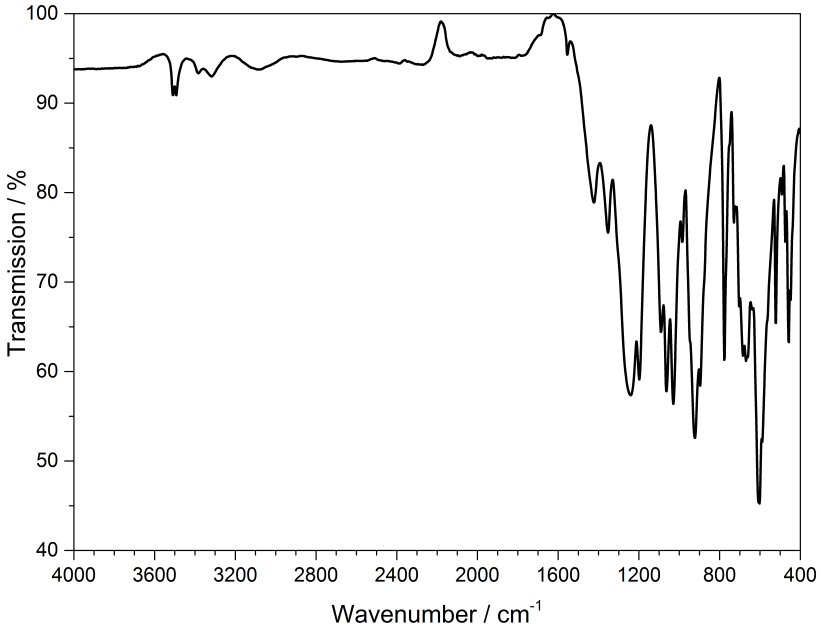

Figure 5.6: Infrared spectrum of $Cs_2[B_{10}O_{14}(OH)_4]\cdot H_2O$.

Table 5.6: Position / cm^{-1} and assignment of the IR bands in $Cs_2[B_{10}O_{14}(OH)_4]\cdot H_2O$

Position	Assignment
3500–3090	ν(OH) [156, 157]
1555–1240	δ(OH) [156]
1100–920	ν_{as}(BO) [156, 158]
777, 669	ν_{s}(BO) [156, 158]
604, 521, 459	δ(BO) [156, 158]

The bands between 3500–3090 and 1555–1240 cm^{-1} can be assigned to the stretching and deformation vibrations of the OH groups [156, 157]. Asymmetric and symmetric B–O stretching vibrations occur between 1100–920 and at 777 and 669 cm^{-1}, respectively. Characteristic bands of B–O bending vibrations are found at 604, 521 and 459 cm^{-1}, respectively [156, 158].

5.5.2 Fluorescence Spectroscopy

In order to investigate the optical properties of $Cs_2[B_{10}O_{14}(OH)_4]\cdot H_2O$, the host structure of $Cs_2[B_{10}O_{14}(OH)_4]\cdot H_2O$ was doped with 5.0 mol% Eu^{3+} (synthesis see Chapter 5.1). The charge compensation due to the partial occupation of Cs^+ lattice sites by Eu^{3+} ions is presumably accomplished by vacancies. Under excitation with UV light at 254 nm $Cs_2[B_{10}O_{14}(OH)_4]\cdot H_2O$:$Eu^{3+}$ shows a weak red fluorescence. The fluorescence spectrum (Figure 5.7) shows the characteristic f–f emissions of Eu^{3+} [53]. Between 230 and 280 nm a broad band in the excitation spectrum reveals an $O^{2-}\rightarrow Eu^{3+}$ charge-transfer.

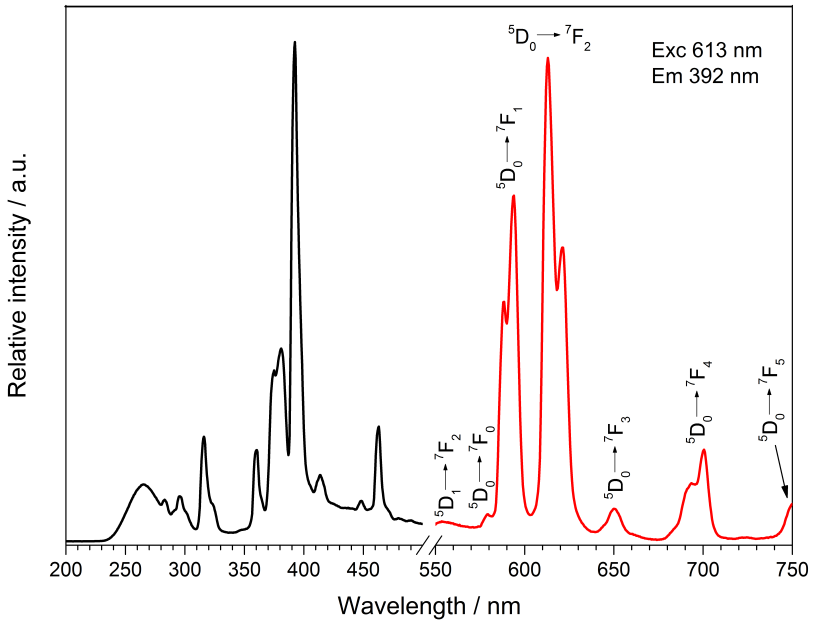

Figure 5.7: Excitation (black) and emission (red) spectrum of $Cs_2[B_{10}O_{14}(OH)_4]\cdot H_2O$:$Eu^{3+}$.

Under excitation at 392 nm $Cs_2[B_{10}O_{14}(OH)_4]\cdot H_2O$:$Eu^{3+}$ exhibits sharp emission lines between 550 and 750 nm, which can be assigned to the $^5D_0\rightarrow{}^7F_0$ (554 nm), $^5D_0\rightarrow{}^7F_1$ (594 nm), $^5D_0\rightarrow{}^7F_2$ (613 nm), $^5D_0\rightarrow{}^7F_3$ (651 nm), $^5D_0\rightarrow{}^7F_4$ (701 nm) and $^5D_0\rightarrow{}^7F_5$ (750 nm) transitions of Eu^{3+} [53]. The most intense transition $^5D_0\rightarrow{}^7F_2$ at 614 nm is called hypersensitive due to its sensitivity to the surrounding of Eu^{3+}. It is dominant over the $^5D_0\rightarrow{}^7F_1$ transition because of the asymmetric surrounding of Eu^{3+} in $Cs_2[B_{10}O_{14}(OH)_4]\cdot H_2O$:$Eu^{3+}$, which proves its occupation of Cs^+ sites [55, 56].

5.6 Thermal Analysis

The thermal behaviour of $Cs_2[B_{10}O_{14}(OH)_4]\cdot H_2O$ was investigated between room temperature and 1400 °C (Figure 5.8). After a mass loss of 8.2 wt% in the temperature range between 240 and 430 °C the title compound reveals a certain stability between 430 and 950 °C. The thermal investigation of other hydrated pentaborates always revealed a complete loss of water between 140 and 400 °C leading to the sum formula $A[B_5O_8]$ (A = Rb, Cs, Tl) [151, 159]. This also holds for $Cs_2[B_{10}O_{14}(OH)_4]\cdot H_2O$, which looses three molecules of H_2O (theor. mass loss: 7.90 wt%) in order to obtain α-$Cs[B_5O_8]$ [159] (Figure 5.9).

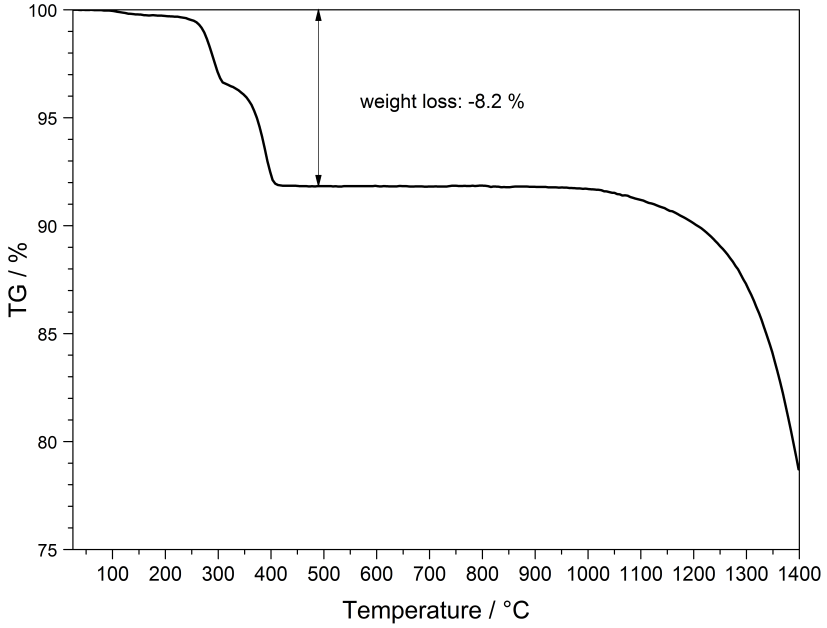

Figure 5.8: Thermogravimetric analysis of $Cs_2[B_{10}O_{14}(OH)_4]\cdot H_2O$.

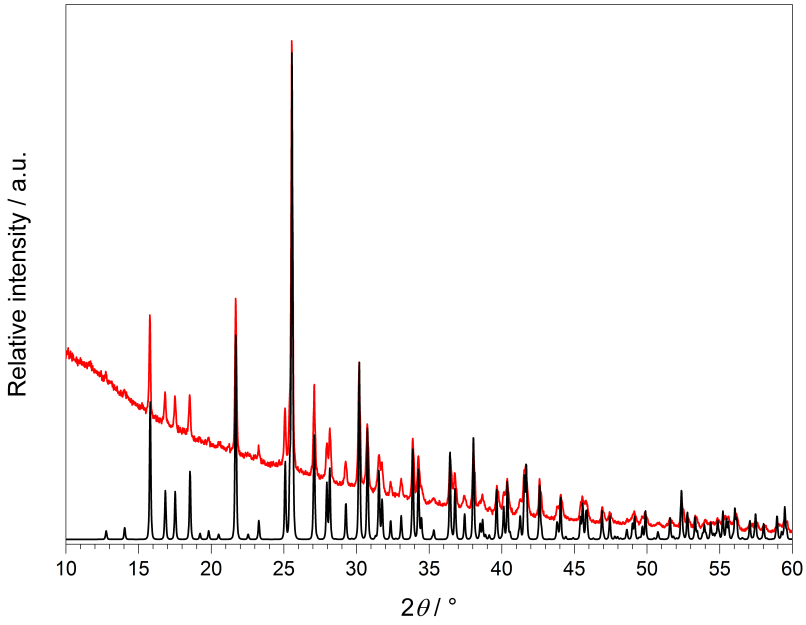

Figure 5.9: X-ray powder diffraction pattern of α-$Cs[B_5O_8]$ (red) after heating $Cs_2[B_{10}O_{14}(OH)_4]\cdot H_2O$ up to 650 °C under N_2 atmosphere and calculated powder diffraction pattern from single-crystal data of α-$Cs[B_5O_8]$ [159] (black).

Thus, the following decomposition equation is suggested (Equation 5.1):

$$Cs_2[B_{10}O_{14}(OH)_4]\cdot H_2O \xrightarrow[N_2]{\Delta} 2\alpha\text{-}Cs[B_5O_8] + 3H_2O \tag{5.1}$$

5.7 Discussion

$Cs_2[B_{10}O_{14}(OH)_4]\cdot H_2O$ **(1)** was obtained as a phase pure colourless crystalline solid. Nevertheless, crystals with a suitable quality for single-crystal analysis could not be obtained. Hence, a *Rietveld* refinement was carried out using the single-crystal data of the isotypic compound $Rb_2[B_{10}O_{14}(OH)_4]\cdot H_2O$ **(2)** [15] as starting model. The polyanion reveals lB pentamers as FBU, which form $^1_\infty[B_5\Phi_9]$ (Φ = O, OH) chains exhibiting $B\Phi_3$ triangles and $B\Phi_4$ tetrahedra. The FBU can be illustrated with the descriptor 4Δ□:<2Δ□>–<2Δ□>. Besides one water molecule two caesium atoms are present, which are coordinated irregularly by ten and fourteen oxygen atoms. In contrast, for **(2)** *Belokoneva et al.* determined an irregularly coordination sphere of nine oxygen atoms for both caesium atoms [15]. The results in this work include an even larger coordination sphere due to the larger ionic radius of Cs^+ compared to Rb^+, which was confirmed besides the electrostatic consistency by MAPLE calculations. In general, the lattice parameters of the caesium compound are larger than of the rubidium compound, which appears analogously to the ionic radii of Cs^+

(1.81–1.88 Å, CN = 10–14) and Rb^+ (1.66–1.83, CN = 10–14) [60] (Table 5.7). As expected, the B–O bond lengths correlate in the two compounds, and the $B_{\square}$–O_{br} distances are larger than the B_{Δ}–O_{br} distances (Table 5.7). Unfortunately several bond lengths of **(2)** do not include standard deviations, whereas bond lengths of **(1)** could not be stated as accurately as in the rubidium compound due to the results received from powder data.

Table 5.7: Comparison of the crystallographic data of $Cs_2[B_{10}O_{14}(OH)_4]\cdot H_2O$ **(1)** and $Rb_2[B_{10}O_{14}(OH)_4]\cdot H_2O$ **(2)**; standard deviations in brackets

Sum formula	$Cs_2[B_{10}O_{14}(OH)_4]\cdot H_2O$	$Rb[B_5O_7(OH)_2]\cdot 0.5H_2O$
Molar weight / g·mol^{-1}	683.96	589.08
Crystal system	triclinic	triclinic
Space group	$P\bar{1}$ (no. 2)	$P\bar{1}$ (no. 2)
Colour	colourless	colourless
a / Å	7.8038(2)	7.679(4)
b / Å	9.1840(3)	9.253(6)
c / Å	12.3403(3)	12.053(9)
α / °	98.979(2)	98.55(5)
β / °	106.345(2)	106.80(5)
γ / °	91.081(2)	91.71(5)
Volume / Å^3	836.44(4)	808.35
Z	2	4
B_{Δ}–O_{br} / Å	1.34(7)–1.41(6)	1.332–1.409
$B_{\square}$–O_{br} / Å	1.43(5)–1.54(5)	1.465–1.503
$d(A1$–O) (A = Rb, Cs) / Å	2.80(2)–3.50(2)	2.756(10)–3.482(8)
$d(A2$–O) (A = Rb, Cs) / Å	2.97(2)–4.00(3)	2.927(10)–3.381(10)
CN	9/9	10/14
Calculated density D_x / g·cm^{-3}	2.716	2.420(6)
Radiation	Cu-K_α	Mo-K_α
Wavelength λ / Å	1.5406	0.71069
R_p / R	0.013	0.057
R_{wp} / R_w	0.018	0.064
χ^2	3.28	

Besides the $^5D_0 \rightarrow {}^7F_1$ transition the fluorescence spectrum of the title compound doped with Eu^{3+} reveals the hypersensitive and more intense $^5D_0 \rightarrow {}^7F_2$ transition at 614 nm. The latter is very sensitive to its surrounding and reaches a higher intensity if Eu^{3+} occupies an asymmetric site. Both Cs^+ ions are located on lattice sites exhibiting an irregular coordination sphere, which proves the occupation of

Eu^{3+} on Cs^+ lattice sites. Due to the presence of a number of protons one weak and some moderately strong hydrogen bonds could be determined, which contribute to the thermal stability of the compound. After the loss of three molecules of water the thermogram of the title compound shows a broad temperature range without any mass loss between 430 and 950 °C. Simulating the heating process under N_2 up to 650 °C proved the formation of α-$Cs[B_5O_8]$ as decomposition product. A comparison with the thermogram of Tl_2O-$5B_2O_3$-$3H_2O$ **(3)** [147] reveals a very similar decomposition behaviour (Figure 5.10). In both thermogravimetric curves two decomposition steps with a ratio of approximately 1:2 are present. Even the temperature range of the steps of mass loss is nearly equal.

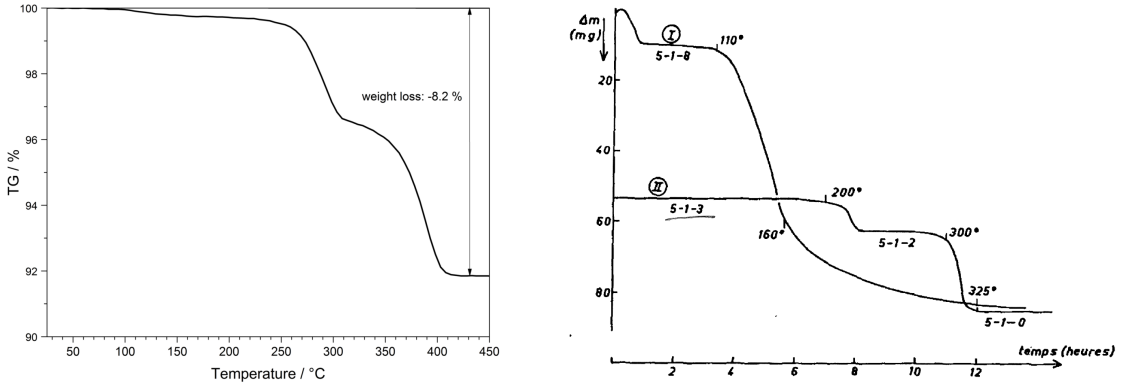

Figure 5.10: Comparison of the thermogravimetric analysis of $Cs_2[B_{10}O_{14}(OH)_4]\cdot H_2O$ **(1)** (left) and Tl_2O-$5B_2O_3$-$3H_2O$ **(3)** (right, II) [147].

Although up to now no single-crystal data of **(1)** and **(3)** has been solved, it seems obvious to claim a strong structural resemblance with regard to the very similar thermal behaviour, which was already predicted by *Benhassaine* [146].

Monovalent pentaborates comprise a large variety in structure and composition. The amount of protonated terminal oxygen atoms in the pentaborate anion determines the degree of condensation. In $A[B_5O_6(OH)_4]\cdot 2H_2O$ (A = Na [160], Rb [161], Cs [14, 151], Tl [162]) due to complete protonation of the terminal oxygen atoms condensation is not possible and isolated pentameric units of $^0_\infty[B_5\Phi_{10}]$ (Φ = O, OH) are present (Figure 5.11 left). In pentaborates with a sum formula of $A[B_5O_7(OH)_2]\cdot H_2O$ (A = K [149], Rb [15], NH_4 [148]) and one molecule of crystal water the O:OH ratio is larger and thus leads to a one-dimensional condensation of the pentameric borate units (Figure 5.2). A number of compounds exhibiting units of $[B_5O_8(OH)]\cdot xH_2O$, e.g. $A_2[B_5O_8(OH)]\cdot 2H_2O$ (A = Na [163], K[164]), $Na[B_5O_8(OH)]\cdot H_2O$ [165] and $Na_4[B_{10}O_{16}(OH)_2]_2\cdot H_2O$ [166] possess a layer structure (Figure 5.11 middle). Due to the missing hydroxyl groups most of the binary penta-borates reveal a three-dimensional structure (Figure 5.11 right), e.g. $K[B_5O_8]$ [167], $Rb[B_5O_8]$ [168] and

$Tl[B_5O_8]$ [169]. Up to now $K[B_5O_8]_4\cdot H_2O$ is the only representative of the ternary monovalent pentaborates exhibiting only a monomeric structure [170].

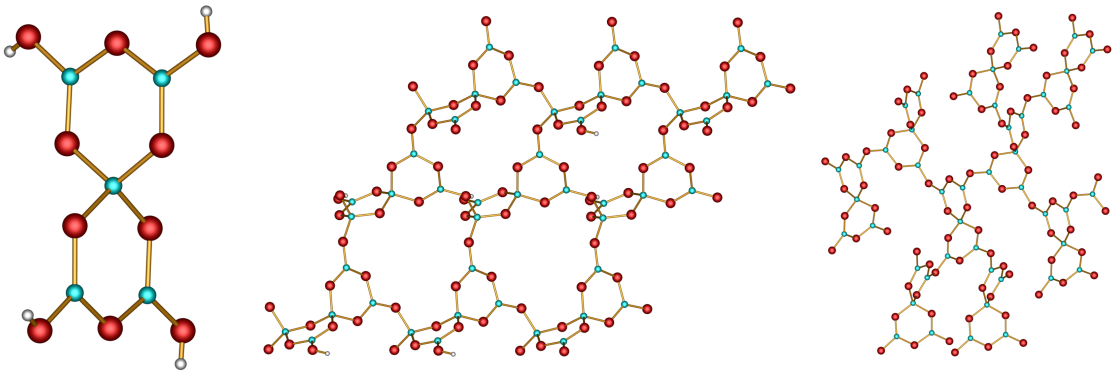

Figure 5.11: Anionic structures of monovalent pentaborates: monomer (left), layer (middle) and three-dimensional network (right); boron turquoise, oxygen red, hydrogen white.

6 Phosphates

6.1 Lanthanide Hydrogen-Polyphosphates $Ln[H(PO_3)_4]$ (Ln = Tb, Dy, Ho)

In 1975 *Palkina et al.* synthesised $Bi[H(PO_3)_4]$ [171], which crystallises isostructural to $Ln[H(PO_3)_4]$ (Ln = Sm, Eu) in the triclinic space group $P\bar{1}$ [172]. Surprisingly, acid polyphosphates of the elements at the origin of the lanthanide row (La, Pr, Nd) and at the end (Tm, Yb) have not been observed yet. Instead, only non-protonated polyphosphates and ultraphosphates are formed depending on the synthesis temperature [173]. $Ln[H(PO_3)_4]$ (Ln = Tb-Er) crystallise in the monoclinic space group $P2_1/c$. $Gd[H(PO_3)_4]$ represents an exception, which crystallises in both configurations at the same time. Up to now only the crystal structure of $Er[H(PO_3)_4]$ was solved from single-crystal data [173].
Lanthanide based compounds are promising candidates as luminescent materials for lighting applications and thus attract great interest [4, 9, 49, 51, 58, 174–179]. As a consequence, both the spectroscopic properties and the thermal stability of the host lattice are important characteristics. In the following chapter the crystal structures of $Ln[H(PO_3)_4]$ (Ln = Tb, Dy, Ho) determined from single-crystal data (Ln = Tb, Ho) on the one hand and refined via a *Rietveld* refinement (Ln = Dy) on the other hand are presented. Additionally, their optical, magnetic and thermal properties are investigated. All results discussed in this chapter are published in a science journal [180].

6.1.1 Synthesis

$Ln[H(PO_3)_4]$ (Ln = Tb, Dy) were synthesised via solid-state reactions starting from the respective lanthanide oxides and phosphorous acid. 94.70 mg (0.1264 mmol) Tb_4O_7, 94.20 mg (0.2525 mmol) and Dy_2O_3, respectively, and 279.6 mg (3.410 mmol) H_3PO_3 were ground in an agate mortar and transferred into a silica glass crucible. The reaction mixtures were covered with 20 mL H_2O_2 (30 %) to suppress the formation of LnP_3O_9 and heated up to 380 °C with a heating rate of 100 °C/h using

a muffle furnace. The temperature was kept for three hours before cooling down to room temperature by switching off the furnace. The products were washed with hot water and dried in air overnight. Different experiments showed that addition of H_2O_2 to the reaction mixture lead to phase pure crystalline powders of colourless $Tb[H(PO_3)_4]$ and $Dy[H(PO_3)_4]$.
$Ho[H(PO_3)_4]$ was synthesised analogously to $Ln[H(PO_3)_4]$ (Ln = Tb, Dy) but could be obtained as phase pure crystalline yellow/pink powder without addition of H_2O_2 to the reaction mixture.

$Dy[H(PO_3)_4]$:Ce^{3+} (5, 10, 30 %) and $Dy[H(PO_3)_4]$:Eu^{3+} (5 %) were synthesised by substituting the corresponding amount of Dy_2O_3 by $Ce(NO_3)_3{\cdot}6H_2O$ and $Eu(NO_3)_3{\cdot}5H_2O$, respectively.

6.1.2 X-Ray Powder Diffraction

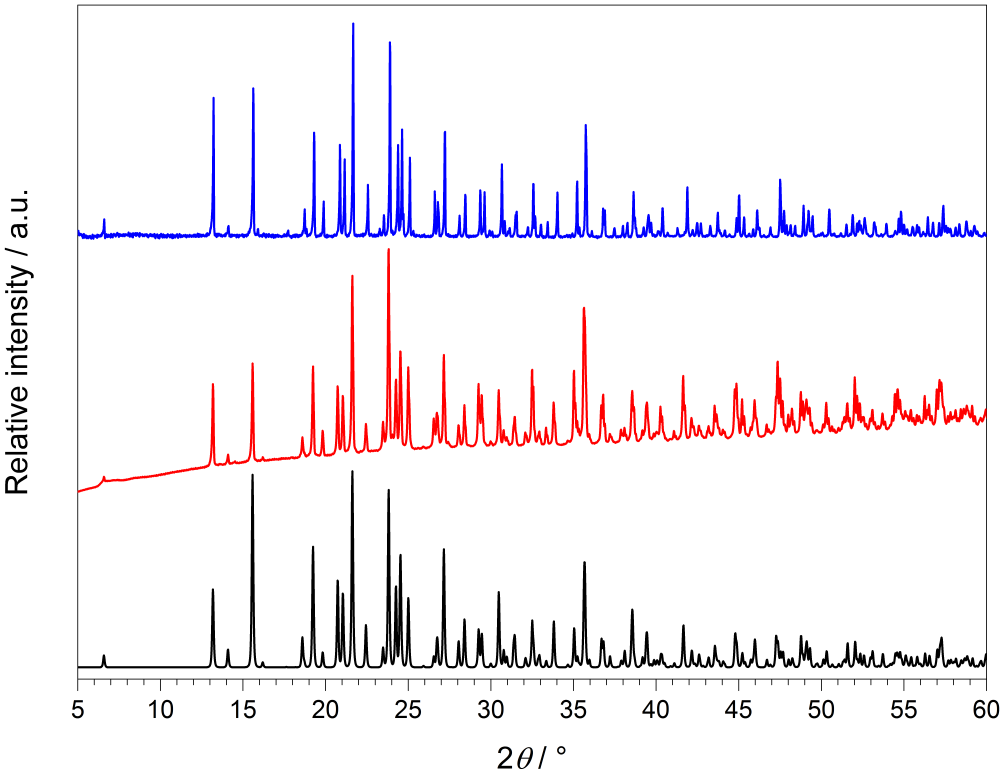

Figure 6.1: X-ray powder diffraction patterns of $Tb[H(PO_3)_4]$ (red) and $Ho[H(PO_3)_4]$ (blue) and calculated X-ray powder diffraction pattern from single-crystal data of $Tb[H(PO_3)_4]$ (black).

The phase purity of the samples was checked by X-ray powder diffraction (Figure 6.1). $Ln[H(PO_3)_4]$ (Ln = Tb, Dy, Ho) crystallise isotypically, but suitable crystals for single-crystal analysis could be obtained only for $Tb[H(PO_3)_4]$ and $Ho[H(PO_3)_4]$. The crystal structure of $Dy[H(PO_3)_4]$ was refined via the *Rietveld* method (Chapter 6.1.4) using the single-crystal data of $Tb[H(PO_3)_4]$ as starting structure model.

The *Rietveld* plot is shown in Figure 6.2. The composition of selected crystals of $Ln[H(PO_3)_4]$ (Ln = Tb, Dy, Ho) was checked via EDX spectroscopy. Within the accuracy of the measurement's limit no other elements were found.

6.1.3 Crystal Structure Determination

Colourless crystals of $Tb[H(PO_3)_4]$ (0.047 × 0.018 × 0.019 mm) and $Ho[H(PO_3)_4]$ (0.050 × 0.018 × 0.020 mm) were isolated and mounted on a *MicroMount*, respectively. The collection of the crystal data was run on a Bruker D8 Venture single-crystal diffractometer using Mo radiation. A multi-scan absorption correction was subsequently performed. The structure of the non-merohedrally twinned crystal of $Tb[H(PO_3)_4]$ was solved defining the twinned components (twin matrix: 0 0 1 0 -1 0 1 0 0; BASF = 0.430(1)) using TWINABS [181]. $Tb[H(PO_3)_4]$ and $Ho[H(PO_3)_4]$ crystallise in the monoclinic space group $P2_1/c$ with the lattice parameters $a_{Tb} = 13.6824(4)$ Å, $b_{Tb} = 7.1042(2)$ Å, $c_{Tb} = 9.6579(3)$ Å and $\beta_{Tb} = 101.200(1)°$ and $a_{Ho} = 13.6334(5)$ Å, $b_{Ho} = 7.0924(3)$ Å, $c_{Ho} = 9.5907(4)$ Å and $\beta_{Ho} = 101.055(1)°$, respectively. For $Tb[H(PO_3)_4]$ 3112 reflections were collected. Out of 3111 independent reflections 2790 were observed ($F_o^2 > 2\ \sigma\ (F_o^2)$). For $Ho[H(PO_3)_4]$ 27195 reflections were collected. Out of 1607 independent reflections 1421 were observed ($F_o^2 > 2\sigma\ (F_o^2)$, R_{int} = 0.0537). The crystallographic data, the parameters of the measurements and refinements are summarised in Tables 6.1 and 6.5. The structures were solved by direct methods and refined by full matrix least-squares technique using the programs SHELXS-97 and SHELXTL-97 [21, 22]. The anisotropic refinement revealed R-values of $R1 = 0.0277$ and $wR2 = 0.0622$ for $Tb[H(PO_3)_4]$ and $R1 = 0.0291$ and $wR2 = 0.0602$ for $Ho[H(PO_3)_4]$, respectively. The Tb, Ho, P and O atoms could be clearly located. Hydrogen atoms were localised via Difference-*Fourier*-Synthesis, added geometrically and were confirmed by MAPLE calculations [32, 33, 152]. The refined atomic coordinates, anisotropic displacement parameters, selected interatomic distances and angles are summarised in Tables 6.2 to 6.4 and 6.6 to 6.8.

Table 6.1: Single-crystal refinement parameters of $Tb[H(PO_3)_4]$; standard deviations in brackets

Sum formula	$Tb[H(PO_3)_4]$
Temperature / K	293(2)
Molar weight / g·mol^{-1}	475.81
Crystal system	monoclinic
Space group	$P2_1/c$ (no. 14)
Crystal shape	plate
Crystal size / mm^3	0.047 × 0.018 × 0.019
Colour	colourless
a / Å	13.6824(4)
b / Å	7.1042(2)
c / Å	9.6579(3)
β / °	101.200(1)
Volume / Å^3	920.89(5)
Z	4
Calculated density D_x / g·cm^{-3}	3.432
Absorption coefficient μ / mm^{-1}	8.440
F(000)	888
Radiation (λ / Å)	Mo-K_α (0.7093)
Diffractometer	Bruker D8 Venture
Absorption correction	multi-scan
Transmission factor (min./max.)	0.6359 / 0.7457
Index range h|k|l (min./max.)	0/16 | -8/0 | -11/11
Theta range / °	$3.04 \leq \theta \leq 25.00$
Reflections collected	3112
Independent reflections	3111
Observed reflections	2790 ($F_o^2 > 2\sigma\ (F_o^2)$)
Refined parameters	160
R_{int}, R_σ	no value due to twin refinement, 0.023
$R1$ (all data)	0.0277
$wR2$ (all data)	0.0622
Weighting scheme	$w^{-1}=\sigma^2\ F_o^2 + (0.0389\ P)^2 + 0.0000\ P$; $P = (F_o^2 + 2\ F_c^2)/3$
GooF	1.131
Residual electron density (min./max.) / e$^-$·Å^{-3}	-0.50/0.14

Table 6.2: Refined atomic coordinates, *Wyckoff* symbols and isotropic displacement parameters U_{eq} / Å^2 in Tb[H(PO$_3$)$_4$]; standard deviations in brackets

Atom	*Wyckoff* symbol	x	y	z	U_{eq}
Tb1	4*e*	0.729401(15)	0.05792(3)	0.05897(2)	0.00704(9)
P1	4*e*	0.90133(8)	−0.32485(16)	0.12591(13)	0.0083(3)
P2	4*e*	0.90026(9)	0.15142(17)	−0.18737(12)	0.0080(3)
P3	4*e*	0.61157(9)	−0.20990(17)	0.29579(12)	0.0077(2)
P4	4*e*	0.59385(9)	0.40127(16)	0.20937(12)	0.0078(3)
$O_{br}1$	4*e*	0.9446(3)	−0.4771(5)	0.2377(3)	0.0135(7)
$O_{br}2$	4*e*	0.9990(2)	−0.2305(4)	0.0948(3)	0.0114(7)
$O_{br}3$	4*e*	0.5802(2)	−0.3766(4)	0.1876(3)	0.0117(7)
$O_{br}4$	4*e*	0.5152(2)	−0.1724(4)	0.3594(3)	0.0098(7)
$O_{term}1$	4*e*	0.8343(3)	−0.1896(5)	0.1741(3)	0.0145(8)
$O_{term}2$	4*e*	0.8414(3)	0.0764(5)	−0.0888(3)	0.0174(8)
$O_{term}3$	4*e*	0.8587(3)	0.2914(5)	−0.2952(3)	0.0156(8)
$O_{term}4$	4*e*	0.6343(3)	−0.0457(4)	0.2130(3)	0.0132(7)
$O_{term}5$	4*e*	0.6902(3)	−0.2722(4)	0.4168(3)	0.0123(7)
$O_{term}6$	4*e*	0.6158(2)	0.3586(5)	0.3627(3)	0.0115(7)
$O_{term}7$	4*e*	0.6615(2)	0.3364(4)	0.1191(3)	0.0114(7)
O_H1	4*e*	0.8569(3)	−0.4300(5)	−0.0105(4)	0.0158(8)
H1	4*e*	0.804(3)	−0.350(8)	−0.048(5)	0.05

O_{br} = bridging oxygen atom; O_{term} = terminal oxygen atom; O_H = hydroxyl group

Table 6.3: Anisotropic displacement parameters U_{ij} / Å^2 in Tb[H(PO$_3$)$_4$]; standard deviations in brackets

Atom	U_{11}	U_{22}	U_{33}	U_{12}	U_{13}	U_{23}
Tb1	0.00640(13)	0.00779(13)	0.00678(13)	−0.00024(9)	0.00093(10)	0.00006(9)
P1	0.0056(6)	0.0087(6)	0.0100(6)	0.0002(5)	0.0001(5)	−0.0004(5)
P2	0.0051(6)	0.0086(6)	0.0104(6)	0.0007(5)	0.0017(5)	0.0010(5)
P3	0.0068(6)	0.0074(6)	0.0082(5)	0.0005(5)	−0.0005(5)	−0.0001(5)
P4	0.0070(6)	0.0062(6)	0.0094(6)	−0.0008(5)	−0.0001(5)	−0.0002(5)
$O_{br}1$	0.0099(18)	0.0108(17)	0.0184(19)	0.0068(14)	−0.0009(14)	0.0002(15)
$O_{br}2$	0.0129(19)	0.0104(17)	0.0091(14)	0.0030(14)	−0.0025(13)	−0.0011(14)
$O_{br}3$	0.0195(19)	0.0051(16)	0.0087(16)	−0.0010(13)	−0.0021(14)	0.0022(15)
$O_{br}4$	0.0076(17)	0.0136(19)	0.0084(16)	0.0024(13)	0.0021(13)	0.0023(14)
$O_{term}1$	0.020(2)	0.0089(18)	0.0137(17)	0.0017(14)	0.0021(15)	0.0029(16)
$O_{term}2$	0.0116(18)	0.027(2)	0.0156(17)	−0.0013(16)	0.0066(15)	−0.0042(15)
$O_{term}3$	0.0087(19)	0.0172(18)	0.0182(17)	0.0070(16)	−0.0042(14)	0.0015(16)
$O_{term}4$	0.0148(19)	0.0093(18)	0.0171(18)	0.0040(14)	0.0068(15)	0.0012(14)
$O_{term}5$	0.0082(19)	0.0111(18)	0.0155(15)	0.0013(14)	−0.0032(13)	0.0025(13)
$O_{term}6$	0.012(18)	0.0126(17)	0.0075(16)	0.0000(14)	−0.0025(14)	−0.0054(15)
$O_{term}7$	0.0073(17)	0.0113(18)	0.0168(18)	−0.0026(14)	0.0054(14)	−0.0006(14)
O_H1	0.012(2)	0.0154(19)	0.0176(18)	−0.0077(15)	−0.0019(15)	−0.0002(14)

Table 6.4: Selected interatomic distances / Å and angles / ° in Tb[H(PO$_3$)$_4$]; standard deviations in brackets

P–O_{br}	1.561(3)–1.611(3)
P–O_{term}	1.462(3)–1.494(3)
P–O_H	1.533(3)
Tb–O	2.280(3)–2.451(3)
P_{OH}–O_{br}–P_O	135.8(2)–135.90(2)
P_O–O_{br}–P_O	130.0(2)–132.5(20)
O_{term}–P–O_{term}	117.4(2)–121.4(2)
O_{term}–P–O_{br}	105.9(2)–114.3(2)
O_{term}–P–O_H	115.1(2)
O_{br}–P–O_{br}	99.4(2)–104.1(2)
O_{br}–P–O_H	104.6(2)–106.9(2)

Table 6.5: Single-crystal refinement parameters of $Ho[H(PO_3)_4]$; standard deviations in brackets

Sum formula	$Ho[H(PO_3)_4]$
Temperature / K	296(2)
Molar weight / g·mol^{-1}	481.82
Crystal system	monoclinic
Space group	$P2_1/c$ (no. 14)
Crystal shape	irregular
Crystal size / mm^3	0.050 × 0.018 × 0.020
Colour	yellow/pink
a / Å	13.6334(5)
b / Å	7.0924(3)
c / Å	9.5907(4)
β / °	101.055(1)
Volume / Å^3	910.15(6)
Z	4
Calculated density D_x / g·cm^{-3}	3.499
Absorption coefficient μ / mm^{-1}	8.979
F(000)	892
Radiation (λ / Å)	Mo-K_α (0.7093)
Diffractometer	Bruker D8 Venture
Absorption correction	multi-scan
Transmission factor (min./max.)	0.6029 / 0.7458
Index range h|k|l (min./max.)	-16/16 | -8/8 | -11/11
Theta range / °	$3.04 \leq \theta \leq 25.00$
Reflections collected	27195
Independent reflections	1607
Observed reflections	1421 ($F_o^2 > 2\sigma\ (F_o^2)$)
Refined parameters	158
R_{int}, R_σ	0.0537, 0.0206
$R1$ (all data)	0.0291
$wR2$ (all data)	0.0602
Weighting scheme	$w^{-1}=\sigma^2\ F_o^2 + (0.0423\ P)^2 + 1.5848\ P$; $P = (F_o^2 + 2\ F_c^2)/3$
GooF	1.030
Residual electron density (min./max.) / e$^-$·Å^{-3}	-0.84/1.98

Table 6.6: Refined atomic coordinates, *Wyckoff* symbols and isotropic displacement parameters U_{eq} / Å^2 in Ho[H(PO$_3$)$_4$]; standard deviations in brackets

Atom	*Wyckoff* symbol	x	y	z	U_{eq}
Ho1	4*e*	0.729532(17)	0.05657(3)	0.05931(3)	0.00637(13)
P1	4*e*	0.90118(10)	−0.3250(2)	0.12488(15)	0.0080(3)
P2	4*e*	0.89935(9)	0.1530(2)	−0.18799(15)	0.0073(3)
P3	4*e*	0.38820(10)	0.2885(2)	0.20467(15)	0.0070(3)
P4	4*e*	0.59443(10)	0.3988(2)	0.21039(15)	0.0070(3)
$O_{br}1$	4*e*	0.9438(3)	−0.0209(6)	−0.2624(4)	0.0138(9)
$O_{br}2$	4*e*	0.9995(3)	−0.2308(5)	0.0942(4)	0.0101(8)
$O_{br}3$	4*e*	0.4186(3)	0.1212(5)	0.3132(4)	0.0111(8)
$O_{br}4$	4*e*	0.4853(3)	0.3257(6)	0.1412(4)	0.0107(8)
$O_{term}1$	4*e*	0.8334(3)	−0.1891(5)	0.1737(4)	0.0117(8)
$O_{term}2$	4*e*	0.8395(3)	0.0788(6)	−0.0889(5)	0.0166(9)
$O_{term}3$	4*e*	0.8581(3)	0.2080(6)	0.2034(4)	0.0154(9)
$O_{term}4$	4*e*	0.6349(3)	−0.0475(5)	0.2120(4)	0.0125(9)
$O_{term}5$	4*e*	0.6904(3)	−0.2267(6)	−0.0824(4)	0.0119(8)
$O_{term}6$	4*e*	0.6161(3)	0.1414(6)	−0.1351(4)	0.0132(9)
$O_{term}7$	4*e*	0.6633(3)	0.3331(5)	0.1200(4)	0.0121(9)
O_H1	4*e*	0.8568(3)	−0.4297(6)	−0.0126(5)	0.0178(10)
H1	4*e*	0.795(3)	−0.394(12)	−0.068(7)	0.050

O_{br} = bridging oxygen atom; O_{term} = terminal oxygen atom; O_H = hydroxyl group

Table 6.7: Anisotropic displacement parameters U_{ij} / Å^2 in Ho[H(PO$_3$)$_4$]; standard deviations in brackets

Atom	U_{11}	U_{22}	U_{33}	U_{12}	U_{13}	U_{23}
Ho1	0.00672(16)	0.00555(17)	0.00677(17)	−0.00023(10)	0.00109(10)	−0.00002(10)
P1	0.0072(6)	0.0059(7)	0.0103(7)	0.0007(6)	0.0004(6)	−0.0001(6)
P2	0.0053(6)	0.0069(7)	0.0094(7)	−0.0003(6)	0.0008(5)	−0.0011(6)
P3	0.0066(6)	0.0054(7)	0.0088(7)	−0.0006(6)	0.0010(5)	−0.0006(5)
P4	0.0069(6)	0.0048(7)	0.0090(7)	−0.0015(6)	0.0002(6)	0.0001(5)
O$_{br}$1	0.0094(19)	0.012(2)	0.019(2)	−0.0050(18)	−0.0009(17)	0.0009(17)
O$_{br}$2	0.0121(19)	0.011(2)	0.0064(18)	0.0006(17)	0.0004(15)	−0.0025(16)
O$_{br}$3	0.018(2)	0.0037(19)	0.010(2)	0.0033(17)	0.0002(17)	−0.0011(17)
O$_{br}$4	0.0084(18)	0.015(2)	0.0093(19)	−0.0018(17)	0.0029(15)	−0.0026(16)
O$_{term}$1	0.0139(19)	0.010(2)	0.011(2)	0.0014(17)	0.0020(16)	0.0033(16)
O$_{term}$2	0.014(2)	0.019(2)	0.018(2)	0.0005(19)	0.0064(18)	−0.0033(17)
O$_{term}$3	0.0119(19)	0.014(2)	0.018(2)	−0.0014(19)	−0.0037(17)	−0.0012(17)
O$_{term}$4	0.014(2)	0.010(2)	0.016(2)	0.0020(17)	0.0069(17)	−0.0008(16)
O$_{term}$5	0.0091(18)	0.010(2)	0.0015(2)	0.0004(18)	−0.0015(16)	0.0002(16)
O$_{term}$6	0.016(2)	0.010(2)	0.013(2)	−0.0019(17)	0.0000(17)	0.0043(17)
O$_{term}$7	0.0105(18)	0.010(2)	0.018(2)	−0.0016(18)	0.0068(17)	0.0006(16)
O$_{H}$1	0.015(2)	0.018(2)	0.017(2)	−0.0100(19)	−0.0039(18)	0.0004(17)

Table 6.8: Selected interatomic distances / Å and angles / ° in Ho[H(PO$_3$)$_4$]; standard deviations in brackets

P–O$_{br}$	1.568(4)–1.601(4)
P–O$_{term}$	1.463(4)–1.495(4)
P–O$_{H}$	1.533(4)
Ho–O	2.254(4)–2.427(4)
P$_{OH}$–O$_{br}$–P$_{O}$	135.8(2)–136.3(3)
P$_{O}$–O$_{br}$–P$_{O}$	129.8(3)–132.6(3)
O$_{term}$–P–O$_{term}$	117.4(2)–121.2(2)
O$_{term}$–P–O$_{br}$	105.9(2)–114.1(2)
O$_{term}$–P–O$_{H}$	115.0(2)
O$_{br}$–P–O$_{br}$	99.1(2)–104.2(2)
O$_{br}$–P–O$_{H}$	104.7(2)–106.7(2)

6.1.4 Rietveld Refinement of $Dy[H(PO_3)_4]$

Since $Dy[H(PO_3)_4]$ was obtained as polycrystalline powder a *Rietveld* refinement (Figure 6.2) was carried out using the single-crystal data of $Tb[H(PO_3)_4]$ as starting structure model. The phase purity of $Dy[H(PO_3)_4]$ could be confirmed.

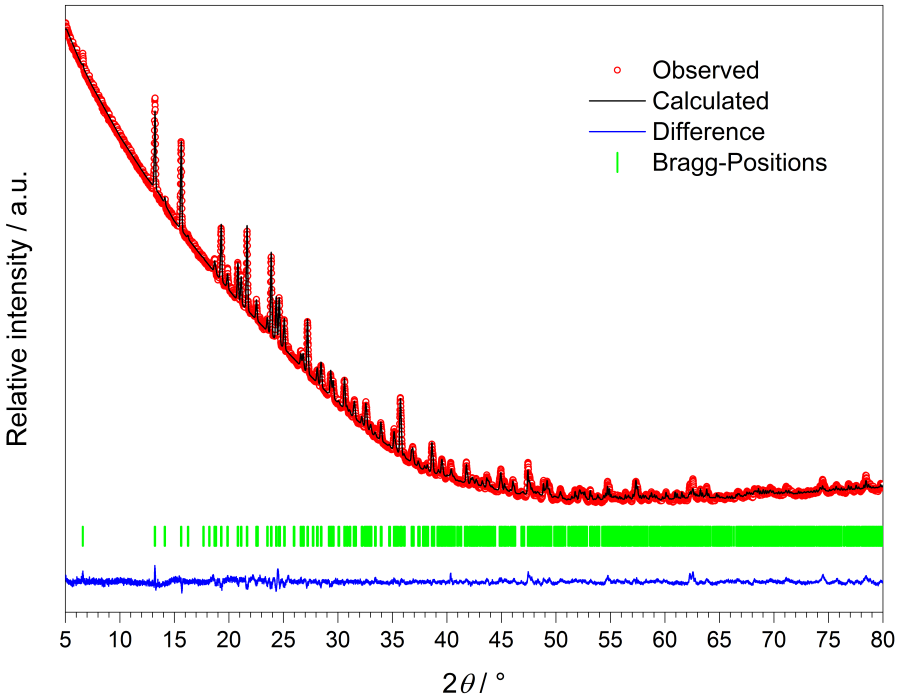

Figure 6.2: X-ray powder diffraction pattern and result of the *Rietveld* refinement of $Dy[H(PO_3)_4]$.

$Dy[H(PO_3)_4]$ crystallises isotypically to $Tb[H(PO_3)_4]$ and $Ho[H(PO_3)_4]$ in the monoclinic space group $P2_1/c$ with the lattice parameters $a_{Dy} = 13.6585(3)$ Å, $b_{Dy} = 7.09739(12)$ Å, $c_{Dy} = 9.6215(2)$ Å and $\beta_{Dy} = 101.116(1)°$. In Table 6.9 the results of the *Rietveld* refinement including the obtained unit cell parameters, the values of the fit residuals (R_p and R_{wp}) and χ^2 are listed. The structure model of $Dy[H(PO_3)_4]$ was refined to excellent residuals of $R_p = 0.009$, $R_{wp} = 0.012$ and $\chi^2 = 4.04$. The atomic coordinates, isotropic displacement factors (B_{iso}) and selected interatomic distances and angles are given in Tables 6.10 and 6.11.

Table 6.9: *Rietveld* refinement parameters of $Dy[H(PO_3)_4]$; standard deviations in brackets

Sum formula	$Dy[H(PO_3)_4]$
Molar weight / g·mol^{-1}	479.40
Crystal system	monoclinic
Space group	$P2_1/c$ (no. 14)
Colour	colourless
a / Å	13.6585(3)
b / Å	7.0974(1)
c / Å	9.6215(2)
β / °	101.116(1)
Volume / Å^3	915.21(3)
Z	4
Calculated density D_x / g·cm^{-3}	3.479
Radiation	Cu-K_α
Wavelength λ / Å	1.5406
Diffractometer	Bruker D8 Advance
Theta range / °	$5.00 \leq 2\theta \leq 140.00$
Refined parameters	62
R_p	0.009
R_wp	0.012
χ^2	4.04

Table 6.10: Refined atomic coordinates and isotropic displacement parameters B_{iso} / Å^2 of Dy[H(PO$_3$)$_4$]; standard deviations in brackets

Atom	x	y	z	B_{iso}
Dy	0.7286(2)	0.0603(4)	0.0591(3)	0.50
P1	0.8854(9)	−0.32830(16)	0.1209(15)	0.50
P2	0.8999(9)	0.1516(16)	−0.1981(14)	0.50
P3	0.6206(10)	−0.2125(17)	0.2932(14)	0.50
P4	0.6018(8)	0.4120(17)	0.2182(13)	0.50
$O_{br}1$	0.9425(14)	−0.4496(39)	0.2328(23)	1.00
$O_{br}2$	0.9908(18)	−0.2090(29)	0.0955(24)	1.00
$O_{br}3$	0.6037(17)	−0.3523(30)	0.1950(26)	1.00
$O_{br}4$	0.5279(19)	−0.18251(31)	0.3422(25)	1.00
$O_{term}1$	0.8400(16)	−0.1565(28)	0.1784(25)	1.00
$O_{term}2$	0.8417(14)	0.0488(37)	−0.0989(23)	1.00
$O_{term}3$	0.8535(17)	0.2955(32)	−0.2627(28)	1.00
$O_{term}4$	0.6438(14)	−0.0189(31)	0.2283(22)	1.00
$O_{term}5$	0.6957(18)	−0.2524(26)	0.4392(27)	1.00
$O_{term}6$	0.6238(17)	0.32260(31)	0.3568(28)	1.00
$O_{term}7$	0.6653(17)	0.3533(30)	0.1060(27)	1.00
O_H1	0.8624(13)	−0.4513(36)	−0.0350(23)	1.00

O_{br} = bridging oxygen atom; O_{term} = terminal oxygen atom;
O_H = hydroxyl group

Table 6.11: Selected interatomic distances / Å and angles / ° in Dy[H(PO$_3$)$_4$]; standard deviations in brackets

P–O_{br}	1.45(3)–1.88(3)
P–O_{term}	1.30(2)–1.60(3)
P–O_H	1.71(3)
Ho–O	2.24(2)–2.47(2)
P_{OH}–O_{br}–P_O	126.5(18)–134.3(16)
P_O–O_{br}–P_O	129.5(19)–141.5(19)
O_{term}–P–O_{term}	111(2)–118(3)
O_{term}–P–O_{br}	94(2)–130(3)
O_{term}–P–O_H	135(2)
O_{br}–P–O_{br}	93(2)–111(2)
O_{br}–P–O_H	98.1(20)–108.9(20)

6.1.5 Crystal Structure Description

$Ln[H(PO_3)_4]$ (Ln = Tb, Dy, Ho) crystallise isotypically to $Er[H(PO_3)_4]$ [173] in the centrosymmetric, monoclinic space group $P2_1/c$ with four formula units per unit cell. All atoms are located on the general *Wyckoff* position 4*e*. The anionic partial structure of $Ln[H(PO_3)_4]$ (Ln = Tb, Dy, Ho) consists of two different infinite helical chains of corner-sharing phosphate tetrahedra arranged parallel to each other along [010] with alternating hydrogen-polyphosphate and polyphosphate chains (Figure 6.3).

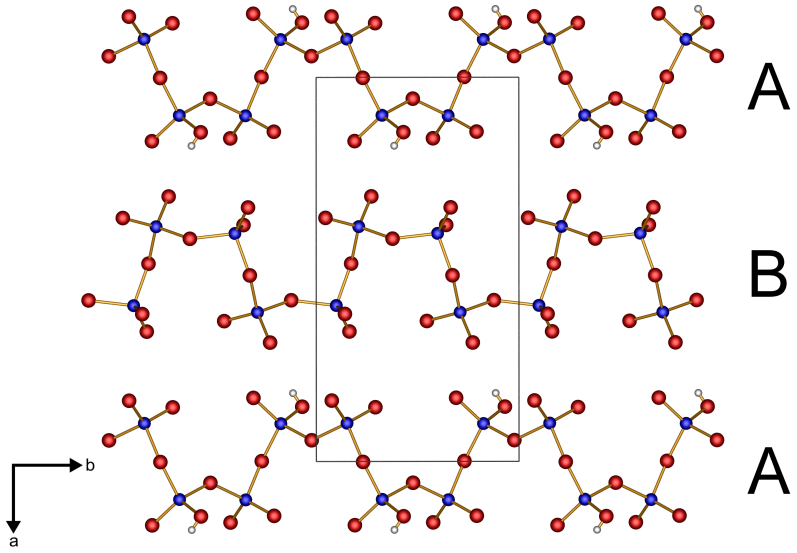

Figure 6.3: Infinite, parallel hydrogen polyphosphate (A) and polyphosphate (B) chains of $Ln[H(PO_3)_4]$ (Ln = Tb, Dy, Ho) along [010]; phosphorus blue, oxygen red, hydrogen white.

The protonated chain (A) reveals a larger diameter compared to the non-protonated polyphosphate chain (B) (Figure 6.4) due to widened P–O–P angles (136 ° in A vs. 130–133 ° in B).

Adjacent A and B chains in [100] and [001] direction, respectively, exhibit a phase shift of a half towards each other (Figure 6.5).

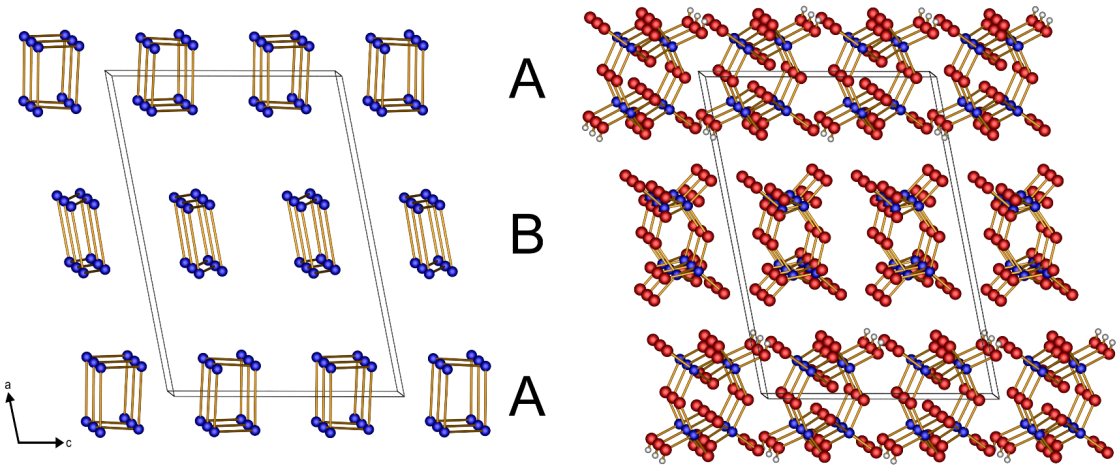

Figure 6.4: Reduced (left) and complete (right) presentation of the infinite helical hydrogen-polyphosphate (A) and polyphosphate (B) chains of $Ln[H(PO_3)_4]$ (Ln = Tb, Dy, Ho) in [010] direction; phosphorus blue, oxygen red, hydrogen white.

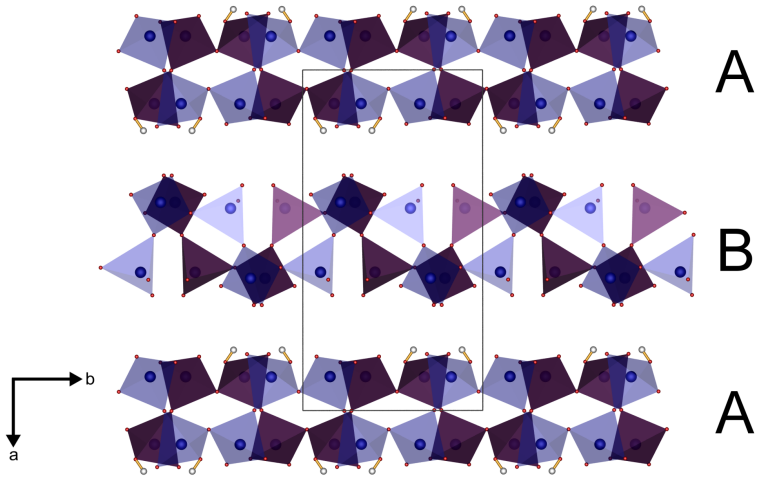

Figure 6.5: Phase shifted chains of hydrogen-polyphosphate (A) and polyphosphate (B) tetrahedra (blue: front, violet: back) of $Ln[H(PO_3)_4]$ (Ln = Tb, Dy, Ho); phosphate tetrahedra blue, oxygen red, hydrogen white.

In the phosphate tetrahedra P–O bond lengths range between 1.46 and 1.61 Å. The bond lengths P–O_H are 1.53 Å. P–O_{br} distances range between 1.56 and 1.61 Å, whereas P–O_{term} distances range between 1.46 and 1.50 Å. These values correspond to data found for other hydrogen-polyphosphates [171–173] or polyphosphates [182–188]. In general, P–O distances increase from P–O_{term} to P–O_H and up to P–O_{br} due to the decreasing effective negative charge on the involved oxygen atom which leads to weaker electrostatic interactions between P and O. Angles of the P_{OH}–O_{br}–P_O (A) and P_O–O_{br}–P_O (B) bridges range at 136°, and between 130–133°, respectively. O–P–O angles lie between 99–121°C (Ø = 109°) Selected bond lengths and angles of $Ln[H(PO_3)_4]$ (Ln = Tb, Ho) are listed in Tables 6.4 and 6.8.

For the calculation of deviation of tetrahedra from ideal symmetry the method introduced by *Balić-Žunić* and *Makovicky* [35, 36] was adopted. The four crystallographically different phosphate and hydrogenphosphate tetrahedra in $Tb[H(PO_3)_4]$ and $Ho[H(PO_3)_4]$ feature the values −0.32 % (P1), −0.29 % (P2), −0.22 % (P3), −0.20 % (P4) and −0.32 % (P1), −0.29 % (P2), −0.21 % (P3), −0.21 % (P4), respectively. Those values are on the typical scale for phosphate tetrahedra [97, 98, 187, 189–191]. Exhibiting a deviation far below 1 %, all tetrahedra are classified as regular.

The parallel hydrogen-polyphosphate and polyphosphate chains of $Ln[H(PO_3)_4]$ (Ln = Tb, Dy, Ho) are interconnected via common O corners of LnO_7 polyhedra (Figure 6.6).

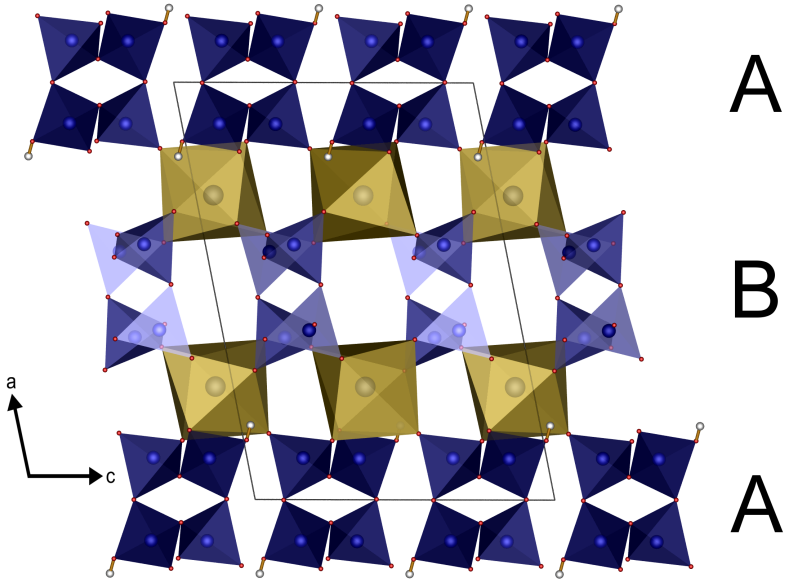

Figure 6.6: Infinite helical chains of hydrogen-polyphosphate (A) and polyphosphate (B) tetrahedra in $Ln[H(PO_3)_4]$ (Ln = Tb, Dy, Ho) interconnected via LnO_7 polyhedra (yellow); phosphate tetrahedra blue, oxygen red, hydrogen white.

The single-crystal structure reveals a single site of Ln^{3+}, which is coordinated single capped trigonal prismatic by seven terminal oxygen atoms of the polyphosphate chains (Figures 6.7 and 6.8). The Ln–O bond lengths range between 2.25 and 2.45 Å (Tables 6.4 and 6.8). Those values are in the same range as the Er–O bond lengths (2.25–2.43 Å) and Bi–O bond lengths (2.27–2.55 Å) determined by *Palkina et al.* [171, 173]. Ln^{3+} ions (Ln^{3+} = Tb, Ho, Er) possess very similar ionic radii (0.95–0.98 Å) [60]. Thus, the sum of the ionic radii of Ln^{3+} (Ln^{3+} = Tb, Ho) and O^{2-} (1.35 Å[60]) also exhibits values in the same order of magnitude. Bi^{3+} in $Bi[H(PO_3)_4]$ [171] does not represent an ion of the lanthanide row. Nevertheless, it reveals an ionic radius of 1.03 Å[60], which is very close to the discussed ionic radii of lanthanide ions. Hence, it does not surprise that the Bi–O bond lengths (2.27–2.55 Å) are also

in the same range as the *Ln*–O bond lengths.

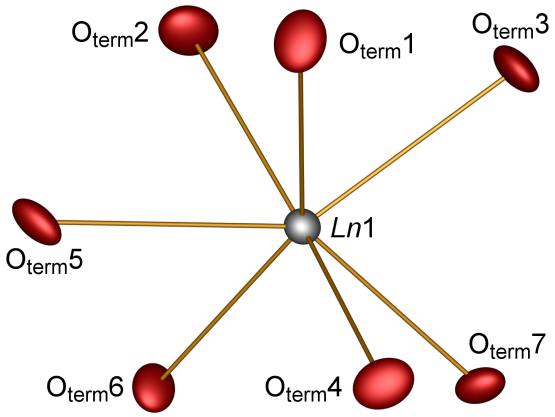

Figure 6.7: Coordination sphere of the lanthanide in $Ln[H(PO_3)_4]$ (Ln = Tb, Dy, Ho). The displacement ellipsoids are drawn on a probability level of 70 %.

According to *Steiner* [150] the single hydrogen bond can be considered as moderately strong in $Ln[H(PO_3)_4]$ (Ln = Tb, Ho) with a hydrogen to acceptor distance d(H1–O$_{term}$5) of 1.76 Å and a bond angle $\sphericalangle(DHA)$ of 165° in Tb$[H(PO_3)_4]$ [1]. In Ho$[H(PO_3)_4]$ the hydrogen to acceptor distance d(H1–O$_{term}$5) is 1.85 Å and the bond angle $\sphericalangle(DHA)$ is 145° [2] (Figure 6.8).

[1] donor to hydrogen distance d(O$_H$1–H1) = 0.93 Å, donor to acceptor distance d(O$_H$1–O$_{term}$5) = 2.67 Å.

[2] donor to hydrogen distance d(O$_H$1–H1) = 0.94 Å, donor to acceptor distance d(O$_H$1–O$_{term}$5) = 2.66 Å.

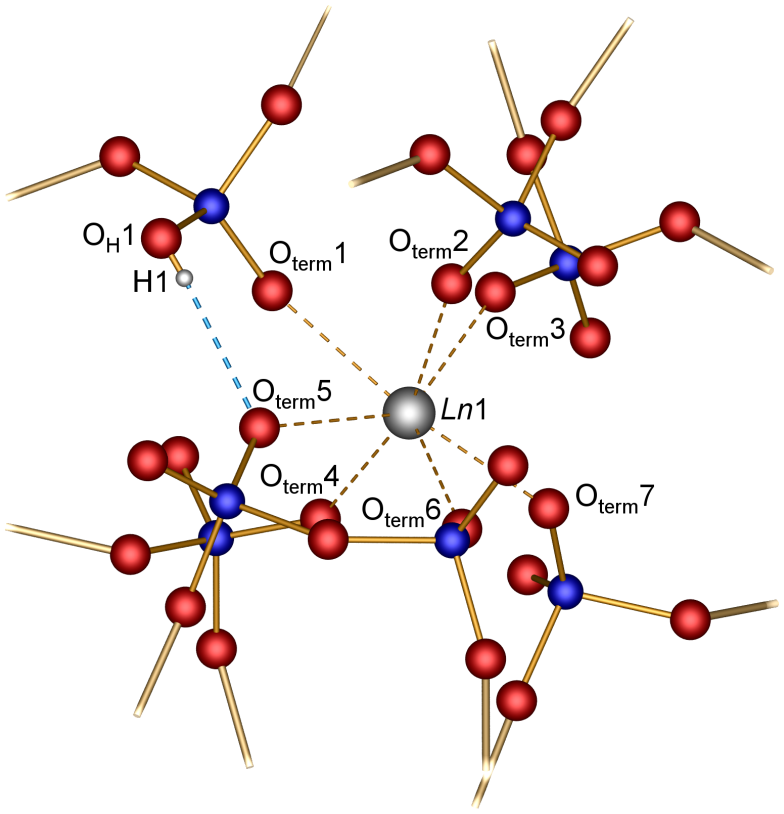

Figure 6.8: Moderate hydrogen bond (dotted blue line) and coordination sphere of the *Ln* atom in $Ln[H(PO_3)_4]$ (Ln = Tb, Ho); phosphorus blue, oxygen red, hydrogen white.

6.1.6 Electrostatic Calculations

The coordination numbers of the lanthanide ions (Tables 12.2 and 12.3) and the electrostatic consistency of the structure model were confirmed by calculations based on the MAPLE concept (= *Ma*delung *P*art of *L*attice *E*nergy) [32, 33, 152]. The allocation of the single proton could also be proven. The structure models of $Tb[H(PO_3)_4]$ and $Ho[H(PO_3)_4]$ show electrostatic consistency (Table 6.12) due to a deviation of less than 1 %.

Table 6.12: MAPLE calculations for $Ln[H(PO_3)_4]$ (Ln = Tb, Ho) [32, 33, 152]

$Tb[H(PO_3)_4]$	α-TbP_3O_9 [187] + 0.5 H_2O [192] + 0.5 P_2O_5 [193]
MAPLE = 98590 kJ·mol^{-1}	MAPLE = 98466 kJ·mol^{-1}
Δ = 0.13 %	
$Ho[H(PO_3)_4]$	α-HoP_3O_9 [187] + 0.5 H_2O [192] + 0.5 P_2O_5 [193]
MAPLE = 98811 kJ·mol^{-1}	MAPLE = 98326 kJ·mol^{-1}
Δ = 0.49 %	

6.1.7 Spectroscopic Properties

6.1.7.1 IR Spectroscopy

The infrared spectra of $Ln[H(PO_3)_4]$ (Ln = Tb, Dy, Ho) were recorded between 4000 and 400 cm^{-1} and are shown in Figure 6.9. The positions of the bands and the corresponding assignments are given in Table 6.13.

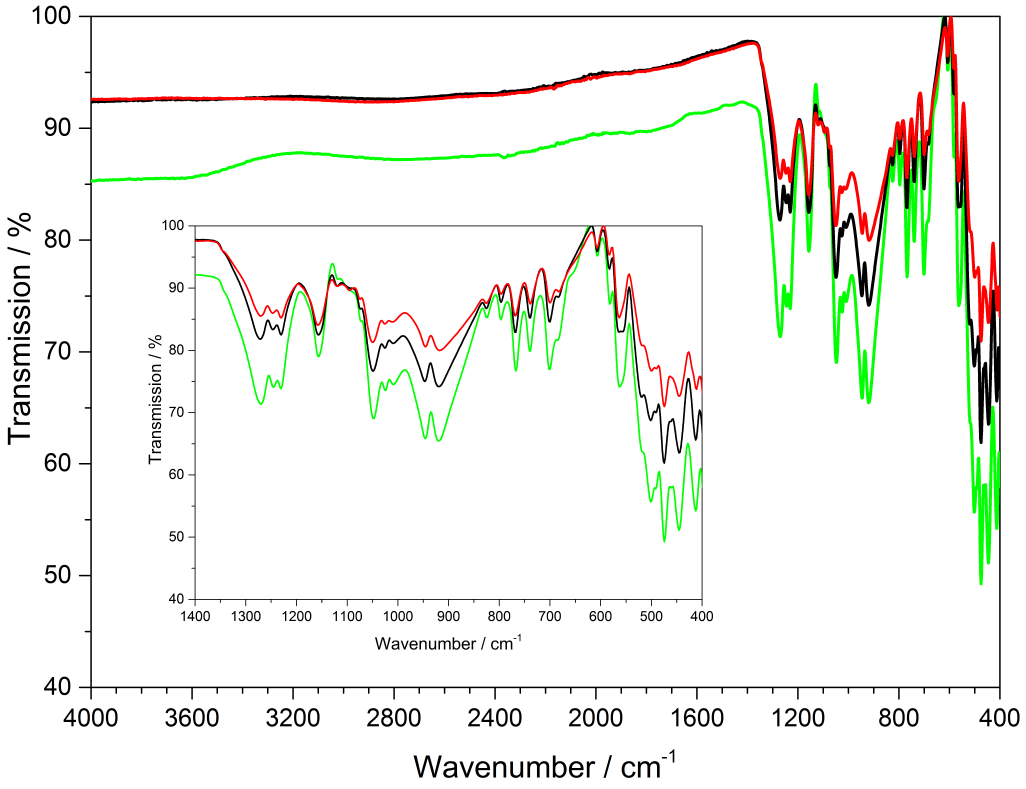

Figure 6.9: Infrared spectra of $Ln[H(PO_3)_4]$ (Ln = Tb, Dy, Ho); terbium green, dysprosium black, holmium red.

Table 6.13: Position / cm^{-1} and assignment of the IR bands in $Ln[H(PO_3)_4]$ (Ln = Tb, Dy, Ho)

Position	Assignment
1350–1200	$\nu_{as}(PO_2)$ [186, 194–196]
1200–990	$\nu(PO_{term})$ [186, 194–196]
985–845	$\nu_{as}(PO_{br})$, $\nu_{as}(POP)$ [186, 194–196]
780–650	$\nu_{s}(PO_{br})$ [186, 196, 197]
< 620	$\delta(PO_4)$ [186, 194–196]

The bands between 1350 and 1200 cm^{-1} can be assigned to the asymmetric stretching vibrations of PO_2, while vibrations between 1200–990 cm^{-1} can be assigned to the

stretching vibrations of PO_{term}. The $\nu_{as}(PO_{br})$ and $\nu_{as}(POP)$ vibrational bands range between 985 and 845 cm^{-1} [186, 194–196]. The four symmetric stretching modes of the PO_{br} vibrations are detected between 780 and 650 cm^{-1} peaking at 681, 700, 741 and 770 cm^{-1}, which had been empirically correlated to the periodicity of polyphosphate chains in *catena*-polyphosphates [186, 196, 197]. This also holds for $Ln[H(PO_3)_4]$ (Ln = Tb, Dy, Ho), due to the periodicity $P = 4$ of its hydrogenpolyphosphate chains. Vibrations observed below 620 cm^{-1} are assigned to bending vibrations of the PO_4 tetrahedra [186, 194–196]. Surprisingly no broad vibrations of the hydroxyl groups were detected, which leads to the assumption that presumably the ratio of O–H/P–O vibrations of 1:16 is too small to be detected via ATR.

6.1.7.2 UV-Vis Spectroscopy

The UV-Vis reflection spectra of $Ln[H(PO_3)_4]$ (Ln = Tb, Dy, Ho) (Figures 6.11 to 6.13) reveal the typical absorption bands of the f–f transitions of Tb^{3+}, Dy^{3+} and Ho^{3+} ions, according to the well-known energy level schemes [64, 67, 68]. All transitions start from the respective ground states $^7F_6$, $^6H_{15/2}$ and $^5I_8$ with the electronic configuration [Xe]$4f^8$, [Xe]$4f^9$ and [Xe]$4f^{10}$, respectively. The corresponding assignments are listed in Tables 6.14–6.16. No significant deviations from the spectra of other inorganic salts of terbium, dysprosium and holmium were detected and the spectra are in accordance with the powder colours white ($Tb[H(PO_3)_4]$ and $Dy[H(PO_3)_4]$) and yellow/pink ($Ho[H(PO_3)_4]$). Like other holmium compounds [198, 199] $Ho[H(PO_3)_4]$ shows the *alexandrite effect* (Chapter 3.4.3.6). Due to an absorption gap in the yellow region, it exhibits a yellow body colour in ambient day light. In artificial light, e.g. fluorescent lamps, with distinct emissions in the blue (~450 nm), green (~540 nm) and red (~610 nm) range [3], it reveals a pink body colour, due to the reflection of the wavelengths between 550 and 620 nm (Figure 6.10).

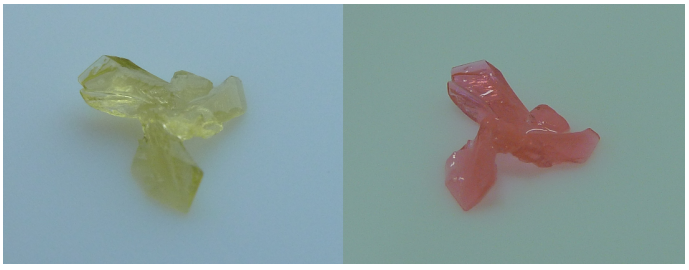

Figure 6.10: Yellow and pink body colour of $Ho[H(PO_3)_4]$ in ambient day light (left) and in artificial light (right), respectively.

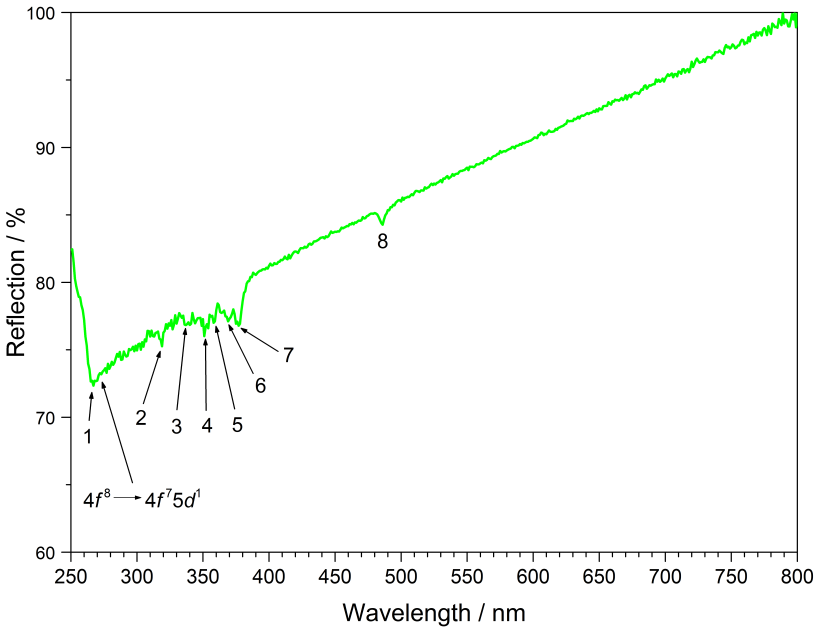

Figure 6.11: UV-Vis spectrum of $Tb[H(PO_3)_4]$.

Table 6.14: Absorption band energies for the strongest transitions in $Tb[H(PO_3)_4]$ and in free Tb^{3+} ions between 250 and 800 nm

Number	Absorption	λ / nm	$Tb[H(PO_3)_4]$ Energy / $10^3 \cdot cm^{-1}$	Free Tb^{3+} [64] Energy / $10^3 \cdot cm^{-1}$
1	$^7F_6 \rightarrow {}^5I_4$	267	37.5	37.5
2	$^7F_6 \rightarrow {}^5H_7$	319	31.3	31.6
3	$^7F_6 \rightarrow {}^5G_2$	336	29.8	29.6
4	$^7F_6 \rightarrow {}^5L_9$	351	28.5	28.5
5	$^7F_6 \rightarrow {}^5G_5$	358	27.9	27.8
6	$^7F_6 \rightarrow {}^5L_{10}$	369	27.1	27.1
7	$^7F_6 \rightarrow {}^5G_6$	377	26.5	26.4
8	$^7F_6 \rightarrow {}^5D_4$	486	20.6	20.5

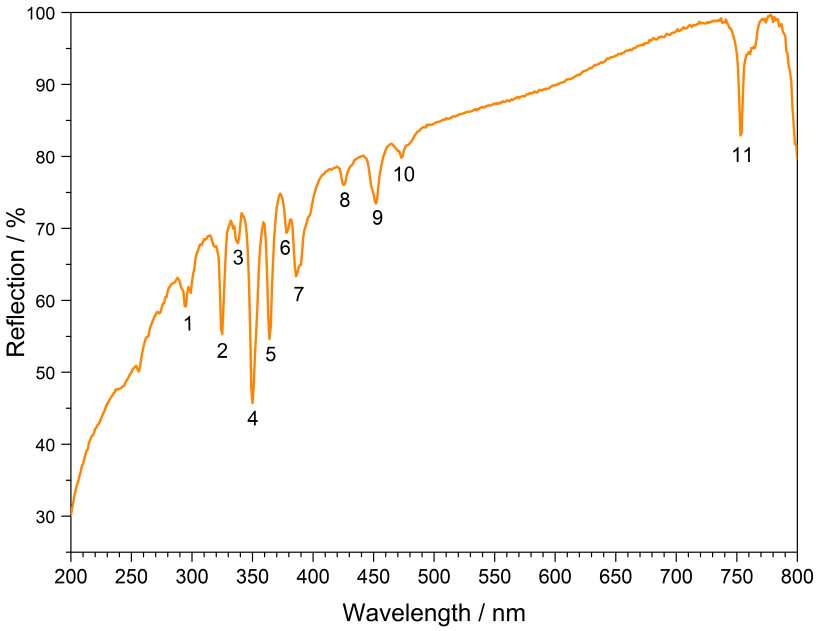

Figure 6.12: UV-Vis spectrum of $Dy[H(PO_3)_4]$.

Table 6.15: Absorption band energies for the strongest transitions in $Dy[H(PO_3)_4]$ and in free Dy^{3+} ions between 200 and 800 nm

Number	Absorption	λ / nm	$Dy[H(PO_3)_4]$ Energy / $10^3 \cdot cm^{-1}$	Free Dy^{3+} [67] Energy / $10^3 \cdot cm^{-1}$
1	$^6H_{15/2} \rightarrow {}^4D_{7/2}$	295	33.9	33.8
2	$^6H_{15/2} \rightarrow {}^6P_{3/2}$	325	30.8	30.8
3	$^6H_{15/2} \rightarrow {}^4F_{5/2} + {}^4D_{5/2}$	338	29.6	29.6
4	$^6H_{15/2} \rightarrow {}^6P_{7/2}$	350	28.6	28.6
5	$^6H_{15/2} \rightarrow {}^6P_{5/2}$	364	27.5	27.5
6	$^6H_{15/2} \rightarrow {}^4K_{17/2}$	378	26.5	26.4
7	$^6H_{15/2} \rightarrow {}^4I_{13/2}$	386	25.9	25.9
8	$^6H_{15/2} \rightarrow {}^4G_{11/2}$	425	23.5	23.3
9	$^6H_{15/2} \rightarrow {}^4I_{15/2}$	452	22.1	22.3
10	$^6H_{15/2} \rightarrow {}^4F_{9/2}$	473	21.1	21.1
11	$^6H_{15/2} \rightarrow {}^6F_{3/2}$	753	13.3	13.2

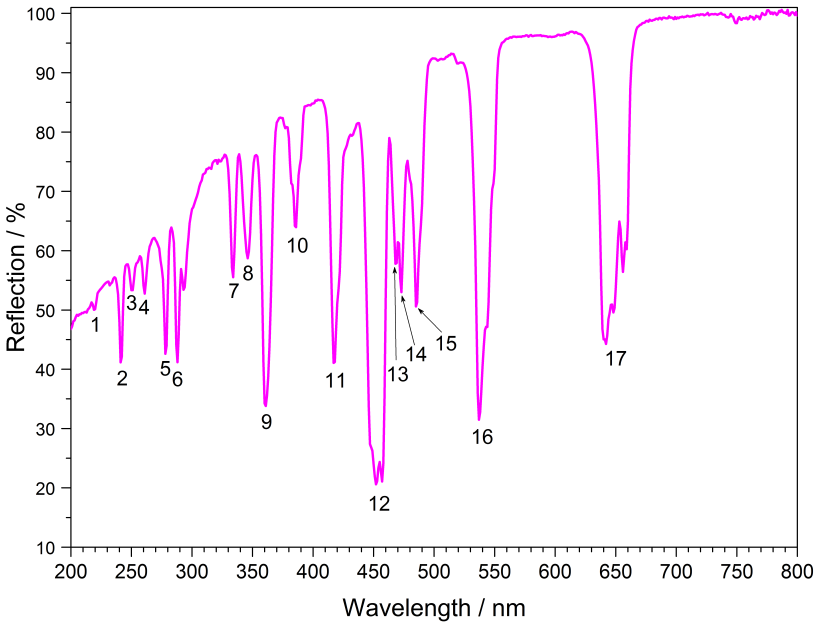

Figure 6.13: UV-Vis spectrum of $Ho[H(PO_3)_4]$.

Table 6.16: Absorption band energies for the strongest transitions in $Ho[H(PO_3)_4]$ and in free Ho^{3+} ions between 200 and 800 nm

Number	Absorption	λ / nm	$Ho[H(PO_3)_4]$ Energy / $10^3 \cdot cm^{-1}$	Free Ho^{3+} [67] Energy / $10^3 \cdot cm^{-1}$
1	$^5I_8 \rightarrow {}^3H_6 + {}^1I_6$	219	45.7	45.7
2	$^5I_8 \rightarrow {}^3F_4 + {}^5D_4$	241	41.6	41.5
3	$^5I_8 \rightarrow {}^5D_3$	250	40.0	40.0
4	$^5I_8 \rightarrow {}^3I_7$	261	38.2	38.5
5	$^5I_8 \rightarrow {}^3P_0$	278	36.0	36.0
6	$^5I_8 \rightarrow {}^5G_4 + {}^5D_4 + {}^3G_4$	290	34.5	34.8
7	$^5I_8 \rightarrow {}^3F_4 + {}^3H_4 + {}^3G_4$	334	29.9	30.0
8	$^5I_8 \rightarrow {}^3L_9$	346	28.9	29.0
9	$^5I_8 \rightarrow {}^3H_6$	361	27.7	27.7
10	$^5I_8 \rightarrow {}^5G_4$	386	25.9	25.8
11	$^5I_8 \rightarrow {}^5G_5 + {}^3G_5$	417	24.0	24.0
12	$^5I_8 \rightarrow {}^5F_1$	451	22.2	22.4
13	$^5I_8 \rightarrow {}^3K_8$	468	21.4	21.3
14	$^5I_8 \rightarrow {}^5F_2$	473	21.1	21.1
15	$^5I_8 \rightarrow {}^5F_3$	485	20.6	20.7
16	$^5I_8 \rightarrow {}^5F_4$	538	18.6	18.6
17	$^5I_8 \rightarrow {}^5F_5$	648	15.4	15.5

6.1.7.3 Fluorescence Spectroscopy

The fluorescence spectra of $Tb[H(PO_3)_4]$ (Figure 6.14) and $Dy[H(PO_3)_4]$ (Figure 6.16) show the characteristic f–f emissions of Tb^{3+} and Dy^{3+}, respectively [64, 67, 68].

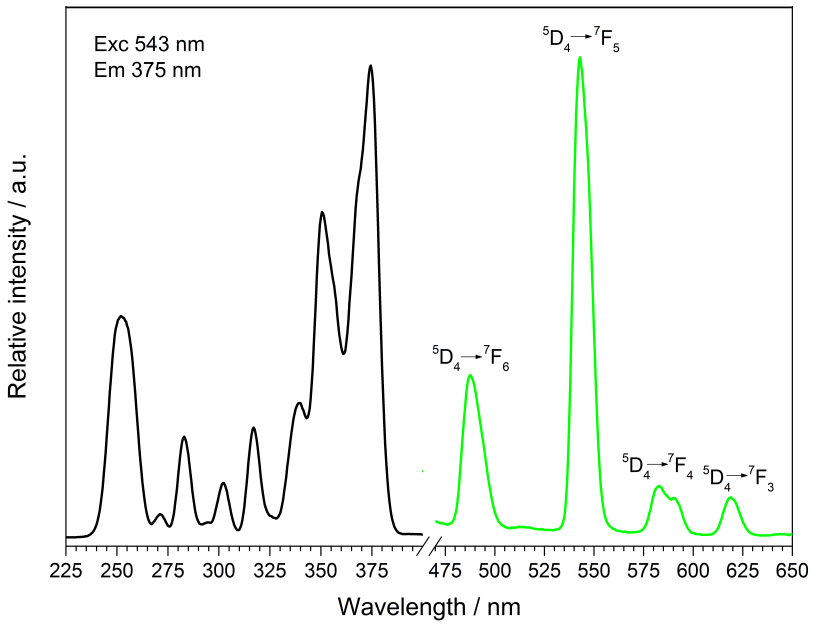

Figure 6.14: Excitation (black) and emission (green) spectrum of $Tb[H(PO_3)_4]$.

Between 230 and 270 nm a broader band in the excitation spectrum indicates the parity allowed $4f^8 \rightarrow 4f^7 5d^1$ transition, which is influenced by the chemical surrounding of Tb^{3+}. Compounds doped with Tb^{3+} also reveal such an excitation, e.g. in $K_2GdZr(PO_4)_3$:Tb at 223 nm [70]. In both compounds Tb^{3+} is in a phosphate environment. In contrast to the helically condensed phosphate chains in $Tb[H(PO_3)_4]$, $K_2GdZr(PO_4)_3$:Tb comprises isolated phosphate ions, which reveal less stability against vibration. Thus, a higher energy for the excitation in the d orbitals is needed. Under excitation at 375 nm $Tb[H(PO_3)_4]$ exhibits sharp emission lines between 475 and 630 nm, which can be assigned to the $^5D_4 \rightarrow {}^7F_6$ (488 nm), $^5D_4 \rightarrow {}^7F_5$ (543 nm), $^5D_4 \rightarrow {}^7F_4$ (583 nm) and $^5D_4 \rightarrow {}^7F_3$ (619 nm) transitions [64]. The transition with the highest intensity is located at 543 nm and is responsible for the green emission (Figure 6.15).

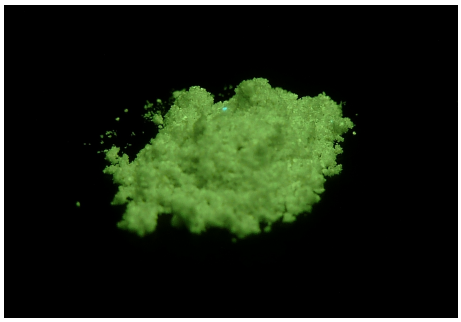

Figure 6.15: Green fluorescence of $Tb[H(PO_3)_4]$ at 254 nm.

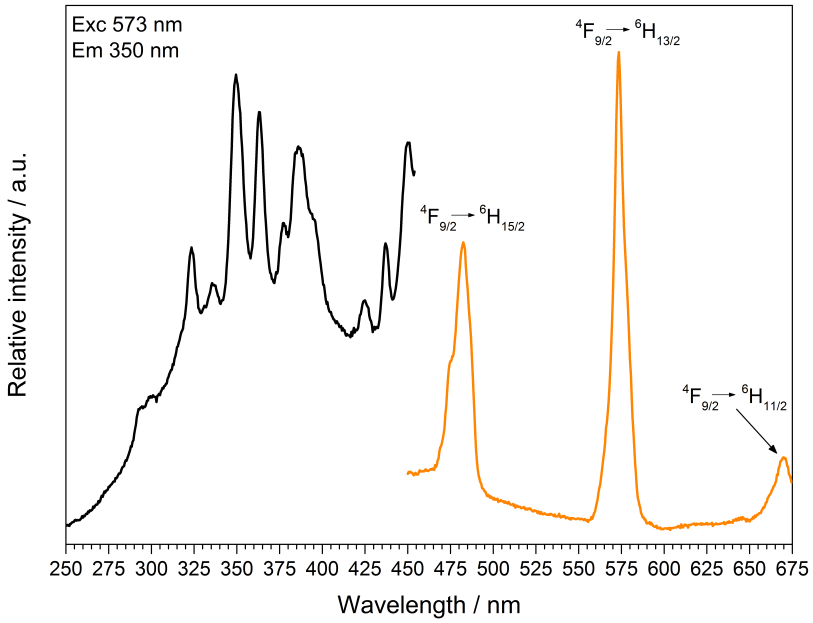

Figure 6.16: Excitation (black) and emission (orange) spectrum of $Dy[H(PO_3)_4]$.

The excitation spectrum of $Dy[H(PO_3)_4]$ shows a broad band around 290 nm, which indicates the $4f^9 \rightarrow 4f^8 5d^1$ transition. In other compounds exhibiting Dy^{3+} ions this transition occurs as well. In $Gd_3Ga_5O_{12}$:Dy [200] it is shifted to shorter wavelengths and occurs around 250 nm. In $Dy[H(PO_3)_4]$ Dy^{3+} is coordinated by seven oxygen atoms of the phosphate chains, whereas in $Gd_3Ga_5O_{12}$:Dy it is eightfold coordinated by oxygen atoms. Since the chemical surrounding has an influence on the *d* orbitals of Dy^{3+} it does not surprise that a surrounding of oxygen atoms has a different influence on the Dy^{3+} *d* orbitals than the surrounding of oxygen atoms of phosphate tetrahedra in $Dy[H(PO_3)_4]$ [8]. Solely oxygen atoms as coordination sphere possess a stronger ionic character compared to oxygen atoms covalently bound to an infinite phosphate chain. Due to the *nephelauxetic effect* an increased interaction between coordinating anion and central ion is achieved. Thus, a stronger ligand field splitting occurs and the wavelength is shifted to longer wavelengths in $Dy[H(PO_3)_4]$. Under excitation at 349 nm $Dy[H(PO_3)_4]$ exhibits sharp emission lines between 460 and

675 nm, which correspond to the f–f electronic transitions $^4F_{9/2}\rightarrow{}^6H_{15/2}$ (482 nm), $^4F_{9/2}\rightarrow{}^6H_{13/2}$ (573 nm) and $^4F_{9/2}\rightarrow{}^6H_{11/2}$ (671 nm) [67]. The most intense transition $^4F_{9/2}\rightarrow{}^6H_{13/2}$ is sensitive to the surrounding of Dy^{3+}, and is thus called hypersensitive. The surrounding of Dy^{3+} in $Dy[H(PO_3)_4]$ is of relatively low symmetry (single capped trigonal prismatic), therefore the intensity of the hypersensitive transition is increased with respect to the $^4F_{9/2}\rightarrow{}^6H_{15/2}$ transition [54, 70].

Doping of $Dy[H(PO_3)_4]$ with increasing concentrations of Ce^{3+} (5, 10, 30 mol%) was carried out to investigate the effect of Ce^{3+} as sensitizer. The presence of cerium and the corresponding ratios of Dy:Ce were investigated via EDX spectroscopy. The resulting ratios are 1:0.04 (expected: 1:0.05), 1:0.07 (1:0.10) and 1:0.26 (1:0.30), which are within the limits of accuracy of the measurements very close to the expected values. Due to an overlap in the wavelength range of the emission bands of Ce^{3+} and the excitation spectrum of Dy^{3+} an energy transfer could be expected. Transitions in Ce^{3+} are f–d transitions, which are allowed due to the selection rules, and thus lead to broad and intense bands in the fluorescence spectrum [46]. The fluorescence spectra of the doped samples $Dy[H(PO_3)_4]:Ce^{3+}$ are shown in Figure 6.17. The excitation spectra exhibit strongly increasing broad band intensities of Ce^{3+} at 302 nm ($^2F_{5/2}\rightarrow 5d$). In the emission spectra, next to a broad band emission of Ce^{3+} peaking at 317 nm ($5d\rightarrow{}^2F_{5/2}$) and 336 nm ($5d\rightarrow{}^2F_{7/2}$) two comparably weak emission bands of Dy^{3+}, corresponding to the f–f electronic transitions $^4F_{9/2}\rightarrow{}^6H_{15/2}$ and $^4F_{9/2}\rightarrow{}^6H_{13/2}$, can be observed.

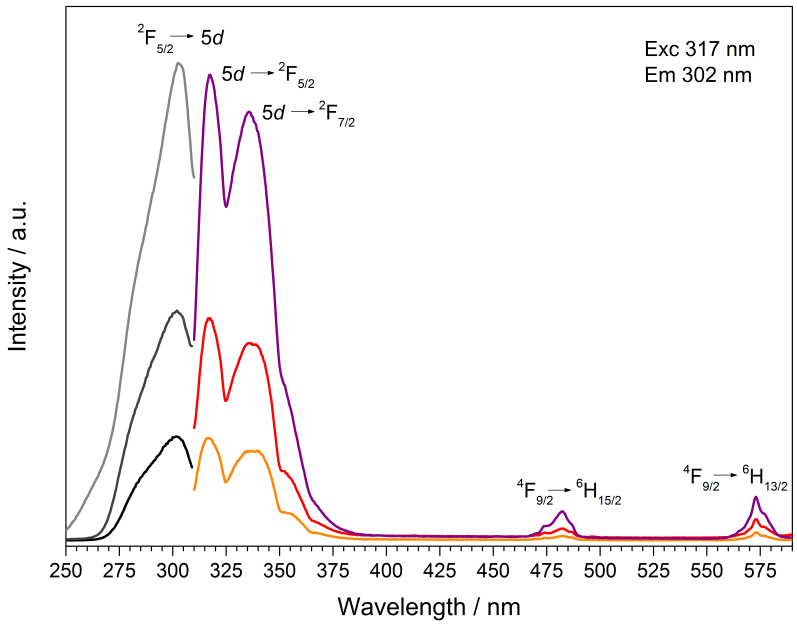

Figure 6.17: Excitation and emission spectra of $Dy[H(PO_3)_4]:Ce^{3+}$ (5% black/orange, 10% dark grey/red, 30% grey/violet).

Despite the low Dy^{3+} emission intensities the hypersensitive transition $^4F_{9/2}\rightarrow{}^6H_{13/2}$

can still be observed with higher intensity compared to the $^4F_{9/2}\rightarrow{}^6H_{15/2}$ transition. Doubling the content of Ce^{3+} from 5 to 10 mol% the emission intensity of Dy^{3+} also increases equally ($^4F_{9/2}\rightarrow{}^6H_{15/2}$), whereas the hypersensitive transition $^4F_{9/2}\rightarrow{}^6H_{13/2}$ even triples. A further increase of the Ce^{3+} content to 30 mol% leads to a raised intensity of a factor of 2.5 for the $^4F_{9/2}\rightarrow{}^6H_{15/2}$ transition and a factor of 1.7 for the $^4F_{9/2}\rightarrow{}^6H_{13/2}$ transition. Thus, the emission intensities of Dy^{3+} increase slightly with increasing Ce^{3+} content but do not prove an efficient $Ce^{3+}\rightarrow Dy^{3+}$ energy transfer. The intensity of the *f*–*d* transition in the excitation spectrum increases corresponding to the increasing Ce^{3+} content.

According to *Luo* and *Yang* satisfying energy transfer rates in the system Dy^{3+}/Ce^{3+} could be reached, if the ratio of Dy^{3+} to Ce^{3+} ions is decreased to about 1:3, before luminescence quenching of Ce^{3+} occurs [201–203]. By reversing the Dy^{3+}/Ce^{3+} ratio and increasing the content of Ce^{3+} to $Ce_{0.75}Dy_{0.25}[H(PO_3)_4]$ an efficient energy transfer might be reached, which represents rather a substitution than a doping process.

Doping $Dy[H(PO_3)_4]$ with 5 mol% Eu^{3+} leads to the typical sharp excitation and emission bands of Dy^{3+} and Eu^{3+} (Figure 6.18).

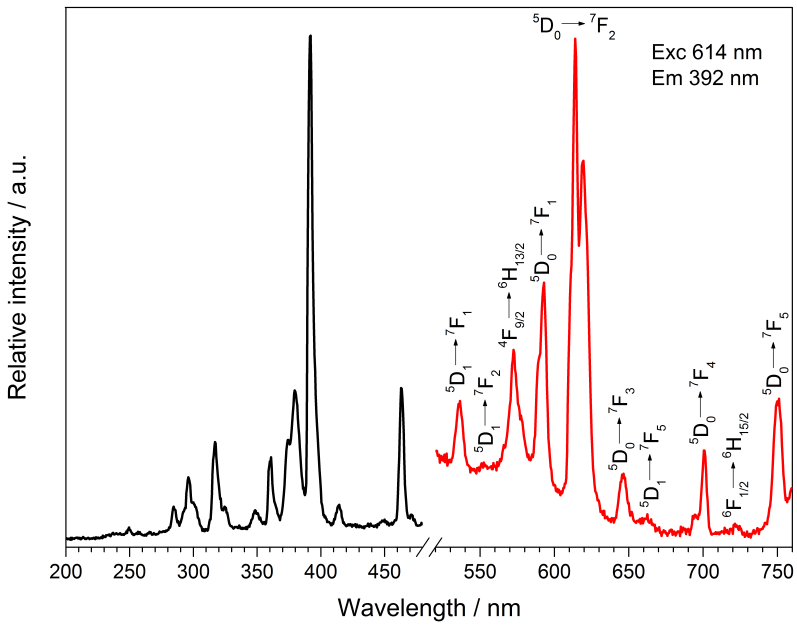

Figure 6.18: Excitation (black) and emission (red) spectrum of $Dy[H(PO_3)_4]:Eu^{3+}$.

The ratio of Dy:Eu was investigated via EDX spectroscopy comprising a ratio of 1:0.04, which is very close to the expected ratio (1:0.05). Under excitation at 392 nm $Dy[H(PO_3)_4]:Eu^{3+}$ exhibits sharp emission lines between 530 and 757 nm, which can be assigned to the $^5D_1\rightarrow{}^7F_1$ (536 nm), $^5D_0\rightarrow{}^7F_0$ (553 nm), $^5D_0\rightarrow{}^7F_1$ (593 nm), $^5D_0\rightarrow{}^7F_2$ (614 nm), $^5D_0\rightarrow{}^7F_3$ (646 nm), $^5D_1\rightarrow{}^7F_5$ (663 nm), $^5D_0\rightarrow{}^7F_4$ (700 nm) and

$^5D_0 \rightarrow {}^7F_5$ (750 nm) transitions of Eu^{3+} [53]. The most intense transition $^5D_0 \rightarrow {}^7F_2$ at 614 nm is called hypersensitive due to its sensitivity to the surrounding of Eu^{3+}. It is dominant over the $^5D_0 \rightarrow {}^7F_1$ transition because of the asymmetric surrounding of Eu^{3+} in $Dy[H(PO_3)_4]:Eu^{3+}$, which proves its partial substitution of Dy^{3+} sites [55, 56]. Besides the emission bands of Eu^{3+} two emission bands of Dy^{3+} can be observed at 573 and 722 nm, which can be assigned to the $^4F_{9/2} \rightarrow {}^6H_{13/2}$ and $^6F_{1/2} \rightarrow {}^6H_{15/2}$ transitions of Dy^{3+} [67].

6.1.8 Magnetic Properties

Due to the presence of one proton and the thus postulated sum formula of $Tb[H(PO_3)_4]$, the valence state of terbium was confirmed by a magnetic susceptibility measurement, which was recorded in a field of 1000 Oe over the temperature range of $1.8\,K < T < 400\,K$ (Figure 6.19). In the whole temperature range the molar susceptibility obeys *Curie's* law ($\chi_m = C/T$) very well with a *Curie* constant of $C = 11.3792\,emu{\cdot}mol^{-1}{\cdot}K^{-1}$. The *Curie* constant corresponds to an effective magnetic moment per Tb^{3+} ion of $\mu_{eff} = 9.54\,\mu_B$, which is close to the theoretical value ($\mu_{eff} = 9.72\,\mu_B$) and to experimental effective magnetic moments of Tb^{3+} ions (9.7–9.8 μ_B) [80].

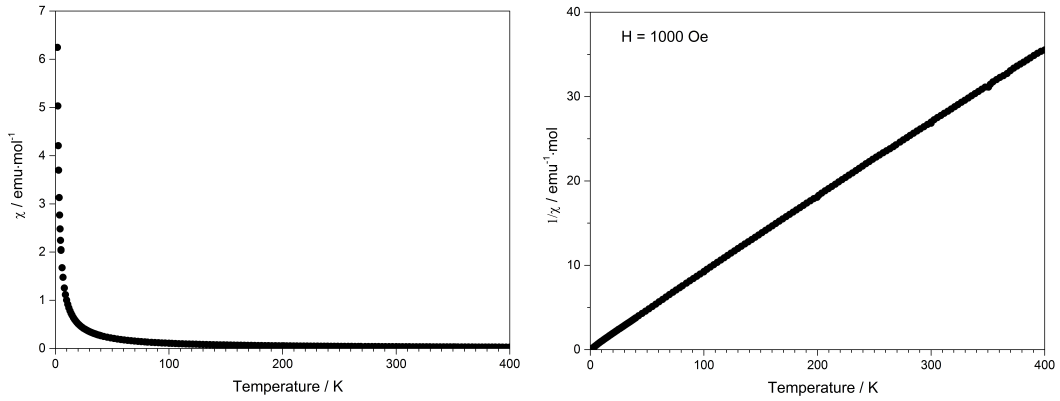

Figure 6.19: Temperature dependence of the magnetic susceptibility χ of $Tb[H(PO_3)_4]$.

6.1.9 Thermal Analysis

The thermal behaviour of $Tb[H(PO_3)_4]$ was investigated between room temperature and 1450 °C (Figure 6.20). The thermogravimetric curve reveals several undefined steps with a total mass loss of 15.2 wt% in the temperature range of 500–1450 °C. Assuming that besides 0.5 moles of H_2O a further 0.5 moles of P_2O_5 evaporate (theor. mass loss: 16.8 wt%) a final composition of TbP_3O_9 may be assumed (Equation 6.1). After the thermal treatment the product was glazed and the expected composition could not be confirmed via X-ray powder diffraction.

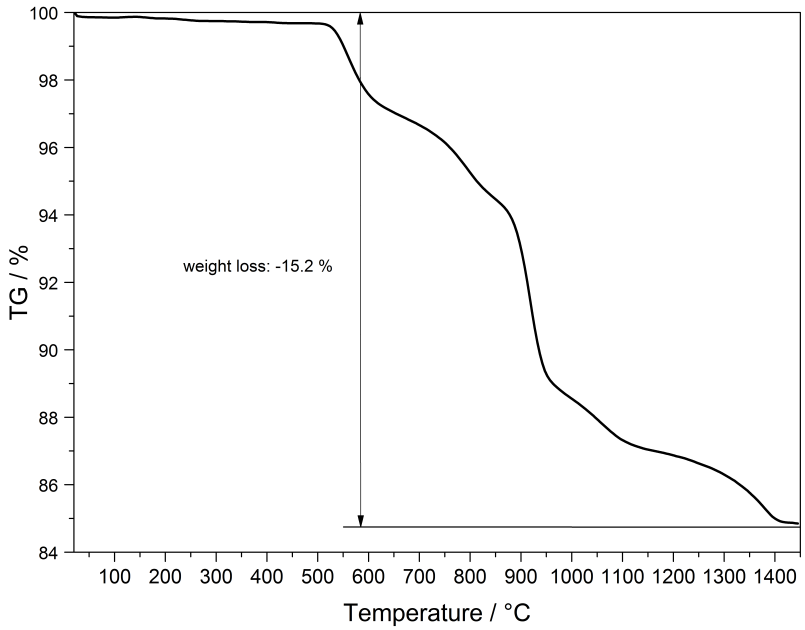

Figure 6.20: Thermogravimetric analysis of $Tb[H(PO_3)_4]$.

$$Tb[H(PO_3)_4] \xrightarrow[N_2]{\Delta} TbP_3O_9 + 0.5P_2O_5 + 0.5H_2O \tag{6.1}$$

Temperature-dependent X-ray powder diffraction confirms that $Tb[H(PO_3)_4]$ is stable up to 500 °C (Figure 6.21). At 900 °C α-TbP_3O_9 (grey) represents the main phase next to a small part of TbP_5O_{14} [92] (marked with *). This leads to the conclusion that the assumption of losing half a mole of each, H_2O and P_2O_5, in the thermal analysis is correct.

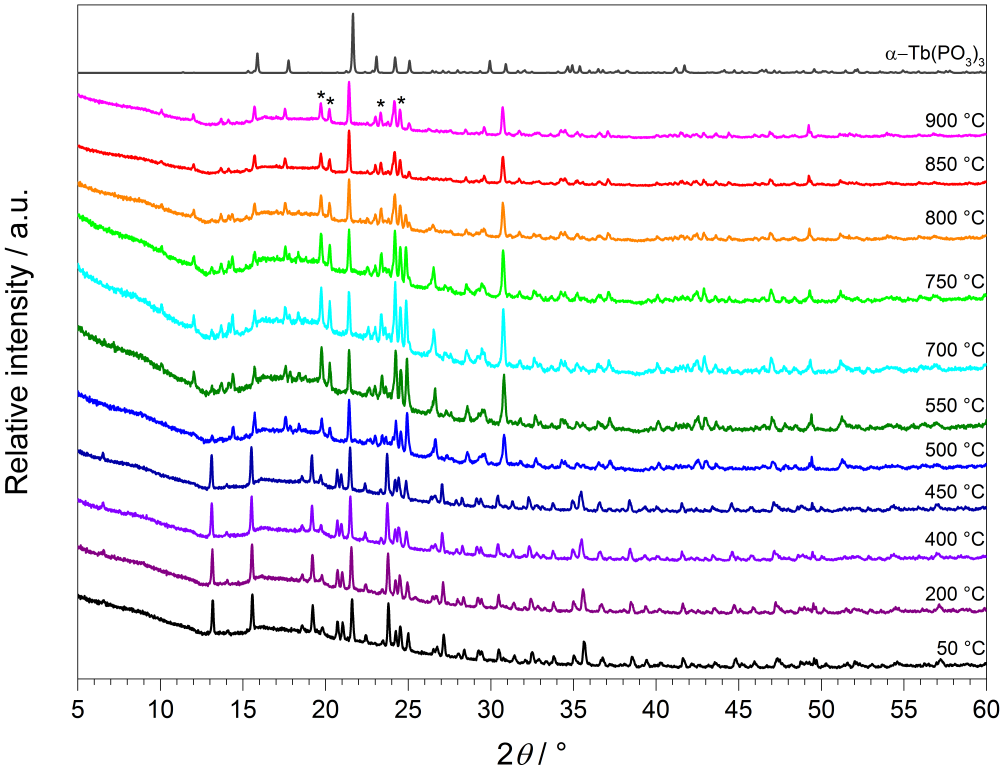

Figure 6.21: Temperature-dependent X-ray diffraction patterns of $Tb[H(PO_3)_4]$ recorded between 50 and 900 °C, calculated powder diffraction pattern from single-crystal data of α-TbP_3O_9 (grey) and side phase TbP_5O_{14} (*).

$Tb[H(PO_3)_4]$ exhibits infinite chains of $[HP_4O_{12}]^{3-}$ and $[P_3O_9]^{3-}$ anions. Hence it does not surprise that thermal decomposition leads to elimination of the hydroxyl groups by evaporation of water. Astonishingly, under nitrogen flow this process does not occur below 500 °C. Since an increasing stability is expected with an increasing connectivity, the thermal stability of $Tb[H(PO_3)_4]$ possessing infinite polyphosphate chains, is estimated to be higher, than for non-condensed cyclotetraphosphates, e.g. $Ba_2(P_4O_{12})\cdot 3.5H_2O$ [98], which decomposes till 380 °C. In contrast, thermal decomposition of the ultraphosphate YP_5O_{14}, which comprises a higher degree of condensation, does not occur until 760 °C [204].

6.1.10 Discussion

The samples of the lanthanide hydrogen-polyphosphates $Ln[H(PO_3)_4]$ (Ln = Tb, Dy, Ho) were obtained as phase pure powders and their structures could be solved and refined based on single-crystal X-ray diffraction (Ln = Tb, Ho) and refined by a *Rietveld* refinement (Ln = Dy). Via MAPLE calculations the allocation of the single proton could be proved on the one hand, and on the other hand the electrostatic consistency of the structure model of $Ln[H(PO_3)_4]$ (Ln = Tb, Ho) was confirmed. The postulated structure by *Palkina et al.* [173] and the calculated unit cell parameters by *Selevich et al.* [205] are very close to the data obtained in this work. An X-ray diffraction study of a number of the synthesised phosphates was carried out by *Selevich et al.* and the crystallographic data of $Er[H(PO_3)_4]$ [173] was used for the calculation of the theoretical lattice parameters of $Ln[H(PO_3)_4]$ (Ln = Eu–Er, Y) [205]. In Table 6.17 the lattice parameters of $Ln[H(PO_3)_4]$ (Ln = Eu–Er, Y) [205], $Er[H(PO_3)_4]$ [173] and $Ln[H(PO_3)_4]$ (Ln = Tb–Ho) [180] are summarised. For a better comparison of the values the assignment of the axes in $Ln[H(PO_3)_4]$ (Ln = Tb–Ho) [180] was adapted to the assignment by *Selevich et al.* and *Palkina et al.*.

Table 6.17: Comparison of the lattice parameters of $Ln[H(PO_3)_4]$ (Ln = Eu–Er, Y) by *Selevich et al.* [205], $Er[H(PO_3)_4]$ by *Palkina et al.* [173] and $Ln[H(PO_3)_4]$ (Ln = Tb–Ho) [180]

Ln	a / Å	b / Å	c / Å	β / °	V / Å	Ref.
Eu	9.681(13)	7.110(13)	13.752(15)	101.26(10)	928(2)	[205]
Gd	9.647(8)	7.089(6)	13.706(8)	101.17(7)	920(1)	[205]
Tb	9.633(8)	7.096(6)	13.672(9)	101.11(6)	917(1)	[205]
Tb	9.6579(3)	7.1042(2)	13.6824(4)	101.200(1)	920.89(5)	[180]
Dy	9.594(7)	7.085(5)	13.645(8)	101.07(7)	910(1)	[205]
Dy	9.6215(2)	7.0974(1)	13.6585(3)	101.116(1)	915.21(3)	[180]
Ho	9.596(7)	7.086(6)	13.642(9)	101.01(7)	911(1)	[205]
Ho	9.5907(4)	7.0924(3)	13.6334(5)	101.055(1)	910.15(6)	[180]
Er	9.555(7)	7.070(5)	13.599(9)	101.00(6)	902(1)	[205]
Er	9.574(2)	7.096(1)	13.637(3)	100.95(1)	909.6	[173]
Y	9.575(9)	7.068(6)	13.606(9)	101.02(6)	904(1)	[205]

Both the results presented by *Selevich et al.* and in this work reveal a decrease of the lattice parameters of $Ln[H(PO_3)_4]$ (Ln = Eu–Er, Y) going from left to right in the periodic table. This trend fits very well to the decreasing ionic radii in this period [60]. Due to the increasing positive nuclear charge electrons of the s and p orbitals are stronger attracted by the core. Thus, the so called lanthanide contraction occurs.

In contrast to the calculated lattice parameters of $Ln[H(PO_3)_4]$ (Ln = Eu–Er, Y) investigated by *Selevich et al.* the lattice parameters of $Ln[H(PO_3)_4]$ (Ln = Tb–Ho) were received by single-crystal structure analysis (Ln = Tb, Ho) and a *Rietveld* refinement (Ln = Dy). Hence, it does not surprise that the values presented in this work show a higher accuracy. Furthermore, all data received by single-crystal structure analysis [173, 180] reveal slightly larger values with an exception of the c axis in $Ho[H(PO_3)_4]$. Depending on the source of the values of ionic radii, deviations between calculated and experimental lattice parameters can occur. The largest influence of the lanthanide ion occurs on the a and c axis. Lanthanide ions in $Ln[H(PO_3)_4]$ (Ln = Eu–Er, Y) are situated between the helical phosphate chains and particularly influence the a and c axis depending on their size (Figure 6.6). The phosphate chains are running along the b axis and thus this dimension is not influenced that strongly (Table 6.17).

The optical properties show the typical UV-Vis reflection and fluorescence spectra of Tb^{3+}, Dy^{3+} and Ho^{3+} ions exhibiting their characteristic absorption and emission bands, respectively. A further proof of the valence state of Tb^{3+} revealed a magnetic susceptibility measurement. The received effective magnetic moment μ_{eff} of terbium agrees well with the theoretical value and other experimental effective magnetic moments of Tb^{3+}. Doping of $Dy[H(PO_3)_4]$ with increasing amounts of Ce^{3+} showed increasing and intense emission bands of Ce^{3+} in the UV region and very weak but still slightly increasing emission bands of Dy^{3+}. The well-known energy transfer from Ce^{3+} to Dy^{3+} could not be observed very efficiently due to the rather high ratio of Dy^{3+} to Ce^{3+}. Reversing the ratio might lead to a satisfying energy transfer but up to now compounds with a ratio of Dy^{3+}:Ce^{3+} < 0.7:0.3 have not been observed yet. Doping of $Dy[H(PO_3)_4]$ with Eu^{3+} exhibited, next to the characteristic emission lines of Eu^{3+}, two emission bands of Dy^{3+}. The evidence of Eu^{3+} partially occupying Dy^{3+} sites is given due to the dominant hypersensitive $^5D_0 \rightarrow {}^7F_2$ transition, which indicates an asymmetric surrounding of Eu^{3+} (CN = 7).

Compounds comprising protons tend to be unstable at higher temperatures [206]. In contrast, $Tb[H(PO_3)_4]$ possesses a relatively high thermal stability up to 500 °C and releases next to 0.5 moles of H_2O another 0.5 moles of P_2O_5 (Equation 6.1). Via temperature-dependent X-ray powder diffraction the postulated decomposition to TbP_3O_9 (main phase) and TbP_5O_{14} (side phase) was confirmed. *Selevich et al.* performed the thermal analysis within the temperature range of 25–1000 °C with a heating rate of 10 °C·min^{-1}. Due to the lack of any indication of the applied atmosphere during the heating process I assume the same conditions were applied as during the synthesis process. Thus, the thermal analysis was carried out in air and naturally proceeds in a shorter and lower temperature range (350–600 °C) than in an inert atmosphere (500–1450 °C) as done in this work.

Selevich et al. determined the thermal decomposition of $Ln[H(PO_3)_4]$ ($Ln = Y$, Gd–Er) between 350–600 °C via the thin layer method. Initially, this method was developed to investigate phase equilibria of viscous hardly crystallising systems with a volatile component. Layers of 2–5 mm thickness contained the corresponding lanthanide starting material and phosphoric acid in an moderate excess. The temperature was raised in steps of 25 °C. The isothermal phases were held between several days and months until the phase formation was finished [205]. The method applied by *Selevich et al.* exhibits several aspects, which differ quite strongly from the basic conditions applied for $Tb[H(PO_3)_4]$ in this work.

6.2 Strontiumtetraphosphate $Sr_3P_4O_{13}$

In 1955 *McKeag* and *Steward* first synthesised $Sr_3P_4O_{13}$ [207]. Their focus was on the investigation of the luminescent and structural properties of tin or tin and manganese co-activated strontium and barium pyro- and tetraphosphates. For the first time the crystal structures of those compounds were investigated via X-ray powder diffraction. In 1958 *General Electrics* patented the above mentioned compounds als luminescent materials [208]. Several years later in 1967 *Kreidler* and *Hummel* investigated the phase relationships in the system SrO–P_2O_5 (Figure 6.22) [209]. Besides the publication of more detailed X-ray powder diffraction data, they postulated $Sr_3P_4O_{13}$ existing in only one crystallographic modification.

In 2004 *Zhang et al.* determined the single-crystal structure of $Sr_3P_4O_{13}$, which crystallises in the triclinic space group $P\bar{1}$ with the lattice parameters $a = 7.2755(1)$ Å, $b = 7.7260(1)$ Å, $c = 10.1935(2)$ Å, $\alpha = 102.28(0)°$, $\beta = 103.46(0)°$ and $\gamma = 94.35(0)°$, exhibiting an unit cell volume of $V = 537.75(16)$ Å^3. The compound possesses a layered structure containing SrO_7 polyhedra and tetraphosphate $[P_4O_{13}]^{6-}$ anions [106].

Recently, *Zhang et al.* investigated the temperature dependence of the luminescence properties of $Sr_3P_4O_{13}$:Eu^{2+}. In the temperature range of 20 to 503 K a blue emission was observed. In contrast to room temperature, where an emission maximum is found at $\lambda_{max} = 410$ nm, at low temperatures a splitting into two emission maxima ($\lambda_{max1} = 400$ nm, $\lambda_{max2} = 430$ nm) occured. Consequently, *Zhang et al.* expected two chemically different environments of Eu^{2+} sites [110].

In 2008 *Okonek* performed structural investigations of $Sr_3P_4O_{13}$ at room temperature and at 150 K. At room temperature her results coincide with *Zhang et al.* (2004). At low temperatures a structure solution was not possible, due to strong superstructure reflections, but a phase transition was assumed [210].

In the following chapter the synthesis and the crystal structures at room temperature and at 100 K are described. Furthermore, the luminescence properties of $Sr_3P_4O_{13}$:Eu^{3+} and $Sr_3P_4O_{13}$:Eu^{2+} are characterised.

6.2.1 Synthesis

$Sr_3P_4O_{13}$ was synthesised via solid-state synthesis according to the following reaction equation:

$$3\,SrCO_3 + 4\,(NH_4)_2HPO_4 \xrightarrow{\Delta} Sr_3P_4O_{13} + 3\,CO_2(g) + 6\,H_2O(g) + 8\,NH_3(g) \qquad (6.2)$$

A mixture of 221.4 mg (1.500 mmol) $SrCO_3$ and 264.2 mg (2.001 mmol) $(NH_4)_2HPO_4$ was finely ground in an agate mortar and transferred into an alumina boat. The mixture was heated up to 930 °C with a heating rate of 120 °C/h, kept at this temperature for three hours and cooled down to room temperature with a cooling rate of 180 °C/h. $Sr_3P_4O_{13}$ was obtained as a colourless micro-crystalline powder.

In order to obtain single-crystals of $Sr_3P_4O_{13}$, β-$Sr(PO_3)_2$was synthesised first as a precursor:

$$SrCO_3 + 2\,H_3PO_3 \xrightarrow{\Delta} \beta\text{-}Sr(PO_3)_2 + CO_2(g) + 3\,H_2O(g) \qquad (6.3)$$

A mixture of 148.0 mg (1.003 mmol) $SrCO_3$ and 210.1 mg (2.562 mmol) H_3PO_3 was finely ground in an agate mortar and transferred into an alumina boat. The mixture was heated up to 500 °C with a heating rate of 30 °C/h, kept at this temperature for one hour and cooled down to room temperature with a cooling rate of 120 °C/h. β-$Sr(PO_3)_2$ was obtained phase pure as colourless intermediate.

The synthesis of highly crystalline $Sr_3P_4O_{13}$ was carried out by annealing β-$Sr(PO_3)_2$ at 950 °C for several days. Single-crystals of $Sr_3P_4O_{13}$ were obtained as a side phase next to β-$Sr(PO_3)_2$. According to *Kreidler* and *Hummel* glowing β-$Sr(PO_3)_2$ for a long period of time first leads to $Sr_3P_4O_{13}$ before the thermodynamically more stable strontiumpyrophosphate $Sr_2P_2O_7$ arises, due to the evaporation of P_2O_5 (Figure 6.22 red arrows) [209]. $Sr_3P_4O_{13}$ was doped with 3.4 mol% Eu^{3+} by substituting the corresponding amount of $SrCO_3$ by 1.7 mol% (9.1 mg) Eu_2O_3.

$Sr_3P_4O_{13}$:Eu^{2+} was synthesised by heating $Sr_3P_4O_{13}$:Eu^{3+} up to 850 °C for two hours in a *forming gas* flow with a heating rate of 300 °C/h and cooling down to room temperature with a cooling rate of 100 °C/h. This synthesis route always lead to $Sr_2P_2O_7$ as side product. Long annealing steps lead to higher contents of $Sr_2P_2O_7$, whereas shorter annealing steps only resulted in a partial reduction of Eu^{3+} to Eu^{2+}.

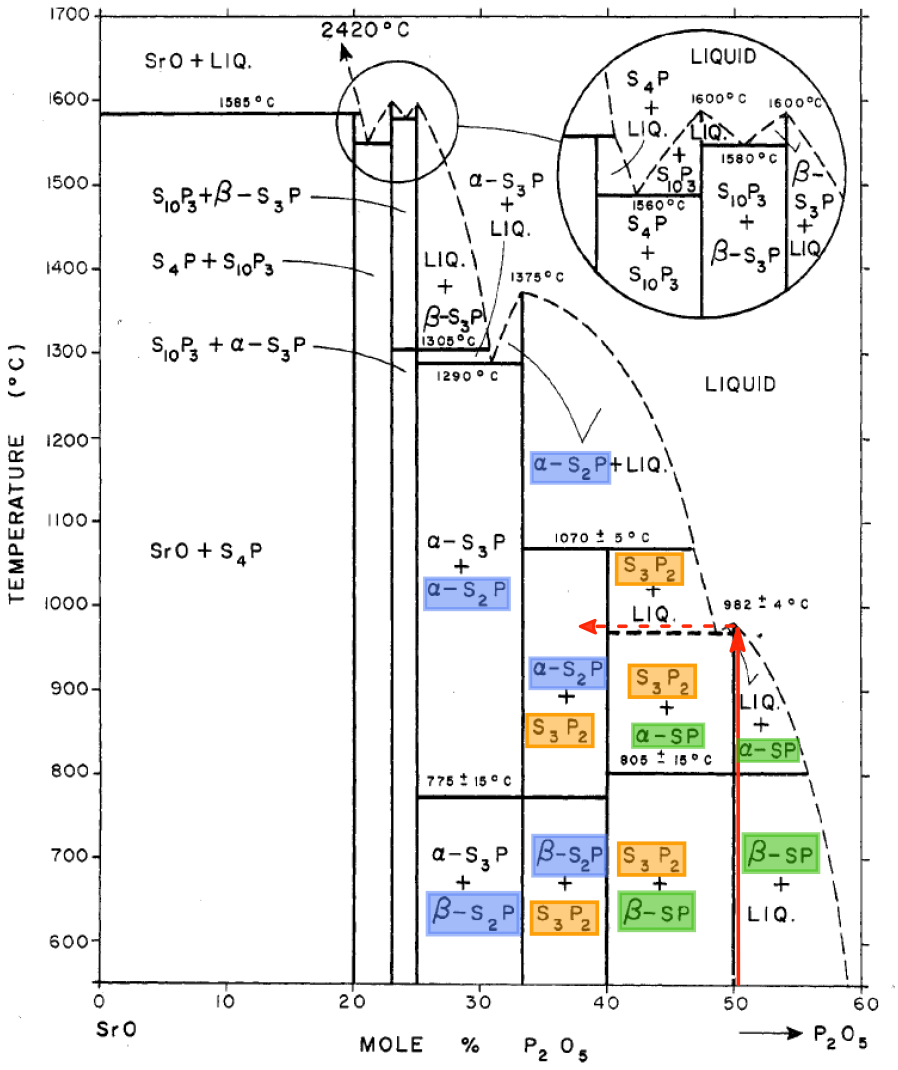

Figure 6.22: Phase diagram in the system SrO–P_2O_5 between a P_2O_5 content of 0–60 %; $S_3P = Sr_3(PO_4)_2$, $S_2P = Sr_2P_2O_7$ (blue), $S_3P_2 = Sr_3P_4O_{13}$ (orange), $SP = Sr_3(PO_3)_2$ (green) [209]; red arrows: evaporation of P_2O_5 by annealing β-$Sr(PO_3)_2$ at 950 °C.

6.2.2 X-Ray Powder Diffraction

The phase purity of the samples was checked by X-ray powder diffraction. Phase pure micro-crystalline $Sr_3P_4O_{13}$ (Figure 6.23) was obtained via reaction Equation 6.2. After annealing β-$Sr(PO_3)_2$, synthesised via reaction Equation 6.3, for several days β-$Sr(PO_3)_2$ represents still the main phase including highly crystalline $Sr_3P_4O_{13}$ as side phase (Figure 6.24).

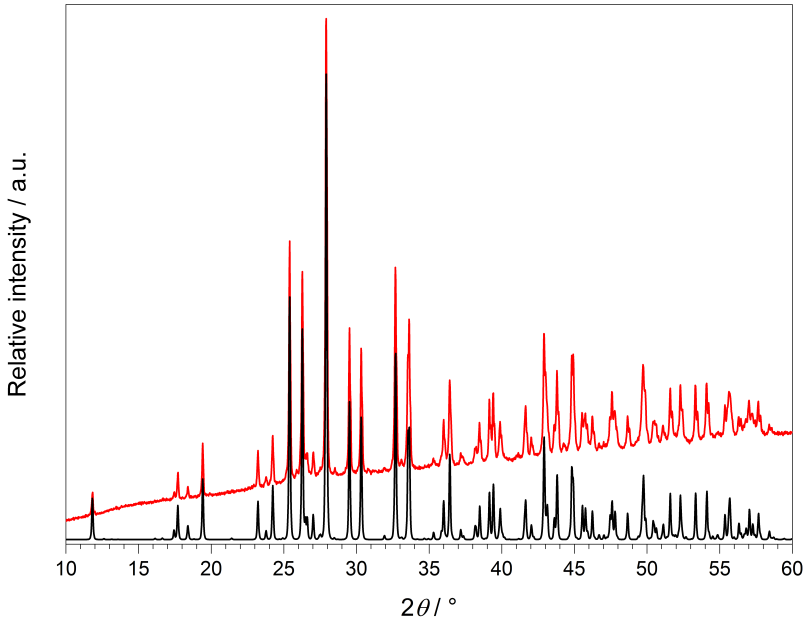

Figure 6.23: X-ray powder diffraction pattern of micro-crystalline $Sr_3P_4O_{13}$ (red) and calculated X-ray powder diffraction pattern from single-crystal data of $Sr_3P_4O_{13}$ (black).

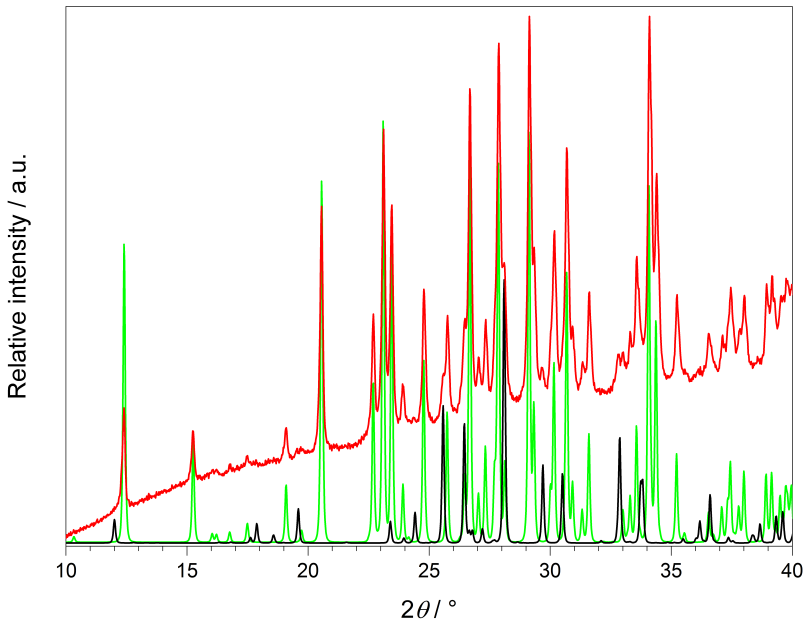

Figure 6.24: X-ray powder diffraction pattern of β-$Sr(PO_3)_2$ (red), calculated X-ray powder diffraction patterns from single-crystal data of β-$Sr(PO_3)_2$ [211] (green) and $Sr_3P_4O_{13}$ (black).

6.2.3 Crystal Structure Determination

A colourless single-crystal of $Sr_3P_4O_{13}$ with a size of $0.044 \times 0.034 \times 0.026\,mm^3$ was isolated and mounted on a *MicroMount*. The selection of the crystal data at room temperature and at 100 K was run on a Bruker D8 Venture single-crystal diffractometer using Mo radiation. A multi-scan absorption correction was subsequently performed.

6.2.3.1 Crystal Structure Determination at Room Temperature

At room temperature RT-$Sr_3P_4O_{13}$ crystallises in the triclinic space group $P\bar{1}$ with the lattice parameters $a = 5.5244(2)$ Å, $b = 6.9126(2)$ Å, $c = 7.7199(2)$ Å, $\alpha = 83.316(1)^\circ$, $\beta = 75.788(1)^\circ$ and $\gamma = 70.553(1)^\circ$ (Table 6.18).

12693 reflections were collected. Out of 1571 independent reflections 1478 were observed ($F_o^2 > 2\sigma\ (F_o^2)$, R_{int} = 0.0340). The crystallographic data as well as the parameters of the measurement and refinement are summarised in Table 6.18. The structure was solved by direct methods and refined by full matrix least-squares technique using the programs SHELXS-97 and SHELXTL-97 [21, 22]. The anisotropic refinement revealed R-values of $R1 = 0.0179$ and $wR2 = 0.0449$. The Sr, P and O atoms could be clearly located. The refined atomic coordinates, anisotropic displacement parameters, selected interatomic distances and angles are summarised in Tables 6.19 to 6.21. The occupancy of $O_{term}4A$, $O_{term}4B$, $O_{term}5A$ and $O_{term}5B$ was checked with free variables. Almost exactly a value of 50 % disorder was observed. The structure solution and refinement was also carried out in the space group $P1$, whereas the ratio of the two individuals was equal, too. Hence, the structure solution in the space group $P\bar{1}$ is the more reasonable one.

Table 6.18: Single-crystal refinement parameters of RT-$Sr_3P_4O_{13}$; standard deviations in brackets

Sum formula	$Sr_3P_4O_{13}$
Temperature / K	297(2)
Molar weight / g·mol^{-1}	594.75
Crystal system	triclinic
Space group	$P\bar{1}$ (no. 2)
Crystal shape	irregular
Crystal size / mm^3	0.044 × 0.034 × 0.026
Colour	colourless
a / Å	5.5244(2)
b / Å	6.9126(2)
c / Å	7.7199(2)
α / °	83.316(1)
β / °	75.788(1)
γ / °	70.553(1)
Volume / Å^3	269.29(1)
Z	1
Calculated density D_x / g·cm^{-3}	3.667
Absorption coefficient μ / mm^{-1}	15.47
F(000)	278
Radiation (λ / Å)	Mo-K_α (0.7093)
Diffractometer	Bruker D8 Venture
Absorption correction	multi-scan
Transmission factor (min./max.)	0.6719 / 0.7484
Index range h|k|l (min./max.)	-7/7 | -9/9 | -10/10
Theta range / °	$2.72 \leq \theta \leq 29.98$
Reflections collected	12693
Independent reflections	1571
Observed reflections	1478 ($F_o^2 > 2\sigma\ (F_o^2)$)
R_{int}	0.0340
Refined parameters	89
R_σ	0.0155
$R1$ (all data)	0.0179
$wR2$ (all data)	0.0449
Weighting scheme	$w^{-1}=\sigma^2\ F_o^2 + (0.0251\ P)^2 + 0.2203\ P$; $P = (F_o^2 + 2\ F_c^2)/3$
GooF	1.073
Residual electron density (min./max.) / e$^-$·Å^{-3}	-0.42/0.70

Table 6.19: Refined atomic coordinates, *Wyckoff* symbols, occupancy and isotropic displacement parameters U_{eq} / Å^2 in RT-$Sr_3P_4O_{13}$; standard deviations in brackets

Atom	*Wyckoff* symbol	x	y	z	Occ.	U_{eq}
Sr1	2*i*	0.34323(3)	0.91935(3)	0.27661(2)	1	0.01167(6)
Sr2	1*g*	0.0000	0.5000	0.5000	0.5	0.01625(7)
P1	2*i*	0.34368(9)	0.69045(7)	0.69075(6)	1	0.00810(10)
P2	2*i*	0.00938(9)	0.28467(7)	–0.03825(6)	1	0.00857(10)
$O_{br}1$	2*i*	–0.2393(3)	0.2530(3)	0.09919(19)	1	0.0151(3)
$O_{br}2$	2*i*	0.0581(6)	0.4807(5)	0.0314(4)	0.5	0.0138(6)
$O_{term}1$	2*i*	0.4366(3)	0.2175(3)	0.3775(2)	1	0.0175(3)
$O_{term}2$	2*i*	0.1121(3)	0.7960(2)	0.60231(19)	1	0.0125(3)
$O_{term}3$	2*i*	0.5756(4)	0.5387(2)	0.3135(2)	1	0.0244(4)
$O_{term}4A$	2*i*	0.0182(6)	0.7630(5)	0.2199(4)	0.5	0.0140(4)
$O_{term}4B$	2*i*	0.2600(6)	0.1667(5)	0.0118(4)	0.5	0.0114(4)
$O_{term}5A$	2*i*	0.0451(6)	0.6829(5)	0.2179(4)	0.5	0.0140(4)
$O_{term}5B$	2*i*	0.2495(6)	0.1148(5)	–0.0122(4)	0.5	0.0114(4)

O_{br} = bridging oxygen atom; O_{term} = terminal oxygen atom;

Table 6.20: Anisotropic displacement parameters U_{ij} / Å^2 in RT-$Sr_3P_4O_{13}$; standard deviations in brackets

Atom	U_{11}	U_{22}	U_{33}	U_{12}	U_{13}	U_{23}
Sr1	0.01016(9)	0.01077(9)	0.01161(9)	0.00215(6)	–0.00093(6)	–0.00199(6)
Sr2	0.01537(13)	0.00893(12)	0.02560(15)	–0.00481(10)	–0.00782(11)	–0.00160(9)
P1	0.0070(2)	0.0084(2)	0.0077(2)	–0.00056(15)	–0.00056(16)	–0.00159(16)
P2	0.0093(2)	0.0078(2)	0.0069(2)	–0.00038(16)	–0.00089(16)	–0.00112(17)
$O_{br}1$	0.0115(7)	0.0269(8)	0.0088(6)	–0.0047(6)	0.0006(5)	–0.0089(6)
$O_{term}1$	0.0113(7)	0.0265(8)	0.0168(7)	–0.0076(6)	0.0031(5)	–0.0108(6)
$O_{term}2$	0.0102(6)	0.0146(7)	0.0122(6)	0.0007(5)	–0.0044(5)	–0.0023(5)
$O_{term}3$	0.0351(10)	0.0088(7)	0.0151(7)	0.0008(5)	0.0046(7)	0.0039(6)

Table 6.21: Selected interatomic distances / Å and angles / ° in RT-$Sr_3P_4O_{13}$; standard deviations in brackets

P–O_{br}	1.543(3)–1.638(3)
P–O_{term}	1.467(3)–1.531(3)
Sr–O	2.518(2)–3.238(2)
P–O_{br}–P	128.5(1)–149.1(2)
O_{term}–P–O_{term}	111.4(1)–117.4(2)
O_{term}–P–O_{br}	101.5(2)–114.0(2)
O_{br}–P–O_{br}	99.9(1)–105.6(1)

6.2.3.2 Crystal Structure Determination at 100 K

Before starting the measurement a single-crystal of $Sr_3P_4O_{13}$ was cooled down to 100 K with a cooling rate of 20 °C/h in order to obtain a proper arrangement of all atoms. Faster cooling rates (≥ 25 °C/h) did not lead to a complete phase transition. At 100 K exclusively the larger unit cell (see Chapter 6.2.3.1) could be found, which is around twice as big in size compared to the unit cell dimensions at room temperature. Thus, $Z = 2$ and the lattice parameters are $a = 7.2636(3)$ Å, $b = 7.7033(3)$ Å, $c = 10.1576(4)$ Å, $\alpha = 102.207(1)°$, $\beta = 103.511(1)°$ and $\gamma = 94.448(1)°$. 67206 reflections were collected. Out of 8999 independent reflections 7169 were observed ($F_o^2 > 2\sigma\ (F_o^2)$, $R_{int} = 0.0695$). The crystallographic data as well as the parameters of the measurement and refinement are summarised in Table 6.22. The structure was solved by direct methods and refined by full matrix least-squares technique using the programs SHELXS-97 and SHELXTL-97 [21, 22]. The anisotropic refinement revealed R-values of $R1 = 0.0379$ and $wR2 = 0.0686$. The Sr, P and O atoms could be clearly located. The refined atomic coordinates, anisotropic displacement parameters, selected interatomic distances and angles are summarised in Tables 6.23 to 6.25.

Table 6.22: Single-crystal refinement parameters of LT-$Sr_3P_4O_{13}$; standard deviations in brackets

Sum formula	$Sr_3P_4O_{13}$
Temperature / K	100(2)
Molar weight / g·mol^{-1}	594.74
Crystal system	triclinic
Space group	$P\bar{1}$ (no. 2)
Crystal shape	irregular
Crystal size / mm^3	0.044 × 0.034 × 0.026
Colour	colourless
a / Å	7.2636(3)
b / Å	7.7033(3)
c / Å	10.1576(4)
α / °	102.207(1)
β / °	103.511(1)
γ / °	94.448(1)
Volume / Å^3	535.29(4)
Z	2
Calculated density D_x / g·cm^{-3}	3.690
Absorption coefficient μ / mm^{-1}	15.57
F(000)	556
Radiation (λ / Å)	Mo-K_α (0.7093)
Diffractometer	Bruker D8 Venture
Absorption correction	multi-scan
Transmission factor (min./max.)	0.6857 / 0.7489
Index range h|k|l (min./max.)	-14/14 | -15/15 | -20/20
Theta range / °	$2.12 \leq \theta \leq 45.44$
Reflections collected	67206
Independent reflections	8999
Observed reflections	7169 ($F_o^2 > 2\sigma\ (F_o^2)$)
R_{int}	0.0695
Refined parameters	182
R_σ	0.0492
$R1$ (all data)	0.0379
$wR2$ (all data)	0.0686
Weighting scheme	$w^{-1}=\sigma^2\ F_o^2 + (0.0268\ P)^2 + 0.4712\ P$; $P = (F_o^2 + 2\ F_c^2)/3$
GooF	1.039
Residual electron density (min./max.) / e$^-$·Å^{-3}	-1.13/1.98

Table 6.23: Refined atomic coordinates, *Wyckoff* symbols and isotropic displacement parameters U_{eq} / Å^2 in LT-$Sr_3P_4O_{13}$; standard deviations in brackets

Atom	*Wyckoff* symbol	x	y	z	U_{eq}
Sr1	2*i*	0.20754(2)	0.71729(2)	0.136892(15)	0.00271(3)
Sr2	2*i*	0.74758(2)	0.47952(2)	0.241538(15)	0.00312(3)
Sr3	2*i*	0.28517(2)	0.27088(2)	0.375768(16)	0.00300(3)
P1	2*i*	0.17056(6)	0.69144(6)	0.48811(4)	0.00246(6)
P2	2*i*	0.63845(6)	0.96210(5)	0.34604(4)	0.00256(6)
P3	2*i*	0.86346(6)	0.03954(5)	0.14080(4)	0.00241(6)
P4	2*i*	0.32468(6)	0.31006(6)	0.02339(4)	0.00253(6)
$O_{br}1$	2*i*	0.75897(18)	0.09558(16)	0.48534(12)	0.00411(18)
$O_{br}2$	2*i*	0.70703(18)	0.03344(16)	0.22662(13)	0.00474(19)
$O_{br}3$	2*i*	0.76505(18)	−0.10143(15)	−0.00158(12)	0.00382(18)
$O_{term}1$	2*i*	0.09654(18)	0.62788(17)	0.33219(12)	0.00487(19)
$O_{term}2$	2*i*	0.65281(18)	0.39432(16)	0.45604(13)	0.00456(19)
$O_{term}3$	2*i*	0.97296(18)	0.31954(16)	0.42716(13)	0.00497(19)
$O_{term}4$	2*i*	0.68333(19)	0.77954(16)	0.35910(13)	0.0060(2)
$O_{term}5$	2*i*	0.43219(18)	0.98641(16)	0.31757(13)	0.00513(19)
$O_{term}6$	2*i*	0.04462(18)	0.98674(16)	0.21457(13)	0.00522(19)
$O_{term}7$	2*i*	0.87550(19)	0.21960(16)	0.10741(13)	0.00519(19)
$O_{term}8$	2*i*	0.50629(19)	0.69286(17)	0.03851(14)	0.0072(2)
$O_{term}9$	2*i*	0.83727(18)	0.59998(16)	0.04793(13)	0.00469(19)
$O_{term}10$	2*i*	0.37852(19)	0.38420(17)	0.18053(12)	0.0056(2)

O_{br} = bridging oxygen atom; O_{term} = terminal oxygen atom;

Table 6.24: Anisotropic displacement parameters U_{ij} / Å^2 in LT-$Sr_3P_4O_{13}$; standard deviations in brackets

Atom	U_{11}	U_{22}	U_{33}	U_{12}	U_{13}	U_{23}
Sr1	0.00271(6)	0.00291(5)	0.00245(5)	0.00022(4)	0.00103(4)	0.00013(4)
Sr2	0.00332(6)	0.00301(6)	0.00342(6)	0.00068(4)	0.00169(4)	0.00041(4)
Sr3	0.00256(6)	0.00309(5)	0.00325(6)	0.00013(4)	0.00119(4)	0.00017(4)
P1	0.00248(16)	0.00260(14)	0.00224(15)	0.00046(11)	0.00071(12)	−0.00001(12)
P2	0.00281(16)	0.00207(14)	0.00286(15)	0.00055(12)	0.00091(12)	0.00027(12)
P3	0.00252(16)	0.00212(14)	0.00267(15)	0.00060(11)	0.00084(12)	0.00020(12)
P4	0.00220(16)	0.00253(15)	0.00261(15)	0.00021(12)	0.00059(12)	0.00006(12)
$O_{br}1$	0.0056(5)	0.0035(4)	0.0027(4)	0.0008(3)	0.0004(4)	−0.0005(3)
$O_{br}2$	0.0046(5)	0.0059(4)	0.0046(4)	0.0012(4)	0.0030(4)	0.0004(4)
$O_{br}3$	0.0046(5)	0.0025(4)	0.0035(4)	−0.0007(3)	0.0009(4)	−0.0004(3)
$O_{term}1$	0.0051(5)	0.0063(5)	0.0017(4)	−0.0001(3)	−0.0006(4)	−0.0017(4)
$O_{term}2$	0.0037(5)	0.0049(4)	0.0053(5)	0.0016(4)	0.0011(4)	0.0009(4)
$O_{term}3$	0.0055(5)	0.0052(4)	0.0052(5)	0.0013(4)	0.0032(4)	0.0006(4)
$O_{term}4$	0.0085(5)	0.0027(4)	0.0067(5)	0.0013(4)	0.0017(4)	0.0009(4)
$O_{term}5$	0.0035(5)	0.0057(5)	0.0062(5)	0.0011(4)	0.0015(4)	0.0005(4)
$O_{term}6$	0.0033(5)	0.0051(4)	0.0064(5)	0.0008(4)	0.0000(4)	0.0009(4)
$O_{term}7$	0.0075(5)	0.0033(4)	0.0054(5)	0.0014(4)	0.0026(4)	0.0006(4)
$O_{term}8$	0.0059(5)	0.0054(5)	0.0111(5)	−0.0003(4)	0.0058(4)	−0.0006(4)
$O_{term}9$	0.0041(5)	0.0042(4)	0.0056(5)	0.0022(4)	0.0000(4)	0.0005(4)
$O_{term}10$	0.0077(5)	0.0056(5)	0.0021(4)	0.0000(3)	0.0001(4)	−0.0008(4)

Table 6.25: Selected interatomic distances / Å and angles / ° in LT-$Sr_3P_4O_{13}$; standard deviations in brackets

P–O_{br}	1.579(1)–1.636(1)
P–O_{term}	1.487(1)–1.534(1)
Sr–O	2.482(1)–3.233(1)
P–O_{br}–P	127.7(1)–147.4(1)
O_{term}–P–O_{term}	111.0(1)–116.8(1)
O_{term}–P–O_{br}	103.3(1)–115.6(1)
O_{br}–P–O_{br}	102.6(1)–104.0(1)

6.2.4 Crystal Structure Description

6.2.4.1 Crystal Structure Description at Room Temperature

At room temperature $Sr_3P_4O_{13}$ crystallises in the triclinic space group $P\bar{1}$ with one formula unit per unit cell. All atoms are located on the general *Wyckoff* position $2i$ except for Sr2, which possesses the *Wyckoff* symbol $1g$. The structure of RT-$Sr_3P_4O_{13}$ consists of $[P_4O_{13}]^{6-}$ chains of corner-sharing phosphate tetrahedra separated by layers of edge- and corner-sharing six-membered rings in chair conformation of Sr^{2+} ions (Figures 6.25 and 6.26).

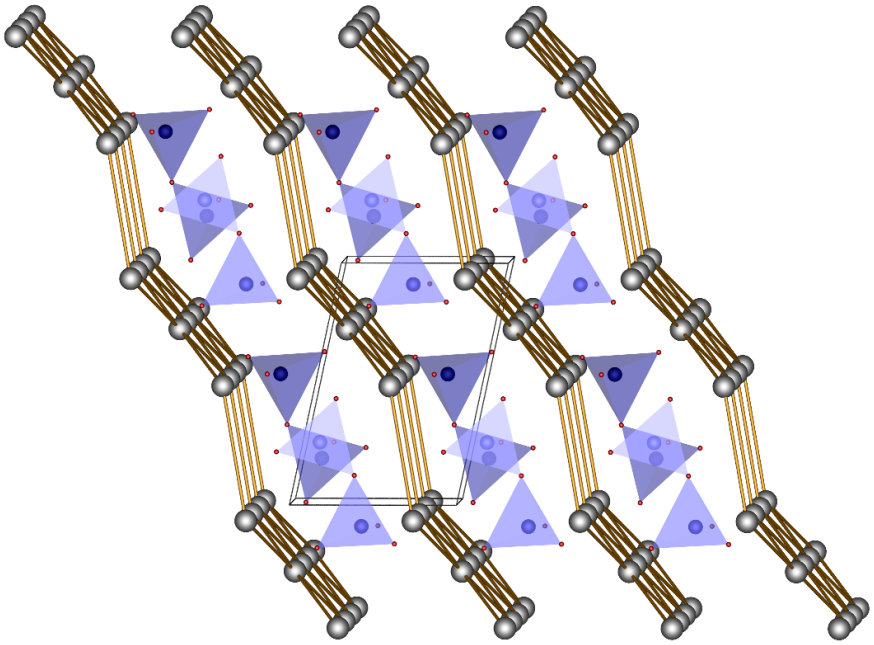

Figure 6.25: $[P_4O_{13}]^{6-}$ chains separated by layers of edge- and corner-sharing six-membered rings in chair conformation of Sr^{2+} ions in viewing direction [010] in RT-$Sr_3P_4O_{13}$; phosphate tetrahedra blue, strontium atoms grey.

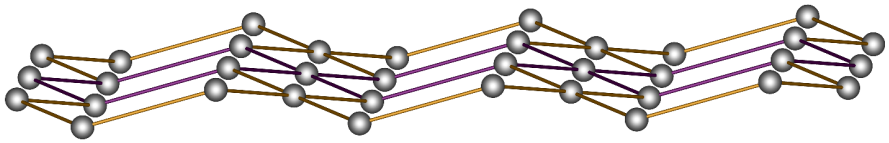

Figure 6.26: Layer of edge- and corner-sharing chairs of strontium atoms (grey) in RT-$Sr_3P_4O_{13}$.

Due to the presence of the inversion centre located directly between the two P2 atoms, splitting of $O_{br}2$ occurs, which is shown in Figure 6.27.

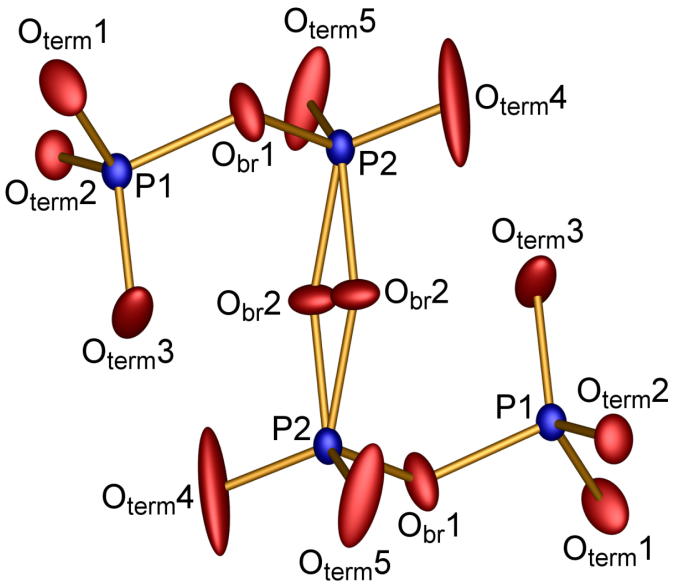

Figure 6.27: $[P_4O_{13}]^{6-}$ chain in RT-$Sr_3P_4O_{13}$. The displacement ellipsoids are drawn on a probability level of 75 %.

The presence of two different individuals is indicated by the disordered $O_{br}2$ atom site. $O_{term}4$ and $O_{term}5$, which are also connected to P2, show quite large principal mean square atomic displacements (Table 6.26).

Table 6.26: Principal Mean Square Atomic Displacements U of RT-$Sr_3P_4O_{13}$

0.0168	0.0096	0.0087	Sr1
0.0275	0.0136	0.0078	Sr2
0.0098	0.0083	0.0064	P1
0.0117	0.0075	0.0066	P2
0.0273	0.0104	0.0076	$O_{br}1$
0.0247	0.0121	0.0060	$O_{br}2$
0.0312	0.0144	0.0072	$O_{term}1$
0.0167	0.0131	0.0082	$O_{term}2$
0.0529	0.0125	0.0072	$O_{term}3$
0.1143	0.0173	0.0064	$O_{term}4$
0.0795	0.0120	0.0078	$O_{term}5$

Thus, two individuals of $O_{term}4$ and $O_{term}5$ with a ratio of 1:1 could be resolved, which decreased the corresponding principal mean square atomic displacements (Table 6.27).

Table 6.27: Principal Mean Square Atomic Displacements U of disordered RT-$Sr_3P_4O_{13}$

0.0167	0.0096	0.0086	Sr1
0.0274	0.0136	0.0077	Sr2
0.0097	0.0083	0.0063	P1
0.0117	0.0073	0.0065	P2
0.0275	0.0101	0.0077	$O_{br}1$
0.0247	0.0119	0.0066	$O_{br}2$
0.0315	0.0139	0.0074	$O_{term}1$
0.0161	0.0130	0.0082	$O_{term}2$
0.0527	0.0128	0.0073	$O_{term}3$
0.0178	0.0139	0.0057	$O_{term}4A$
0.0222	0.0201	0.0093	$O_{term}4B$
0.0186	0.0151	0.0095	$O_{term}5A$
0.0165	0.0096	0.0045	$O_{term}5B$

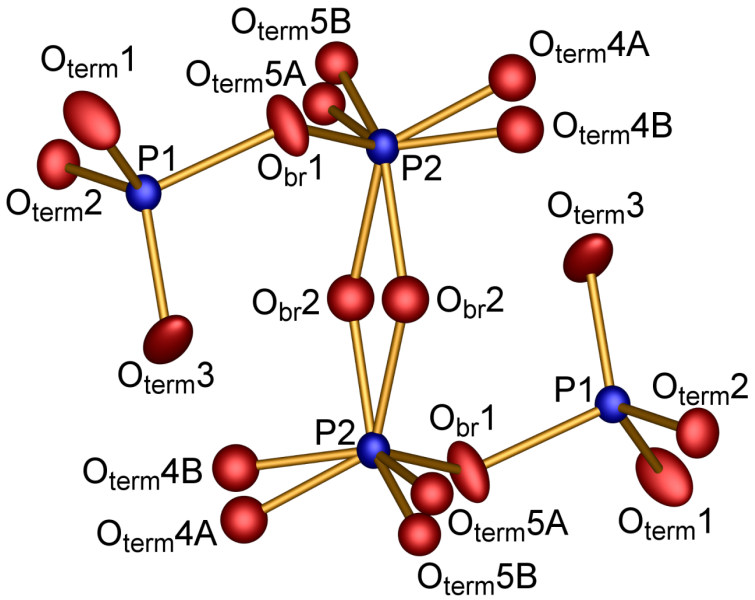

Figure 6.28: Disordered $[P_4O_{13}]^{6-}$ chain in RT-$Sr_3P_4O_{13}$. The displacement ellipsoids are drawn on a probability level of 75 %.

However, for the schematic representation $O_{br}2$, $O_{term}4A$, $O_{term}4B$, $O_{term}5A$ and $O_{term}5B$ are handled as regular spheres with isotropic displacements (Figure 6.28). Furthermore, interaction between disordered oxygen atoms was suppressed by treating them as two individuals with an occupation of 0.5.

The P–O distances range between 1.47 and 1.64 Å. The bond lengths P–O_{br} lie between 1.54 and 1.64 Å, whereas P–O_{term} distances lie between 1.47 and 1.53 Å, respectively. These values are in agreement with values found for other phosphates [196, 212]. P–O_{br}–P angles range between 129 and 149°. O_{term}–P–O_{term}, O_{term}–P–O_{br} and O_{br}–P–O_{br} angles range between 111–117° (Ø = 114°), 102–114° (Ø = 108°) and 100–106° (Ø = 103°). respectively. Selected bond lengths and angles of RT-$Sr_3P_4O_{13}$ are listed in Table 6.21.

The deviation of tetrahedra from ideal symmetry was calculated by using the method of *Balić-Žunić* and *Makovicky* [35, 36]. The two crystallographically different phosphate tetrahedra in RT-$Sr_3P_4O_{13}$ feature the values −0.06 % (P1), −0.56 % (P2A) and −0.56 % (P2B), which are also found in other phosphate tetrahedra [97, 98, 187, 190, 191]. Exhibiting a deviation of less than 1 %, all tetrahedra are classified as regular. In contrast, the deviation of tetrahedra considering the two different $O_{br}2$ with non-splitted oxygen atoms $O_{term}4$ and $O_{term}5$ shows larger values (P2: −4.29 % and P2': −2.28 %).

The single-crystal structure analysis reveals two crystallographically different sites of the Sr^{2+} ions, which are coordinated distorted double capped trigonal prismatic (Sr1) and distorted fourfold capped octahedral (Sr2) by eight and ten terminal oxygen atoms, respectively (Figure 6.29). The Sr–O bond lengths range between 2.52–3.24 Å (Table 6.21). In the inner coordination sphere (exclusively solid lines in Figure 6.29) the coordination numbers of both Sr atoms decrease to seven (Sr1) and six (Sr2) terminal oxygen atoms forming a distorted single capped trigonal prismatic polyhedron (Sr1) and a distorted octahedron (Sr2). The Sr–O bond lengths of the inner coordination sphere range between 2.52 and 2.71 Å. These values are in excellent agreement with the sum of the ionic radii of Sr^{2+} (1.21 Å) and O^{2-} (1.35 Å) [60]. Sr1 is linked to Sr2 via two terminal oxygen atoms, $O_{term}1$ and $O_{term}3$, respectively. The differentiation between inner and extended coordination sphere arises due to the presence of a gap regarding the coordination distances d(Sr–O) in a range between 2.70–3.12 Å (Sr1) and 2.59–2.96 Å (Sr2).

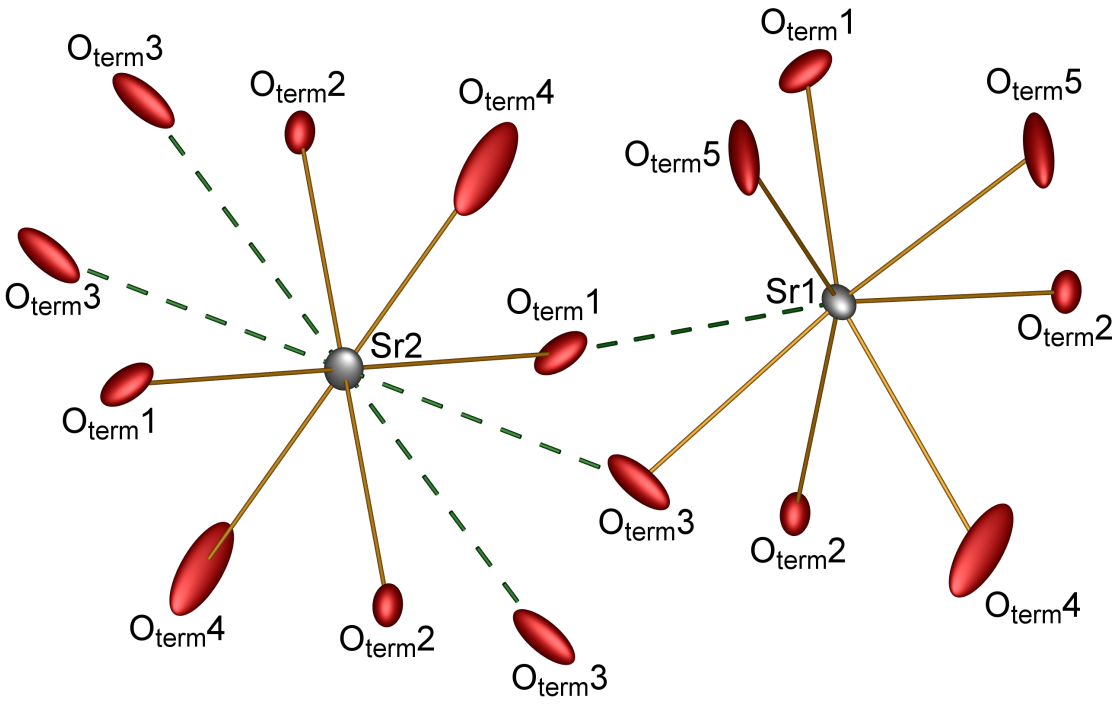

Figure 6.29: Inner (solid lines) and extended (green dotted lines included) coordination sphere of the two crystallographically different Sr^{2+} ions in RT-$Sr_3P_4O_{13}$. The displacement ellipsoids are drawn on a probability level of 50 %.

6.2.4.2 Crystal Structure Description at 100 K

At 100 K LT-$Sr_3P_4O_{13}$ also crystallises in the triclinic space group $P\bar{1}$ exhibiting a doubled unit cell volume with two formula units. All atoms are located on the general *Wyckoff* position 2*i*. The structure of LT-$Sr_3P_4O_{13}$ also consists of $[P_4O_{13}]^{6-}$ chains of corner-sharing phosphate tetrahedra separated by layers of edge- and corner-sharing six-membered rings in chair conformation of Sr^{2+} ions (Figures 6.30 and 6.31).

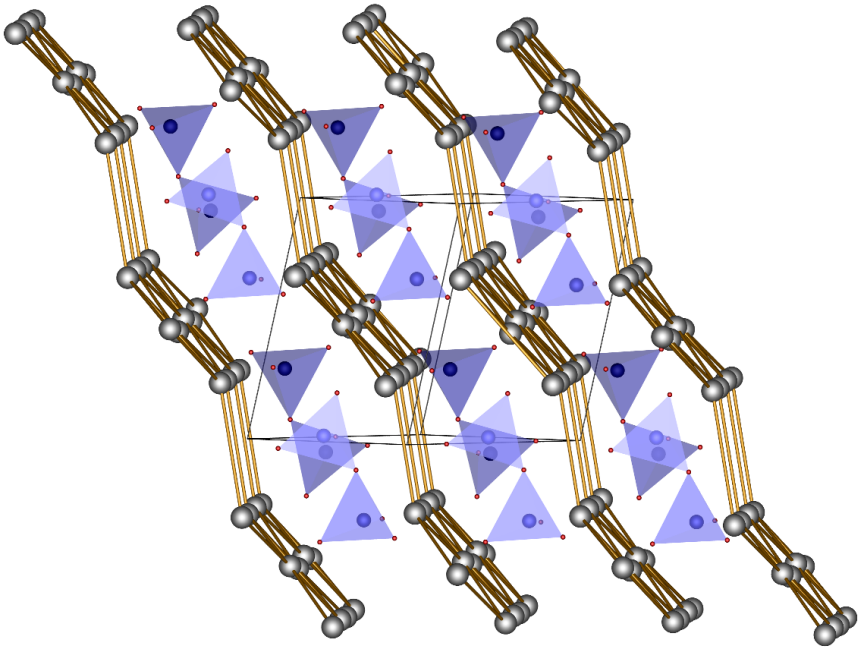

Figure 6.30: $[P_4O_{13}]^{6-}$ chains separated by layers of edge- and corner-sharing six-membered rings in chair conformation of Sr^{2+} ions in viewing direction [101] in LT-$Sr_3P_4O_{13}$; phosphate tetrahedra blue, strontium atoms grey.

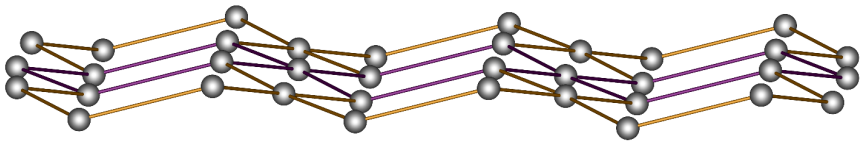

Figure 6.31: Layer of edge- and corner-sharing chairs of strontium atoms (grey) in LT-$Sr_3P_4O_{13}$.

The $[P_4O_{13}]^{6-}$ tetraphosphate chain kept its S-shaped curve (Figure 6.32).

The P–O distances range between 1.49 and 1.64 Å. The bond lengths P–O_{br} lie between 1.58 and 1.64 Å, whereas P–O_{term} distances lie between 1.49 and 1.53 Å, respectively. These values are in agreement with the values found by *Zhang et*

al. (2004) [106] and correspond to typical data found for other phosphates [196, 212]. P–O_{br}–P angles range between 128 and 147°. O_{term}–P–O_{term}, O_{term}–P–O_{br} and O_{br}–P–O_{br} angles range between 111–117° (Ø = 114°), 103–116° (Ø = 108°) and 103–104° (Ø = 103°), respectively. Selected bond lengths and angles of LT-$Sr_3P_4O_{13}$ are listed in Table 6.25.

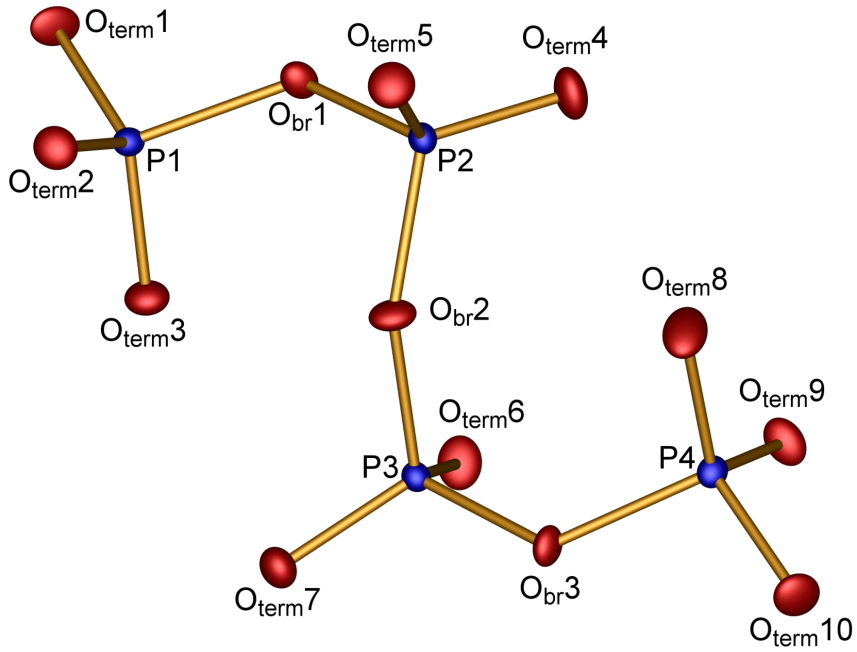

Figure 6.32: $[P_4O_{13}]^{6-}$ chain in LT-$Sr_3P_4O_{13}$. The displacement ellipsoids are drawn on a probability level of 95 %.

The deviation of tetrahedra from ideal symmetry was also calculated by using the method of *Balić-Žunić* and *Makovicky* [35, 36]. The four crystallographically different phosphate tetrahedra in LT-$Sr_3P_4O_{13}$ feature the values −0.17 % (P1), −0.74 % (P2), −0.18 % (P3) and −0.05 % (P4). Exhibiting a deviation of less than 1 %, tetrahedra are classified as regular, which was also found for other phosphate tetrahedra [97, 98, 187, 190, 191] and for RT-$Sr_3P_4O_{13}$ (Chapter 6.2.4.1).

The single-crystal structure of LT-$Sr_3P_4O_{13}$ reveals three crystallographically different sites of the Sr^{2+} ions, which are coordinated distorted double capped trigonal prismatic by eight terminal oxygen atoms (Sr1 and Sr3) and distorted triple capped trigonal prismatic by nine terminal oxygen atoms (Sr2) (Figure 6.33). The Sr–O bond lengths range between 2.34–3.12 Å (Table 6.25). In the inner coordination sphere (exclusively solid lines, Figure 6.33) the coordination numbers of all Sr atoms decrease to seven terminal oxygen atoms forming distorted single capped trigonal prisms. The Sr–O bond lengths of the inner coordination sphere range between 2.48–2.76 Å. These values are in excellent agreement with the sum of the ionic radii

of Sr^{2+} (1.21 Å) and O^{2-} (1.35 Å) [60]. Sr2 is linked to Sr1 and Sr3 via two terminal oxygen atoms ($O_{term}8/10$ and $O_{term}2/4$, respectively).

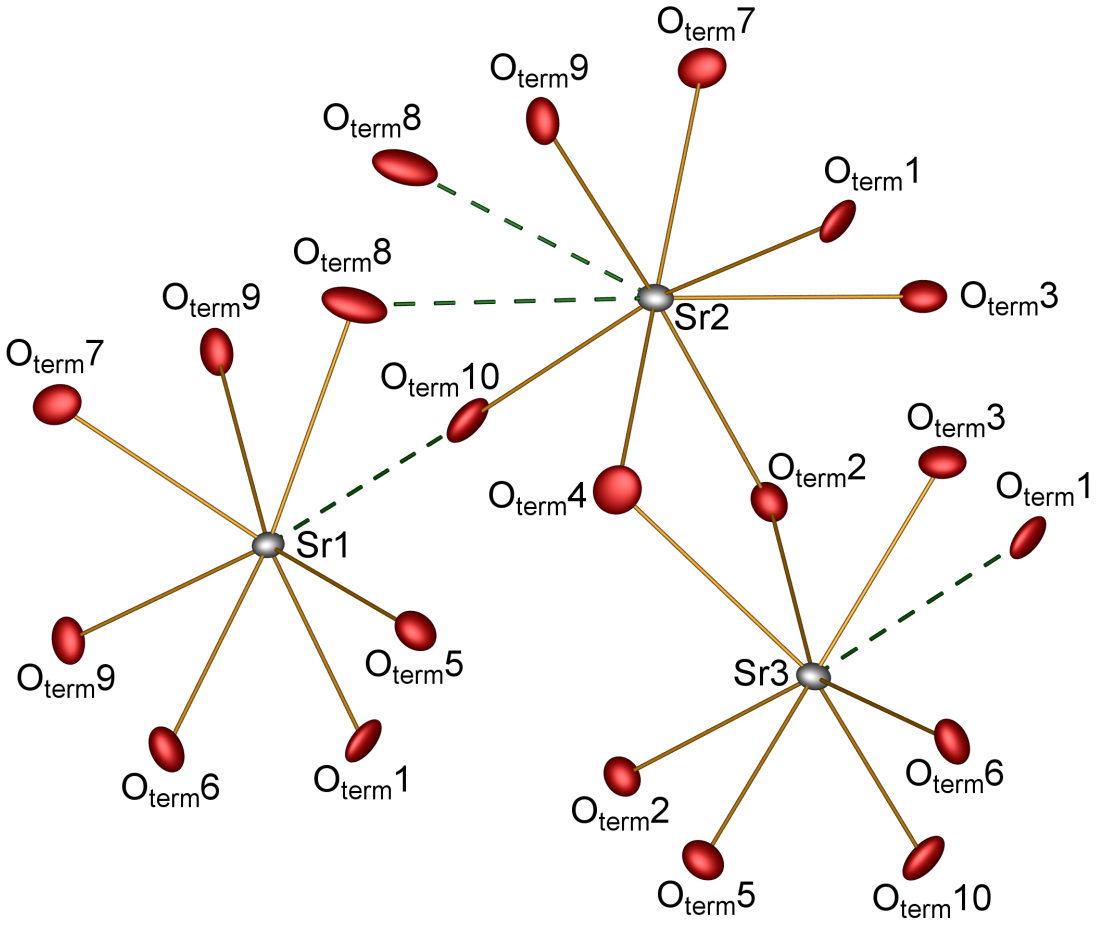

Figure 6.33: Inner (solid lines) and extended (dotted lines included) coordination sphere of the three crystallographically different Sr^{2+} ions in LT-$Sr_3P_4O_{13}$. The displacement ellipsoids are drawn on a probability level of 95 %.

6.2.5 Electrostatic Calculations

Besides the coordination numbers of the Sr atoms (Tables 12.4 and 12.5) the electrostatic consistency of both the structure solution at room temperature and at 100 K were verified based on the MAPLE concept (= *Ma*delung *P*art of *L*attice *E*nergy) [32, 33, 152]. According to the calculations, both structure models, RT-$Sr_3P_4O_{13}$ and LT-$Sr_3P_4O_{13}$, respectively, show electrostatic consistency (Table 6.28). The MAPLE value of the low temperature phase is slightly increased of about 430 $kJ \cdot mol^{-1}$. Due to less vibrations at 100 K a higher density (Tables 6.18 and 6.22) and a smaller cation–anion distance d_0 occur. As a consequence the Madelung energy (Equation 3.11) increases. Thus, the comparison with MAPLE data of SrO [213] and P_2O_5 [193] at room temperature results in a total difference of about 1.2 %. A more precise sum of MAPLE values was received by using data of P_2O_5 [214] at 233 K instead.

Table 6.28: MAPLE calculations for RT-$Sr_3P_4O_{13}$ and LT-$Sr_3P_4O_{13}$ [32, 33, 152]

RT-$Sr_3P_4O_{13}$	3 SrO [213] + 2 P_2O_5 [193]
MAPLE = 99347 $kJ \cdot mol^{-1}$	MAPLE = 98610 $kJ \cdot mol^{-1}$
$\Delta = 0.7\,\%$	
LT-$Sr_3P_4O_{13}$	**3 SrO [213] + 2 P_2O_5 [214]**
MAPLE = 99779 $kJ \cdot mol^{-1}$	MAPLE = 99082 $kJ \cdot mol^{-1}$
$\Delta = 0.7\,\%$	

6.2.6 Spectroscopic Properties

6.2.6.1 IR Spectroscopy

The infrared spectrum of RT-$Sr_3P_4O_{13}$ was recorded between 4000 and 400 cm^{-1} and is shown in Figure 6.34. The position of the bands and the corresponding assignments are given in Table 6.29.

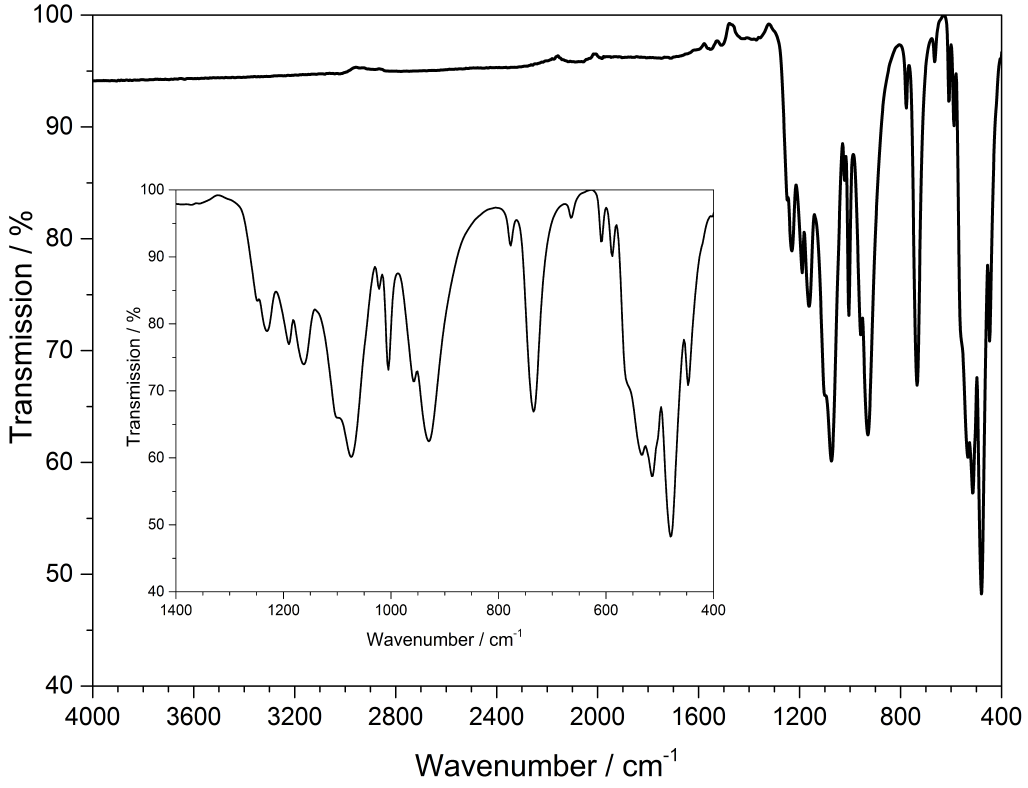

Figure 6.34: Infrared spectrum of RT-$Sr_3P_4O_{13}$.

Table 6.29: Position / cm^{-1} and assignment of the IR bands in RT-$Sr_3P_4O_{13}$

Position	Assignment
1230, 1190, 1163	ν_{as}(PO) [215–219]
1074, 1022, 1005	ν_{as}(POP) [215, 216, 218]
958, 930, 777	ν_{s}(POP) [215–218]
735	δ(POP) [215, 218]
665, 609, 588, 534, 515, 480, 447	$\delta(PO_2)$, δ(OPO) [215, 217–219]

The bands at 1230, 1190 and 1163 cm^{-1} can be assigned to the asymmetric P–O stretching vibrations [215–219], while vibrations between 1074 and 1005 cm^{-1} and between 958 and 777 cm^{-1} can be assigned to asymmetric and symmetric P–O–P stretching vibrations, respectively [215–218]. The δ(POP) vibration is found at

735 cm^{-1} [215, 218]. Characteristic bands of $\delta(PO_2)$ and $\delta(OPO)$ are found between 665 and 447 cm^{-1} [215, 217–219].

6.2.6.2 UV-Vis Spectroscopy

In order to investigate the optical properties of RT-$Sr_3P_4O_{13}$, the host structure of RT-$Sr_3P_4O_{13}$ was doped with 3.4 mol% Eu^{3+} (synthesis see Chapter 6.2.1). The charge compensation due to the partial occupation of Sr^{2+} lattice sites by Eu^{3+} ions is presumably accomplished by vacancies. Annealing of RT-$Sr_3P_4O_{13}$:Eu^{3+} in *forming gas* led to products with different compositions.
After an extended time of annealing completed reduction lead to RT-$Sr_3P_4O_{13}$:Eu^{2+} with $Sr_2P_2O_7$:Eu^{2+} as side product. After a shorter period of reductive annealing RT-$Sr_3P_4O_{13}$ could be obtained phase pure with a co-doping of Eu^{3+} and Eu^{2+}.

The UV-Vis spectra of RT-$Sr_3P_4O_{13}$:Eu^{3+} (red), RT-$Sr_3P_4O_{13}$:Eu^{2+}/$Sr_2P_2O_7$:Eu^{2+} (blue), RT-$Sr_3P_4O_{13}$:$Eu^{2+/3+}$ (violet) and $Sr_2P_2O_7$:Eu^{2+} (turquoise) are shown in Figure 6.35. Between 450–800 nm no significant absorptions can be observed. For RT-$Sr_3P_4O_{13}$:Eu^{3+} and RT-$Sr_3P_4O_{13}$:$Eu^{2+/3+}$ a weak f–f absorption at 394 nm can be observed, which is typical for Eu^{3+} ions [53]. Around 235 and 234 nm, respectively, a ligand-to-metal charge transfer (LMCT) can be observed for both compounds. In contrast to RT-$Sr_3P_4O_{13}$:Eu^{3+}, RT-$Sr_3P_4O_{13}$:$Eu^{2+/3+}$ shows a broad f–d transition peaking at 318 nm ($4f^7\,5d^0 \rightarrow 4f^6\,5d^1$) of the Eu^{2+} ion. RT-$Sr_3P_4O_{13}$:Eu^{2+}/ $Sr_2P_2O_7$:Eu^{2+} also reveals a broad f–d transition at 316 nm exhibiting a shoulder to longer wavelengths and a CT with two bands at 212 nm and 243 nm. $Sr_2P_2O_7$:Eu^{2+} shows a similar behaviour. Broad and strong absorptions occur at 322 nm, 230 and 213 nm.

In RT-$Sr_3P_4O_{13}$ Sr–O coordination distances lie between 2.52–3.24 Å, whereas in $Sr_2P_2O_7$ distances are 2.39–2.99 Å. Due to shorter Sr–O distances in $Sr_2P_2O_7$ a stronger interaction between strontium and oxygen atoms can be expected. Thus, the f–d transition of $Sr_2P_2O_7$:Eu^{2+} occurs at longer wavelengths ($\lambda = 322$ nm) compared to RT-$Sr_3P_4O_{13}$:Eu^{2+} ($\lambda = 318$ nm). The bands at 212 nm and 243 nm (RT-$Sr_3P_4O_{13}$:Eu^{2+}/$Sr_2P_2O_7$:Eu^{2+}), and at 213 nm and 230 nm ($Sr_2P_2O_7$:Eu^{2+}), respectively, correspond presumably also to the CT of the phosphate groups in both compounds. Due to the overlap of the $O^{2-} \rightarrow Eu^{3+}$ CT and the $O^{2-} \rightarrow P^{5+}$ CT no precise assignment can be made.

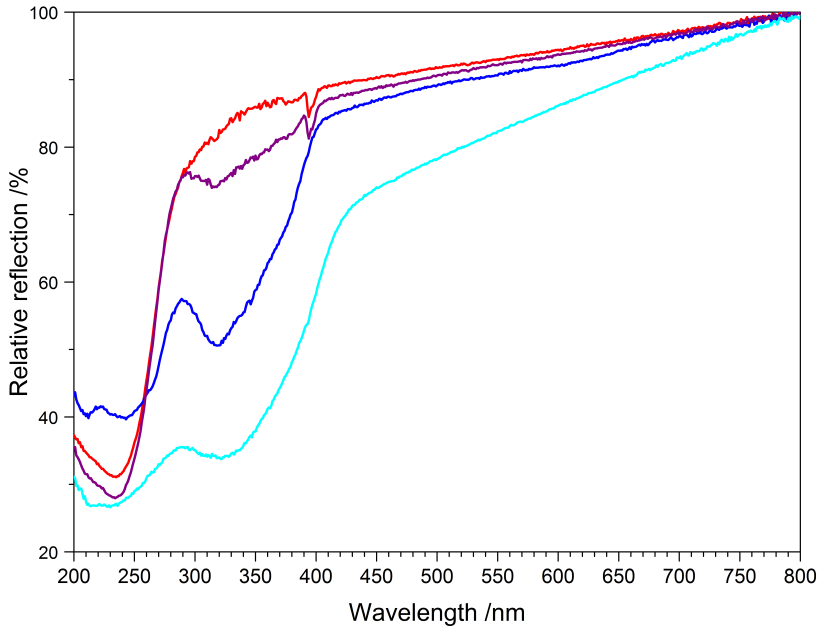

Figure 6.35: UV-Vis spectra of RT-$Sr_3P_4O_{13}$:Eu^{3+} (red), RT-$Sr_3P_4O_{13}$:Eu^{2+}/$Sr_2P_2O_7$:Eu^{2+} (blue) and RT-$Sr_3P_4O_{13}$:$Eu^{2+/3+}$ (violet).

6.2.6.3 Fluorescence Spectroscopy

The colourless powder of $Sr_3P_4O_{13}$:Eu^{3+} shows a strong red fluorescence under excitation with UV light at 254 nm (Figure 6.36). The fluorescence spectrum of RT-$Sr_3P_4O_{13}Eu^{3+}$ (Figure 6.37) reveals the characteristic f–f emissions of Eu^{3+} [53].

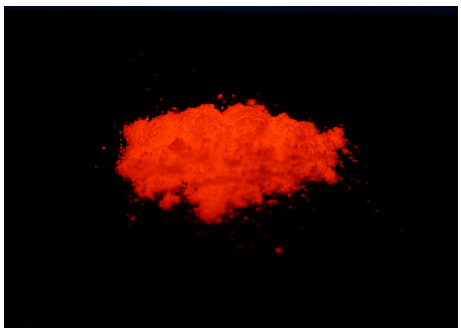

Figure 6.36: Red fluorescence of RT-$Sr_3P_4O_{13}$:Eu^{3+} at 254 nm.

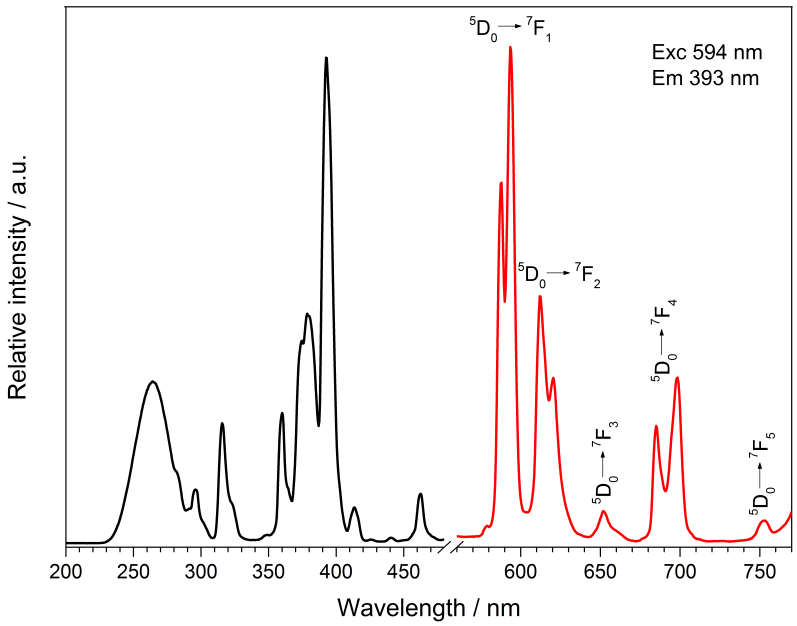

Figure 6.37: Excitation (black) and emission (red) spectrum of RT-$Sr_3P_4O_{13}$:Eu^{3+}.

An O^{2-}→Eu^{3+} charge-transfer leads to a broad band in the excitation spectrum between 230 and 290 nm. Under excitation at 393 nm RT-$Sr_3P_4O_{13}$:Eu^{3+} exhibits sharp emission lines between 570 and 760 nm, which can be assigned to the $^5D_0$→$^7F_1$ (594 nm), $^5D_0$→$^7F_2$ (612 nm), $^5D_0$→$^7F_3$ (652 nm), $^5D_0$→$^7F_4$ (699 nm) and $^5D_0$→$^7F_5$ (754 nm) transitions. The hypersensitive transition ($^5D_0$→$^7F_2$) is weaker compared to the $^5D_0$→$^7F_1$ transition due to the presence of the inversion centre at the Sr2 site. At lower temperatures the chemical surrounding of Eu^{3+} changes from two to three different strontium sites and the inversion centre at the Sr2 site disappears. A change of the optical properties is expected as all strontium sites do not occupy any centre of symmetry. Hence, the hypersensitive transition ($^5D_0$→$^7F_2$) is expected to be stronger compared to the $^5D_0$→$^7F_1$ transition and the emission colour changes to a deeper red.

After an extended time of annealing complete reduction was achieved, which led to RT-$Sr_3P_4O_{13}$:Eu^{2+} with $Sr_2P_2O_7$:Eu^{2+} as side product exhibiting a strong blue fluorescence under excitation with UV light at 366 nm (Figure 6.38). The fluorescence spectrum is shown in Figure 6.39.

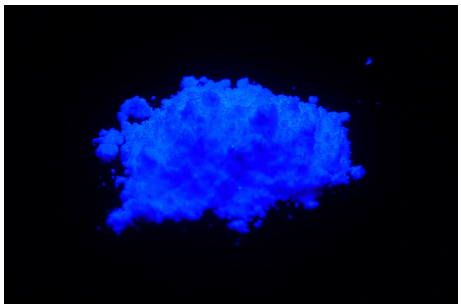

Figure 6.38: Blue fluorescence of RT-$Sr_3P_4O_{13}$:Eu^{2+} containing $Sr_2P_2O_7$:Eu^{2+} [220] as side phase at 366 nm.

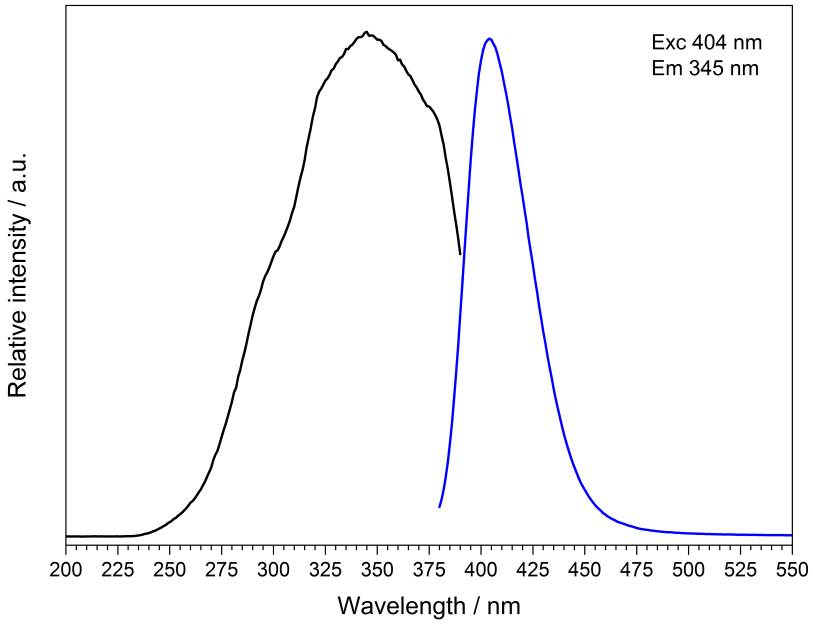

Figure 6.39: Excitation (black) and emission (blue) spectrum of RT-$Sr_3P_4O_{13}$:Eu^{2+} containing $Sr_2P_2O_7$:Eu^{2+} [220] as side phase.

In the excitation spectrum between 250 and 390 nm the broad and intense spin and parity allowed $4f^7$–$4f^6 6d^1$ transition peaking at 345 nm with a shoulder around 316 nm can be observed. The absorption band at 316 nm showing a shoulder to longer wavelengths in the UV-Vis spectrum of $Sr_3P_4O_{13}$:Eu^{2+}/$Sr_2P_2O_7$:Eu^{2+} (Figure 6.35) fits very well to the band in the excitation spectrum (Figure 6.39). Both emission spectra of $\lambda_{exc} = 316$ nm and $\lambda_{exc} = 345$ nm reveal a broad band in the blue region between 380 and 480 nm with a maximum at 404 nm. Compared to the emission maxima of the chemically similar compounds α-$Sr(PO_3)_2$:Eu^{2+} [221] ($\lambda_{Em} = 404$ nm) and of $Sr_2P_2O_7$:Eu^{2+} [220] ($\lambda_{Em} = 422$ nm) the emission wavelength range in the blue region was expected and fits very well to the wavelength found by *Zhang et al.* (2013) for RT-$Sr_3P_4O_{13}$:Eu^{2+} (404 nm) [110]. A closer look shows an asymmetric emission band with a shoulder towards the long wavelength range and a centre at about 425 nm, which certainly originates from the side phase $Sr_2P_2O_7$:Eu^{2+} [220]. As no f–f transitions were found, the reduction of Eu^{3+} to Eu^{2+} was complete, but only

under the circumstance that $Sr_2P_2O_7$:Eu^{2+} as side phase was formed.

RT-$Sr_3P_4O_{13}$:$Eu^{2+/3+}$ was obtained after a shorter period of reductive annealing showing a pink fluorescence under excitation with UV light at 254 nm (Figure 6.40). The fluorescence spectrum (Figure 6.41) confirms besides the intense and broad f–d transition of Eu^{2+} ($\lambda_{Em} = 417$ nm) the presence of Eu^{3+} in terms of the typical red line emissions at 594 nm ($^5D_0 \rightarrow {}^7F_1$), 612 nm ($^5D_0 \rightarrow {}^7F_2$), 652 nm ($^5D_0 \rightarrow {}^7F_3$), 699 nm ($^5D_0 \rightarrow {}^7F_4$) and 754 nm ($^5D_0 \rightarrow {}^7F_5$) [53].

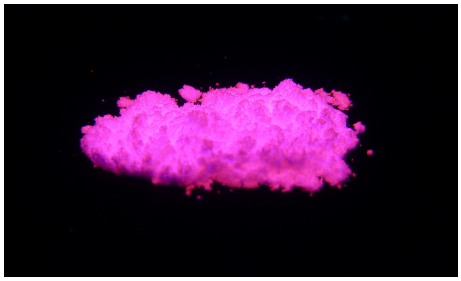

Figure 6.40: Pink fluorescence of RT-$Sr_3P_4O_{13}$:$Eu^{2+/3+}$ at 254 nm.

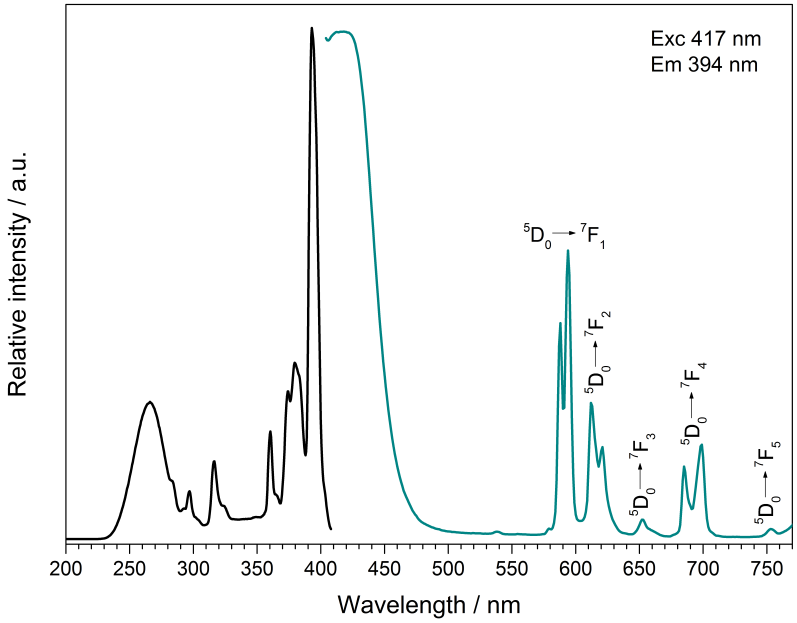

Figure 6.41: Excitation (black) and emission (cyan) spectrum of RT-$Sr_3P_4O_{13}$:$Eu^{2+/3+}$.

6.2.7 Discussion of the Structural Properties

The single-crystal structure of RT-$Sr_3P_4O_{13}$ was solved in the triclinic space group $P\bar{1}$, which is in accordance with *Okonek* [210]. The single-crystal structure of RT-$Sr_3P_4O_{13}$ was also investigated by *Zhang et al.* (2004) [106], who solved it also

in the triclinic space group $P\bar{1}$ but with the lattice parameters $a = 7.2755(1)$ Å, $b = 7.7260(1)$ Å, $c = 10.1935(2)$ Å, $\alpha = 102.28(0)°$, $\beta = 103.46(0)°$ and $\gamma = 94.35(0)°$. This unit cell is twice as large in size. By considering weak superstructure reflections, which occurred during the single-crystal structure analysis, the structure could be solved with the larger unit cell parameters too [210], which was confirmed in this work. The presence of superstructure reflections indicate a phase transition by symmetry reduction, which was assumed to occur at lower temperatures.

The structure solution at RT reveals a disorder of the $O_{br}2$, $O_{term}4$ and $O_{term}5$ positions. Two individuals with different orientations of the central bridging oxygen atom $O_{br}2$ are present in a ratio of 1:1.
By slowly cooling the crystal to 100 K with a cooling rate of 20 °C/h the phase transition could be observed by a proper arrangement of the bridging oxygen atom $O_{br}2$, $O_{term}4$ and $O_{term}5$, and the larger unit cell was found exclusively. The comparison of the different structure solutions is given in Table 6.30.

Table 6.30: Single-crystal refinement parameters of RT-$Sr_3P_4O_{13}$, LT-$Sr_3P_4O_{13}$ and $Sr_3P_4O_{13}$ (*Zhang et al.*) [106]; standard deviations in brackets

Sum formula	RT-$Sr_3P_4O_{13}$	LT-$Sr_3P_4O_{13}$	$Sr_3P_4O_{13}$ [106]
Temperature / K	297(2)	100(2)	293(2)
Crystal system	triclinic	triclinic	triclinic
Space group	$P\bar{1}$ (no. 2)	$P\bar{1}$ (no. 2)	$P\bar{1}$ (no. 2)
a / Å	5.5244(2)	7.2636(3)	7.2755(1)
b / Å	6.9126(2)	7.7033(3)	7.7260(1)
c / Å	7.7199(2)	10.1576(4)	10.1935(2)
α / °	83.316(1)	102.207(1)	102.28(0)
β / °	75.788(1)	103.511(1)	103.46(0)
γ / °	70.553(1)	94.448(1)	94.35(0)
Volume / Å^3	269.29(1)	535.29(4)	537.75(16)
Z	1	2	2
Calculated density D_x / g·cm^{-3}	3.667	3.697	3.659
R_{int}	0.0340	0.0339	0.0410
$R1$ (all data)	0.0155	0.0176	0.0668
$wR2$ (all data)	0.0449	0.0415	0.1304
GooF	1.073	1.091	1.046
Residual electron density (min./max.) / e$^-$·Å^{-3}	-0.42/0.70	-1.35/0.73	-0.93/1.13

Deviations of the lattice parameters between LT-$Sr_3P_4O_{13}$ and $Sr_3P_4O_{13}$ by *Zhang et al.* [106] are negligible due to different measuring temperatures.

Apparently, c_{RT} corresponds to the value of the b_{LT} axis. The calculation of the cell transformation matrix confirms the relation and gives the following transformation vectors:

$a' = a–b$
$b' = -c$
$c' = a+b$

Arranging the smaller unit cell along the c axis and the larger unit cell along the b axis, the relationship between both structures becomes obvious (Figure 6.42).

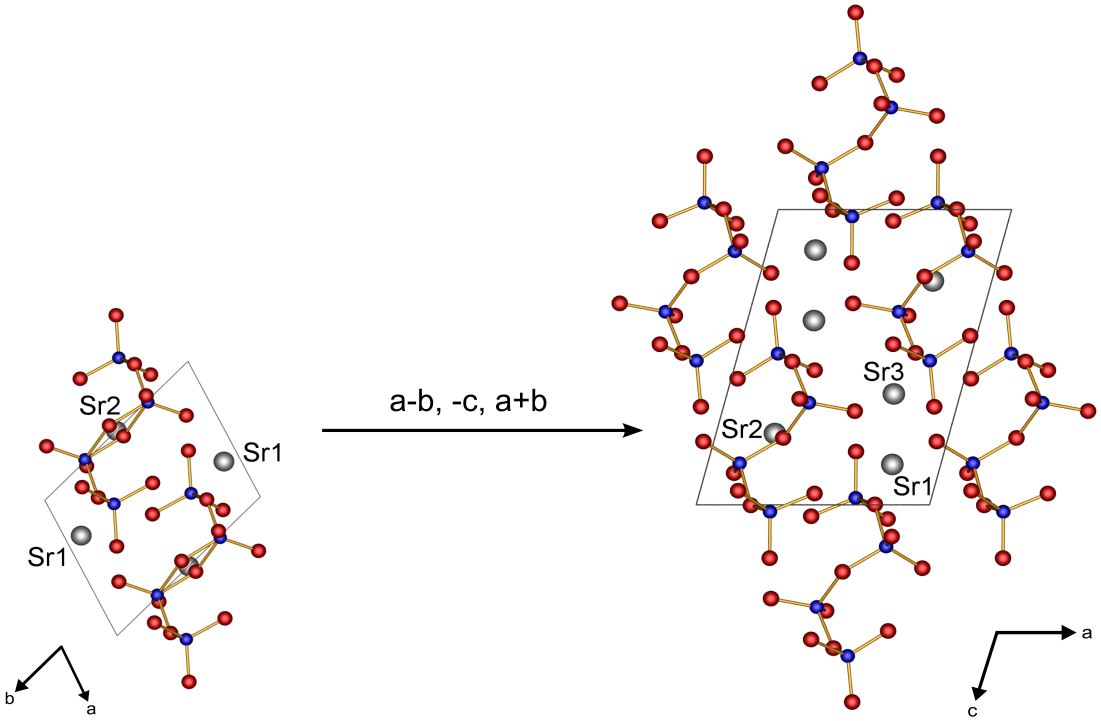

Figure 6.42: Unit cell transformation from RT-$Sr_3P_4O_{13}$ (left) to LT-$Sr_3P_4O_{13}$ (right).

The group-subgroup relationship between both structure solutions can be visualised by the *Bärnighausen* formalism [222] (Figure 6.43). The symmetry reduction by doubling the unit cell volume results in an isomorphic transition with the index 2. Due to the relationship between c_{RT} and b_{LT}, and for reasons of clarity the b and c unit cell axes and the y and z coordinates of the atoms in LT-$Sr_3P_4O_{13}$ were reversed.

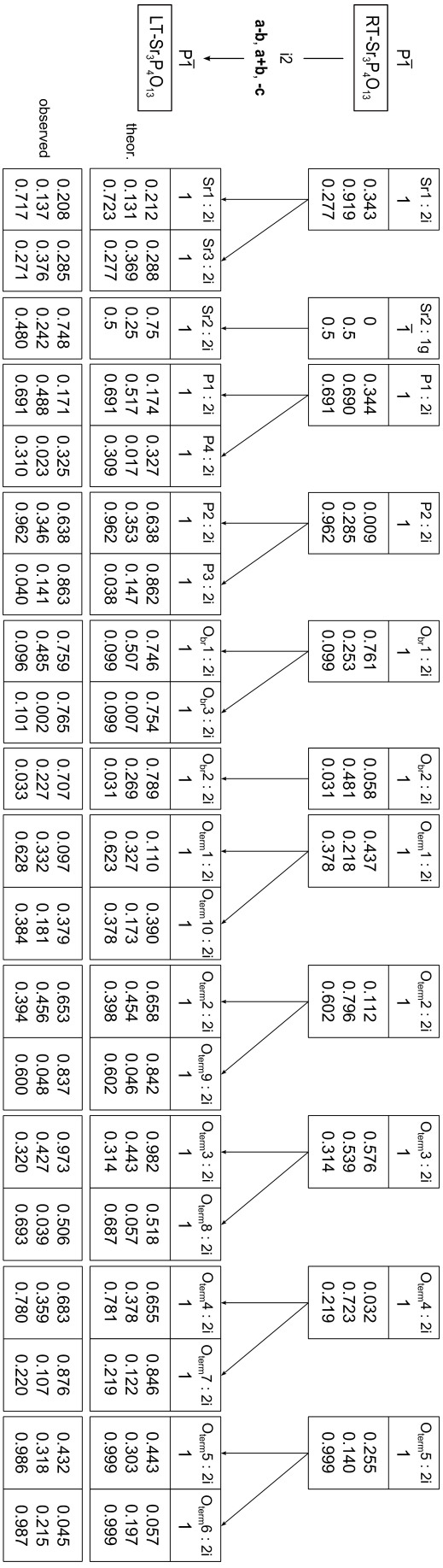

Figure 6.43: *Bärnighausen* formalism [222] showing the group-subgroup relation of the isomorphic transition $i2$ between RT-$Sr_3P_4O_{13}$ and LT-$Sr_3P_4O_{13}$.

The application of the transformation to the disordered terminal oxygen atoms $O_{term}4A$, $O_{term}4B$, $O_{term}5A$ and $O_{term}5B$ confirmed that neither individual A nor B is preferred by the phase transition.

By only slightly increasing the cooling rate to 25 °C/h LT-$Sr_3P_4O_{13}$ did no longer show a proper arrangement of the disordered atoms sites. Nevertheless, a strong tendency pointing towards a phase transition could be already observed. The contour plot [223] of the electron density of the structure solution in the smaller unit cell at 100 K exhibits a clear separation of the electron density between the P atoms, which comes close to a stationary disorder (Figure 6.44 right). In contrast, at RT the contour plot indicates no resolution of the electron density of the bridging oxygen atoms, which rather presents a dynamic disorder.

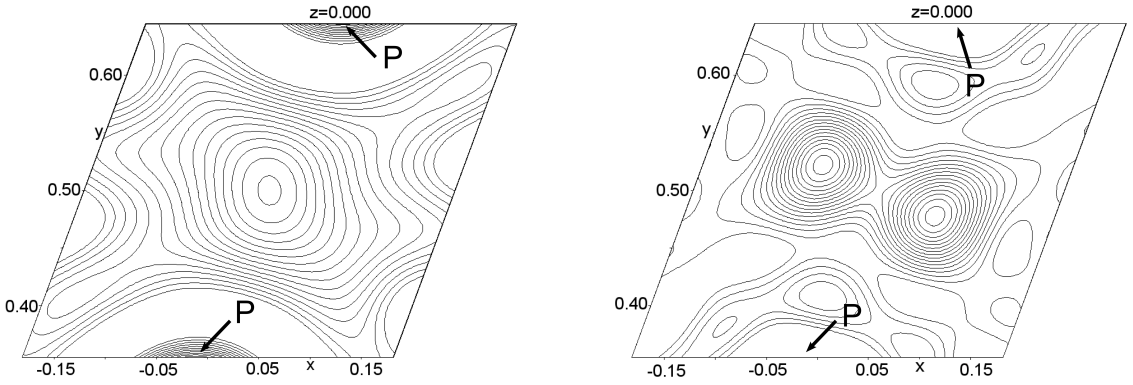

Figure 6.44: Contour plot of the electron density between the central phosphorous atoms of RT-$Sr_3P_4O_{13}$ (left) and LT-$Sr_3P_4O_{13}$ (right) in $P\bar{1}$ in the smaller unit cell; contour lines distances are 0.3 e^- (left) and 0.6 e^- (right), respectively.

Table 6.31: Selected P–O distances / Å and angles / ° of RT-$Sr_3P_4O_{13}$ and LT-$Sr_3P_4O_{13}$

P–O bonds	RT-$Sr_3P_4O_{13}$	LT-$Sr_3P_4O_{13}$
P–O_{br}	1.54–1.64	1.58–1.64
P–O_{term}	1.47–1.53	1.49–1.53
P–O_{br}–P	129–149	128–147
O_{term}–P–O_{term}	111–117	111–117
O_{term}–P–O_{br}	102–114	103–116
O_{br}–P–O_{br}	100–106	103–104

The change of the bond lengths and angles in the $[P_4O_{13}]^{6-}$ tetraphosphate anion between room temperature and 100 K is insignificantly small (Table 6.31). Both

structures exhibit longer P–O_{br} bond lengths compared to P–O_{term}, due to the decreasing effective negative charge on the bridging oxygen atom, which leads to weaker electrostatic interactions between P and O_{br}.

At RT two individuals with different orientations are present. This is also indicated by their ratio of 1:1 in the space group P1. Consequently, the two individuals are not generated by inversion symmetry. By slowly cooling to 100 K both individuals are considered equally with the exception of $O_{br}2$ by forming the tetraphosphate chain present in the larger unit cell. Additionally, considering the contour plot at RT (Figure 6.44), the electron density of the bridging oxygen atoms $O_{br}2$ can not be resolved. Thus, the decision for the structure solution at RT seems to deliver the more appropriate description.

6.2.8 Discussion of the Optical Properties

According to our investigations RT-$Sr_3P_4O_{13}$ reveals two crystallographically different strontium sites, whereas Sr2 occupies an inversion centre. The structure could be solved in a unit cell half of the size compared to the structure solution of *Zhang et al.* (2004) [106], which exhibits three different strontium sites.

At RT the coordination sphere of the strontium atoms is distorted double capped trigonal prismatic (Sr1) and distorted fourfold octahedral (Sr2) by eight and ten terminal oxygen atoms. At 100 K the strontium atoms are coordinated distorted double capped trigonal prismatic by eight terminal oxygen atoms (Sr1 and Sr3) and distorted triple capped trigonal prismatic by nine terminal oxygen atoms (Sr2) (Figure 6.45).

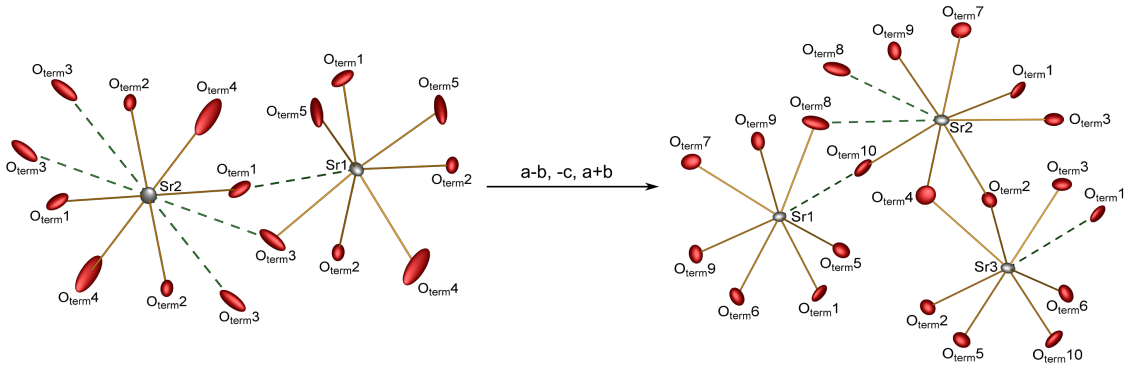

Figure 6.45: Extended coordination spheres (dotted lines included) of the Sr^{2+} ions in RT-$Sr_3P_4O_{13}$ (left) and LT-$Sr_3P_4O_{13}$ (right). The displacement ellipsoids are drawn on a probability level of 50 % (left) and 95 % (right), respectively.

Although the extended coordination sphere of the strontium atoms changes only slightly, their inner coordination sphere changes strongly. Besides the increase of

strontium sites from two to three the special position of Sr2 gets lost. The general trend shows a slight decrease of the Sr–O distances with the exception of Sr2–O in the inner coordination sphere (Table 6.32).

Table 6.32: Sr–O distances / Å of the extended and inner coordination sphere in RT-$Sr_3P_4O_{13}$ and LT-$Sr_3P_4O_{13}$; coordination numbers (CN) in brackets

extended coordination sphere	RT-$Sr_3P_4O_{13}$ (CN)	LT-$Sr_3P_4O_{13}$ (CN)
Sr1–O	2.52–3.12 (8)	2.51–3.01 (8)
Sr2–O	2.52–3.24 (10)	2.50–3.20 (9)
Sr3–O		2.48–3.23 (8)
inner coordination sphere	**RT-$Sr_3P_4O_{13}$ (CN)**	**LT-$Sr_3P_4O_{13}$ (CN)**
Sr1–O	2.52–2.71 (7)	2.51–2.59 (7)
Sr2–O	2.52–2.59 (6)	2.50–2.76 (7)
Sr3–O		2.48–2.76 (7)

The fluorescence spectrum of RT-$Sr_3P_4O_{13}$:Eu^{3+} indicates the occupation of the symmetric Sr2 site by Eu^{3+} due to the dominant $^5D_0 \rightarrow {}^7F_1$ transition. Excitation of $Sr_3P_4O_{13}$:Eu^{2+}/$Sr_2P_2O_7$:Eu^{2+} at 316 nm as well as at 345 nm revealed the broad parity and spin allowed $4f^6 6d^1$–$4f^7$ transition peaking at 404 nm with a shoulder towards 425 nm, which was also observed by *Zhang* (2013) [110].

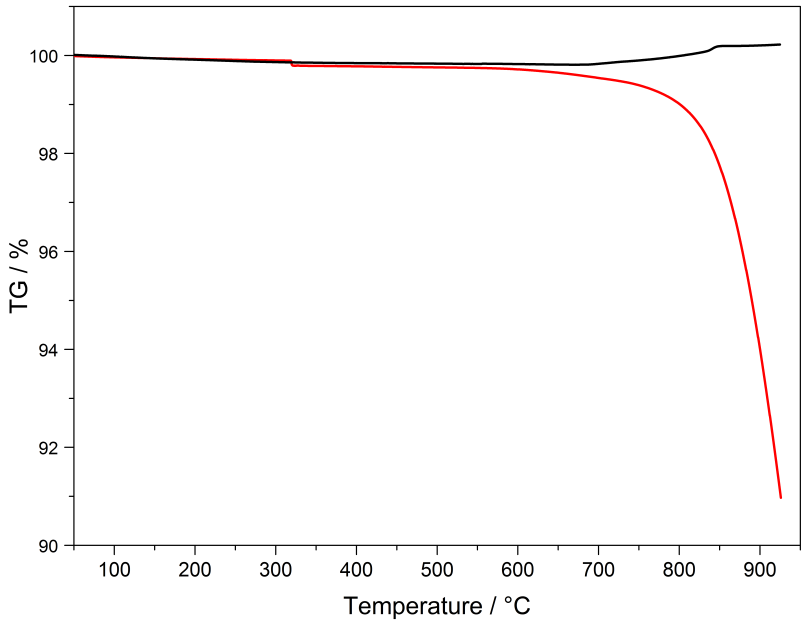

Figure 6.46: Thermogravimetric analysis of β-$Sr(PO_3)_2$ in synthetic air (black) and *forming gas* (red) between 50 and 925 °C with a heating rate of 20 °C·min^{-1}.

Regarding the X-ray powder diffraction patterns of $Sr_{3-x}Eu_xP_4O_{13}$:Eu^{2+} [110] reflections belonging to $Sr_2P_2O_7$ can also be observed. Following our synthesis route start-

ing from β-$Sr(PO_3)_2$, $Sr_3P_4O_{13}$:Eu^{2+} also could only be obtained with $Sr_2P_2O_7$:Eu^{2+} as side phase. Presumably the reducing conditions favour the evaporation of P_2O_5, which is indicated by a qualitative thermogravimetric measurement between 50 and 925 °C (Figure 6.46). A considerable mass loss occurs during the heating process of β-$Sr(PO_3)_2$ in *forming gas* starting at about 600 °C, while in synthetic air virtually no mass loss occurs. Taking account of the results of *Kreidler* and *Hummel* this process is due to the evaporation of P_2O_5 [209].

Natarajan et al. examined the fluorescence spectrum of $Sr_2P_2O_7$:Eu^{2+}, which shows one broad emission band at 422 nm [220]. Thus the shoulder in the fluorescence emission spectrum of $Sr_3P_4O_{13}$:Eu^{2+} of *Zhang et al.* (2013) and in Figure 6.39 is very likely due to the presence of the side phase $Sr_2P_2O_7$:Eu^{2+}.

Zhang et al. (2013) investigated the optical properties of LT-$Sr_3P_4O_{13}$:Eu^{2+} between 20 and 297 K as well. At 20 K a considerable splitting of the emission band peaking at 400 and 430 nm becomes visible due to the presence of two different europium sites. The assumption is correct, but the splitting presumably results from the coexistence of $Sr_3P_4O_{13}$:Eu^{2+} and $Sr_2P_2O_7$:Eu^{2+}, which have different coordination distances and thus a differing ligand field splitting.

A splitting of the emission band in phase pure LT-$Sr_3P_4O_{13}$:Eu^{2+} is doubtful. Although the number of strontium atoms increases from two to three, the environment barely changes. By symmetry reduction the surrounding of Sr1 in RT-$Sr_3P_4O_{13}$ is transformed to Sr1 and Sr3 in LT-$Sr_3P_4O_{13}$, whereas the coordination numbers do not change. The inversion symmetric site of Sr2 in RT-$Sr_3P_4O_{13}$ disappears in LT-$Sr_3P_4O_{13}$. The inner coordination sphere of Sr2 increases from six to seven, which is equal to Sr1 and Sr3. A proof is only possible if the compound is synthesised phase pure and fluorescence spectroscopy is carried out.

7 Borophosphates

7.1 Diammonium Manganese(II) Borophosphate Chloride $(NH_4)_2Mn(II)[B_2P_3O_{11}(OH)_2]Cl$

In borophosphate chemistry the FBU represents the essential structural motif, which comprises a certain B:P ratio and furthermore an O:OH ratio (if protonated borophosphates are present). Quite a number of compounds with a B:P ratio of 2:3 is well known [124, 144, 224–227]. Depending on the O:OH ratio and the FBU, the polymeric borophosphate anions form chains or layers. *Ewald et al.* observed that protonated borophosphates with a B:P ratio of 2:3 and an O:OH ratio of 12:1 reveal either layer or chain structures featuring either oB dreier-single rings or olB dreier-single rings, respectively [13]. Reducing the O:OH ratio to 11:2 leads exclusively to the formation of chain borophosphates featuring both mentioned FBUs [13, 144, 226]. Up to now no layered structures with an olB vierer-single ring have been observed. $(NH_4)_2Mn(II)[B_2P_3O_{11}(OH)_2]Cl$ is the first representative possessing a layered structure associated with an O:OH ratio of 11:2, which exhibits an oB vierer-single ring as novel FBU. The results of this chapter are published in a science journal [122].

7.1.1 Synthesis

$(NH_4)_2Mn(II)[B_2P_3O_{11}(OH)_2]Cl$ was synthesised under hydrothermal conditions. A mixture of 251.5 mg (2.014 mmol) $MnCl_2$, 528.4 mg (4.002 mmol) $(NH_4)_2HPO_4$, 123.7 mg (2.053 mmol) H_3BO_3 and 0.4 mL H_3PO_4 (85 %) was transferred into a 10 mL *Teflon* autoclave and was kept at 180 °C. After eight days a slightly pink suspension was obtained. The product was washed with hot water, filtered off and dried in air overnight. $(NH_4)_2Mn(II)[B_2P_3O_{11}(OH)_2]Cl$ was obtained as an almost colourless crystalline powder.

7.1.2 X-Ray Powder Diffraction

The phase purity of the sample was checked by X-ray powder diffraction. Via a *Rietveld* analysis (Figure 7.1) the structure model of $(NH_4)_2Mn(II)[B_2P_3O_{11}(OH)_2]Cl$ was refined to very good residuals of $R_p = 0.009$, $R_{wp} = 0.013$ and $\chi^2 = 1.46$.

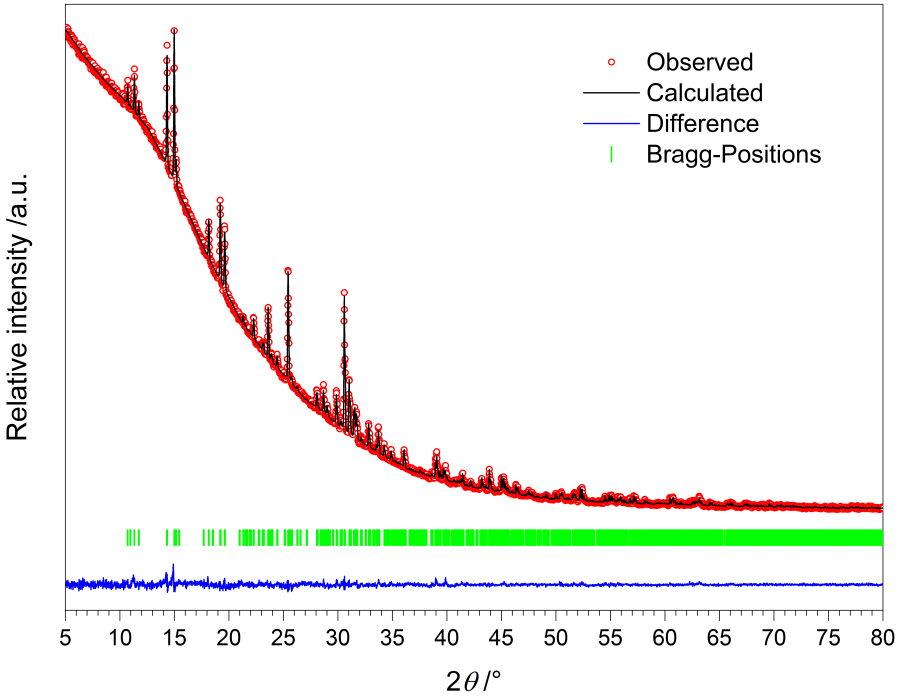

Figure 7.1: X-ray powder diffraction pattern and result of the *Rietveld* refinement based on the structure model of $(NH_4)_2Mn(II)[B_2P_3O_{11}(OH)_2]Cl$ obtained from single-crystal data.

The composition of a selected crystal of $(NH_4)_2Mn(II)[B_2P_3O_{11}(OH)_2]Cl$ was checked via EDX spectroscopy. Within the accuracy of the measurement's limit no other elements were found.

7.1.3 Crystal Structure Determination

A colourless single-crystal of $(NH_4)_2Mn(II)[B_2P_3O_{11}(OH)_2]Cl$ with a size of 0.044 × 0.034 × 0.026 mm^3 was isolated and mounted on a *MicroMount*. The collection of the crystal data was run on a Bruker D8 Venture single-crystal diffractometer using Mo radiation. A multi-scan absorption correction was subsequently performed. $(NH_4)_2Mn(II)[B_2P_3O_{11}(OH)_2]Cl$ crystallises in a new structure type in the monoclinic space group $P2_1/n$ with the lattice parameters $a = 9.0524(3)$ Å, $b = 8.4729(3)$ Å, $c = 16.5232(5)$ Å and $\beta = 92.303(1)$ °.

33345 reflections were collected. Out of 2227 independent reflections 2032 were observed ($F_o^2 > 2\sigma\ (F_o^2)$, R_{int} = 0.0329). The crystallographic data, the parameters of the measurement and refinement are summarised in Table 7.1. The structure was solved by direct methods and refined by full matrix least-squares technique using the programs SHELXS-97 and SHELXTL-97 [21, 22]. The anisotropic refinement revealed R-values of $R1 = 0.0257$ and $wR2 = 0.0632$. The Mn, B, P, O and Cl atoms could be clearly located and the N atoms were subsequently assigned from the difference *Fourier* map. Hydrogen atoms were added geometrically and were confirmed by MAPLE calculations [32, 33, 152]. The refined atomic coordinates, anisotropic displacement parameters, selected interatomic distances and angles and hydrogen bonds are summarised in Tables 7.2 to 7.5.

Table 7.1: Single-crystal refinement parameters of $(NH_4)_2Mn(II)[B_2P_3O_{11}(OH)_2]Cl$; standard deviations in brackets

Sum formula	$(NH_4)_2Mn(II)[B_2P_3O_{11}(OH)_2]Cl$
Temperature / K	297(2)
Molar weight / g·mol^{-1}	450.87
Crystal system	monoclinic
Space group	$P2_1/n$ (no. 14)
Crystal shape	irregular
Crystal size / mm^3	0.044 × 0.034 × 0.026
Colour	colourless
a / Å	9.0524(3)
b / Å	8.4729(3)
c / Å	16.5232(5)
β / °	92.303(1)
Volume / Å^3	1266.31(7)
Z	4
Calculated density D_x / g·cm^{-3}	2.366
Absorption coefficient μ / mm^{-1}	1.709
F(000)	900
Radiation (λ / Å)	Mo-K_α (0.7093)
Diffractometer	Bruker D8 Venture
Absorption correction	multi-scan
Transmission factor (min./max.)	0.6995 / 0.7458
Index range h|k|l (min./max.)	-10/9 | -10/10 | -19/19
Theta range / °	$2.47 \leq \theta \leq 25.00$
Reflections collected	33345
Independent reflections	2227
Observed reflections	2032 ($F_o^2 > 2\sigma\ (F_o^2)$)
R_{int}	0.0329
Refined parameters	230
R_σ	0.0122
$R1$ (all data)	0.0257
$wR2$ (all data)	0.0632
Weighting scheme	$w^{-1}=\sigma^2\ F_o^2 + (0.0358\ P)^2 + 1.4709\ P$; $P = (F_o^2 + 2\ F_c^2)/3$
GooF	1.093
Residual electron density (min./max.) / e$^-$·Å^{-3}	-0.39/0.38

Table 7.2: Refined atomic coordinates, *Wyckoff* symbols and isotropic displacement parameters U_{eq} / Å^2 in $(NH_4)_2Mn(II)[B_2P_3O_{11}(OH)_2]Cl$; standard deviations in brackets

Atom	*Wyckoff* symbol	x	y	z	U_{eq}
Mn1	4*e*	0.59947(4)	0.32262(4)	0.12898(2)	0.01131(12)
P1	4*e*	0.29995(6)	0.42565(7)	0.01813(3)	0.00913(15)
P2	4*e*	0.83510(6)	0.04259(7)	0.06081(3)	0.01033(15)
P3	4*e*	0.27024(6)	0.23252(7)	0.20832(3)	0.00903(15)
B1	4*e*	0.33471(27)	0.54262(29)	0.17167(14)	0.01004(49)
B2	4*e*	0.11641(27)	0.17615(30)	0.06227(15)	0.01146(51)
$O_{br}1$	4*e*	0.21768(17)	0.19093(18)	0.29369(9)	0.01171(33)
$O_{br}2$	4*e*	0.30029(17)	0.55874(18)	0.08407(9)	0.01298(34)
$O_{br}3$	4*e*	0.15299(16)	0.33059(18)	0.03034(9)	0.01301(34)
$O_{br}4$	4*e*	0.81065(18)	−0.04636(20)	−0.02001(10)	0.01898(37)
$O_{br}5$	4*e*	0.95485(17)	0.16714(19)	0.05047(10)	0.01709(36)
$O_{br}6$	4*e*	0.15748(18)	0.15510(19)	0.14815(9)	0.01694(36)
$O_{br}7$	4*e*	0.24530(16)	0.41299(18)	0.20464(9)	0.01178(33)
$O_{term}1$	4*e*	0.43177(17)	0.31916(19)	0.03094(9)	0.01482(35)
$O_{term}2$	4*e*	0.28263(17)	0.50380(19)	−0.06326(8)	0.01442(34)
$O_{term}3$	4*e*	0.69026(17)	0.11351(19)	0.08056(10)	0.01616(35)
$O_{term}4$	4*e*	0.42660(17)	0.18466(19)	0.19614(9)	0.01609(36)
O_H1	4*e*	0.48995(17)	0.51826(20)	0.18746(10)	0.01638(36)
O_H2	4*e*	0.89443(19)	−0.07823(21)	0.12516(10)	0.02272(40)
Cl1	4*e*	0.79760(7)	0.30866(8)	0.24497(4)	0.02499(17)
N1	4*e*	0.02421(24)	0.42006(28)	−0.14034(13)	0.02330(48)
N2	4*e*	0.45673(25)	−0.11800(28)	0.09563(13)	0.02375(48)
H1	4*e*	0.548(3)	0.585(3)	0.224(2)	0.050
H2	4*e*	0.834(3)	−0.103(4)	0.171(1)	0.050
H3	4*e*	−0.045(3)	0.501(3)	−0.126(2)	0.050
H4	4*e*	−0.007(4)	0.322(2)	−0.117(2)	0.050
H5	4*e*	0.120(2)	0.448(4)	−0.117(2)	0.050
H6	4*e*	0.016(4)	0.396(4)	−0.197(1)	0.050
H7	4*e*	0.366(2)	−0.069(4)	0.076(2)	0.050
H8	4*e*	0.527(3)	−0.033(3)	0.102(2)	0.050
H9	4*e*	0.499(4)	−0.193(3)	0.058(2)	0.050
H10	4*e*	0.446(4)	−0.165(4)	0.1480(11)	0.050

O_{br} = bridging oxygen atom; O_{term} = terminal oxygen atom; O_H = hydroxyl group

Table 7.3: Anisotropic displacement parameters U_{ij} / Å^2 in $(NH_4)_2Mn(II)[B_2P_3O_{11}(OH)_2]Cl$; standard deviations in brackets

Atom	U_{11}	U_{22}	U_{33}	U_{12}	U_{13}	U_{23}
Mn1	0.0108(2)	0.0113(2)	0.0119(2)	−0.0006(2)	0.0017(1)	0.0009(1)
P1	0.0094(3)	0.0104(3)	0.0076(3)	−0.0006(2)	0.0008(2)	−0.0021(2)
P2	0.0085(3)	0.0094(3)	0.0132(3)	−0.0017(2)	0.0022(2)	−0.0006(2)
P3	0.0112(3)	0.0077(3)	0.0083(3)	0.0006(2)	0.0012(2)	−0.0004(2)
B1	0.0125(12)	0.0096(13)	0.0083(11)	−0.0009(9)	0.0025(9)	0.0006(1)
B2	0.0108(12)	0.0115(13)	0.0120(12)	−0.0027(9)	−0.0008(9)	−0.0024(10)
$O_{br}1$	0.0180(8)	0.0080(8)	0.0093(7)	0.0008(6)	0.0025(6)	−0.0001(6)
$O_{br}2$	0.0188(8)	0.0112(8)	0.0090(7)	−0.0011(6)	0.0012(6)	−0.0014(6)
$O_{br}3$	0.0113(8)	0.0120(9)	0.0157(8)	0.0022(6)	0.0003(6)	−0.0029(6)
$O_{br}4$	0.0195(9)	0.0180(9)	0.0193(8)	−0.0076(7)	−0.0020(7)	0.0056(7)
$O_{br}5$	0.0091(8)	0.0142(9)	0.0278(9)	0.0030(7)	−0.0017(6)	−0.0026(6)
$O_{br}6$	0.0242(9)	0.0151(9)	0.0113(8)	0.0005(6)	−0.0024(6)	−0.0080(7)
$O_{br}7$	0.0128(8)	0.0081(8)	0.0147(7)	0.0020(6)	0.0030(6)	0.0003(6)
$O_{term}1$	0.0122(8)	0.0161(9)	0.0160(8)	−0.0032(6)	−0.0016(6)	0.0013(6)
$O_{term}2$	0.0152(8)	0.0186(9)	0.0093(7)	0.0025(6)	−0.0005(6)	−0.0049(7)
$O_{term}3$	0.0112(8)	0.0142(9)	0.0234(8)	−0.0054(7)	0.0053(6)	−0.0005(7)
$O_{term}4$	0.0140(8)	0.0139(9)	0.0207(8)	0.0029(6)	0.0047(7)	0.0027(7)
O_H1	0.0121(8)	0.0168(9)	0.0201(8)	−0.0066(7)	−0.0009(6)	−0.0014(7)
O_H2	0.0221(9)	0.0235(10)	0.0228(9)	0.0094(7)	0.0045(7)	0.0042(8)
Cl1	0.0238(3)	0.0320(4)	0.0190(3)	−0.0022(3)	−0.0019(2)	0.0054(3)
N1	0.0168(11)	0.0259(13)	0.0266(11)	−0.0025(10)	−0.0071(9)	0.0000(9)
N2	0.0267(12)	0.0222(13)	0.0225(11)	−0.0017(9)	0.0022(9)	−0.0072(10)

Table 7.4: Selected interatomic distances / Å and angles / ° in $(NH_4)_2Mn(II)[B_2P_3O_{11}(OH)_2]Cl$; standard deviations in brackets

B–O_{br}	1.454(3)–1.481(3)
B–O_H	1.434(3)
P–O_{br}	1.527(2)–1.575(2)
P–O_{term}	1.490(2)–1.504(2)
P–O_H	1.556(2)
Mn–O	2.123(2)–2.277(2)
Mn–Cl	2.575(1)
B–O_{br}–P	127.6(1)–136.7(2)
O–P–O	102.2(1)–116.4(1)
O–B–O	103.8(2)–112.8(2)

Table 7.5: Distances / Å and angles / ° of the hydrogen bonds in $(NH_4)_2Mn(II)[B_2P_3O_{11}(OH)_2]Cl$; *D*: Donor, *A*: Acceptor

D–*H*	*A*	*d*(*D*–*H*)	*d*(*H*–*A*)	∢(*DHA*)	*d*(*D*–*A*)
O_H1–H1	Cl1	0.96	2.40	154	3.29
O_H2–H2	Cl1	0.97	2.02	170	2.97
N1–H3	O_{br}7	0.96	2.31	126	2.98
N1–H3	O_{br}3	0.96	2.37	152	3.25
N1–H3	O_{br}2	0.96	2.49	123	3.12
N1–H4	O_H2	0.96	2.31	128	3.00
N1–H5	O_{term}2	0.97	1.75	173	2.71
N1–H5	O_{br}3	0.97	2.63	110	3.10
N1–H6	O_{term}4	0.97	2.02	159	2.95
N2–H7	O_{br}4	0.97	2.06	172	3.02
N2–H7	O_{term}3	0.97	2.64	114	3.15
N2–H8	O_{term}3	0.96	1.98	160	2.90
N2–H8	O_{term}4	0.96	2.59	111	3.07
N2–H9	O_{term}1	0.97	1.95	170	2.91
N2–H10	O_{br}1	0.96	2.17	137	2.95
N2–H10	Cl1	0.96	2.87	119	3.44

7.1.4 Crystal Structure Description

$(NH_4)_2Mn(II)[B_2P_3O_{11}(OH)_2]Cl$ crystallises in a new structure type in the monoclinic space group $P2_1/n$ with four formula units per unit cell. All atoms are located on the general *Wyckoff* position 4*e*. The anionic partial structure consists of infinite layers of corner-sharing borate, hydroxo-borate, phosphate and hydroxo-phosphate tetrahedra avoiding any P–O–P connection (Figure 7.2).

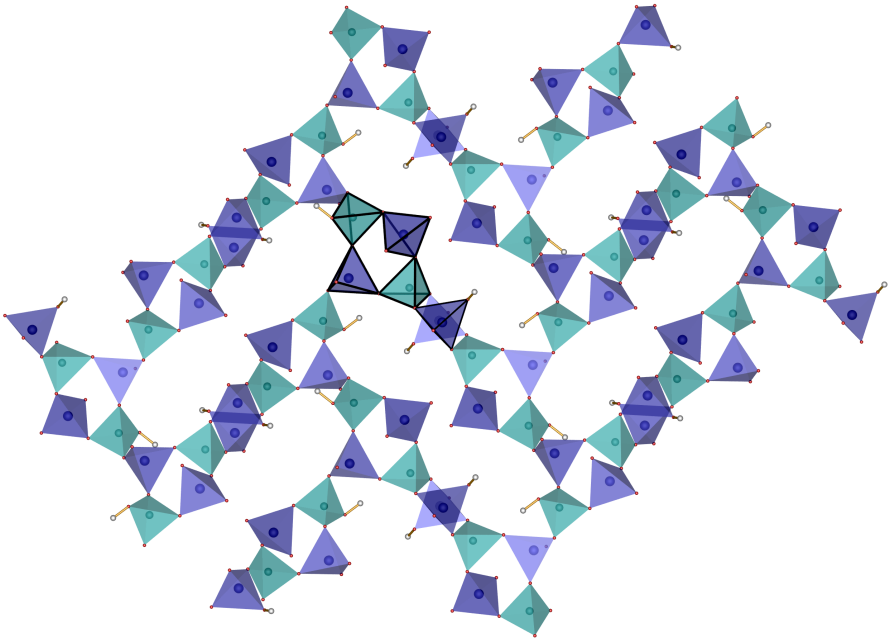

Figure 7.2: LB vierer-single layered anionic partial structure of $(NH_4)_2Mn(II)[B_2P_3O_{11}(OH)_2]Cl$; FBU highlighted; phosphate tetrahedra blue, borate tetrahedra turquoise, hydrogen white.

The polyanion is constructed by cyclic pentameric $^2_\infty[B_2P_3\Phi_{13}]$ (Φ = O, OH) units comprising a B:P ratio of 2:3. The lB vierer-single layer contains an oB vierer-single ring as a novel FBU (Figure 7.3) formed by two $B\Phi_4$ and three $P\Phi_4$ (Φ = O, OH) tetrahedra, illustrated with the descriptor 5□:<4□>□ [13, 82, 83, 113].

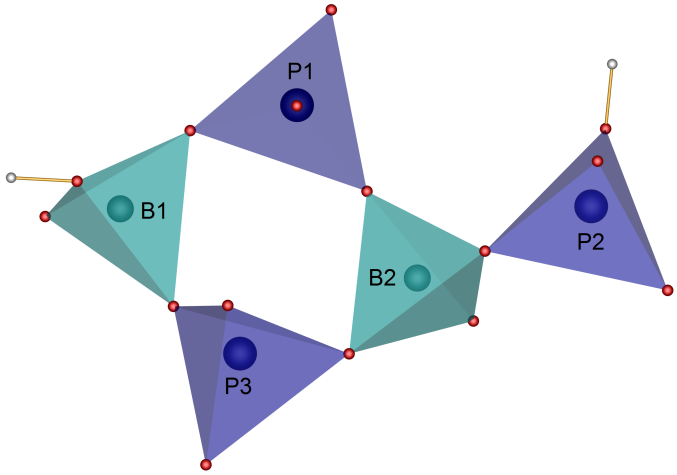

Figure 7.3: Novel FBU as an oB vierer-single ring 5□:<4□>□ of $(NH_4)_2Mn(II)[B_2P_3O_{11}(OH)_2]Cl$; phosphate tetrahedra blue, borate tetrahedra turquoise, hydrogen white.

Up to now protonated borophosphates with a B:P ratio of 2:3 are divided into anionic partial structures with oB dreier-single rings and olB dreier-single rings (Figure 7.4).

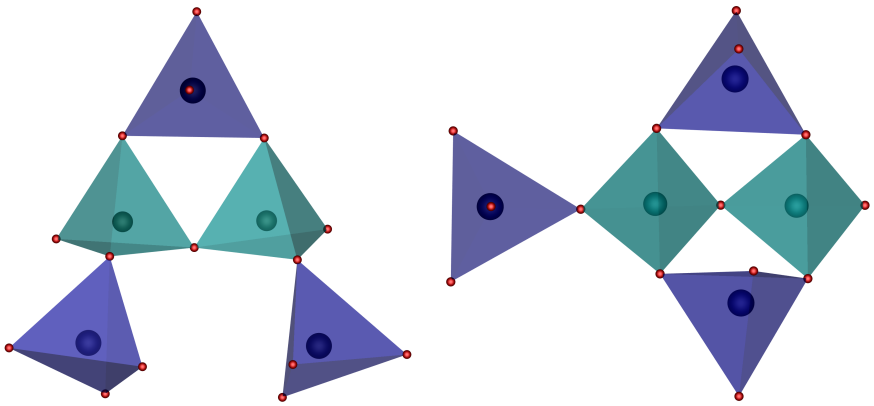

Figure 7.4: FBUs exhibiting an oB dreier-single ring (left) and an olB dreier-single ring (right); phosphate tetrahedra blue, borate tetrahedra turquoise, oxygen red.

Whereas chain borophosphates can be either formed by olB or oB dreier-single rings with an O:OH ratio of 11:2 or 12:1, layer borophosphates are exclusively formed with oB dreier-single rings and reveal an O:OH ratio of 12:1 [13]. So far borophosphate compounds with an O:OH ratio of 11:2 never showed a layered structure, but with $(NH_4)_2Mn(II)[B_2P_3O_{11}(OH)_2]Cl$ this structural feature was observed for the first time. Moreover, in borophosphate chemistry no such FBU as the oB vierer-single ring $^{2}_{\infty}[B_2P_3\Phi_{13}]$ (Φ = O, OH) is known so far.

Both B and P atoms are coordinated tetrahedrally by either oxygen atoms or hydroxyl groups. B–O bond lengths in the borate tetrahedra range between 1.43 and

1.48 Å whereas P–O bond lengths in the phosphate tetrahedra lie between 1.49 and 1.57 Å. The bond lengths B–O_H and P–O_H are 1.43 and 1.56 Å, respectively. B–O_{br} distances range between 1.46 and 1.48 Å whereas P–O_{br} distances range between 1.53 and 1.58 Å and P–O_{term} distances lie between 1.49 and 1.50 Å. These values correspond to typical data found for other borophosphates [144, 224, 225, 228]. B–O_{br}–P angles range between 128 and 137 °, whereas O–B–O and O–P–O angles range between 104–114° (Ø = 110°) and 102–116° (Ø = 109°). Selected bond lengths and angles of $(NH_4)_2Mn(II)[B_2P_3O_{11}(OH)_2]Cl$ are listed in Table 7.4.

For the calculation of deviation of tetrahedra from ideal symmetry the method introduced by *Balić-Žunić* and *Makovicky* was adopted [35, 36]. The five crystallographically different borate, hydroxo-borate, phosphate and hydroxo-phosphate tetrahedra feature the values −0.22 % (B1), −0.60 % (B2), −0.19 % (P1), −0.21 % (P2) and −0.46 % (P3), which are similar to tetrahedra in other compounds [97, 98, 129, 187, 189–191]. Exhibiting a deviation of < 1 %, tetrahedra are classified as regular.

The parallel borophosphate layers are interconnected via common oxygen corners of MnO_5Cl octahedra as demonstrated in Figure 7.5.

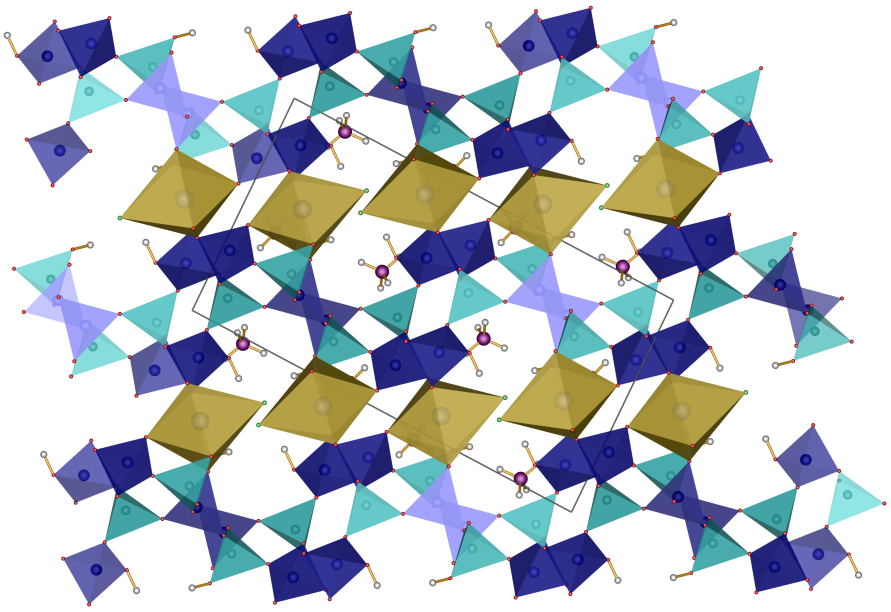

Figure 7.5: Layered crystal structure viewed along [010] interconnected via common oxygen corners of MnO_5Cl octahedra (yellow) of $(NH_4)_2Mn(II)[B_2P_3O_{11}(OH)_2]Cl$; phosphate tetrahedra blue, borate tetrahedra turquoise, nitrogen violet, hydrogen white.

The single-crystal structure analysis reveals a unique site of the Mn^{2+} ion which is coordinated distorted octahedrally by one chlorine and five oxygen atoms (Figure 7.6). The coordinating oxygen atoms originate from a hydroxyl group of a borate and terminal oxygen atoms of four phosphate tetrahedra belonging to two adja-

cent borophosphate layers. The Mn–O bond lengths range between 2.12–2.28 Å, the Mn–Cl distance amounts to 2.57 Å (Table 7.4). These values are in excellent agreement with the sum of the ionic radii of *high-spin* Mn^{2+} and the coordinating atoms, e.g. 2.15 (OH^-), 2.18 (O^{2-}) and 2.64 Å (Cl) [60], respectively.

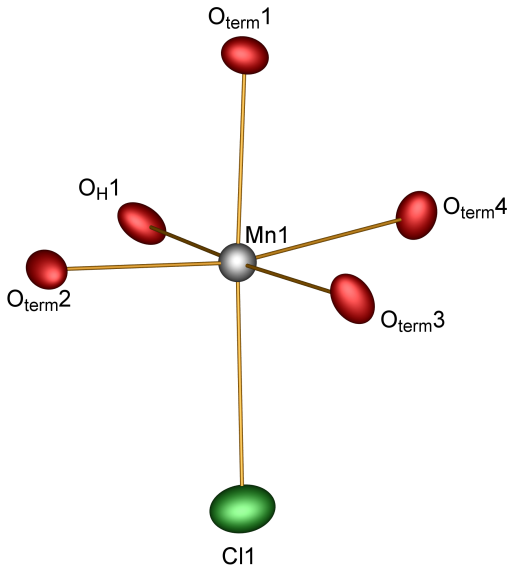

Figure 7.6: Coordination sphere of manganese in $(NH_4)_2Mn(II)[B_2P_3O_{11}(OH)_2]Cl$. The displacement ellipsoids are drawn on a probability level of 65 %.

Along [100] and [111] oval shaped channels (approx. 7.00 × 4.40 Å^2) are formed, in which the NH_4^+ ions are situated (Figure 7.7).

According to *Steiner* [150] the hydrogen bonds between 1.75–2.17 Å can be considered as moderately strong, whereas others larger than 2.20 Å are assigned as weak existing between NH_4^+ ions and terminal and bridging oxygen atoms (Table 7.5). Further hydrogen bonds can also be observed between the chlorine atom and the protonated borate (weak) and phosphate tetrahedra (moderately strong) as well as the NH_4^+ ions (weak) (Figure 7.8).

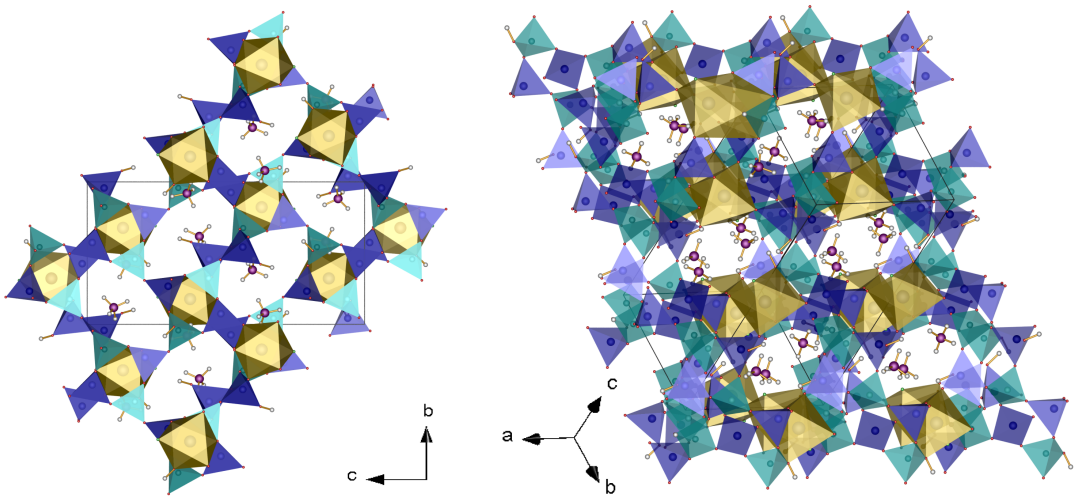

Figure 7.7: Oval shaped channels in [100] and [111] in $(NH_4)_2Mn(II)[B_2P_3O_{11}(OH)_2]Cl$. Yellow octahedra centred by manganese, blue and turquoise tetrahedra centred by phosphorus and boron, respectively.

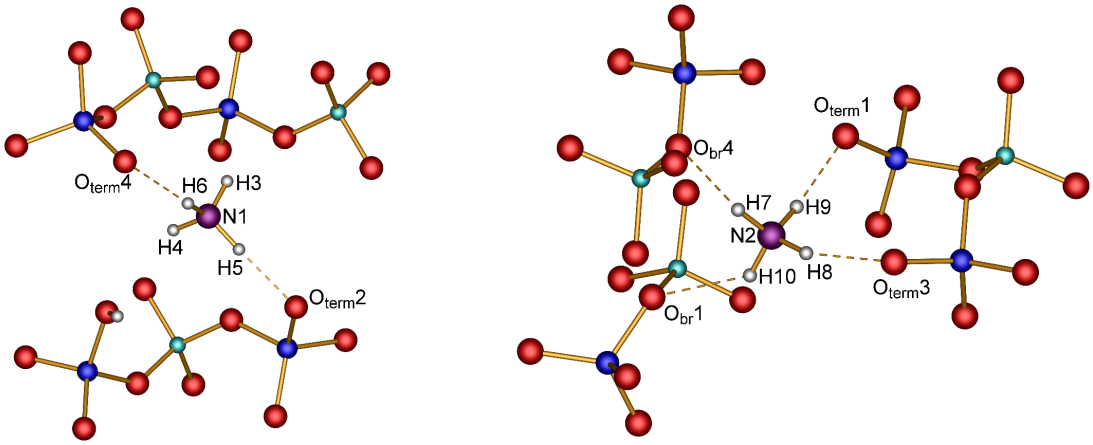

Figure 7.8: Moderately strong hydrogen bonds in $(NH_4)_2Mn(II)[B_2P_3O_{11}(OH)_2]Cl$. Weak hydrogen bonds are omitted for clarity; phosphorus blue, boron turquoise, chlorine green, oxygen red, nitrogen violet, hydrogen white.

7.1.5 Electrostatic Calculations

The coordination number of manganese (Table 12.7) and the electrostatic consistency of the structure model were proved by calculations by calculations based on the MAPLE concept [32, 33, 152]. According to the calculations, the structure model of $(NH_4)_2Mn(II)[B_2P_3O_{11}(OH)_2]Cl$ thus shows electrostatic consistency, as presented in Table 7.6.

Table 7.6: MAPLE calculations for $(NH_4)_2Mn(II)[B_2P_3O_{11}(OH)_2]Cl$ [32, 33, 152]

$(NH_4)_2Mn(II)[B_2P_3O_{11}(OH)_2]Cl$	MnO [229] + B_2O_3 [154] + NH_4Cl [230] + $NH_4H_2PO_4$ [231] + P_2O_5 [193]
MAPLE = 124335 kJ·mol^{-1} ($\Delta = 0.7\,\%$)	MAPLE = 125167 kJ·mol^{-1}

7.1.6 Spectroscopic Properties

7.1.6.1 IR Spectroscopy

The infrared spectrum of $(NH_4)_2Mn(II)[B_2P_3O_{11}(OH)_2]Cl$ was recorded between 4000 and 400 cm^{-1} and is shown in Figure 7.9. The positions of the bands and the corresponding assignments are given in Table 7.7.

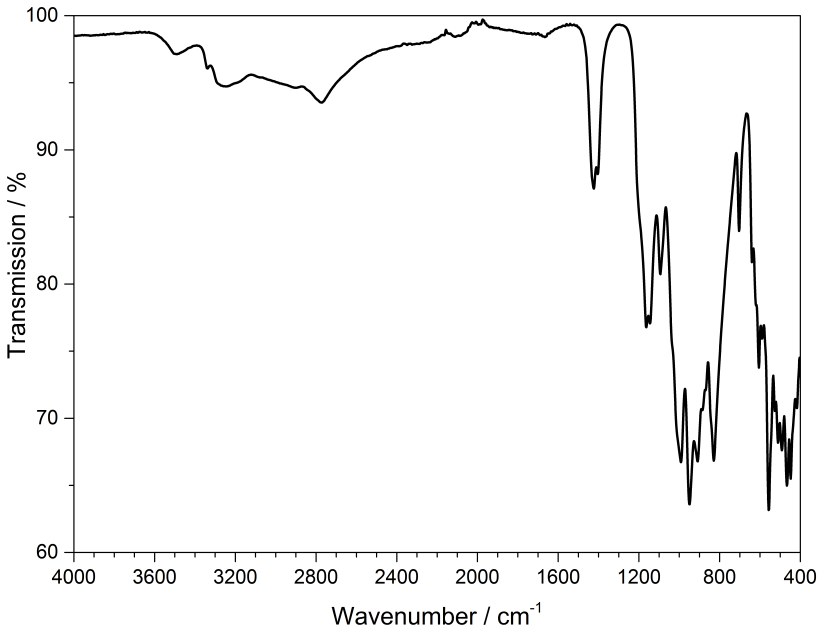

Figure 7.9: Infrared spectrum of $(NH_4)_2Mn(II)[B_2P_3O_{11}(OH)_2]Cl$.

Table 7.7: Position / cm^{-1} and assignment of the IR bands in $(NH_4)_2Mn(II)[B_2P_3O_{11}(OH)_2]Cl$

Position	Assignment
3490	ν(OH), δ(OH) [120, 121, 226, 228, 232]
3338	ν(OH), δ(OH) [120, 121, 226, 228, 232]
3370–2600	ν(NH) [120, 233, 234]
1666	ν(OH), δ(OH) [120, 121, 226, 228, 232]
1423	ν(NH) [120, 233, 234]
1163	$\nu(BO_4)$ [235, 236]
1100–400	$\nu(PO_4)$ [235, 236]
908, 887, 870	$\nu(BO_4)$ [235, 236]
830	ν_{as}(BOP) [235, 236]
704	ν_{s}(BOP) [235, 236]
606	δ(BOP) [235, 236]
557	δ(OPO) [236]
511	$\nu(BO_4)$ [235, 236]

The bands at 3490, 3338 and 1666 cm^{-1} can be assigned to the stretching and deformation vibrations of the OH groups [120, 121, 226, 228, 232], while vibrations between 3365–2617 cm^{-1} and at 1423 cm^{-1} can be assigned to N–H stretching vibrations [120, 233, 234]. BO_4 vibrations can be found at 1163, 908, 887, 870 and 511 cm^{-1}, whereas typical PO_4 vibrations range in the region between 1094 and 417 cm^{-1}, respectively. Characteristic bands of symmetric or asymmetric B–O–P stretching and bending vibrations are found at 830 (ν_{as}), 704 (ν_s), 606 (δ) and for δ(O–P–O) at 557 cm^{-1} [235, 236].

7.1.6.2 UV-Vis Spectroscopy

All excitations in a *high-spin* d^5 Mn^{2+} ion (see also Chapter 7.1.7) in an octahedral environment are spin and parity forbidden. Since the coordination environment of Mn^{2+} is slightly distorted those selection rules do not apply that strongly and two weak absorption bands can be observed. The UV–Vis reflection spectrum of $(NH_4)_2Mn(II)[B_2P_3O_{11}(OH)_2]Cl$ was recorded at room temperature between 200–800 nm (Figure 7.10) and shows two weak absorption bands at 360 ($^6S \rightarrow {}^4T_2$) and 405 nm ($^6S \rightarrow {}^4E$) [128, 237].

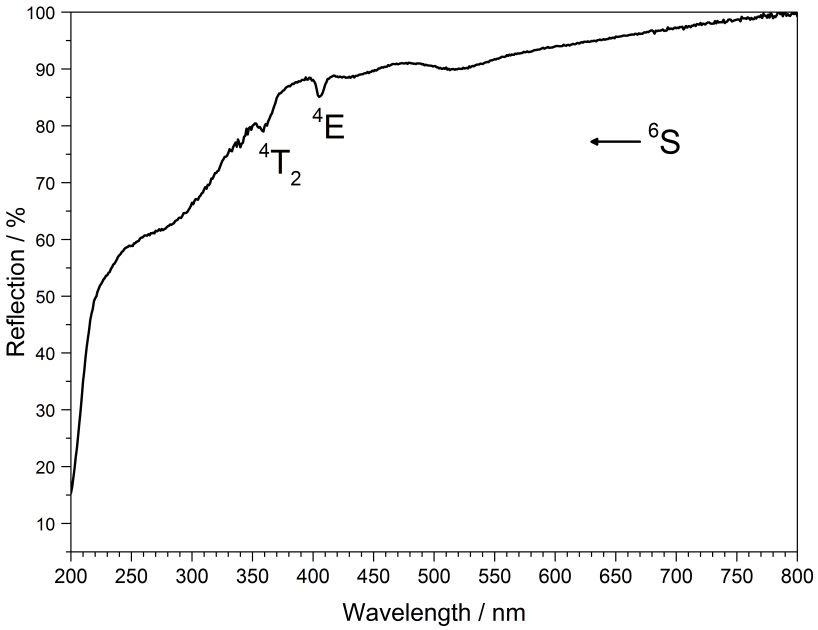

Figure 7.10: UV–Vis spectrum of $(NH_4)_2Mn(II)[B_2P_3O_{11}(OH)_2]Cl$.

7.1.7 Magnetic Properties

Since the crystal structure determination based on single-crystal data revealed the presence of several protons the valence state of manganese could only be postulated and in a first approach be confirmed by UV-Vis spectroscopy (Chapter 7.1.6.2). A reliable proof of the valence and spin state of manganese should be delivered by a magnetic susceptibility measurement of $(NH_4)_2Mn(II)[B_2P_3O_{11}(OH)_2]Cl$ recorded in a field of 1000 Oe over the temperature range of $1.8\,K < T < 400\,K$ is shown in Figure 7.11.

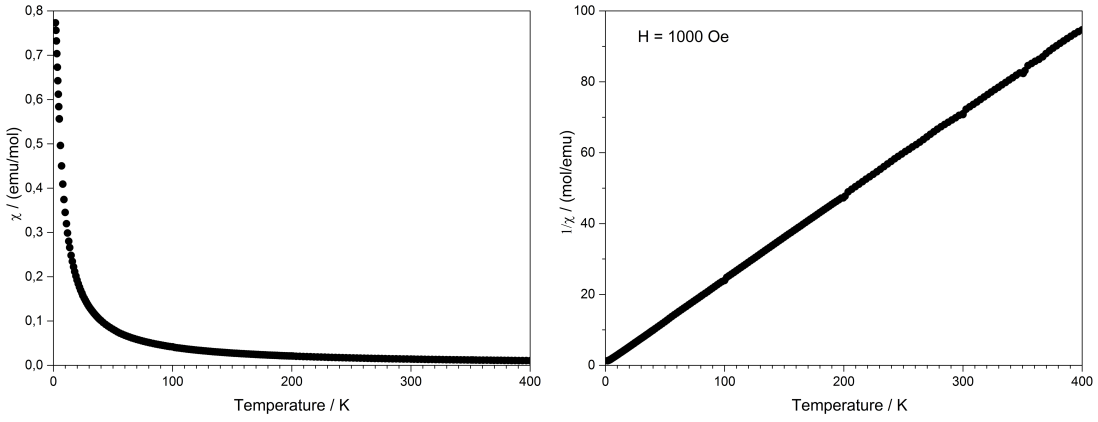

Figure 7.11: Temperature dependence of the magnetic susceptibility χ of $(NH_4)_2Mn(II)[B_2P_3O_{11}(OH)_2]Cl$.

The molar susceptibility obeys *Curie's* law ($\chi_m = C/T$) very well in the whole temperature range with a *Curie* constant of $C = 4.1897$ emu·mol^{-1}·K^{-1}. The *Curie* con-

stant corresponds to an effective magnetic moment per Mn^{2+} ion of $\mu_{eff} = 5.79\,\mu_B$, which is close to the theoretical value of $\mu_{eff} = 5.92\,\mu_B$ and fits very well in the range of experimental effective magnetic moments of *high-spin* Mn^{2+} ions (5.65–6.10 μ_B) [80].

7.1.8 Thermal Analysis

The thermal behaviour of $(NH_4)_2Mn(II)[B_2P_3O_{11}(OH)_2]Cl$ was investigated between room temperature and 1400 °C (Figure 7.12) and shows a reasonable stability against thermal treatment. The thermogravimetric curve shows a single step of mass loss of 21.1 wt% in the temperature range between 340 and 640 °C. Assuming that along with one mole of NH_4Cl a further mole of NH_3 and 1.5 moles of H_2O evaporate (theor. mass loss: 21.6 wt%) a composition of $Mn(II)[B_2P_3O_{11}(OH)]$ might be expected. With further increasing temperature and maintaining the sample at 1400 °C further mass loss of 2.6 wt% is observed. X-ray powder diffraction analysis revealed $MnPO_4$ as crystalline product after the treatment at 1400 °C competing with an intense background. The latter might be due to amorphous B_2O_3 and P_2O_5 which show a strong tendency to become amorphous at higher temperatures.

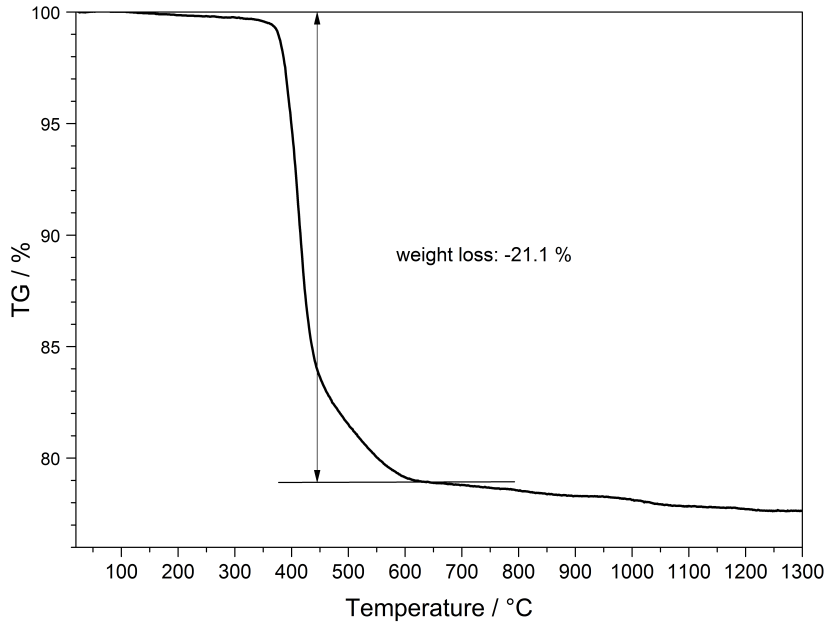

Figure 7.12: Thermogravimetric analysis of $(NH_4)_2Mn(II)[B_2P_3O_{11}(OH)_2]Cl$.

Heating the compound up to 600 °C under nitrogen atmosphere a crystalline intermediate was obtained. As main and side product $Mn_2P_2O_7$ [238] and BPO_4 [239] were identified via X-ray powder diffraction analysis (Figure 7.13).

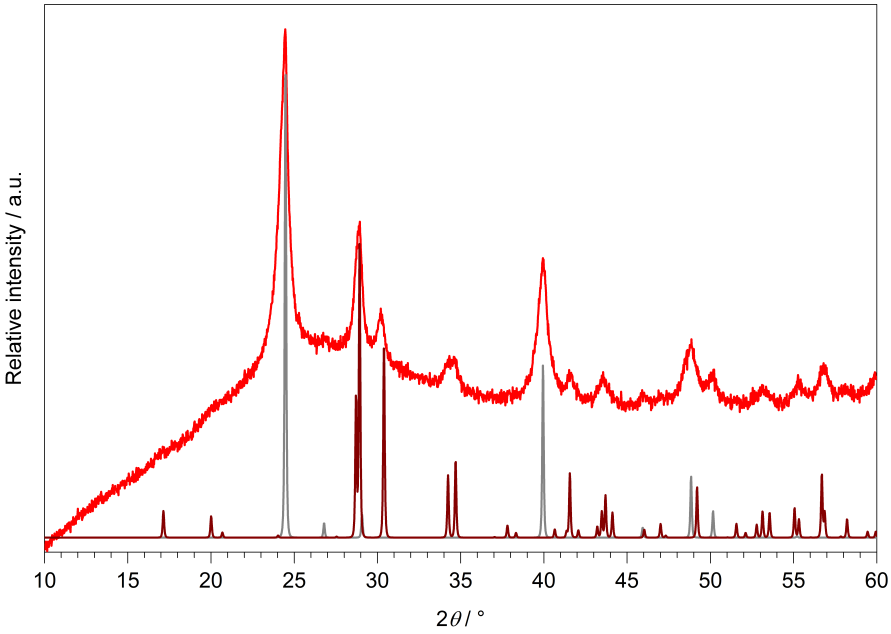

Figure 7.13: X-ray powder diffraction pattern of BPO_4 [239] and $Mn_2P_2O_7$ [238] (red) after heating $(NH_4)_2Mn(II)[B_2P_3O_{11}(OH)_2]Cl$ up to 600 °C under N_2 atmosphere and calculated powder diffraction patterns from single-crystal data of BPO_4 [239] (grey) and $Mn_2P_2O_7$ [238] (brown).

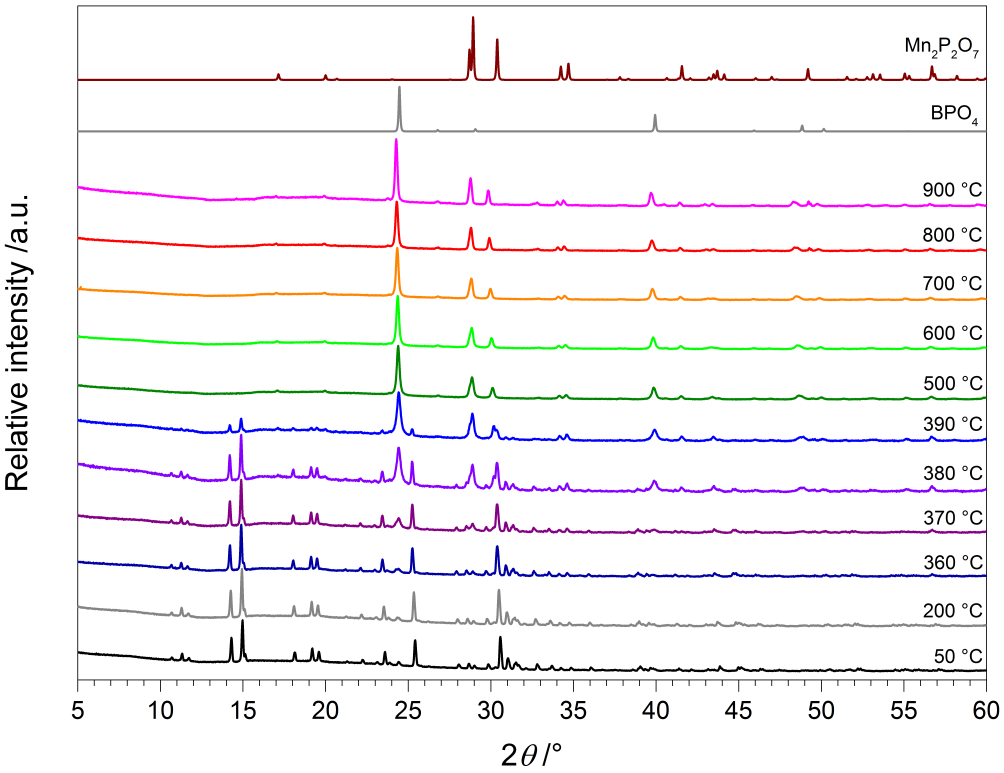

Figure 7.14: Temperature-dependent X-ray powder diffraction patterns of $(NH_4)_2Mn(II)[B_2P_3O_{11}(OH)_2]Cl$ recorded between 50 and 900 °C and calculated powder diffraction patterns from single-crystal data of BPO_4 [239] (grey) and $Mn_2P_2O_7$ [238] (brown).

Temperature-dependent X-ray powder diffraction (Figure 7.14) confirms that the title compound is stable up to 360 °C. At higher temperatures the formation of $Mn_2P_2O_7$ and BPO_4 is confirmed. It can be concluded that instead of forming $Mn(II)[B_2P_3O_{11}(OH)]$ the borophosphate decomposes to form several low-molecular decomposition products (Equation 7.1).

$$(NH_4)_2Mn[B_2P_3O_{11}(OH)_2]Cl \xrightarrow[N_2]{\Delta} NH_4Cl + NH_3 + 1.5H_2O + 0.5\,Mn_2P_2O_7 + 2\,BPO_4 \tag{7.1}$$

Further heating (T>600 °C) leads to the formation of $MnPO_4$ and presumably amorphous portions of B_2O_3 and P_2O_5 due to an intense background (Figure 7.15). The latter evaporate slowly, which leads to a further weight loss of 2.6 wt%.

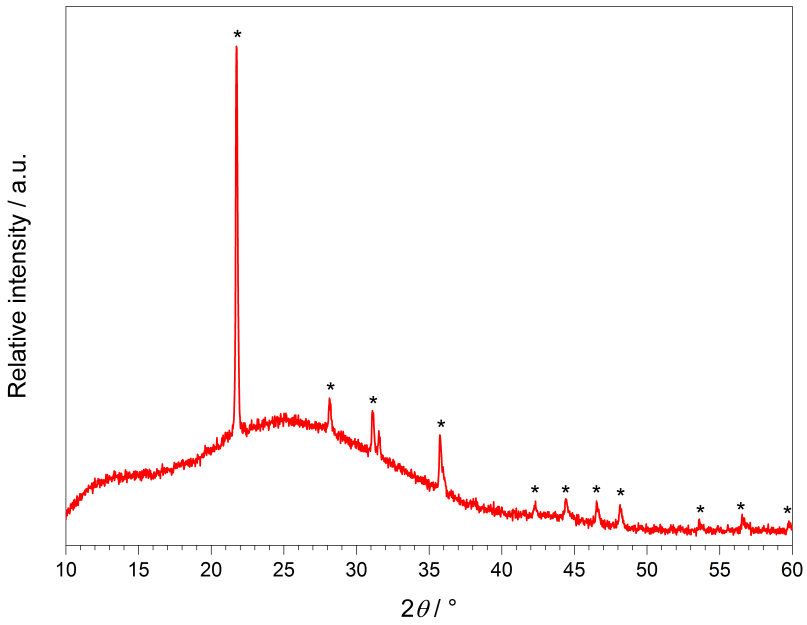

Figure 7.15: X-ray powder diffraction pattern of $MnPO_4$ (red) after the heating process of the thermogravimetric analysis of $(NH_4)_2Mn(II)[B_2P_3O_{11}(OH)_2]Cl$ at 1400 °C under N_2 atmosphere. The calculated diffraction angles of $MnPO_4$ are marked with an asterix (*).

7.1.9 Discussion

$(NH_4)_2Mn(II)[B_2P_3O_{11}(OH)_2]Cl$ was obtained phase pure as a new representative of the borophosphate family. The crystal structure was determined and refined via a single-crystal structure analysis and *Rietveld* refinement, respectively. The polyanion exhibits a cyclic pentameric $^2_\infty[B_2P_3\Phi_{13}]$ ($\Phi = O$, OH) unit with an O:OH ratio of 11:2. The oB vierer-single ring is formed by two $B\Phi_4$ and three $P\Phi_4$ ($\Phi = O$, OH) tetrahedra. It represents a novel FBU embedded in a lB vierer-single layer. Up to now borophosphates with a B:P ratio of 2:3 and an O:OH ratio of 11:2 always revealed a chain structure. Layered structures were accompanied by an O:OH ratio of 12:1. In-between the parallel borophosphate layers NH_4^+, Mn^{2+} and Cl^- ions are located. Due to the presence of several protons a number of moderately strong and several weak hydrogen bonds could be determined, which contribute to the stability of the title compound up to 340 °C as well as the two-dimensional layered structure. Moreover, the electrostatic consistency of the structure model could be proofed via MAPLE calculations. The spin and valence state of *hs* Mn^{2+} (d^5) were determined by the magnetic susceptibility measurement. Transitions in *hs* d^5 ions are spin and parity forbidden, but in $(NH_4)_2Mn(II)[B_2P_3O_{11}(OH)_2]Cl$ Mn^{2+} is in a slightly octahedrally distorted coordination environment. Thus, the selection rules do not apply that strongly, which explains the weak absorption in the UV-Vis spectrum in the visible range. Additionally, the Mn–O distances of the coordination sphere lie between 2.12–2.28 Å($\varnothing = 2.18$ Å), which are to expect for *hs* comlexes ($d(Mn^{2+}\text{–}O) \approx 2.18$ Å[60]), and are larger than in *low-spin* compounds ($d(Mn^{2+}\text{–}O) \approx 2.02$ Å[60]). In an octahedral environment the presence of d electrons in the e_g orbitals leads to a repulsion of the ligands due to the orientation of the $d_{x^2-y^2}$ and d_{z^2} along the coordination axes. Thus, the ionic radii of the metal expand ($r_{Mn^{2+},hs} = 0.83$ Å $> r_{Mn^{2+},ls} = 0.67$ Å[60]) [42].

7.2 Diammonium Borophosphate $(NH_4)_2[B_2P_3O_{11}(OH)]$

Borophosphates with a B:P ratio of 2:3 comprise a large number of compounds. Up to now all of them have in common at least one metal cation and a total number of thirteen oxygen atoms, whereas most of them are single or double protonated [13]. $(NH_4)_2[B_2P_3O_{11}(OH)]$ exhibits a closely related sum formula compared to its sister compound $(NH_4)_2Mn(II)[B_2P_3O_{11}(OH)_2]Cl$ (Chapter 7.1). Thus, it does not surprise that both possess the same oB vierer-single ring as FBU, forming parallel layers. $(NH_4)_2[B_2P_3O_{11}(OH)]$ reveals merely two ammonia ions as cations and thus exhibits for charge compensation an O:OH ratio of 11:1 and in total only 12 oxygen atoms. Besides Mn^{2+}, one Cl^- and one OH^- are removed, respectively. So far $(NH_4)_2[B_2P_3O_{11}(OH)]$ represents the first borophosphate with a B:P ratio of 2:3 and an O:OH ratio of 11:1. The results of this chapter will be published in a scientific journal [240].

7.2.1 Synthesis

$(NH_4)_2[B_2P_3O_{11}(OH)]$ was synthesised under hydrothermal conditions. A mixture of 792.8 mg (6.004 mmol) $(NH_4)_2HPO_4$, 247.7 mg (4.006 mmol) H_3BO_3 and 0.77 mL H_3PO_4 (85 %) was transferred into a 10 mL *Teflon* autoclave and was kept at 180 °C. After eight days a colourless solid was obtained. The product was washed several times with warm water, filtered off and dried in air overnight. $(NH_4)_2[B_2P_3O_{11}(OH)]$ was obtained as a colourless crystalline powder.

$(NH_4)_2[B_2P_3O_{11}(OH)]$ was doped with 5 % Eu^{3+} and Tb^{3+}, respectively, by adding the corresponding amount of $Ln(NO_3)_3{\cdot}5H_2O$ (Ln = Eu, Tb). After the same reaction conditions as above $(NH_4)_2[B_2P_3O_{11}(OH)]$:$Ln^{3+}$ (Ln = Eu, Tb) were obtained as colourless powders.

7.2.2 X-Ray Powder Diffraction

The phase purity of all samples was checked by X-ray powder diffraction. A *Rietveld* analysis (Figure 7.16) confirmed the formation of phase pure $(NH_4)_2[B_2P_3O_{11}(OH)]$. The structure model was refined to very good residuals of $R_p = 0.041$, $R_{wp} = 0.061$ and $\chi^2 = 1.90$.

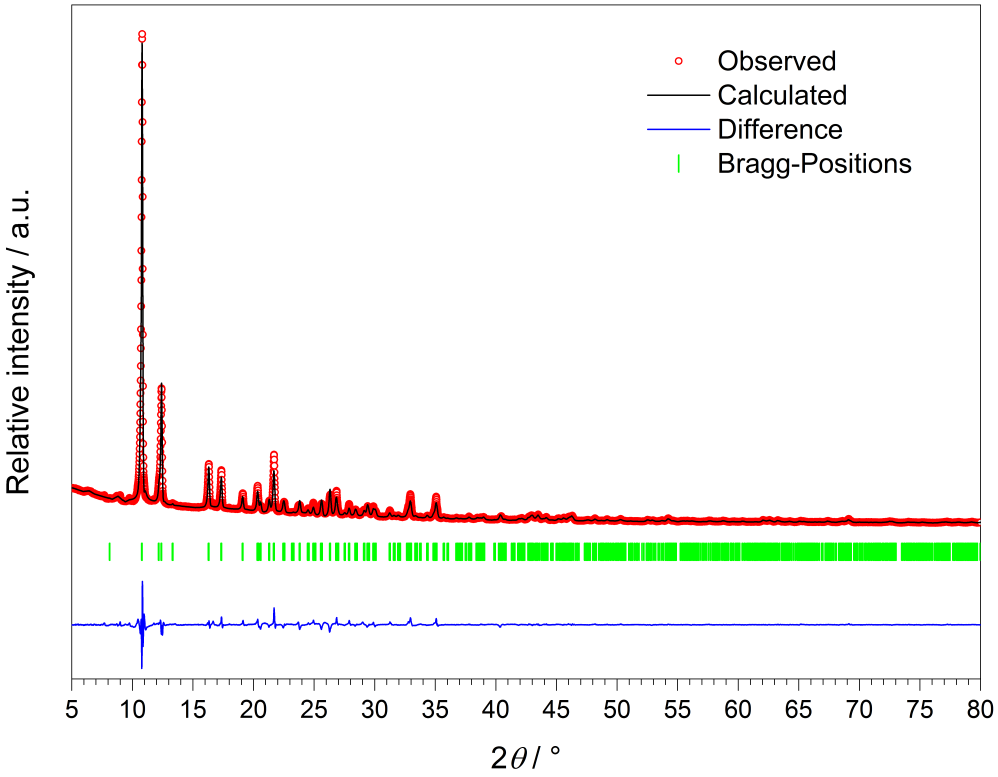

Figure 7.16: X-ray powder diffraction pattern and result of the *Rietveld* refinement based on the structure model of $(NH_4)_2[B_2P_3O_{11}(OH)]$ obtained from single-crystal data.

7.2.3 Crystal Structure Determination

A colourless single-crystal of $(NH_4)_2[B_2P_3O_{11}(OH)]$ with a size of 0.018 × 0.026 × 0.102 mm^3 was isolated and mounted on a *MicroMount*. The collection of the crystal data was run on a Bruker D8 Venture single-crystal diffractometer using Mo radiation. A multi-scan absorption correction was subsequently performed. $(NH_4)_2[B_2P_3O_{11}(OH)]$ crystallises in the orthorhombic space group $P2_12_12_1$ with the lattice parameters $a = 4.509(3)$ Å, $b = 14.490(11)$ Å and $c = 16.401(12)$ Å.

14522 reflections were collected. Out of 1682 independent reflections 1322 were observed ($F_o^2 > 2\sigma\ (F_o^2)$, R_{int} = 0.1309). The crystallographic data, the parameters of the measurement and refinement are summarised in Table 7.8. The structure was solved by direct methods and refined by full matrix least-squares technique using the programs SHELXS-97 and SHELXTL-97 [21, 22]. The anisotropic refinement revealed *R*-values of $R1 = 0.0457$ and $wR2 = 0.0930$. The B, P, O and N atoms could be clearly located. Hydrogen atoms were added geometrically. The refined atomic coordinates, anisotropic displacement parameters, selected interatomic distances and angles and hydrogen bonds are summarised in Tables 7.9 to 7.12.

Table 7.8: Single-crystal refinement parameters of $(NH_4)_2[B_2P_3O_{11}(OH)]$; standard deviations in brackets

Sum formula	$(NH_4)_2[B_2P_3O_{11}(OH)]$
Temperature / K	298(2)
Molar weight / g·mol^{-1}	343.62
Crystal system	orthorhombic
Space group	$P2_12_12_1$ (no. 19)
Crystal shape	needle
Crystal size / mm^3	0.018 × 0.026 × 0.102
Colour	colourless
a / Å	4.509(3)
b / Å	14.490(11)
c / Å	16.401(12)
Volume / Å^3	1071.7(14)
Z	4
Calculated density D_x / g·cm^{-3}	2.130
Absorption coefficient μ / mm^{-1}	0.626
F(000)	696
Radiation (λ / Å)	Mo-K_α (0.7093)
Diffractometer	Bruker D8 Venture
Absorption correction	multi-scan
Transmission factor (min./max.)	0.5617 / 0.7199
Index range h|k|l (min./max.)	-5/5 | -16/16 | -18/18
Theta range / °	$2.48 \leq \theta \leq 24.00$
Reflections collected	14522
Independent reflections	1682
Observed reflections	1322 ($F_o^2 > 2\sigma\ (F_o^2)$)
R_{int}	0.1309
Refined parameters	200
R_σ	0.0728
$R1$ (all data)	0.0457
$wR2$ (all data)	0.0930
Flack parameter	0.05(17)
Weighting scheme	$w^{-1}=\sigma^2\ F_o^2 + (0.0461\ P)^2 + 0.2782\ P$; $P = (F_o^2 + 2\ F_c^2)/3$
GooF	1.037
Residual electron density (min./max.) / e$^-$·Å^{-3}	-0.47/0.38

Table 7.9: Refined atomic coordinates, *Wyckoff* symbols and isotropic displacement parameters U_{eq} / Å^2 in $(NH_4)_2[B_2P_3O_{11}(OH)]$; standard deviations in brackets

Atom	*Wyckoff* symbol	x	y	z	U_{eq}
P1	4*a*	0.1083(3)	0.24777(11)	0.40040(8)	0.0139(4)
P2	4*a*	−0.2579(3)	0.00008(10)	0.36214(9)	0.0160(4)
P3	4*a*	0.3125(3)	−0.15455(10)	0.55036(10)	0.0145(4)
B1	4*a*	0.6029(13)	0.1549(5)	0.4523(4)	0.0153(16)
B2	4*a*	−0.1912(14)	−0.1566(4)	0.4517(4)	0.0149(15)
$O_{br}1$	4*a*	−0.2204(7)	0.2184(2)	0.4028(2)	0.0145(9)
$O_{br}2$	4*a*	0.1562(8)	0.3303(2)	0.4597(2)	0.0164(9)
$O_{br}3$	4*a*	0.2911(7)	0.1659(2)	0.4322(2)	0.0153(9)
$O_{br}4$	4*a*	−0.3112(8)	0.0587(2)	0.4397(2)	0.0174(9)
$O_{br}5$	4*a*	−0.1026(8)	−0.0892(2)	0.3911(2)	0.0153(9)
$O_{br}6$	4*a*	0.4889(8)	−0.1466(3)	0.4702(2)	0.0139(9)
$O_{br}7$	4*a*	0.3633(7)	−0.2529(2)	0.5851(2)	0.0144(9)
$O_{br}8$	4*a*	−0.0191(8)	−0.1456(3)	0.5283(2)	0.0152(9)
$O_{term}1$	4*a*	0.1867(8)	0.2793(2)	0.3171(2)	0.0169(9)
$O_{term}2$	4*a*	−0.5309(8)	−0.0200(3)	0.3144(2)	0.0240(11)
$O_{term}3$	4*a*	0.3891(9)	−0.0856(2)	0.6132(2)	0.0192(10)
O_H1	4*a*	−0.0358(8)	0.0478(3)	0.3051(2)	0.0193(10)
N1	4*a*	0.8881(12)	0.0214(4)	0.6411(4)	0.0263(13)
N2	4*a*	−0.3136(13)	0.2778(4)	0.2137(4)	0.0353(15)
H1	4*a*	0.169(5)	0.026(4)	0.302(4)	0.050
H2	4*a*	0.717(9)	−0.020(4)	0.634(4)	0.050
H3	4*a*	1.079(7)	−0.008(4)	0.630(4)	0.050
H4	4*a*	0.908(15)	0.028(5)	0.7001(10)	0.050
H5	4*a*	0.879(15)	0.081(2)	0.613(3)	0.050
H6	4*a*	−0.136(8)	0.277(5)	0.248(3)	0.050
H7	4*a*	−0.473(10)	0.258(4)	0.251(3)	0.050
H8	4*a*	−0.279(14)	0.233(3)	0.170(3)	0.050
H9	4*a*	−0.304(15)	0.335(2)	0.182(3)	0.050

O_{br} = bridging oxygen atom; O_{term} = terminal oxygen atom; O_H = hydroxyl group

Table 7.10: Anisotropic displacement parameters U_{ij} / Å^2 in $(NH_4)_2[B_2P_3O_{11}(OH)]$; standard deviations in brackets

Atom	U_{11}	U_{22}	U_{33}	U_{12}	U_{13}	U_{23}
P1	0.0128(8)	0.0098(8)	0.0190(9)	−0.0004(8)	−0.0002(6)	−0.0025(7)
P2	0.0151(8)	0.0073(7)	0.0256(9)	0.0002(8)	0.0013(7)	0.0003(7)
P3	0.0126(8)	0.0064(8)	0.0243(10)	−0.0004(7)	−0.0011(8)	−0.0002(7)
B1	0.013(4)	0.012(4)	0.020(4)	0.000(3)	0.010(3)	0.002(3)
B2	0.015(3)	0.011(3)	0.019(4)	0.003(3)	−0.003(4)	0.001(3)
$O_{br}1$	0.016(2)	0.013(2)	0.014(2)	0.0015(16)	0.0001(18)	0.0003(17)
$O_{br}2$	0.022(2)	0.008(2)	0.020(2)	−0.0026(17)	0.0031(19)	−0.0045(18)
$O_{br}3$	0.011(2)	0.0061(19)	0.028(2)	0.0019(17)	0.0004(18)	0.0014(18)
$O_{br}4$	0.024(2)	0.0051(19)	0.023(2)	−0.0033(17)	0.001(2)	0.0053(18)
$O_{br}5$	0.016(2)	0.005(2)	0.026(2)	0.0002(19)	0.005(2)	0.0020(16)
$O_{br}6$	0.0064(19)	0.013(2)	0.022(2)	0.001(2)	0.0024(19)	0.0005(18)
$O_{br}7$	0.0172(19)	0.0067(19)	0.019(2)	0.0000(19)	0.0008(16)	0.0003(19)
$O_{br}8$	0.014(2)	0.014(2)	0.017(2)	−0.004(2)	0.0010(19)	0.0009(19)
$O_{term}1$	0.018(2)	0.017(2)	0.016(2)	0.0006(17)	0.0035(18)	−0.0022(17)
$O_{term}2$	0.018(2)	0.021(3)	0.033(3)	−0.002(2)	−0.002(2)	0.0040(19)
$O_{term}3$	0.021(2)	0.009(2)	0.027(2)	−0.0090(19)	−0.005(2)	0.0003(17)
O_H1	0.016(2)	0.013(2)	0.028(3)	0.0049(19)	0.005(2)	0.0040(19)
N1	0.025(3)	0.016(3)	0.038(3)	−0.001(3)	0.000(3)	0.000(3)
N2	0.023(3)	0.056(4)	0.028(4)	0.001(3)	0.004(3)	−0.004(3)

Table 7.11: Selected interatomic distances / Å and angles / ° in $(NH_4)_2[B_2P_3O_{11}(OH)]$; standard deviations in brackets

B–O_{br}	1.450(7)–1.485(7)
P–O_{br}	1.535(4)–1.557(4)
P–O_{term}	1.483(4)–1.487(4)
P–O_H	1.534(4)
B–O_{br}–P	105.6(2)–135.3(3)
O–P–O	102.2(1)–115.1(2)
O–B–O	103.4(4)–112.2(4)

Table 7.12: Distances / Å and angles / ° of the hydrogen bonds in $(NH_4)_2[B_2P_3O_{11}(OH)]$; *D*: Donor, *A*: Acceptor

D–*H*	*A*	$d(D–H)$	$d(H–A)$	$\sphericalangle(DHA)$	$d(D–A)$
O_H1-H1	$O_{term}2$	0.980	1.521	166.77	2.485
N1-H2	$O_{term}3$	0.982	1.794	173.17	2.771
N1-H3	$O_{term}3$	0.981	1.812	168.06	2.778
N1-H4	$O_{term}2$	0.977	1.960	165.32	2.915
N1-H4	O_H1	0.977	2.647	122.82	3.281
N1-H5	$O_{br}2$	0.977	2.022	149.35	2.906
N1-H5	$O_{term}1$	0.977	2.486	120.96	3.104
N2-H6	$O_{term}1$	0.980	1.843	176.48	2.823
N2-H7	$O_{term}1$	0.981	1.906	153.78	2.820
N2-H8	$O_{br}7$	0.980	2.348	118.89	2.949
N2-H9	$O_{term}2$	0.976	2.231	140.40	3.048
N2-H9	$O_{br}5$	0.976	2.452	132.38	3.193
N2-H9	$O_{br}6$	0.976	2.650	124.71	3.305

7.2.4 Crystal Structure Description

$(NH_4)_2[B_2P_3O_{11}(OH)]$ crystallises in a new structure type in the orthorhombic space group $P2_12_12_1$ with four formula units per unit cell. All atoms are located on the general *Wyckoff* position 4*a*. The anionic partial structure of $(NH_4)_2[B_2P_3O_{11}(OH)]$ consists of infinite layers of corner-sharing borate, phosphate and hydroxo-phosphate tetrahedra (Figure 7.17).

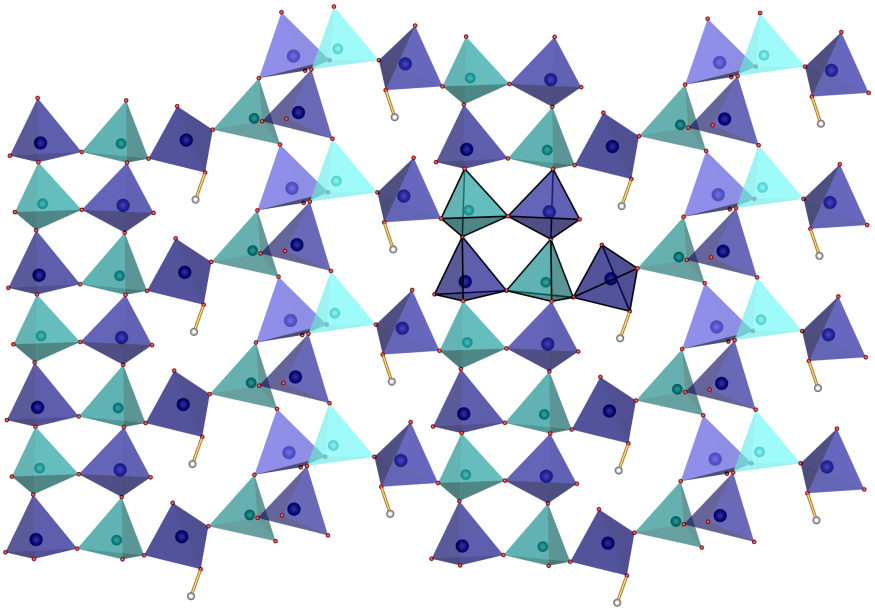

Figure 7.17: LB zweier-single layered anionic partial structure of $(NH_4)_2[B_2P_3O_{11}(OH)]$; FBU highlighted; phosphate tetrahedra blue, borate tetrahedra turquoise, hydrogen white.

No P–O–P connections are observed as in $(NH_4)_2$Mn(II)$[B_2P_3O_{11}(OH)_2]$Cl (see Chapter 7.1) or other borophosphates [13]. The polyanion is constructed by cyclic pentameric $^2_\infty[B_2P_3\Phi_{12}]$ (Φ = O, OH) units comprising a B:P ratio of 2:3. The lB zweier-single layer contains an oB vierer-single ring as FBU (Figure 7.18), which was observed in $(NH_4)_2$Mn(II)$[B_2P_3O_{11}(OH)_2]$Cl [122] for the first time. Formed by two $B\Phi_4$ and three $P\Phi_4$ (Φ = O, OH) tetrahedra it can be illustrated with the descriptor 5□:<4□>□ [13, 82, 83, 113].

As mentioned in Chapter 7.1 up to now all protonated borophosphates with a B:P ratio of 2:3 reveal connection patterns with B–O–B linking in the anionic partial structures as oB dreier-single rings and olB dreier-single rings. Furthermore, the anionic partial structure always consisted of $[B_2P_3\Phi_{13}]$ (Φ = O, OH) layers or chains which exhibited an O:OH ratio of 11:2 or 12:1 [13, 122]. In $(NH_4)_2[B_2P_3O_{11}(OH)]$ the O:OH ratio is reduced to 11:1 which has not been observed yet in ammonia borophosphates. Charge compensation leads to the elimination of a hydroxyl group

due to the absence of an additional metal cation.

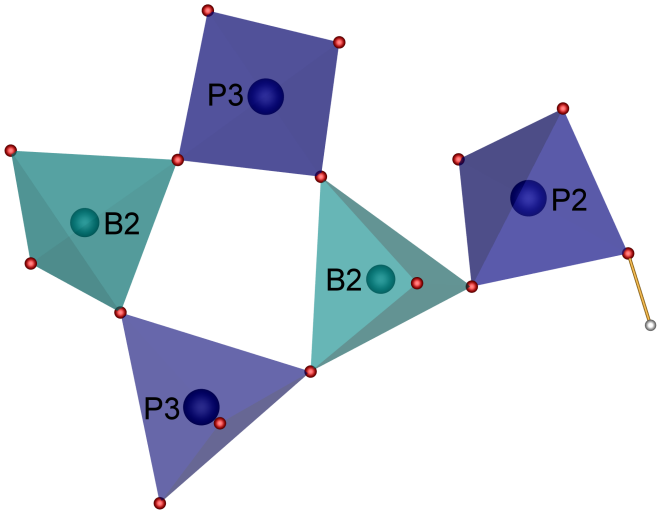

Figure 7.18: FBU as an oB vierer-single ring 5□:<4□>□ of $(NH_4)_2[B_2P_3O_{11}(OH)]$; phosphate tetrahedra blue, borate tetrahedra turquoise, hydrogen white.

Both B and P atoms are coordinated tetrahedrally by either oxygen atoms or hydroxyl groups. B–O bond lengths in the borate tetrahedra range between 1.45 and 1.49 Å whereas P–O bond lengths in the phosphate tetrahedra lie between 1.48 and 1.56 Å. The bond length P–O_H is 1.53 Å. P–O_{br} distances range between 1.54 and 1.56 Å, whereas P–O_{term} distances lie between 1.48 and 1.49 Å. These values correspond to typical data found for other borophosphates [122, 144, 224, 225, 228]. B–O_{br}–P angles range between 106 and 135 °, whereas O–B–O and O–P–O angles lie between 103–112° (Ø = 110°) and 106–115° (Ø = 109°), respectively. Selected bond lengths and angles of $(NH_4)_2[B_2P_3O_{11}(OH)]$ are listed in Table 7.11.

The calculation of deviation of tetrahedra from ideal symmetry was applied by the method of *Balić-Žunić* and *Makovicky* [35, 36]. The five crystallographically different borate, phosphate and hydroxo-phosphate tetrahedra feature the values −0.36 % (B1), −0.24 % (B2), −0.19 % (P1), −0.32 % (P2) and −0.14 % (P3), which are similar to tetrahedra in other compounds [97, 98, 129, 187, 189–191] and can be classified as regular.

The NH_4^+ ions are located between the parallel and corrugated borophosphate layers (Figure 7.19) and form numerous hydrogen bonds (Figure 7.20).

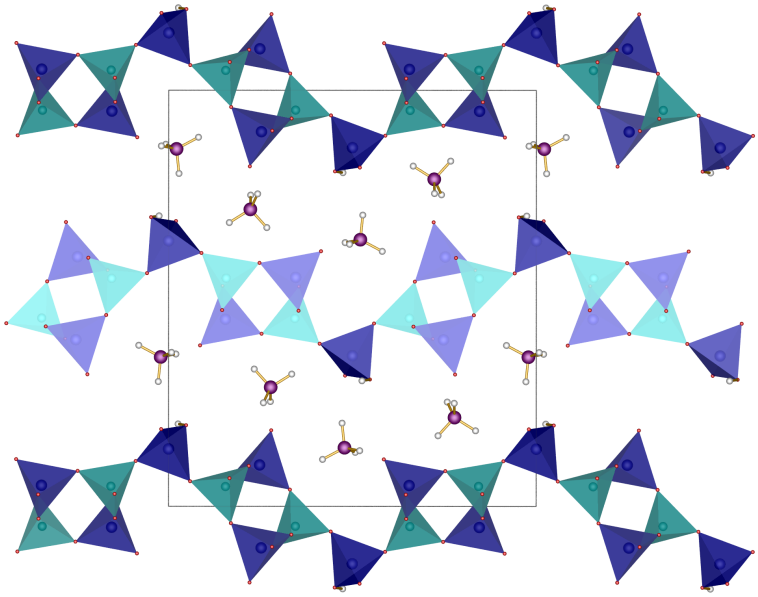

Figure 7.19: Layered crystal structure viewed along [100]; phosphate tetrahedra blue, borate tetrahedra turquoise, nitrogen violet, hydrogen white.

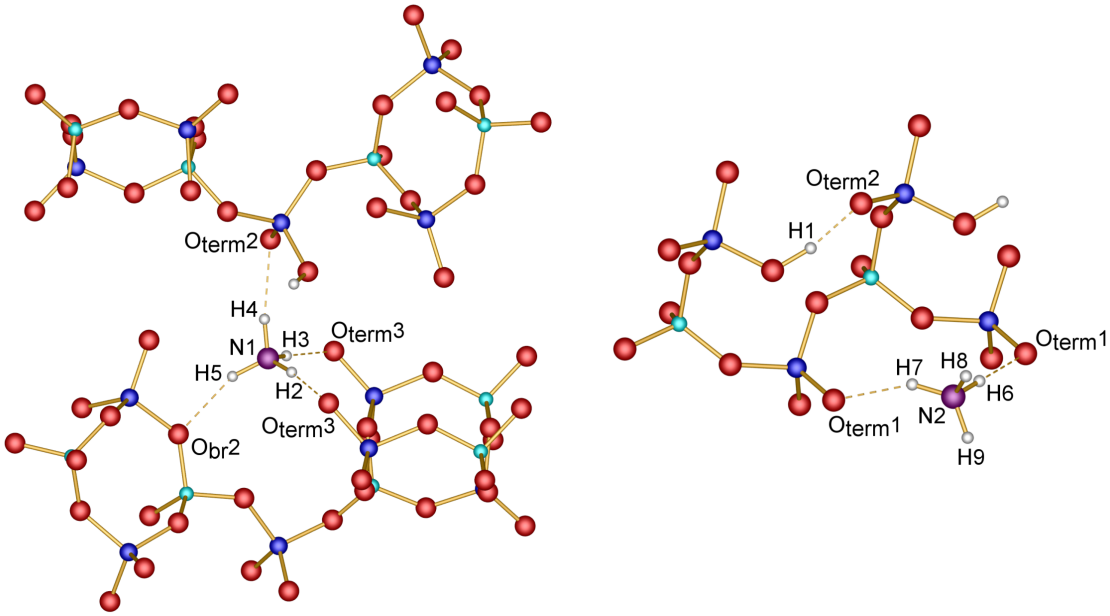

Figure 7.20: Moderately strong hydrogen bonds in $(NH_4)_2[B_2P_3O_{11}(OH)]$. Weak hydrogen bonds are omitted for clarity; phosphorus blue, boron turquoise, oxygen red, nitrogen violet, hydrogen white.

Exhibiting distances d(H–A) between 1.52 and 1.96 Å and between 2.02 and 2.65 Å, moderately strong and weak hydrogen bonds can be assigned, respectively [150]. Both exist between NH_4^+ ions and terminal and bridging oxygen atoms as well as between the hydroxyl group and a terminal oxygen atom (Table 7.12).

7.2.5 Electrostatic Calculations

The electrostatic consistency of the structure model was proved by calculations based on the MAPLE concept (Table 12.8) [32, 33, 152]. The MAPLE value of the structure model of $(NH_4)_2[B_2P_3O_{11}(OH)]$ deviates by 0.7 % from the sum of MAPLE values of chemically similar compounds. $(NH_4)_2[B_2P_3O_{11}(OH)]$ thus shows electrostatic consistency, as presented in Table 7.13.

Table 7.13: MAPLE calculations for $(NH_4)_2[B_2P_3O_{11}(OH)]$ [32, 33, 152]

$(NH_4)_2[B_2P_3O_{11}(OH)]$	$(NH_4)_2HPO_4$ [241] + B_2O_3 [154] + P_2O_5 [242]
MAPLE = 117968 kJ·mol^{-1}	MAPLE = 118780 kJ·mol^{-1}
$\Delta = 0.7$ %	

7.2.6 Spectroscopic Properties

7.2.6.1 IR Spectroscopy

The infrared spectrum of $(NH_4)_2[B_2P_3O_{11}(OH)]$ was recorded between 4000 and 400 cm^{-1} and is shown in Figure 7.21. The positions of the bands and the corresponding assignments are given in Table 7.14.

The bands at 3344 and 1645 cm^{-1} can be assigned to the stretching and deformation vibrations of the hydroxyl groups [120, 121, 226, 228, 232], while vibrations between 3310–2700 cm^{-1} and at 1443 cm^{-1} can be assigned to N–H stretching vibrations [120, 233, 234]. BO_4 vibrations can be found at 1157, 1126, 901, 879, 569, 534 and 500 cm^{-1}, whereas typical PO_4 vibrations range in the region between 1230 and 400 cm^{-1}. Characteristic bands of symmetric or asymmetric B–O–P stretching and bending vibrations are found at 866 (ν_{as}), 677 (ν_s), 652–638 (δ) and for δ(O–P–O) at 592 cm^{-1} [235, 236].

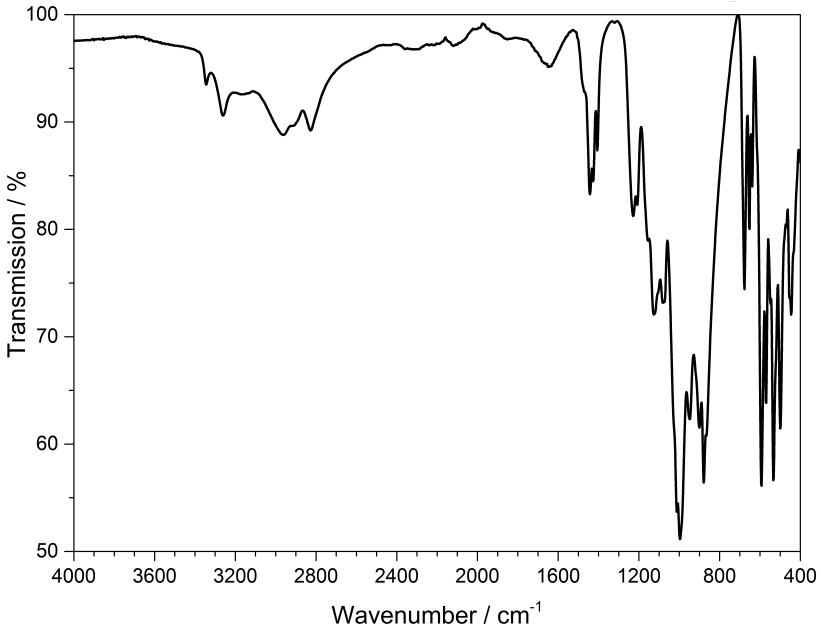

Figure 7.21: Infrared spectrum of $(NH_4)_2[B_2P_3O_{11}(OH)]$.

Table 7.14: Position / cm^{-1} and assignment of the IR bands in $(NH_4)_2[B_2P_3O_{11}(OH)]$

Position	Assignment
3344	ν(OH), δ(OH) [120, 121, 226, 228, 232]
3310–2700	ν(NH) [120, 233, 234]
1645	ν(OH), δ(OH) [120, 121, 226, 228, 232]
1443	δ(NH) [120, 233, 234]
1229, 1207, 1157, 1126	$\nu(BO_4)$, $\nu(PO_4)$ [235, 236]
1082, 1012, 997, 950	$\nu(PO_4)$ [235, 236]
901, 879	$\nu(BO_4)$ [235, 236]
866	ν_{as}(BOP) [235, 236]
677	ν_{s}(BOP) [235, 236]
652, 638	δ(BOP) [235]
592	δ(OPO) [236]
569, 534, 500	$\nu(BO_4)$ [235, 236]
446	$\nu(PO_4)$ [235, 236]

7.2.6.2 UV-Vis Spectroscopy

Despite the relatively large charge difference between NH_4^+ and Ln^{3+} (Ln = Eu, Tb) and the size of the respective radii ($r_{NH_4^+} = 1.43$ Å[243], $r_{Eu^{3+}} = 1.07$ Å[60], $r_{Tb^{3+}} = 1.04$ Å[60]) the optical properties of $(NH_4)_2[B_2P_3O_{11}(OH)]$ were investigated after doping it with 5.0 mol% Eu^{3+} and Tb^{3+} (synthesis see Chapter 7.2.1), respectively. The charge compensation due to the partial occupation of NH_4^+ lattice sites by Eu^{3+} and Tb^{3+} ions, respectively, is presumably accomplished by vacancies.

The UV-Vis reflection spectra of $(NH_4)_2[B_2P_3O_{11}(OH)]$:$Ln^{3+}$ (Ln = Eu, Tb) (Figures 7.22 and 7.23) show the typical absorption bands of the f–f transitions of Eu^{3+} and Tb^{3+} ions, according to the well-known energy level schemes [53, 64]. All transitions start from the respective ground states $^7F_0$ and $^7F_6$ with the electronic configuration [Xe]$4f^6$ and [Xe]$4f^8$, respectively. The corresponding assignments are listed in Tables 7.15 and 7.16. No significant deviations from the spectra of other inorganic salts of europium and terbium were detected and the spectra are in accordance with the colourless powders.

A broad band absorption revealing two maxima at 205 and 238 nm can be assigned to the LMCT (Figure 7.22). The splitting of the absorption is presumably due to two different chemical surroundings of Eu^{3+}.

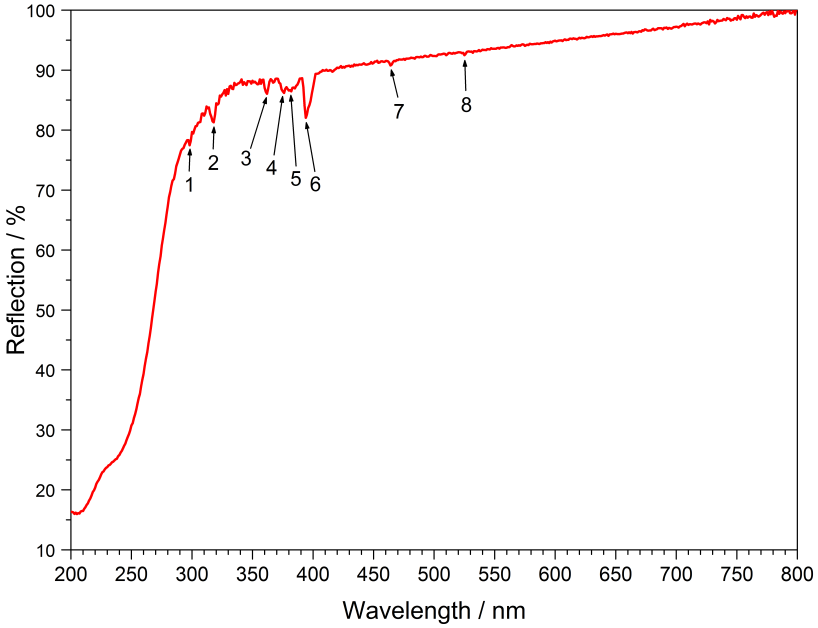

Figure 7.22: UV-Vis spectrum of $(NH_4)_2[B_2P_3O_{11}(OH)]$:$Eu^{3+}$.

Table 7.15: Absorption band energies for the strongest transitions in $(NH_4)_2[B_2P_3O_{11}(OH)]$:$Eu^{3+}$ and in free Eu^{3+} ions between 200 and 800 nm

Number	Absorption	λ / nm	$(NH_4)_2[B_2P_3O_{11}(OH)]$:$Eu^{3+}$ Energy / $10^3 \cdot cm^{-1}$	Free Eu^{3+} [53] Energy / $10^3 \cdot cm^{-1}$
1	$^7F_0 \rightarrow {}^5F_4$	298	33.6	33.6
2	$^7F_0 \rightarrow {}^5H_6$	318	31.4	31.5
3	$^7F_0 \rightarrow {}^5D_4$	362	27.6	27.6
4	$^7F_0 \rightarrow {}^5G_4$	376	26.6	26.7
5	$^7F_0 \rightarrow {}^5G_2$	382	26.2	26.3
6	$^7F_0 \rightarrow {}^5L_6$	394	25.4	25.4
7	$^7F_0 \rightarrow {}^5D_2$	464	21.6	21.5
8	$^7F_0 \rightarrow {}^5D_1$	525	19.0	19.0

A broader transition at about 266 nm can be assigned to the parity allowed $4f^8 \rightarrow 4f^7 5d^1$ transition of Tb^{3+} (Figure 7.23). Due to the overlap of this transition with the $^7F_6 \rightarrow {}^5I_4$ transition the exact minimum can not be determined.

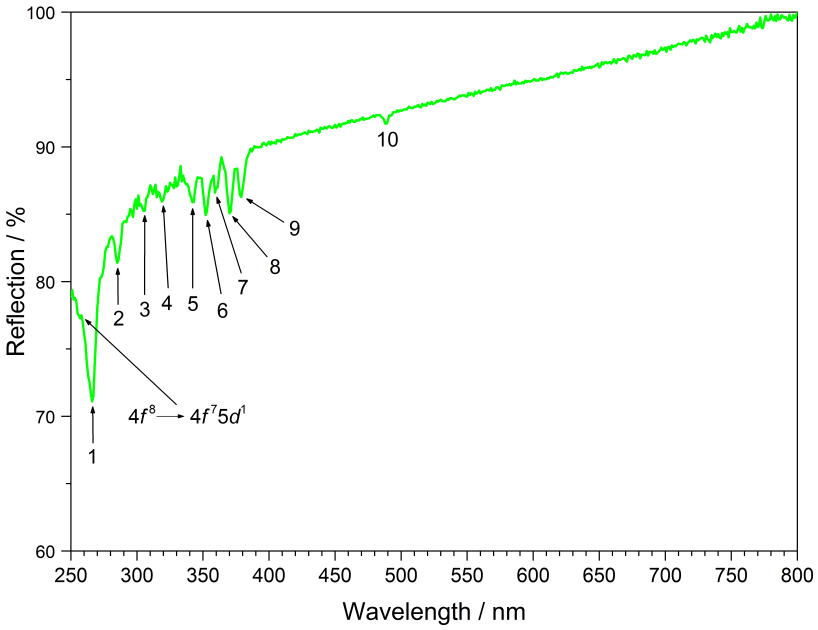

Figure 7.23: UV-Vis spectrum of $(NH_4)_2[B_2P_3O_{11}(OH)]$:$Tb^{3+}$.

Table 7.16: Absorption band energies for the strongest transitions in $(NH_4)_2[B_2P_3O_{11}(OH)]$:$Tb^{3+}$ and in free Tb^{3+} ions between 250 and 800 nm

Number	Absorption	λ / nm	$(NH_4)_2[B_2P_3O_{11}(OH)]$:$Tb^{3+}$ Energy / $10^3 \cdot cm^{-1}$	Free Tb^{3+} [64] Energy / $10^3 \cdot cm^{-1}$
1	$^7F_6 \rightarrow {}^5I_4$	266	37.6	37.5
2	$^7F_6 \rightarrow {}^5H_8$	285	35.1	35.0
3	$^7F_6 \rightarrow {}^5H_6$	306	32.7	33.0
4	$^7F_6 \rightarrow {}^5D_0$	319	31.3	31.2
5	$^7F_6 \rightarrow {}^5L_8$	342	29.2	29.2
6	$^7F_6 \rightarrow {}^5L_9$	352	28.4	28.5
7	$^7F_6 \rightarrow {}^5G_5$	359	27.9	27.8
8	$^7F_6 \rightarrow {}^5L_{10}$	370	27.0	27.1
9	$^7F_6 \rightarrow {}^5G_6$	379	26.4	26.4
10	$^7F_6 \rightarrow {}^5D_4$	489	20.5	20.5

7.2.6.3 Fluorescence Spectroscopy

The fluorescence spectra of $(NH_4)_2[B_2P_3O_{11}(OH)]$:$Ln^{3+}$ (Ln = Eu, Tb) (Figures 7.24 and 7.25) exhibit the characteristic f–f emissions of Eu^{3+} and Tb^{3+}, respectively [53, 64].

$(NH_4)_2[B_2P_3O_{11}(OH)]$:$Eu^{3+}$ reveals a weak red fluorescence under excitation with UV light at 254 nm. Between 230 and 310 nm a broad band in the excitation spectrum reveals an $O^{2-} \rightarrow Eu^{3+}$ charge transfer. Under excitation at 393 nm $(NH_4)_2[B_2P_3O_{11}(OH)]$:$Eu^{3+}$ exhibits sharp emission lines between 530 and 750 nm, which can be assigned to the $^5D_1 \rightarrow {}^7F_1$ (538 nm), $^5D_0 \rightarrow {}^7F_1$ (594 nm), $^5D_0 \rightarrow {}^7F_2$ (613 nm), $^5D_0 \rightarrow {}^7F_3$ (653 nm) and $^5D_0 \rightarrow {}^7F_4$ (699 nm) transitions [53]. The $^5D_0 \rightarrow {}^7F_1$ and $^5D_0 \rightarrow {}^7F_2$ transition are of similar intensity, which means that the surrounding of Eu^{3+} is close to inversion symmetry [55, 56]. The two ammonium ions are surrounded non-symmetrically by oxygen atoms. Instead of ammonia sites Eu^{3+} presumably occupies interstitial sites providing a nearly centrosymmetric environment between the corrugated borophosphate layers. The radius of Eu^{3+} ions is 1.07 Å[60], whereas the radius of NH_4^+ ions is about 1.43 Å[243] and N–O distances range between 2.77–3.30 Å. Hence, a movement of Eu^{3+} to a more narrow but higher symmetric site is possible. As a consequence the $^5D_0 \rightarrow {}^7F_1$ transition is more dominant over the $^5D_0 \rightarrow {}^7F_2$ transition. The presence of Eu_2O_3 could not be proven via X-ray powder diffraction. Additionally, a broader LMCT is expected, which was checked via UV-Vis spectroscopy of Eu_2O_3.

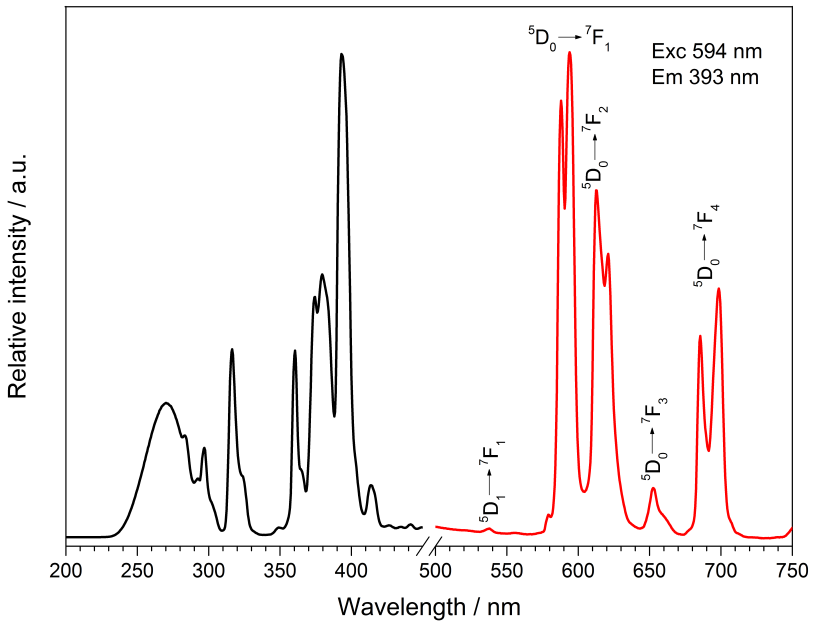

Figure 7.24: Excitation (black) and emission (red) spectrum of $(NH_4)_2[B_2P_3O_{11}(OH)]$:$Eu^{3+}$.

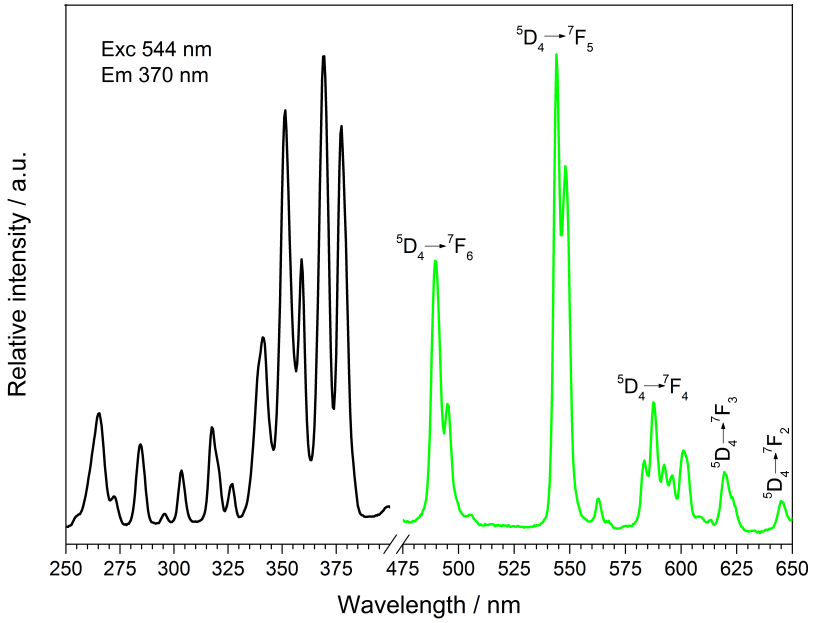

Figure 7.25: Excitation (black) and emission (green) spectrum of $(NH_4)_2[B_2P_3O_{11}(OH)]$:$Tb^{3+}$.

The excitation spectrum of $(NH_4)_2[B_2P_3O_{11}(OH)]$:$Tb^{3+}$ shows a broadened band between 250 and 280 nm, which reveals the parity allowed $4f^8 \rightarrow 4f^7 5d^1$ transition, which was also observed in the UV-Vis spectrum (Figure 7.23). Under excitation at 370 nm $(NH_4)_2[B_2P_3O_{11}(OH)]$:$Tb^{3+}$ exhibits sharp emission lines between 475 and 650 nm, which can be assigned to the $^5D_4 \rightarrow ^7F_6$ (490 nm), $^5D_4 \rightarrow ^7F_5$ (544 nm), $^5D_4 \rightarrow ^7F_4$ (588 nm), $^5D_4 \rightarrow ^7F_3$ (620 nm) and $^5D_4 \rightarrow ^7F_2$ (645 nm) transitions [64].

7.2.7 Thermal Analysis

The thermal behaviour of $(NH_4)_2[B_2P_3O_{11}(OH)]$ was investigated between room temperature and 1400 °C and shows a reasonable stability against thermal treatment up to 300 °C. The thermogravimetric curve (Figure 7.26) comprises several steps of mass loss (total mass loss: 38.7 wt%).

For a better understanding and more transparency a temperature-dependent X-ray powder diffraction (Figure 7.27) was carried out between room temperature and 950 °C. It confirms that the compound is stable up to approximately 330 °C. Temperature fluctuations of ± 30 °C may occur due to the different measurement settings. At higher temperatures the formation of $NH_4H(PO_3)_2$ (400–500 °C), PON (700–900 °C) and BPO_4 (340–950 °C) is ratified.

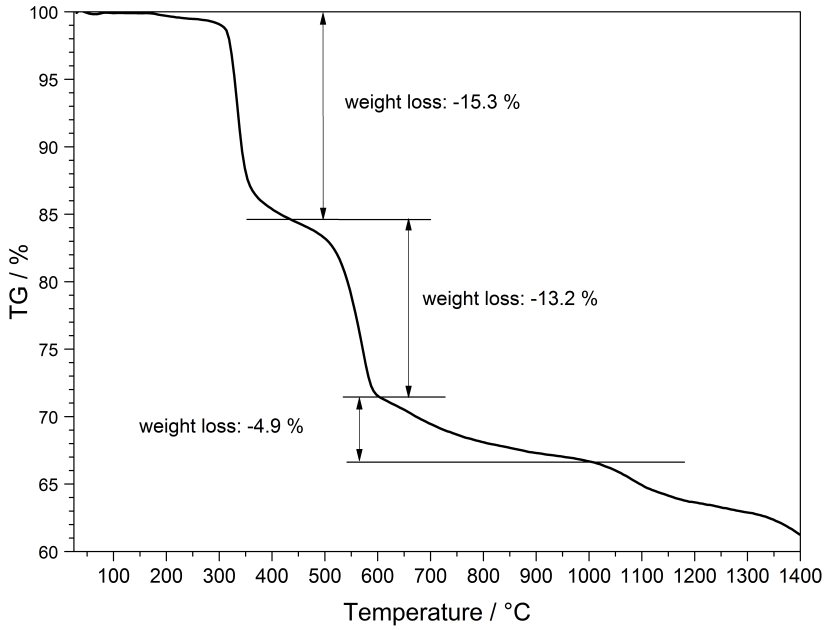

Figure 7.26: Thermogravimetric analysis of $(NH_4)_2[B_2P_3O_{11}(OH)]$.

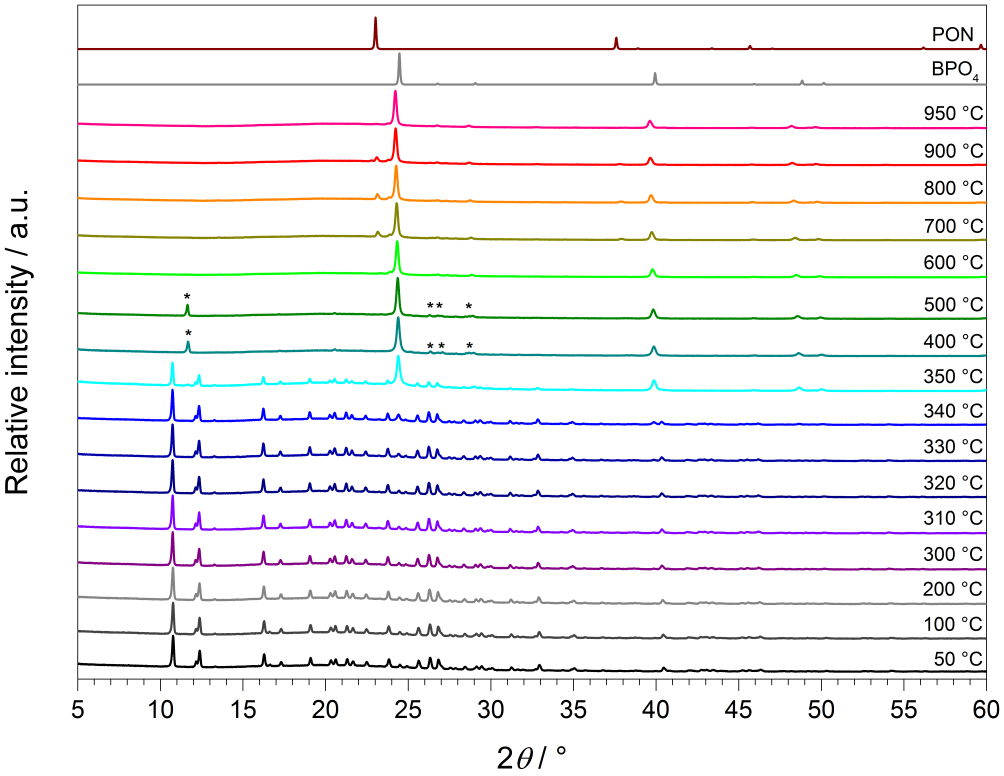

Figure 7.27: Temperature-dependent X-ray powder diffraction patterns of $(NH_4)_2[B_2P_3O_{11}(OH)]$ recorded between 50 and 950 °C and calculated powder diffraction patterns from single-crystal data of BPO_4 [239] (grey) and PON (brown); $NH_4H(PO_3)_2$ as a further intermediate phase is highlighted with an asterix (*).

Based on the temperature-dependent X-ray powder diffraction the following decomposition equation (Equation 7.2) can be suggested:

$$(NH_4)_2[B_2P_3O_{11}(OH)] \xrightarrow[N_2]{\Delta} NH_3 + HBO_2 + 2.5H_2O + 0.5\,P_2O_5 + PON + BPO_4 \quad (7.2)$$

The new insights of the temperature-dependent X-ray powder diffraction including the corresponding theoretical mass losses are summarised in Table 7.17.

Table 7.17: Decomposition process during the temperature-dependent X-ray powder diffraction of $(NH_4)_2[B_2P_3O_{11}(OH)]$ (Figure 7.27)

Compound	Temperature Range / °C	Theoretical Mass Loss / wt%
$(NH_4)_2[B_2P_3O_{11}(OH)]$	RT–350	
-(NH_3 + HBO_2)	≥350	17.7
$NH_4H(PO_3)_2$ + BPO_4	400–500	
-(0.5 P_2O_5 + 2.5 H_2O)	>500	33.8
PON + BPO_4	700–900	
-PON	>900	17.7
BPO_4	≥950	$\sum = 69.2$

The comparison with the thermogravimetric curve of $(NH_4)_2[B_2P_3O_{11}(OH)]$ shows that the total mass loss of 38.7 wt% is surpassed by far by the sum of the theoretical mass losses calculated by the temperature-dependent X-ray powder diffractogram (69.2 wt%). The first step of mass loss at 350 °C reveals 15.3 wt%, which matches well with the theoretical mass loss of one mole of NH_3 and HBO_2 (17.7 wt%), respectively. However, the second step of mass loss at 500 °C (13.2 wt%) does not fit to the theoretical mass loss of half a mole of P_2O_5 and 2.5 moles of H_2O (33.8 wt%) in this temperature range. Thus, the formation of relatively stable amorphous intermediates containing derivatives of phosphoric acid besides PON and BPO_4 is assumed, as mass loss is much lower than expected. For example, the presence of trimetaphosphoric acid was also observed by *Huang et al.* at around 600 °C by investigating the thermal behaviour of hydrated phosphates and H_3PO_4, respectively [244]. With further increasing temperature up to 1400 °C further steadily mass loss is observed, which is due to the continuous evaporation of amorphous intermediates and PON. At 950 °C BPO_4 is present as single crystalline phase. According to *Schmidt et al.* BPO_4 is stable up to at least 1100 °C [239].

7.2.8 Structural Discussion

In contrast to $(NH_4)_2Mn(II)[B_2P_3O_{11}(OH)_2]Cl$ **(1)**, which crystallises in the monoclinic space group $P2_1/n$, $(NH_4)_2[B_2P_3O_{11}(OH)]$ **(2)** crystallises in the orthorhombic space group $P2_12_12_1$. Besides **(1)** the title compound **(2)** represents the second member in the borophosphate family with an oB vierer-single ring as FBU, but exhibits next to a different protonation degree a varied connection pattern in the layers (Figure 7.28). In particular, borophosphate layers in **(1)** comprise loops, which are formed perpendicularly between two FBUs (Figure 7.29).

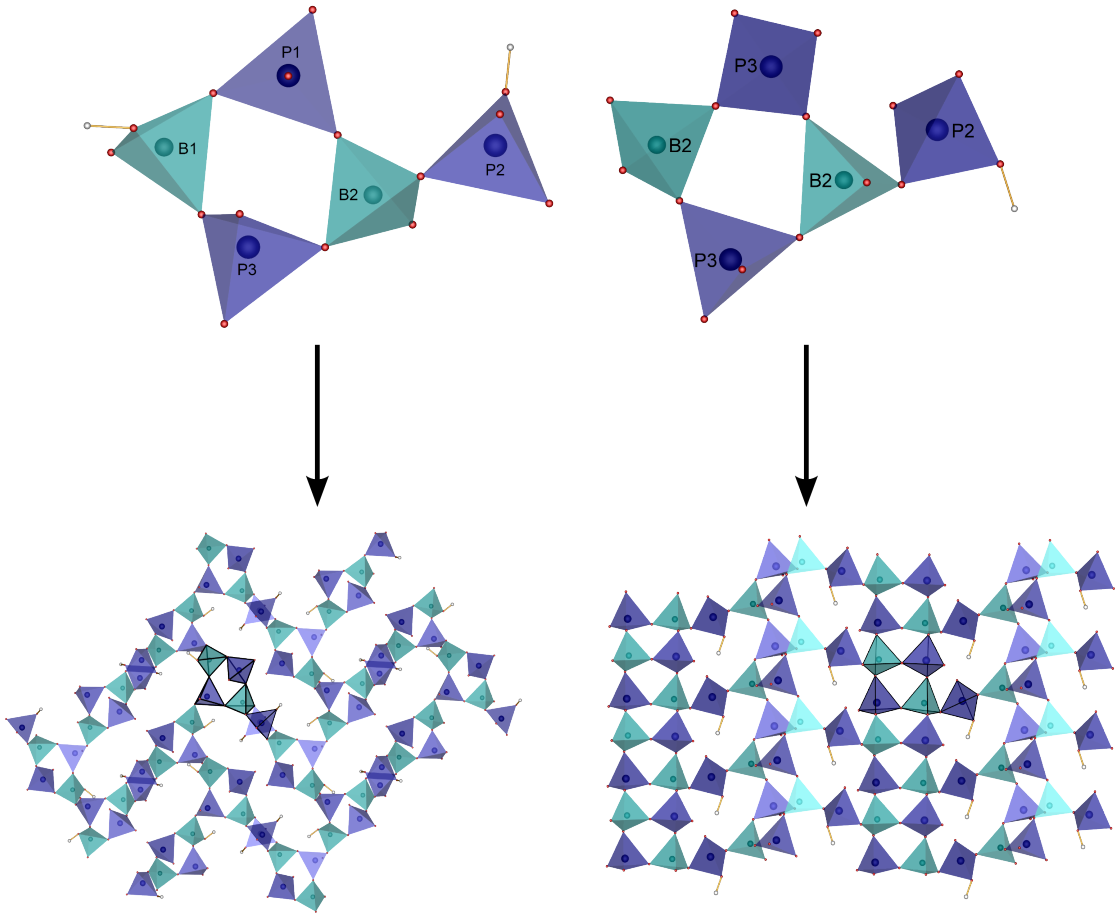

Figure 7.28: Comparison of the FBU and layer structure of $(NH_4)_2Mn(II)[B_2P_3O_{11}(OH)_2]Cl$ (left) and $(NH_4)_2[B_2P_3O_{11}(OH)]$ (right); phosphate tetrahedra blue, borate tetrahedra turquoise, hydrogen white.

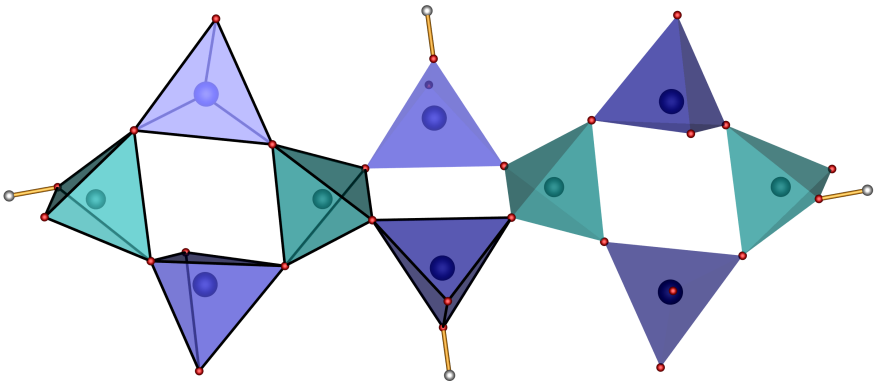

Figure 7.29: Perpendicular intra-layer loops of two FBUs in $(NH_4)_2Mn(II)[B_2P_3O_{11}(OH)_2]Cl$; phosphate tetrahedra blue, borate tetrahedra turquoise, hydrogen white.

The formed layers are both corrugated exhibiting a distance of approximately 8 Å and comprising NH_4^+, Mn^{2+} and Cl^- ions **(1)** and exclusively NH_4^+ ions **(2)** in-between (Figure 7.30).

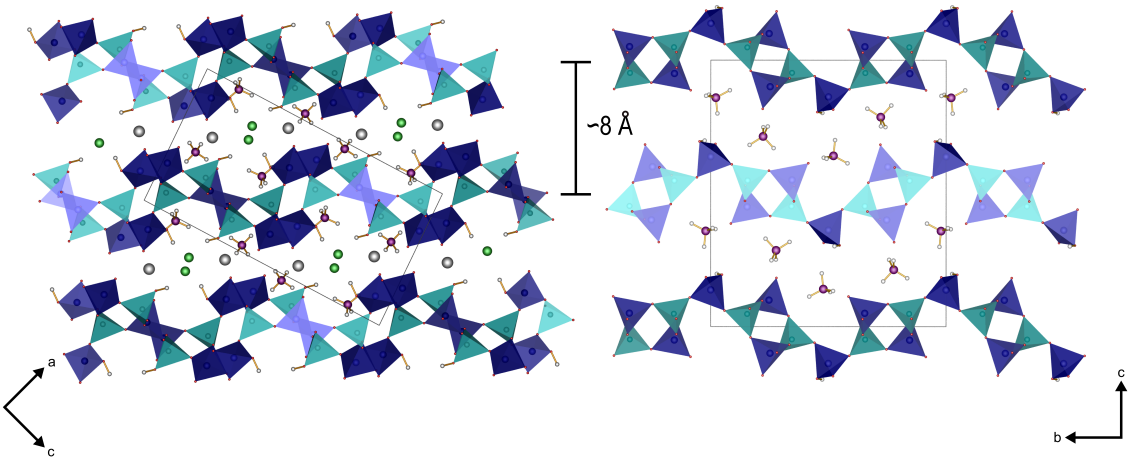

Figure 7.30: Comparison of the corrugated layer structure of $(NH_4)_2Mn(II)[B_2P_3O_{11}(OH)_2]Cl$ (left) and $(NH_4)_2[B_2P_3O_{11}(OH)]$ (right); phosphate tetrahedra blue, borate tetrahedra turquoise, chlorine green, manganese grey, nitrogen violet, hydrogen white.

However, the difference between both structures is to find in the way of corrugation. In **(1)**, which comprises additionally to **(2)** Mn^{2+} and Cl^- ions, reveals a phase shift of a half between the borophosphate layers compared to **(2)**. The fact that the structure of **(1)** is packed more dense seems to appear less reasonable at first sight as more atoms have to be accommodated. But one may not neglect attractive interactions between the Mn^{2+} ion and the anionic partial structure of the borophosphate and the Cl^- ion, which were presented in the coordination sphere (Figure 7.6). Thus, a more dense structure results for **(1)**, which could be confirmed by the cal-

culated density (Table 7.18). In addition, larger MAPLE values stand for a higher density, which could be also observed for **(1)** (124335 kJ·mol^{-1}) in contrast to **(2)** (117968 kJ·mol^{-1}) (Tables 7.6 and 7.13) [32, 33]. Both structures exhibit the same molar content of NH_4^+ ions, but differ in one mole Mn^{2+}, Cl^- and OH^-, respectively. Electrostatic interactions in **(2)** base solely on hydrogen bonds, which are represented to a lower proportion than in **(1)** due to one missing hydroxyl group (Tables 7.20 and 7.8). Nevertheless, the ratio of moderately strong to weak hydrogen bonds in **(2)** is higher than in **(1)** despite the presence of less hydrogen bonds (Tables 7.12 and 7.5).

Table 7.18: Comparison of the single-crystal structure parameters of $(NH_4)_2Mn(II)[B_2P_3O_{11}(OH)_2]Cl$ and $(NH_4)_2[B_2P_3O_{11}(OH)]$; standard deviations in brackets

Sum formula	$(NH_4)_2Mn(II)$ $[B_2P_3O_{11}(OH)_2]Cl$	$(NH_4)_2$ $[B_2P_3O_{11}(OH)]$
Temperature / K	297(2)	298(2)
Molar weight / g·mol^{-1}	450.87	343.62
Crystal system	monoclinic	orthorhombic
Space group	$P2_1/n$ (no. 14)	$P2_12_12_1$ (no. 19)
Crystal shape	irregular	needle
a / Å	9.0524(3)	4.509(3)
b / Å	8.4729(3)	14.490(11)
c / Å	16.5232(5)	16.401(12)
β / °	92.303(1)	
Volume / Å^3	1266.31(7)	1071.7(14)
Z	4	4
Calculated density D_x / g·cm^{-3}	2.366	2.130
R_{int}	0.0329	0.1309
Refined parameters	230	200
R_σ	0.0122	0.0728
$R1$ (all data)	0.0257	0.0457
$wR2$ (all data)	0.0632	0.0930

For the investigation of the optical properties the title compound was doped with Eu^{3+} and Tb^{3+} ions. The products were phase pure according to X-ray powder diffraction measurements. Presumably due to the charge compensation by vacancies luminescence quenching occurs. $(NH_4)_2[B_2P_3O_{11}(OH)]$:$Eu^{3+}$ exhibits a weak red fluorescence under excitation at 254 nm, whereas $(NH_4)_2[B_2P_3O_{11}(OH)]$:$Tb^{3+}$ does not show any visible fluorescence. The UV-Vis and fluorescence spectra were

investigated subsequently, which comprised the typical reflectance and fluorescence spectra of Eu^{3+} and Tb^{3+} ions. Apparently, in $(NH_4)_2[B_2P_3O_{11}(OH)]$:$Eu^{3+}$ Eu^{3+} ions do not tend to occupy NH_4^+ sites. The $^5D_0 \rightarrow {}^7F_1$ transition is more dominant than the $^5D_0 \rightarrow {}^7F_2$ transition, which reveals a symmetric surrounding of Eu^{3+}. Nevertheless, both sites of NH_4^+ ions are coordinated asymmetrically by oxygen atoms. A movement of the smaller Eu^{3+} ions seems obvious but has to be confirmed by appropriate measurements.

7.2.9 Thermal Discussion

Despite the very similar sum formula and the identical FBU (oB vierer-single ring) of $(NH_4)_2Mn(II)[B_2P_3O_{11}(OH)_2]Cl$ **(1)** and $(NH_4)_2[B_2P_3O_{11}(OH)]$ **(2)** the thermal behaviour of the two compounds deviates strongly. **(1)** decomposes in a single step of 21.1 % mass loss in the thermogravimetric analysis, whereas **(2)** exhibits several steps of mass loss (total mass loss 38.7 %) (Figure 7.31).

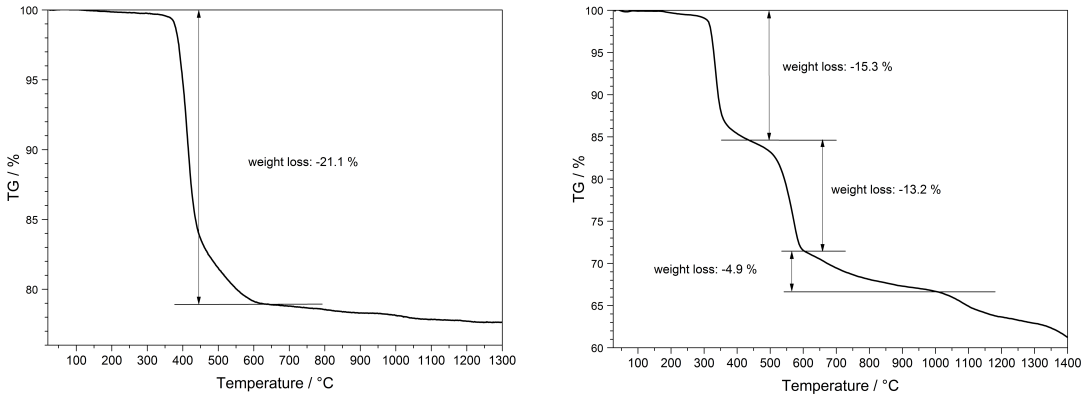

Figure 7.31: Comparison of the thermogravimetric analysis of $(NH_4)_2Mn(II)[B_2P_3O_{11}(OH)_2]Cl$ and $(NH_4)_2[B_2P_3O_{11}(OH)]$.

The thermal stability of **(1)** is slightly higher (340 °C) than of **(2)** (300 °C). As mentioned in the structural discussion (Chapter 7.2.8) the density of **(1)** is higher than **(2)**, which is due to attractive interactions between Mn^{2+} ions and their respective anionic surrounding by Cl^- ions and the borophosphate network. **(1)** forms intra-layer loops perpendicular to the layer plane. The absence of such loops and additional ionic interactions in **(2)** explains the higher thermal stability of about 40 °C of **(1)**. Nevertheless, the corrugated layers of **(2)** exhibiting no phase shift and the better ratio of moderately strong to weak hydrogen bonds are not able to enhance the interaction between the layers to reinforce the thermal stability to the same level as in **(1)**.

7.3 Ammonium Chromium(III) Borophosphate $(NH_4)Cr(III)[BP_2O_8(OH)]$

Borophosphates with a B:P ratio of 1:2 represent the largest group of tetrahedral borophosphates. The FBUs always contain an uB trimer as BBU formed by two phosphate groups connected to a borate tetrahedron and –in the simplest case– are identical with the BBU. The well-known FBUs emerging from this BBU reveal a great variety in composition and structure. Featuring uB trimers as FBU compounds exhibiting oligomer and chain structures are known. Oligomers with $[BP_2\Phi_{10}]$ (Φ = O, OH) units comprise a large variety in the O:OH ratio and composition. Up to now, chain borophosphates, e.g. $(NH_4)Cr(III)[BP_2O_8(OH)]$, featuring $^1_\infty[BP_2\Phi_9]$ (Φ = O, OH) units possess an O:OH ratio of 8:1, but are little represented [13, 120, 245–252].

7.3.1 Synthesis

$(NH_4)Cr(III)[BP_2O_8(OH)]$ was synthesised under hydrothermal conditions. A mixture of 66.7 mg (0.250 mmol) $CrCl_3{\cdot}6H_2O$, 66.0 mg (0.500 mmol) $(NH_4)_2HPO_4$, 31.0 mg (0.500 mmol) H_3BO_3 and 0.1 mL H_3PO_4 (85 %) was enclosed into a silica ampoule and was kept at 180 °C for seven days. A dark green suspension was obtained. The product was washed with hot water, filtered off and dried in air overnight. $(NH_4)Cr(III)[BP_2O_8(OH)]$ was obtained as a dark green crystalline powder with BPO_4 as side phase.

7.3.2 X-Ray Powder Diffraction

The ratio of main ($(NH_4)Cr(III)[BP_2O_8(OH)]$) and side ($BPO_4$) phase was determined via a *Rietveld* analysis (Figure 7.32). The single-crystal structure data of $(NH_4)V(III)[BP_2O_8(OH)]$ [248] served as starting model for the refinement of the title compound. The refinement was carried out in the range between 5–140 °2θ. Initially, zero point, scale factor and lattice parameters of both phases were refined. Subsequently the background was fit manually by linear interpolation and the reflection peak shape was fitted using the pseudo-Voigt function. Additionally, two different asymmetry factors were refined. The atomic coordinates of the starting model were refined individually. Due to the weak scattering contribution of hydrogen atoms and possible rotations of ammonia ions, N and H atoms were not refined. For BPO_4 the refinement of oxygen atoms exclusively occupying a general position was carried out. Temperature factors (B_{iso}), site occupancies and the hydrogen

atoms present in this structure were not included in the refinement. Due to the measuring method preferred orientation was considered as well.

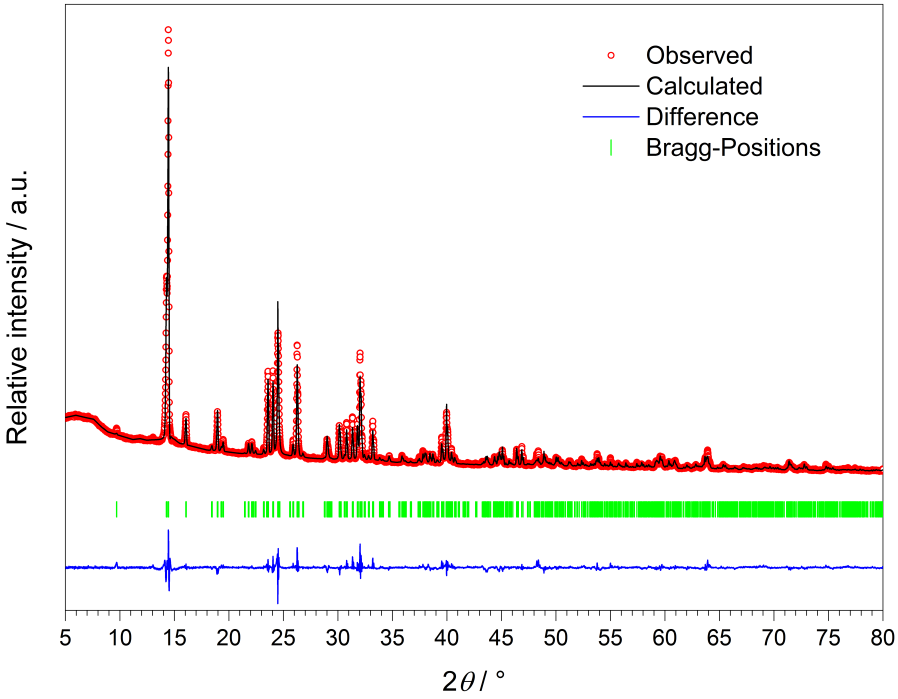

Figure 7.32: X-ray powder diffraction pattern and result of the *Rietveld* refinement for $(NH_4)Cr(III)[BP_2O_8(OH)]$.

$(NH_4)Cr(III)[BP_2O_8(OH)]$ crystallises isotypically to other monovalent trivalent metal borophosphates with the sum formula $A^{I}M^{III}[BP_2O_8(OH)]$ (A^{I} = monovalent metal; M^{III} = trivalent metal), such as A^{I} = Rb and M^{III} = Fe [246], $A^{I} = NH_4$ and M^{III} = Fe [120, 248] and $A^{I} = NH_4$ and M^{III} = V [248]. It crystallises in the monoclinic space group $P2_1/c$ with the lattice parameters $a = 9.3389(1)$ Å, $b = 8.2771(1)$ Å, $c = 9.5910(1)$ Å and $\beta = 102.776(1)$ °. The structure was refined to very good residuals of $R_p = 0.024$, $R_{wp} = 0.035$ and $\chi^2 = 4.75$. Besides the Gaussian peak width parameters, the asymmetry and preferred orientation parameters are also in a good range (Table 7.19). The refined atomic coordinates, isotropic displacement factors (B_{iso}), selected interatomic distances and angles are summarised in Tables 7.20 and 7.21. The *Rietveld* analysis revealed a portion of 20 % of BPO_4 as side phase besides 80 % of $(NH_4)Cr(III)[BP_2O_8(OH)]$. According to *Kritikos et al.* none of their reaction conditions for the synthesis of $NH_4M^{III}[BP_2O_8(OH)]$ (M^{III} = V, Fe) and $(NH_4)(Fe(III)_{0.53}V(III)_{0.47})[BP_2O_8(OH)]$ lead to phase pure samples and exhibited BPO_4 as side phase as well, which was mechanically separated using an optical microscope [248]. This method was also applied for $(NH_4)Cr(III)[BP_2O_8(OH)]$, but could not be performed successfully due to the presence of polycrystalline powder. In contrast, $RbFe[BP_2O_8(OH)]$ was obtained as phase pure product by *Kniep et al.* [246].

Table 7.19: *Rietveld* refinement parameters of $(NH_4)Cr(III)[BP_2O_8(OH)]$; standard deviations in brackets

Sum formula	$(NH_4)Cr(III)[BP_2O_8(OH)]$
Molar weight / g·mol^{-1}	287.80
Crystal system	monoclinic
Space group	$P2_1/c$ (no. 14)
Colour	green
a / Å	9.3384(1)
b / Å	8.2765(1)
c / Å	9.5905(2)
β / °	102.776(1)
Volume / Å^3	722.89(2)
Z	4
Calculated density D_x / g·cm^{-3}	2.607
Radiation	Cu-K_α
Wavelength λ / Å	1.5406
Diffractometer	Seifert XRD T/T 3003
Theta range / °	$5.00 \leq 2\theta \leq 140.00$
Step width / °	0.01 2θ
Data points	14501
No. of atoms	19
Zero point	-0.0741(3)
Scale factor	0.0213(2)
Profile function	pseudo-Voigt
Gaussian peak width parameters / U | V | W	0.220(39) | -0.067(28) | 0.029(4)
Asymmetry parameters	0, 0.0198(0), 0.0007(0)
Preferred orientation parameters	1.0020(131), 0
Refined parameters	62
R_p	0.024
R_{wp}	0.035
χ^2	4.75

Table 7.20: Refined atomic coordinates and isotropic displacement parameters B_{iso} / Å^2 of $(NH_4)Cr(III)[BP_2O_8(OH)]$; standard deviations in brackets

Atom	*Wyckoff* symbol	x	y	z	B_{iso}
Cr1	4*e*	0.2095(4)	0.1508(4)	0.4319(5)	0.70
P1	4*e*	0.0745(6)	0.4335(6)	0.2047(7)	1.00
P2	4*e*	0.4169(6)	0.2375(7)	0.2204(7)	1.00
B1	4*e*	0.336(2)	−0.070(3)	0.679(3)	1.00
$O_{br}1$	4*e*	0.4080(11)	0.4115(12)	0.2565(10)	1.00
$O_{br}2$	4*e*	0.5970(11)	0.2032(11)	0.2489(11)	1.00
$O_{br}3$	4*e*	0.1884(10)	0.5855(11)	0.2262(12)	1.00
$O_{term}1$	4*e*	0.3726(9)	0.2957(10)	0.5565(12)	1.00
$O_{term}2$	4*e*	0.3434(8)	0.1229(10)	0.3126(12)	1.00
$O_{term}3$	4*e*	0.0874(9)	0.1687(10)	0.5862(11)	1.00
$O_{term}4$	4*e*	0.1130(11)	0.3414(11)	0.3486(11)	1.00
$O_{term}5$	4*e*	0.0793(10)	−0.0041(11)	0.2918(10)	1.00
O_H1	4*e*	0.3158(9)	−0.0469(10)	0.5208(11)	1.00

O_{br} = bridging oxygen atom; O_{term} = terminal oxygen atom;
O_H = hydroxyl group

Table 7.21: Selected interatomic distances / Å and angles / ° in $(NH_4)Cr(III)[BP_2O_8(OH)]$; standard deviations in brackets

B–O_{br}	1.47(2)–1.489(18)
B–O_H	1.486(20)
P–O_{br}	1.457(10)–1.626(9)
P–O_{term}	1.453(10)–1.600(10)
Cr–O	1.886(12)–2.125(8)
B–O_{br}–P	116.1(15)–137.8(15)
O–P–O	101.1(8)–116.4(10)
O–B–O	100.8(13)–116.0(13)

7.3.3 Crystal Structure Description

$(NH_4)Cr(III)[BP_2O_8(OH)]$ crystallises in the monoclinic space group $P2_1/c$ with four formula units per unit cell. All atoms are located on the general *Wyckoff* position $4e$. The anionic partial structure of $(NH_4)Cr(III)[BP_2O_8(OH)]$ exhibits layers of zig-zag chains of corner-sharing hydroxo-borate and phosphate tetrahedra (Figure 7.33).

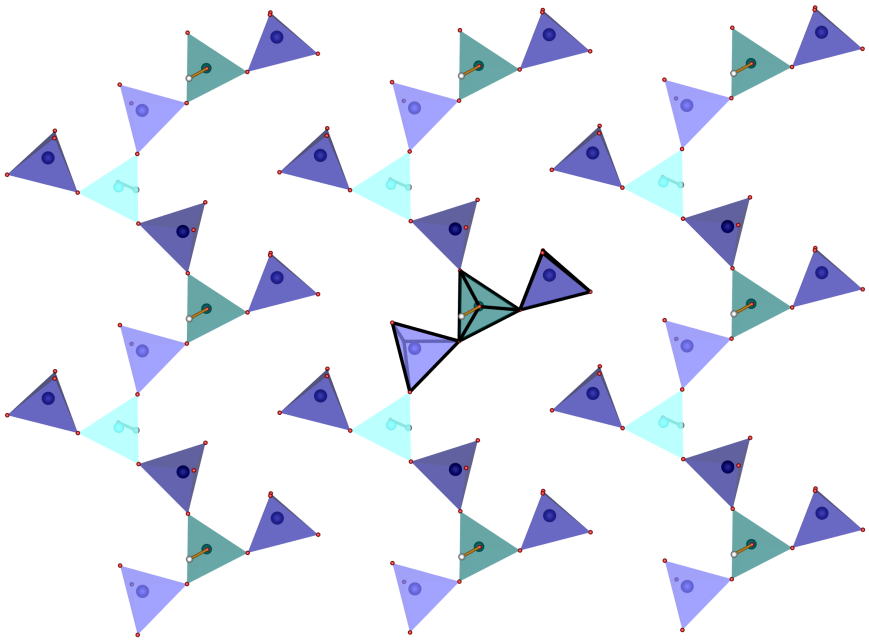

Figure 7.33: Parallel oB vierer-single chains in $(NH_4)Cr(III)[BP_2O_8(OH)]$ in the [110] plane; FBU highlighted; phosphate tetrahedra blue, borate tetrahedra turquoise.

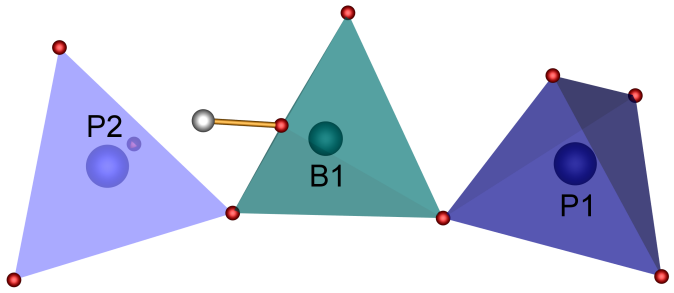

Figure 7.34: BBU/FBU as an uB trimer 3□:3□ of $(NH_4)Cr(III)[BP_2O_8(OH)]$; phosphate tetrahedra blue, borate tetrahedra turquoise, hydrogen white.

As in $(NH_4)_2Mn(II)[B_2P_3O_{11}(OH)_2]Cl$ (Chapter 7.1) no P–O–P and B–O–B connections are observed. The polyanion is constructed by uB trimeric $^1_\infty[BP_2\Phi_9]$ ($\Phi = O$, OH) BBUs (Figure 7.34) comprising a B:P ratio of 1:2. The BBU consisting of one

BΦ_4 and two PΦ_4 (Φ = O, OH) tetrahedra, illustrated with the descriptor 3□:3□, is condensed to form parallel oB vierer-single chains [13].

Both B and P atoms are coordinated tetrahedrally with boron forming BO_4H and phosphorus PO_4 tetrahedra. B–O bond lengths in the borate tetrahedra range between 1.47 and 1.49 Å, whereas P–O bond lengths in the phosphate tetrahedra lie between 1.46 and 1.63 Å. The bond length B–O_H is 1.47 Å. B–O_{br} distances range between 1.47 and 1.49 Å whereas P–O_{br} distances range between 1.46 and 1.63 Å and P–O_{term} distances lie between 1.45 and 1.60 Å. Values in this order of magnitude were also found in other borophosphates [120, 246, 248]. B–O_{br}–P angles range between 116 and 138 °, whereas O–B–O and O–P–O angles lie between 101–116° (Ø = 109°), respectively. Selected bond lengths and angles of $(NH_4)Cr(III)[BP_2O_8(OH)]$ are listed in Table 7.21.

The calculation of deviation of tetrahedra from ideal symmetry was applied by the method of *Balić-Žunić* and *Makovicky* [35, 36]. The three crystallographically different hydroxo-borate and phosphate tetrahedra in $(NH_4)Cr(III)[BP_2O_8(OH)]$ feature the values −1.12 % (B1), −0.73 % (P1) and −1.15 % (P2). One phosphate tetrahedra can be classified as regular since its value is below 1 %. The hydrogen-borate tetrahedra and one phosphate tetrahedra exhibit a slight distortion and are thus close to a regular tetrahedra. Similar values were found in other tetrahedra [97, 98, 122, 129, 187, 189–191].

The parallel borophosphate chains in the [110] plane are built by parallel zig-zag chains running along [010], which are interconnected via common oxygen corners of CrO_6 octahedra as demonstrated in Figure 7.35. The crystal structure possesses one unique site of the Cr^{3+} ion, which is coordinated distorted octahedrally by six oxygen atoms (Figure 7.36).

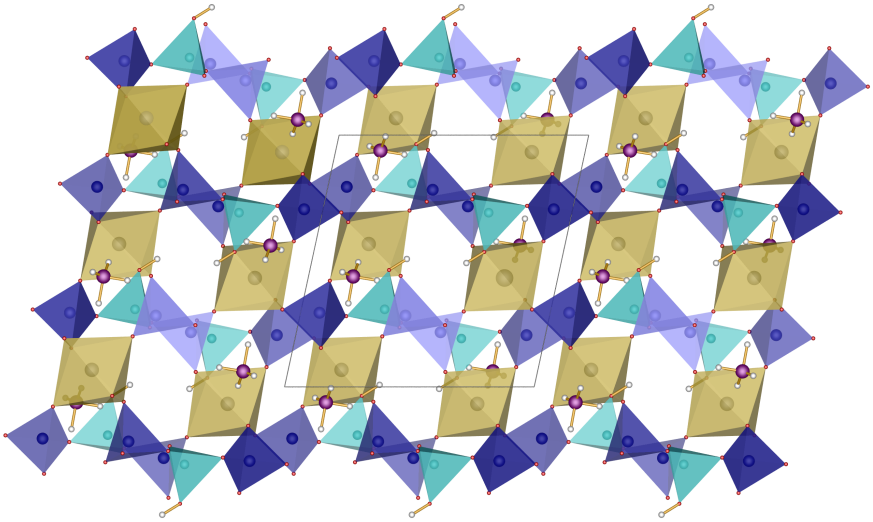

Figure 7.35: Layered crystal structure viewed along [010], interconnected via common oxygen corners of CrO_6 octahedra (yellow) of $(NH_4)Cr(III)[BP_2O_8(OH)]$; phosphate tetrahedra blue, borate tetrahedra turquoise, nitrogen violet, hydrogen white.

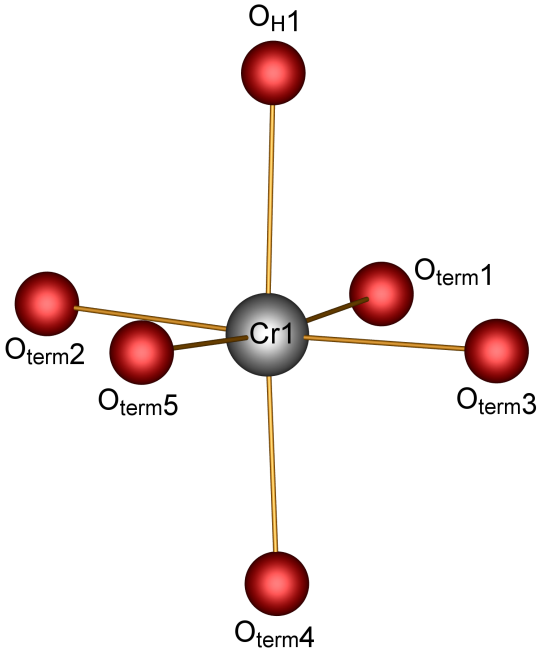

Figure 7.36: Coordination sphere of chromium in $(NH_4)Cr(III)[BP_2O_8(OH)]$.

The coordinating oxygen atoms originate from the hydroxyl group of the borate and terminal oxygen atoms of four phosphate tetrahedra belonging to three adjacent borophosphate chains. The Cr–O bond lengths range between 1.89 and 2.10 Å (Table 7.21). These values are in good agreement with the sum of the ionic radii of Cr^{3+} and the coordinating atoms, e.g. 1.94 (OH^-) and 1.97 Å (O^{2-}) [60], respectively.

Along [100] oval shaped channels (approx. 5.60 × 3.40 $Å^2$) are formed, in which the NH_4^+ ions are situated (Figure 7.37).

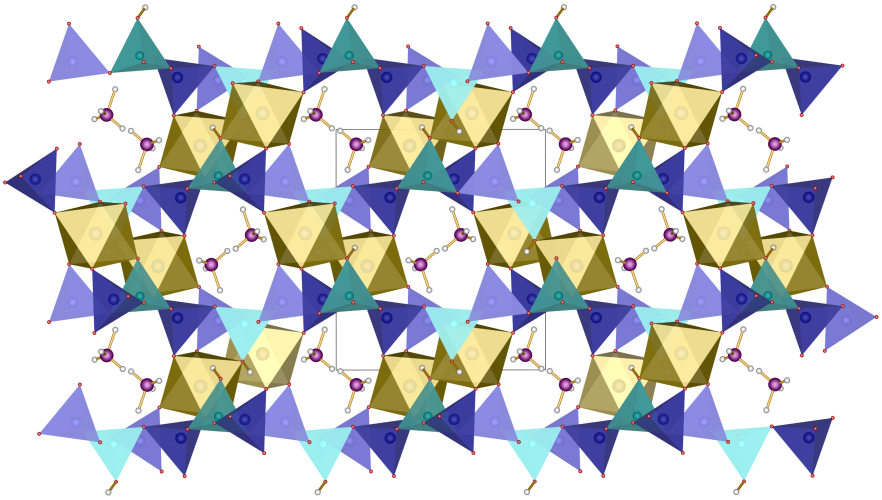

Figure 7.37: Oval shaped channels in [100] in $(NH_4)Cr(III)[BP_2O_8(OH)]$. Yellow octahedra centred by manganese, blue and turquoise tetrahedra centred by phosphorus and boron, respectively.

7.3.4 Electrostatic Calculations

The coordination number of chromium was proofed by calculations based on the MAPLE concept (Table 12.9) [32, 33, 152]. The electrostatic consistency of the structure model was compared with the MAPLE values of the single-crystal data of $(NH_4)V(III)[BP_2O_8(OH)]$ [248]. Both structures reveal considerable deviations from electrostatic consistency. In $(NH_4)V(III)[BP_2O_8(OH)]$ the deviation is slightly larger than in $(NH_4)Cr(III)[BP_2O_8(OH)]$, exhibiting deviations of 5.6 and 5.2 %, respectively (Table 7.22). Applying the rule for electrostatic consistency strictly both crystal structures do not possess a proper structure model with balanced electrostatics.

Table 7.22: MAPLE calculations for $(NH_4)Cr(III)[BP_2O_8(OH)]$ and $(NH_4)V(III)[BP_2O_8(OH)]$ [32, 33, 152]

Compound	MAPLE / kJ·mol^{-1}
$(NH_4)Cr(III)[BP_2O_8(OH)]$	81644
0.5 Cr_2O_3 [253] + 0.5 B_2O_3 [154] + P_2O_5 [193] + NH_3 [254] + H_2O [155]	77437
	$\Delta = 5.2\,\%$
$(NH_4)V(III)[BP_2O_8(OH)]$	82008
0.5 V_2O_3 [255] + 0.5 B_2O_3 [154] + P_2O_5 [193] + NH_3 [254] + H_2O [155]	77341
	$\Delta = 5.7\,\%$

A closer look on the MAPLE results in detail in Table 12.9 shows that in both compounds the coordination of the transition metal is six. The ECoN value indicates the bond proportion of the corresponding ligand, which lies for both compounds in the same range (1.25–0.63 (Cr) and 1.10–0.78 (V)). An unexpected result occurs in the coordination sphere of the ammonia ion. According to this only H2 exhibits bond proportions (ECoN = 1.03) large enough to be electrostatically considered as ligand of N1 in $(NH_4)Cr(III)[BP_2O_8(OH)]$. The same result occurs in $(NH_4)V(III)[BP_2O_8(OH)]$ as the atoms of the ammonia ion have not been refined. Apparently, hydrogen atoms with a distance d(N–H) larger than 0.65 Åwere no more considered as ligands of the ammonia ion. In general, distances d(N–H) show a large scattering reaching from 0.65–1.08 Å. In $(NH_4)_2Mn(II)[B_2P_3O_{11}(OH)_2]Cl$ in contrast, all distances d(N–H) lie between 0.96–0.97 Å(Table 12.7). Besides a narrow distribution a larger distance d(N–H) is considered in general (Table 7.6).
The *MAPLE values of H2 as single ligand of N1 and of H3 as ligand in the nearest distance are strongly increased in contrast to the protons that were not considered as ligands, which emphasises the reduced number of included ligands.

Further MAPLE calculations of both compounds excluding the protons of the ammonia ion by keeping neutrality of charge (N^+ instead of NH_4^+) show even stronger deviating and smaller values (Table 7.23). Due to the missing protons in the structure the *Coulomb* Part of Lattice Energy decreases. The *Coulomb* energy E_C of a compound strongly depends on the charge and the cation-anion distance (Equation 3.10). Hence, it does not surprise that with an increasing cation-anion distance E_C decreases, which could be observed both in $(NH_4)Cr(III)[BP_2O_8(OH)]$ and $(NH_4)V(III)[BP_2O_8(OH)]$ (Table 7.23). The coordination spheres of all Cr^{3+}/V^{3+}, P^{5+} and B^{3+} ions stay unaffected. Due to the missing protons of the NH_4 ion the *MAPLE values of all atoms are in the same scale with the exception of H1 at-

tached to one oxygen atom of the borate tetrahedra (Table 12.10). Covalently attached protons tend to exhibit increased *MAPLE values of about 70–120, which was already observed in other compounds, e.g. $Ln[H(PO_3)_4]$ (Ln = Tb, Ho) and $(NH_4)_2[B_2P_3O_{11}(OH)]$ (Tables 12.2, 12.3 and 12.8).

Table 7.23: MAPLE calculations for $NCr(III)[BP_2O_8(OH)]$ and $NV(III)[BP_2O_8(OH)]$ (protons of NH_4^+ ions excluded) [32, 33, 152]

Compound	MAPLE / kJ·mol^{-1}
$(N)Cr(III)[BP_2O_8(OH)]$	67699
0.5 Cr_2O_3 [253] + 0.5 B_2O_3 [154] + P_2O_5 [193] + NH_3 [254] + H_2O [155]	76150
	Δ = -12.5 %
$(N)V(III)[BP_2O_8(OH)]$	68158
0.5 V_2O_3 [255] + 0.5 B_2O_3 [154] + P_2O_5 [193] + NH_3 [254] + H_2O [155]	77341
	Δ = -11.6 %

7.3.5 Spectroscopic Properties

7.3.5.1 IR Spectroscopy

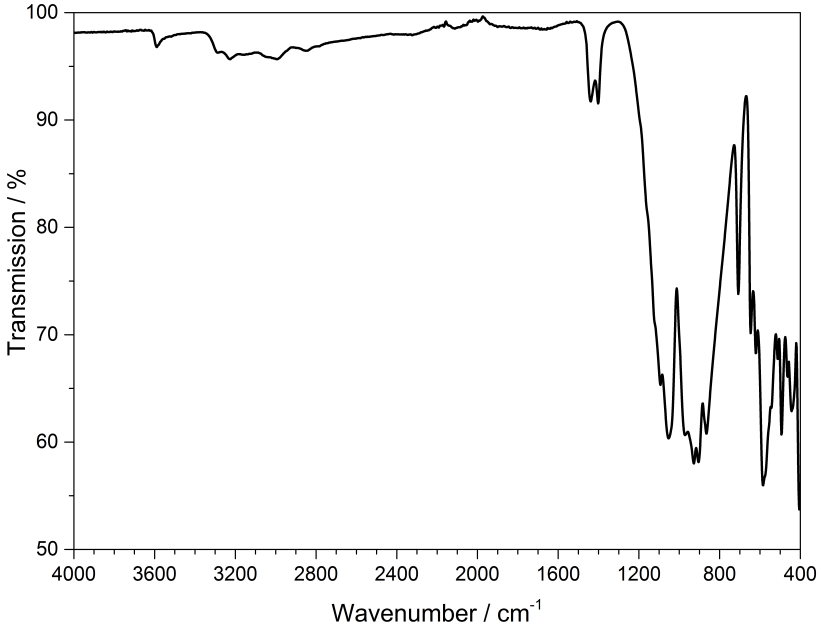

Figure 7.38: Infrared spectrum of $(NH_4)Cr(III)[BP_2O_8(OH)]$.

The infrared spectrum of $(NH_4)Cr(III)[BP_2O_8(OH)]$ was recorded between 4000

and 400 cm^{-1} and is shown in Figure 7.38. The position of the bands and the corresponding assignments are given in Table 7.24.

Table 7.24: Position / cm^{-1} and assignment of the IR bands in $(NH_4)Cr(III)[BP_2O_8(OH)]$

Position	Assignment
3589	ν(OH), δ(OH) [120, 121, 226, 232, 234, 248, 256]
3230–2850	ν(NH) [120, 233]
1664	δ(OH) [120, 121, 226, 228, 232–234]
1440–1400	ν(NH) [120, 233]
1094	$\nu(BO_4)$ [235, 236]
1060–400	$\nu(PO_4)$ [235, 236, 256]
972	$\nu(PO_4)$ [235, 236]
905	$\nu(BO_4)$ [235, 236]
866	$\nu(BO_4)$, ν_{as}(BOP) [235, 236]
708	ν_s(BOP) [235, 236]
646	δ(BOP) [235, 236]
586	δ(OPO) [235, 236]
513, 444	$\nu(BO_4)$ [235, 236]

The bands at 3589 and 1664 cm^{-1} can be assigned to the stretching and deformation vibrations of the OH group [120, 121, 226, 228, 232–234, 248, 256]. Vibrations between 3230–2850 cm^{-1} and 1440–1400 cm^{-1} belong to N–H stretching vibrations [120, 233]. BO_4 vibrations can be found at 1094, 905, 866, 513 and 444 cm^{-1}, whereas typical PO_4 vibrations range in the relatively lower region between 1060–400 cm^{-1}, respectively. Characteristic bands of symmetric or asymmetric B–O–P stretching and bending vibrations are found at 866 (ν_{as}), 708 (ν_s), 646 (δ) and for δ(O–P–O) at 586 cm^{-1} [235, 236]. Exhibiting BPO_4 as side phase of $(NH_4)Cr(III)[BP_2O_8(OH)]$ makes a clear assignment of BO_4, PO_4 and B–O–P bands to one phase impossible. Stretching vibrations of PO_4 appear at 1145 (ν_{as}), 1045 (ν_{as}) and 984 cm^{-1} (ν), whereas PO_4 bending vibrations (δ) are expected at 633, 604, 564 cm^{-1} [257]. BO_4 stretching and bending vibrations appear at 930 and 550 cm^{-1}, respectively [258]. Further impurification can be excluded as no other bands could be detected.

7.3.5.2 UV-Vis Spectroscopy

The UV–Vis reflection spectrum of $(NH_4)Cr(III)[BP_2O_8(OH)]$ was recorded between 200–800 nm. It is shown in Figure 7.39 and reveals four absorption bands.

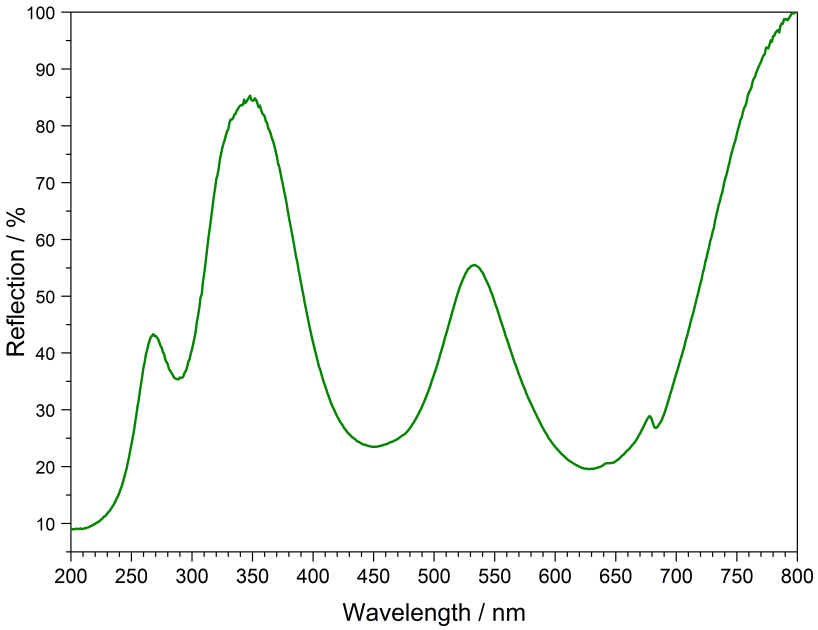

Figure 7.39: UV–Vis spectrum of $(NH_4)Cr(III)[BP_2O_8(OH)]$.

In an octahedral environment d–d transitions in a d^3 Cr^{3+} ion are parity forbidden [8, 37, 41, 42]. In $(NH_4)Cr(III)[BP_2O_8(OH)]$ Cr^{3+} ions are coordinated distorted octahedrally by six oxygen atoms and thus three absorption bands at 288, 450 and 628 nm can be observed. The rule of the spin prohibition [8, 37, 41, 42] is satisfied as only transitions with no change of the total spin occur. Two transitions in the visible region at 628 nm ($^4A_{2g}\rightarrow{}^4T_{2g}$) and 450 nm ($^4A_{2g}\rightarrow{}^4T_{1g}$), absorbing radiation in the red and blue visible region, are responsible for the deeply green body colour of the compound and originate from varying energies which are caused by electron repulsion. In Table 7.25 all observed transitions are summarised.

Table 7.25: Absorption bands of $(NH_4)Cr(III)[BP_2O_8(OH)]$

Transition	Wavelength / nm	Wavenumber / 10^3 cm^{-1}
$^4A_{2g}\rightarrow{}^4T_{2g}$	628	15.9
$^4A_{2g}\rightarrow{}^4T_{1g}$	450	22.2
$^4A_{2g}\rightarrow{}^4T_{1g}$	288	34.7
LMCT	200	50.0

By excitation from the d_{xy} to the $d_{x^2-y^2}$ orbital the location of the electron is only turned by 45° in the xy plain and an energy amount of $10Dq$ is consumed (Figure

7.40 (1)). In contrast, excitation from the d_{xy} to the d_{z^2} or from the d_{xz} and d_{yz} to the $d_{x^2-y^2}$ orbital, respectively, leads to a higher concentration of electron density around the z axis or the xy plane, respectively (Figure 7.40 (2)). Consequently, next to $10\,Dq$ an additional repulsion (x) has to be overcome. In total, three degenerated transitions of $10\,Dq$ (lower energy) and $>10\,Dq$ (higher energy) exist, respectively [8, 42]. The third transition in the ultraviolet region at 288 nm ($^4A_{2g}\rightarrow{}^4T_{1g}$) possesses about twice the energy of the single electron transition and can be assigned to a three-fold degenerated two electron transition from t_{2g} to e_g (Figure 7.40 (3)) [8, 42, 259].

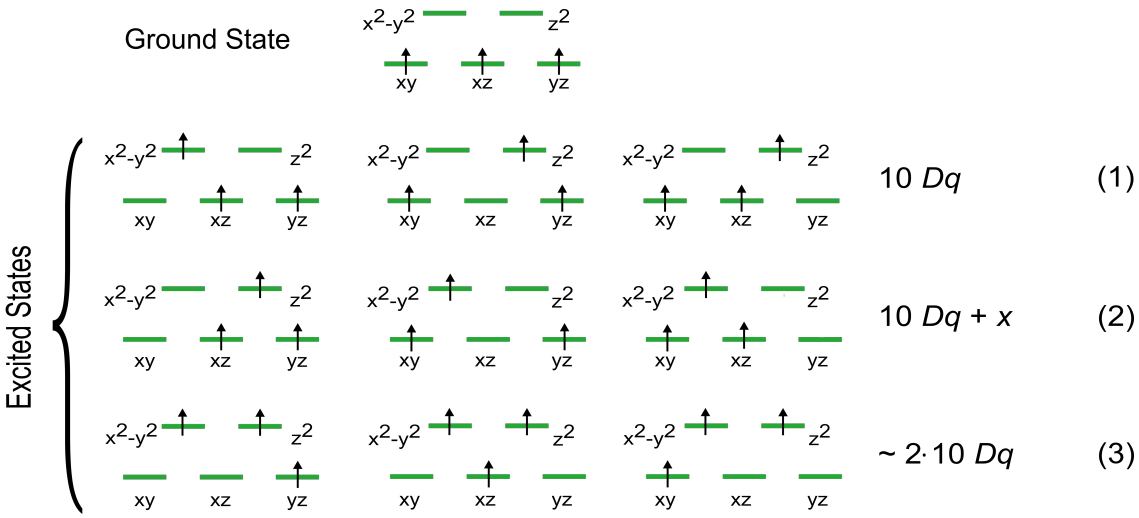

Figure 7.40: Electron transitions in Cr^{3+} (d^3).

Although transitions leading to a change of the multiplicity are forbidden, nevertheless very weak absorptions can be observed. In $(NH_4)Cr(III)[BP_2O_8(OH)]$ the spin-forbidden $^4A_{1g}\rightarrow{}^2E_g$ transition results in a shoulder at 683 nm of the spin-allowed $^4A_{2g}\rightarrow{}^4T_{2g}$ transition at 628 nm. Due to the *Jahn-Teller* effect the width of the transitions is broadened [8, 42]. Between 200 and 270 nm an intense LMCT occurs due to an electron transfer from the p orbital of the ligand to the d orbital of the metal ion [8, 42].

For a more detailed characterisation of the strength of the ligand field of Cr^{3+} in $(NH_4)Cr(III)[BP_2O_8(OH)]$ a *Tanabe-Sugano* diagram of a d^3 ion (Figure 7.41) [42, 260] in an octahedral ligand field was used [43].

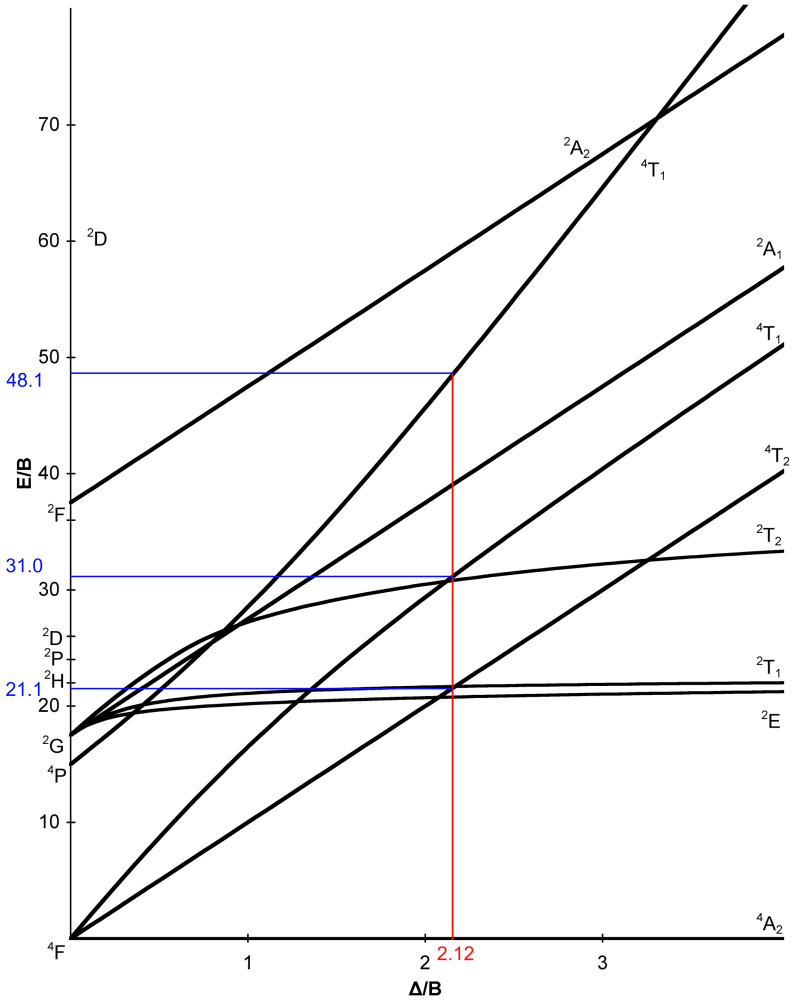

Figure 7.41: *Tanabe-Sugano* diagram of a d^3 ion in an octahedral ligand field [42, 260].

Using the wavenumbers of the observed transitions (Table 7.25) the following ratios can be calculated (Equation 7.3 and 7.4):

$$\frac{^4A_{2g} \rightarrow ^4T_{1g}}{^4A_{2g} \rightarrow ^4T_{2g}} = \frac{22222\,\mathrm{cm}^{-1}}{15924\,\mathrm{cm}^{-1}} = 1.4 \tag{7.3}$$

$$\frac{^4A_{2g} \rightarrow ^4T_{1g}}{^4A_{2g} \rightarrow ^4T_{2g}} = \frac{34722\,\mathrm{cm}^{-1}}{15924\,\mathrm{cm}^{-1}} = 2.2 \tag{7.4}$$

In Figure 7.41 the ratios of these transitions are found at $\Delta/B \approx 2.12$. The graphically determined E/B ratios of the three transitions are used to calculate B' (Equations 7.6 to 7.8) using the general Equation 7.5.

$$\frac{E}{B'} = \mathrm{X} \tag{7.5}$$

$$B_1' = \frac{15924\,\mathrm{cm^{-1}}}{21.1} = 754.69\,\mathrm{cm^{-1}} \tag{7.6}$$

$$B_2' = \frac{22222\,\mathrm{cm^{-1}}}{31.0} = 716.84\,\mathrm{cm^{-1}} \tag{7.7}$$

$$B_3' = \frac{34722\,\mathrm{cm^{-1}}}{48.1} = 721.87\,\mathrm{cm^{-1}} \tag{7.8}$$

Thus, an average value of the *Racah* parameter $B' = 731\,\mathrm{cm^{-1}}$ results. The parameter B' describes the interelectronic repulsion in *high-* and *low-spin* transition metal complexes. Usually the value for free transition metal ions in the gas phase is close to $1000\,\mathrm{cm^{-1}}$. *Racah* parameters for ions in complexes (B') are generally smaller due to less repulsive interactions between electrons compared to the corresponding free ions (B). This also holds for the example calculated above. In the literature the B value for Cr^{3+} in the gas phase is $918\,\mathrm{cm^{-1}}$ [42], which is larger than the value determined via UV-Vis spectroscopy for Cr^{3+} in $(NH_4)Cr(III)[BP_2O_8(OH)]$.

The ligand field splitting (LFS) Δ_o of Cr^{3+} in $(NH_4)Cr(III)[BP_2O_8(OH)]$ can be calculated using the following Equation 7.9 .

$$\Delta_o Dq = \Delta/B \cdot 10 \cdot B' = 2.12 \cdot 10 \cdot 731\,\mathrm{cm^{-1}} = 15.5 \cdot 10^3\,\mathrm{cm^{-1}} \tag{7.9}$$

The comparison with other Δ_o Cr^{3+} complexes shows that the ligand field strength of the sixfold coordination sphere of oxygen atoms in the borophosphate anion is slightly larger than in $Cr(PO_3)_3$ or CrF_6, due to a stronger LFS (Table 7.26).

Table 7.26: Selected Δ_o / $\mathrm{cm^{-1}}$ of Cr^{3+} complexes [42]

CN^-	NH_3	BO_3^{3-} [261]	H_2O	$[BP_2O_8(OH)]^{4-}$	$(PO_3)_3^{3-}$ [262], F^-	Cl^-
26600	21500	18300	17400	15500	15060	13000

However, the LFS of $CrBO_3$ reveals a much larger value for Δ_o [261]. Due to more polarised B–O bonds BO_3^{3-} exhibits a stronger interaction with the Cr^{3+} ion and a larger LFS occurs. A closer look on the coordination sphere in $(NH_4)Cr(III)[BP_2O_8(OH)]$ (Chapter 7.3.3) shows that Cr^{3+} is coordinated by five phosphate oxygen atoms and one hydroxyl group of the borate tetrahedron. Thus, the major coordination sphere is provided by oxygen atoms originating from phosphate groups and Δ_o is close to the value of $Cr(PO_3)_3$ [262]. Nevertheless, the relatively strong contribution of the single hydroxylborate may not be neglected, which shifts Δ_o to higher wavenumbers. This result fits very well to the spectrochemical row of ligands, where F^- represents a weaker ligand than O^{2-} [8, 42].

7.3.6 Thermal Analysis

The thermal behaviour of $(NH_4)Cr(III)[BP_2O_8(OH)]$ was investigated between room temperature and 1400 °C (Figure 7.42) and shows a certain stability against thermal treatment. The thermogravimetric curve shows a single step of mass loss of 11.6 wt% in the temperature range between 300 and 800 °C. Assuming that along with one mole of NH_3 a further mole of H_2O evaporates (theor. mass loss: 12.18 wt%), a composition of $Cr(III)[BP_2O_8]$ might be expected. Such anions are present in borophosphates with the general formula $A^{I}M^{II}(H_2O)_2[BP_2O_8]$ (A^{I} = Na, K; M^{III} = Mg, Mn, Fe, Co, Ni, Zn) [248, 263], but have never been observed in non-hydrated chromium borophosphates. With further increasing temperature and maintaining the sample at 1400 °C further mass loss of 2.9 wt% is observed. According to *Schmidt et al.* anhydrous BPO_4, representing the side phase in the sample of $(NH_4)Cr(III)[BP_2O_8(OH)]$, is stable up to 1100 °C [239]. Thus, the occurring mass loss between 300 and 800 °C can be assigned certainly to the decomposition of $(NH_4)Cr(III)[BP_2O_8(OH)]$. X-ray powder diffraction of the deeply green polycrystalline sample after the heating process reveals an unknown phase (*) with Cr_2O_3 [253] as side phase (Figure 7.43 red). According to *Schmidt et al.* BPO_4 decomposes at about 1100 °C [239]. Thus, it could not be assigned (Figure 7.43). By heating the title compound up to 800 °C BPO_4 as main product and the unknown side phase can be obtained as well (Figure 7.43 blue).

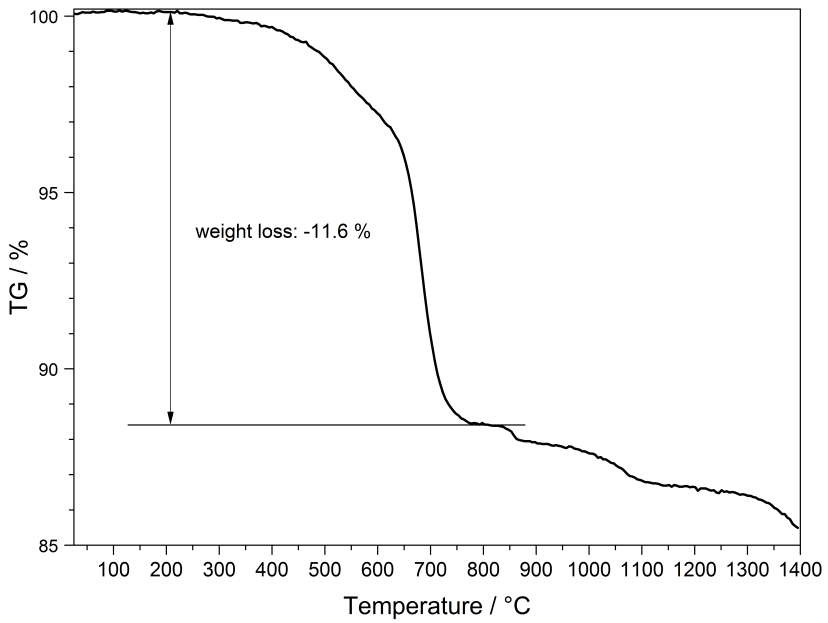

Figure 7.42: Thermogravimetric analysis of $(NH_4)Cr(III)[BP_2O_8(OH)]$.

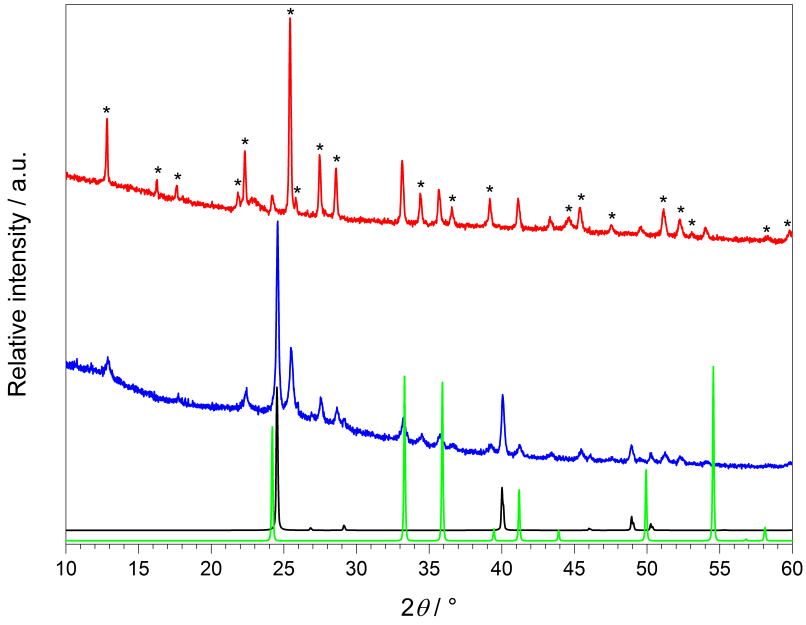

Figure 7.43: X-ray powder diffraction pattern of $(NH_4)Cr(III)[BP_2O_8(OH)]$ after the thermogravimetric analysis at 1400 °C in N_2 (red), after the thermal treatment in N_2 at 800 °C (blue) and calculated X-ray powder diffraction patterns from single-crystal data of Cr_2O_3 (green) [253] and BPO_4 [239] (black) and unknown phase (*).

7.3.7 Structural Discussion

In contrast to the borophosphates presented in the two previous chapters (Chapter 7.1 and 7.2) $(NH_4)Cr(III)[BP_2O_8(OH)]$ **(3)** exhibits a different BBU/FBU (uB trimer), which forms parallel zig-zag chains (oB vierer-single chain) instead of layers. The polyanion as uB trimer $^1_\infty[BP_2\Phi_9]$ ($\Phi = O$, OH) with a B:P ratio of 1:2 is already known in other borophosphates, e.g. $RbFe(III)[BP_2O_8(OH)]$ [246], $(NH_4)Fe(III)[BP_2O_8(OH)]$ [120, 248] and $(NH_4)V(III)[BP_2O_8(OH)]$ **(4)** [248], which crystallise isotypically in the space group $P2_1/c$ (Table 7.27). The single-crystal data of **(4)** served as starting model for the *Rietveld* refinement of **(3)**. Due to the larger ionic radius of V^{3+} (0.79 Å[60]) compared to Cr^{3+} (0.62 Å[60]) the lattice parameters and the cell volume of **(3)** are slightly smaller than in **(4)**. The b axis and the β angle of **(3)** are marginally larger than in **(4)**, which can be neglected due to data received from a powder refinement.

Table 7.27: Comparison of the structure parameters of $(NH_4)Cr(III)[BP_2O_8(OH)]$ **(3)** (*Rietveld* refinement; this work) and $(NH_4)V(III)[BP_2O_8(OH)]$ **(4)** (single-crystal structure; [248]); standard deviations in brackets

Sum formula	$(NH_4)Cr(III)$ $[BP_2O_8(OH)]$ **(3)**	$(NH_4)V(III)$ $[BP_2O_8(OH)]$ **(4)**
Molar weight / g·mol^{-1}	287.80	286.74
Crystal system	monoclinic	monoclinic
Space group	$P2_1/c$ (no. 14)	$P2_1/c$ (no. 14)
Colour	dark green	pale green
a / Å	9.3389(1)	9.425(2)
b / Å	8.2771(1)	8.269(2)
c / Å	9.5910(1)	9.697(2)
β / °	102.776(1)	102.26(2)
Volume / Å^3	723.03(2)	738.5(2)
Z	4	4
Calculated density D_x / g·cm^{-3}	2.644	2.579(1)
R_p / R_{int}	0.024	0.0747
Refined parameters	62	
R_{wp} / $R1$ (all data)	0.035	0.0329
χ^2 / $wR2$ (all data)	4.75	0.0728

The protonated borate and one phosphate ($P2O_4$) tetrahedron exhibit a larger deviation of tetrahedra (–1.12 % and –1.15 %) compared to the $P1O_4$ phosphate tetrahedron (–0.73 %). B–O bonds are distinguished between three B–O_{br} and one B–O_H bond. Due to less effective negative charge on the bridging oxygen atom, the B–O_{br} distances are expected to be longer than the B–O_H distance. However, d(B–O_H) reveals a distance of 1.49 Å, whereas d(B–O_{br}) exhibits distances of 1.47–1.49 Å in **(3)**. In **(4)** the B–O bond lengths are 1.46 Å (B–O_H) and 1.48–1.49 Å (B–O_{br}), which fit very well in the range of B–O bonds [122, 180, 248]. Besides the the B–O bond lengths the P–O bond lengths show a broad range in **(3)**. Whereas P–O_{br} distances lie between 1.46–1.63 Å, P–O_{term} distances range between 1.45–1.60 Å. The general trend indicates a shorter P–O_{term} bond compared to the P–O_{br} bond, but does not show a clear differentiation. Furthermore, the upper limit of the P–O distances reaching 1.60 Å or more is already quite large for borophosphates. Thus, the combination of diverging distances and angles in $P2O_4$ and BO_4, respectively, leads to a deviation of tetrahedra > 1 %. This may be owed to the fact that a *Rietveld* refinement does not provide that accurate atomic positions and hence less precise values of interatomic distances.

MAPLE results for **(3)** deviate by 5.2 % from electrostatic consistency. Omitting the protons of the ammonium ion by keeping neutrality of charge showed a way stronger deviation of the MAPLE value (–12.5 %). Calculations for **(4)** revealed similar results. Exhibiting such a strong impact on the electrostatic balance and thus on the stability, slight shifts of Cr/V, P, B and O atoms may be neglected in contrast to the position of the ammonium ion. Presumably the ammonium ion shows a tendency to rotate. In combination with the quite low scattering contribution of the hydrogen atoms a clear location is quite difficult. Thus, MAPLE values of compounds including NH_4^+ ions should be treated with caution.

In-between the borophosphate chains Cr^{3+} and NH_4^+ ions are located. The Cr^{3+} ions are coordinated by six oxygen atoms. Due to the distortion of the octahedral coordination polyhedra inversion symmetry is broken and optical transitions become allowed. Additionally, in a d^3 transition metal in an octahedral surrounding transitions are only allowed if the total spin does not change (spin prohibition). In **(3)** three optical transitions occur in the UV, blue and orange-red region. Thus, wavelengths in the green region are reflected and lead to an intense dark green body colour.
According to the authors, **(4)** possesses a pale green body colour [248]. In a d^2 system also three different absorption bands are expected. The two electron transition ($^3T_{1g} \rightarrow {}^3A_{2g}$) is weak and appears in the UV at about 277 nm. The $^3T_{1g} \rightarrow {}^3T_{2g}$ and $^3T_{1g} \rightarrow {}^3T_{1g}(P)$ transitions occur at 580 and 390 nm, respectively [42]. Thus, only wavelengths of the yellow-orange region are absorbed, which results in a blueish green body colour. The coordination distances $d(V^{3+}\text{–}O)$ in the range of 1.97–2.08 Å are slightly larger than the $d(Cr^{3+}\text{–}O)$ distances, which lie between 1.89–2.10 Å. This trend is expected since the ionic radii of V^{3+} and Cr^{3+} in an octahedral environment behave in the same way ($r(V^{3+}) = 0.79$ Å, $r(Cr^{3+}) = 0.62$ Å[60]).

7.3.8 Thermal Discussion

Thermal analysis showed that $(NH_4)Cr(III)[BP_2O_8(OH)]$ **(3)** is stable up to 300 °C, before a loss of presumably NH_3 and H_2O over a wide temperature range up to 800 °C occurs. This was also assumed by *Kritikos et al.* [248] (Figure 7.44). In $(NH_4)V(III)[BP_2O_8(OH)]$ **(4)** the first step of thermal decomposition is already finished at 670 °C. Unfortunately the thermal behaviour of **(4)** has not been investigated at temperatures >670 °C for a better comparison. By increasing the temperature further up to 1400 °C Cr_2O_3 besides an unknown but crystalline phase are built (Figure 7.43). Heating **(3)** up to 800 °C in N_2 a grey-green powder is obtained. The first step of mass loss is finished and BPO_4 represents the main phase besides the unknown side phase, which also occurs at higher temperature (Figure 7.43).

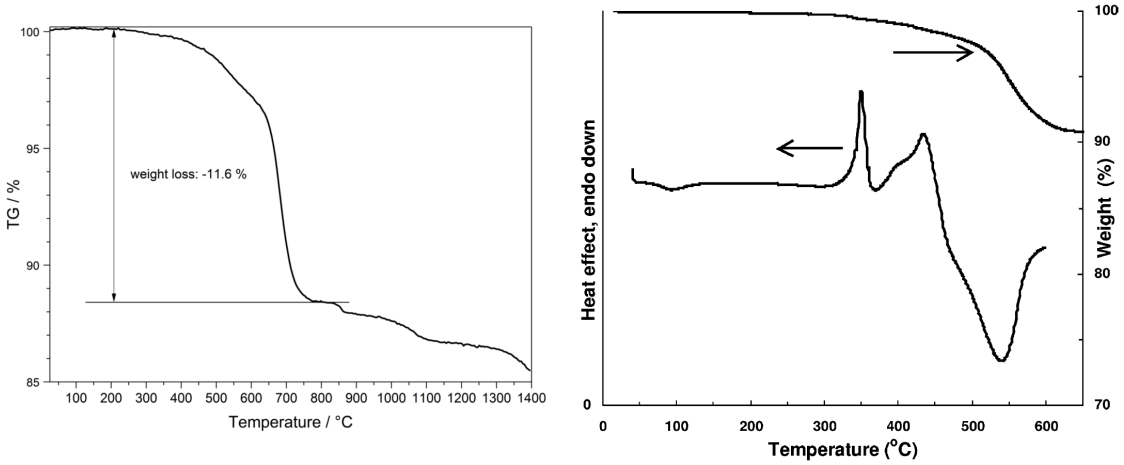

Figure 7.44: Comparison of the thermogravimetric analysis of $(NH_4)Cr(III)[BP_2O_8(OH)]$ and $(NH_4)V(III)[BP_2O_8(OH)]$ [248].

The IR spectrum of the product after the thermal analysis at 1400 °C still confirms the presence of N–H bands at 3210 and 1396 cm^{-1} (Figure 7.45). Thus, the following reaction equation is suggested (Equation 7.10):

$$NH_4Cr[BP_2O_8(OH)] + BPO_4 \xrightarrow[N_2]{\Delta} NH_3 + 1.5H_2O + 2BPO_4 + 0.5\,Cr_2O_3 + NH_4CrP_2O_7 \quad (7.10)$$

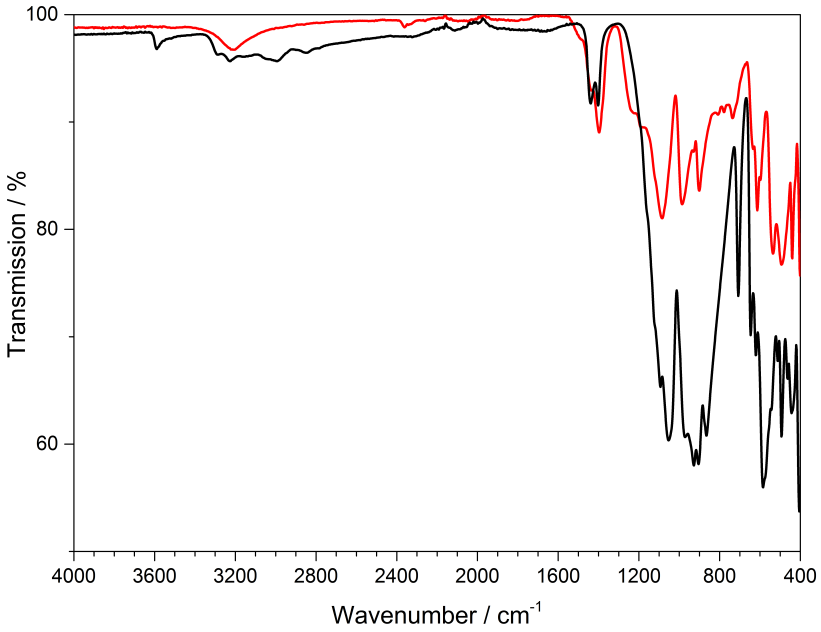

Figure 7.45: Comparison of the infrared spectra of $(NH_4)Cr(III)[BP_2O_8(OH)]$ (black) and $(NH_4)Cr(III)[BP_2O_8(OH)]$ after the thermal analysis (red).

The single-crystal structure of $NH_4CrP_2O_7$ has not been solved yet. However, *Durif* reported that monovalent-trivalent cation diphosphates, which exhibit K, NH_4, Rb, Cs and Tl are derivatives that crystallise with the $NaFeP_2O_7$(I) structure [264]. Nevertheless, the simulated X-ray powder diffractogram of $NaFeP_2O_7$ (I) [265] does not fit to the observed side phase. Additionally, the question raises if an ammonia containing phosphate possesses such an exceptional thermal stability. *Grunze et al.* reported about the synthesis temperature of $NaFeP_2O_7$(II) at about 1100 °C [266]. Thus, it might be possible that $NH_4CrP_2O_7$ crystallises in another modification at 1400 °C.

(3) was obtained containing 20 % of BPO_4 as side phase. Further optimisation of the reaction conditions did not lead to phase pure samples. *Kritikos et al.* were also faced with this problem and thus separated single-crystals of **(4)** mechanically using an optical microscope [248]. Unfortunately the sample of **(3)** is exclusively a polycrystalline powder, which made a separation by hand impossible.

8 The First Borosulphate $K_5[B(SO_4)_4]$

$K_5[B(SO_4)_4]$ is the first representative of its kind exhibiting B–O–S connections. That sort of connection was already suspected by *Schott* and *Kibbel* expecting a highly interconnected anionic network after receiving hygroscopic crystalline products from the reaction of H_3BO_3 with SO_3 and A_2SO_4 (A = alkaline metal) [267]. Due to the hygroscopic and chemically aggressive character only X-ray powder diffraction could be performed, while single-crystal structure analysis was not possible [267]. At the same time *Gillespie* and *Robinson* investigated dilute solutions of H_3BO_3 and B_2O_3 in 100 % H_2SO_4 and dilute oleum and reported the formation of a tetra(hydrogensulphato)boric acid, $HB(HSO_4)_4$, and its hydronium salt as rather strong acids. By adding metal sulphates dissolved in sulphuric acid the solutions were neutralised and after a few hours to days colourless slightly hygroscopic salts were received, which were investigated by cryoscopic and conductometric measurements [268].

$K_5[B(SO_4)_4]$ exhibits a chiral crystal structure and thus reveals great potential as efficient host lattice in luminescent materials doped with activator ions, e.g. Eu^{2+}, Eu^{3+}, Tb^{3+} [45, 61, 64, 269]. Due to the relatively high electronegativity of the S^{6+} ions a weak coordination of the cation and thus also a weak nephelauxetic effect is expected, which influences the luminescence properties of the activator ion [270].

Derived from the well-known and manifold groups of borophosphates, borosulphates comprise a promising structural variety [13, 135, 136, 271]. The non-protonated oB pentamer as FBU of $K_5[B(SO_4)_4]$ is already known for borophosphates, where up to now only a few compounds were found [13]. Most results presented in this chapter are published in a science journal [129, 272].

8.1 Synthesis

$K_5[B(SO_4)_4]$ was synthesised via a solid state reaction. 154.3 mg (0.6067 mmol) $K_2S_2O_7$ and 12.50 mg (0.2022 mmol) H_3BO_3 were ground in an agate mortar and transferred into a corundum crucible. The reaction mixture was heated up to 375 °C with a heating rate of 30 °C/h using a muffle furnace. The temperature was kept for 15 hours before cooling down to room temperature with a cooling rate of 20 °C/h. $K_5[B(SO_4)_4]$ was obtained as colourless, slightly hygroscopic crystalline powder.

Phase pure $K_2S_2O_7$ as precursor was synthesised by heating $KHSO_4$ for 11 days at 200 °C (Equation 8.1).

$$2KHSO_4 \xrightarrow{200\,^\circ C} K_2S_2O_7 + H_2O \tag{8.1}$$

8.2 X-Ray Powder Diffraction

The phase purity of the sample was checked by X-ray powder diffraction (Figure 8.1) and confirmed the formation of phase pure $K_5[B(SO_4)_4]$. The intensities and also the positions of all of the reflections are in very good agreement with the calculated data based on the structure model derived from single-crystal data (Chapter 8.3).

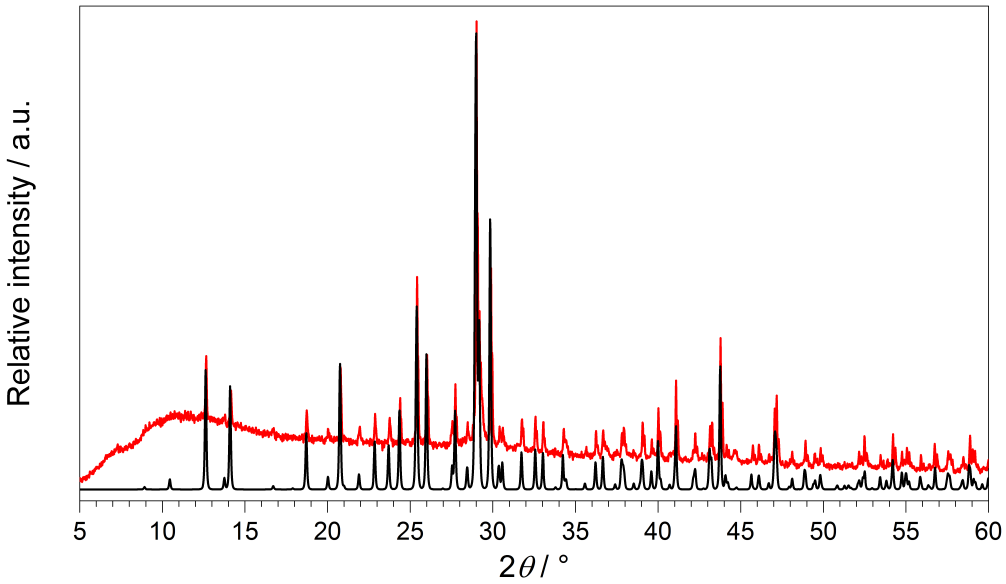

Figure 8.1: X-ray powder diffraction pattern of $K_5[B(SO_4)_4]$ (red) and calculated X-ray powder diffraction pattern from single-crystal data of $K_5[B(SO_4)_4]$ (black).

8.3 Crystal Structure Determination

A colourless single-crystal of $K_5[B(SO_4)_4]$ with a size of 0.25 × 0.22 × 0.15 mm^3 was isolated and mounted on a *MicroMount*. The collection of the crystal data was run on a Stoe IPDS 2 diffractometer. The data were corrected for absorption by applying a numerical correction on the basis of an optimized crystal shape by the software tool X-Shape of the program X-Area [273]. $K_5[B(SO_4)_4]$ crystallises in a new structure type in the tetragonal space group $P4_1$ with the lattice parameters $a = 9.9023(5)$ Å, $c = 16.1871(10)$ Å.

4156 reflections were collected. Out of 2744 independent reflections 2493 were observed ($F_o^2 > 2\sigma\ (F_o^2)$, $R_{int} = 0.042$). The crystallographic data, the parameters of the measurement and refinement are summarised in Table 8.1. The structure was solved by direct methods using the programs SHELXS-97 and SHELXTL-97 [21, 22] and refined applying a twin law ($0\,1\,0\,1\,0\,0\,0\,0\,\bar{1}$; BASF = 0.373(3)) with anisotropic displacement parameters for all atoms. The anisotropic refinement revealed R-values of $R1 = 0.0528$ and $wR2 = 0.1045$. The K, B, S and O atoms could be clearly located. The refined atomic coordinates, anisotropic displacement parameters, selected interatomic distances and angles are summarised in Tables 8.2 to 8.4.

Table 8.1: Single-crystal refinement parameters of $K_5[B(SO_4)_4]$; standard deviations in brackets

Sum formula	$K_5[B(SO_4)_4]$
Temperature / K	293(2)
Molar weight / g·mol^{-1}	590.56
Crystal system	tetragonal
Space group	$P4_1$ (no. 76)
Crystal shape	block
Crystal size / mm^3	0.25 × 0.22 × 0.15
Colour	colourless
a / Å	9.9023(5)
c / Å	16.1871(10)
Volume / Å^3	1587.23
Z	4
Calculated density D_x / g·cm^{-3}	2.464
Absorption coefficient μ / mm^{-1}	1.986
F(000)	1168
Radiation (λ / Å)	Mo-K_α (0.7093)
Diffractometer	Stoe IPDS 2
Absorption correction	numerical
Transmission factor (min./max.)	0.62 / 0.75
Index range h|k|l (min./max.)	-10/11 | -11/11 | -19/19
Theta range / °	$2.06 \leq \theta \leq 24.99$
Reflections collected	4156
Independent reflections	2744
Observed reflections	2493 ($F_o^2 > 2\sigma\ (F_o^2)$)
R_{int}	0.042
Refined parameters	237
R_σ	0.054
$R1$ (all data)	0.0528
$wR2$ (all data)	0.1045
Flack parameter	0.03(11)
Weighting scheme	$w^{-1}=\sigma^2\ F_o^2 + (0.0550\ P)^2$; $P = (F_o^2 + 2\ F_c^2)/3$
GooF	1.093
Residual electron density (min./max.) / e$^-$·Å^{-3}	-0.34/0.36

Table 8.2: Refined atomic coordinates, *Wyckoff* symbols and isotropic displacement parameters U_{eq} / Å^2 in $K_5[B(SO_4)_4]$; standard deviations in brackets

Atom	*Wyckoff* symbol	x	y	z	U_{eq}
K1	4*a*	0.7550(3)	0.0474(3)	0.25636(14)	0.047(6)
K2	4*a*	0.8543(3)	−0.3272(3)	0.08225(17)	0.0479(6)
K3	4*a*	0.5842(2)	0.3492(2)	0.04888(14)	0.0388(6)
K4	4*a*	1.1702(2)	−0.0920(2)	0.10501(14)	0.0383(5)
K5	4*a*	0.2437(2)	−0.4964(2)	0.14896(13)	0.0385(5)
B1	4*a*	0.5157(12)	−0.0071(10)	0.0809(7)	0.027(2)
S1	4*a*	0.7775(3)	0.0143(2)	0.03988(15)	0.0313(5)
S2	4*a*	0.4895(2)	−0.2704(2)	0.11574(15)	0.0306(5)
S3	4*a*	0.3949(3)	0.1576(3)	0.19629(14)	0.0344(6)
S4	4*a*	0.8997(3)	0.3801(2)	0.19499(14)	0.0292(5)
$O_{br}1$	4*a*	0.6575(7)	0.0117(7)	0.1030(4)	0.0302(14)
$O_{br}2$	4*a*	0.4827(7)	−0.1464(6)	0.0555(4)	0.0274(14)
$O_{br}3$	4*a*	0.4303(7)	0.0228(7)	0.1530(4)	0.0304(15)
$O_{br}4$	4*a*	0.9134(7)	0.4908(7)	0.2619(4)	0.0323(15)
$O_{term}1$	4*a*	0.7495(9)	−0.0849(10)	−0.0227(5)	0.063(3)
$O_{term}2$	4*a*	0.8934(8)	−0.0201(9)	0.0889(5)	0.055(2)
$O_{term}3$	4*a*	0.7839(8)	0.1485(8)	0.0092(5)	0.051(2)
$O_{term}4$	4*a*	0.4789(9)	−0.3846(8)	0.0608(5)	0.050(2)
$O_{term}5$	4*a*	0.6166(8)	−0.2662(10)	0.1591(6)	0.067(3)
$O_{term}6$	4*a*	0.3731(7)	−0.2601(7)	0.1699(4)	0.0397(17)
$O_{term}7$	4*a*	0.3374(13)	0.2455(10)	0.1388(5)	0.091(4)
$O_{term}8$	4*a*	0.3114(9)	0.1177(8)	0.2635(5)	0.055(2)
$O_{term}9$	4*a*	0.5225(9)	0.2092(11)	0.2268(6)	0.079(3)
$O_{term}10$	4*a*	0.9353(9)	0.2527(7)	0.2306(5)	0.050(2)
$O_{term}11$	4*a*	0.7595(7)	0.3922(9)	0.1725(4)	0.051(2)
$O_{term}12$	4*a*	0.9878(9)	0.4194(8)	0.1288(4)	0.051(2)

O_{br} = bridging oxygen atom; O_{term} = terminal oxygen atom;

Table 8.3: Anisotropic displacement parameters U_{ij} / Å^2 in $K_5[B(SO_4)_4]$; standard deviations in brackets

Atom	U_{11}	U_{22}	U_{33}	U_{12}	U_{13}	U_{23}
K1	0.0406(13)	0.0635(17)	0.0385(12)	0.0055(13)	0.0013(11)	−0.0016(12)
K2	0.0487(15)	0.0421(15)	0.0529(13)	0.0081(12)	0.0035(12)	0.0024(12)
K3	0.0392(14)	0.0361(13)	0.0413(12)	−0.0045(10)	0.0008(10)	−0.0021(9)
K4	0.0350(12)	0.0395(13)	0.0404(11)	0.0071(11)	−0.0002(10)	−0.0042(10)
K5	0.0374(13)	0.0409(14)	0.0371(11)	0.0032(10)	0.0000(10)	−0.0062(10)
B1	0.037(6)	0.015(5)	0.029(4)	0.000(4)	−0.009(5)	−0.007(4)
S1	0.0282(12)	0.0301(14)	0.0358(13)	−0.0006(11)	0.0039(10)	0.0012(9)
S2	0.0261(12)	0.0304(13)	0.0352(13)	0.0086(11)	0.0016(10)	−0.0012(10)
S3	0.0457(15)	0.0284(12)	0.0291(11)	−0.0002(10)	0.0061(11)	0.0032(12)
S4	0.0293(12)	0.0310(12)	0.0273(10)	−0.0018(10)	−0.0015(10)	−0.0012(10)
$O_{br}1$	0.026(3)	0.037(4)	0.028(3)	−0.005(3)	−0.002(3)	−0.002(3)
$O_{br}2$	0.032(4)	0.022(3)	0.028(3)	0.006(3)	−0.004(3)	−0.004(3)
$O_{br}3$	0.028(4)	0.028(3)	0.035(4)	−0.002(3)	0.008(3)	0.003(3)
$O_{br}4$	0.033(4)	0.033(4)	0.031(3)	−0.012(3)	−0.011(3)	0.007(3)
$O_{term}1$	0.048(5)	0.076(7)	0.066(5)	−0.047(5)	0.021(4)	−0.015(5)
$O_{term}2$	0.025(4)	0.075(6)	0.067(5)	0.024(5)	−0.005(4)	0.012(4)
$O_{term}3$	0.050(5)	0.042(5)	0.060(5)	0.024(4)	0.017(4)	0.002(3)
$O_{term}4$	0.077(6)	0.022(4)	0.051(4)	−0.006(3)	0.014(4)	0.002(4)
$O_{term}5$	0.037(4)	0.085(7)	0.079(6)	0.044(6)	−0.034(4)	−0.014(5)
$O_{term}6$	0.047(4)	0.028(4)	0.043(4)	0.003(3)	0.017(3)	−0.004(3)
$O_{term}7$	0.156(10)	0.074(6)	0.042(4)	0.016(4)	0.019(5)	0.079(7)
$O_{term}8$	0.066(6)	0.045(4)	0.054(5)	0.008(4)	0.038(4)	0.004(4)
$O_{term}9$	0.049(5)	0.092(7)	0.095(7)	−0.050(6)	0.019(5)	−0.026(5)
$O_{term}10$	0.082(6)	0.018(4)	0.050(4)	0.000(3)	−0.017(4)	0.004(4)
$O_{term}11$	0.019(3)	0.077(6)	0.058(5)	−0.019(4)	−0.005(3)	0.003(4)
$O_{term}12$	0.054(5)	0.065(5)	0.033(4)	−0.005(4)	0.017(4)	−0.020(4)

Table 8.4: Selected interatomic distances / Å and angles / ° in $K_5[B(SO_4)_4]$; standard deviations in brackets

B–O_{br}	1.462(14)–1.477(13)
S–O_{br}	1.548(7)–1.571(7)
S–O_{term}	1.397(8)–1.453(8)
K–O	2.674(8)–3.533(2)
B–O_{br}–S	123.3(7)–134.8(7)
O_{br}–B–O_{br}	105.5(9)–113.6(7)
O–S–O	101.7(4)–116.5(6)

8.4 Crystal Structure Description

$K_5[B(SO_4)_4]$ crystallises in a new structure type in the tetragonal space group $P4_1$ with four formula units per unit cell. All atoms are located on the general *Wyckoff* position 4*a*. The anionic partial structure of $K_5[B(SO_4)_4]$ consists of novel, large non-condensed $^0_\infty[B(S\Phi_4)_4]^{5-}$ ($\Phi = O$) anions, which form tetrahedral units (Figure 8.2). The central boron atoms adopt an only slightly distorted body-centered packing (Figure 8.3).

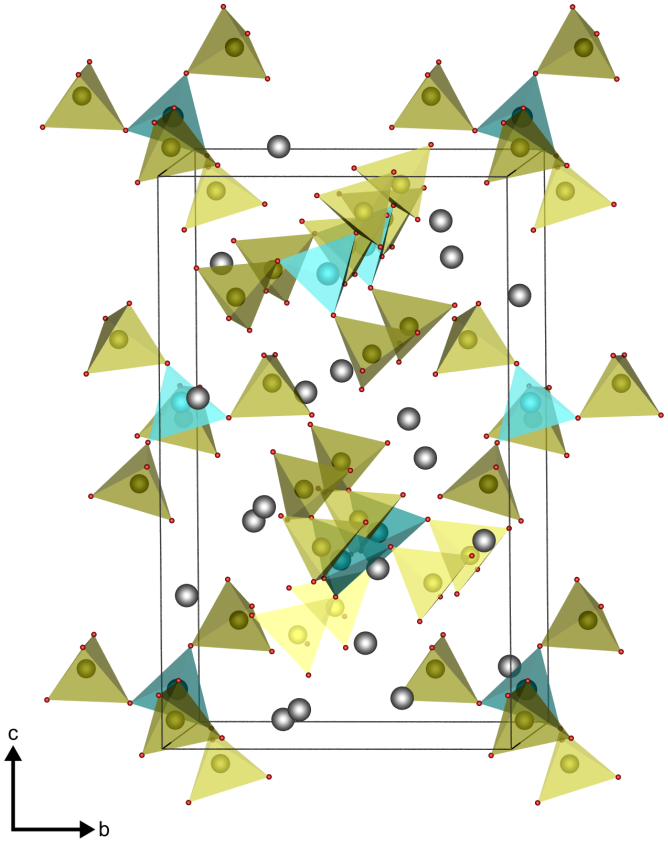

Figure 8.2: Unit cell of $K_5[B(SO_4)_4]$; sulphate tetrahedra yellow, borate tetrahedra turquoise, sodium grey.

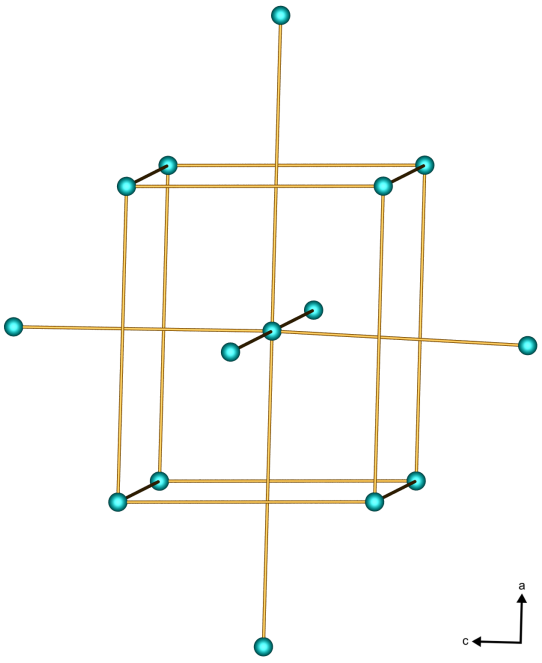

Figure 8.3: Distorted bcc structure of boron atoms.

Adopting the classification of borophosphates, which was overtaken analogously from silicate and borate chemistry, $K_5[B(SO_4)_4]$ exhibits a FBU as oB pentamer with the descriptor 5□:[□]□|□|□|□| [13, 82, 83, 113]. The central borate tetrahedron shares all four corners with neighbouring sulphate tetrahedra (Figure 8.4).

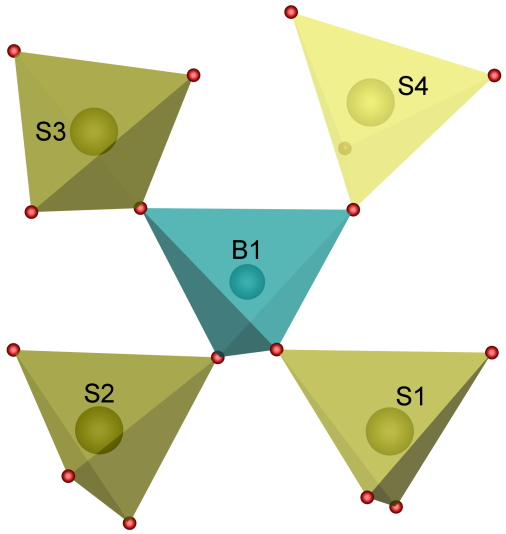

Figure 8.4: OB pentamer as FBU in $K_5[B(SO_4)_4]$; sulphate tetrahedra yellow, borate tetrahedron turquoise.

In borophosphates no P–O–P linking has been observed yet, which appears analogously to alumosilicates according to *Loewenstein's* rule [118]. In contrast, in borosulphates S–O–S connections could be observed exhibiting disulphate groups in isolated monoanions $[B(S_2O_7)_2]^-$, e.g. in $A[B(S_2O_7)_2]$ (A = Li [136], Na, K [135]). The oB pentamer $[B(SO_4)_4]^{5-}$ comprises a B:S ratio of 1:4. Up to now $K_5[B(SO_4)_4]$ is besides the recently discovered $Na_5[B(SO_4)_4]$, which crystallises in two similar modifications, the only representative of a borosulphate with an oB pentamer as FBU [136].

In borophosphate chemistry few compounds are known with a B:P ratio of 1:4 [274–277]. Besides the borophosphate units either an additional phosphate group is present or heteropolyoxoclusters are arranged around spacious organic molecule cations. In contrast to borophosphates, which can be synthesised either hydrothermally or by solid-state reactions, the preparation of borosulphates, depending on the desired composition, can be followed by the solid-state synthesis route [13].

$B–O_{br}$ bond lengths range between 1.46 and 1.48 Å whereas $S–O_{br}$ bond lengths lie between 1.55 and 1.57 Å and $S–O_{term}$ range between 1.40 and 1.45 Å. Those values are typical for B–O and S–O bonds and were also observed in borates and sulphates, respectively [131, 148, 199, 278, 279]. The difference of bond lengths between sulphur and bridging and terminal oxygen atoms, respectively, could be also observed

in accordance with borophosphates, where bonds from phosphorus to bridging oxygen atoms are significantly longer compared to those to the terminal oxygen atoms [122]. Even in condensed sulphates, such as $A[Au(S_2O_7)_2]$ (A = Li, Na), this tendency could be observed [131]. B–O_{br}–S angles range between 123 and 135 °, whereas O_{br}–B–O_{br} and O–S–O angles lie between 106–114° (Ø = 110°) and 102–117° (Ø = 109°), respectively. Selected bond lengths and angles of $K_5[B(SO_4)_4]$ are listed in Table 8.4.

The deviation of tetrahedra from ideal symmetry was calculated using the method of *Balić-Žunić* and *Makovicky* [35, 36]. The five crystallographically different borate and sulphate tetrahedra in $K_5[B(SO_4)_4]$ feature the values −0.38 % (B1), −0.08 % (S1), −0.15 % (S2), −0.12 % (S3) and −0.22 % (S4), which are well below 1 % and thus can be classified as regular. The chiral super-tetrahedron BS_4 exhibits a deviation from ideal symmetry of -4.04 % [140].

The single-crystal structure analysis reveals five sites of K^+ ions which are coordinated quite heterogeneously either by seven, nine or eleven oxygen atoms (Figure 8.5). The K–O bond lengths range between 2.67 and 3.53 Å (Table 8.4). These values agree very well with the sum of the ionic radii of K^+ and O^{2-}, which are 2.86 (CN = 7), 2.95 Å (CN = 9) and 3.04 Å (CN = 11), respectively [60]. These coordination numbers were also confirmed by MAPLE calculations (Chapter 8.5).

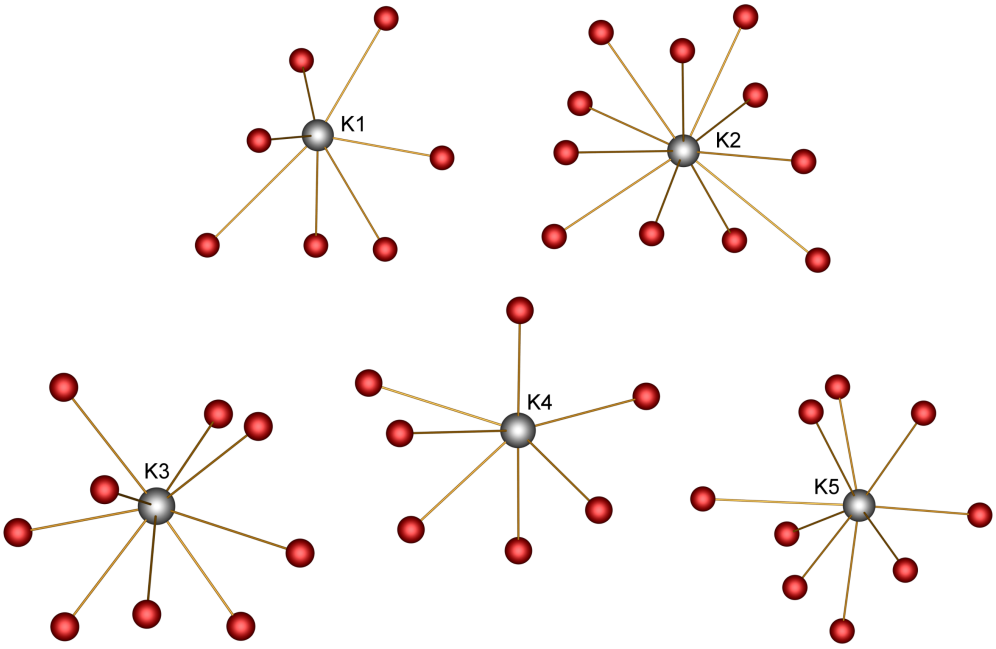

Figure 8.5: Coordination sphere of the five crystallographically different potassium atoms in $K_5[B(SO_4)_4]$.

8.5 Electrostatic Calculations

The coordination numbers of potassium (Table 12.11) and the electrostatic consistency of the structure model were proved by calculations based on the MAPLE concept [32, 33, 152]. The sum of MAPLE values of chemically similar compounds should deviate by less than 1 % from the MAPLE value of the compound of interest. $K_5[B(SO_4)_4]$ thus shows electrostatic consistency, as presented in Table 8.5.

Table 8.5: MAPLE calculations for $K_5[B(SO_4)_4]$ [32, 33, 152]

$K_5[B(SO_4)_4]$	2 $K_2S_2O_7$ [280] + 0.5 K_2O [281] + 0.5 B_2O_3 [154]
MAPLE = 140112 kJ·mol^{-1}	MAPLE = 138974 kJ·mol^{-1}
$\Delta = 0.8$ %	

8.6 Spectroscopic Properties

8.6.1 IR Spectroscopy

The infrared spectrum of $K_5[B(SO_4)_4]$ was recorded between 4000 and 400 cm^{-1}. Typical bands are present in the section between 1300 and 400 cm, which is shown in Figure 8.6. The positions of the bands and the corresponding assignments are given in Table 8.6.

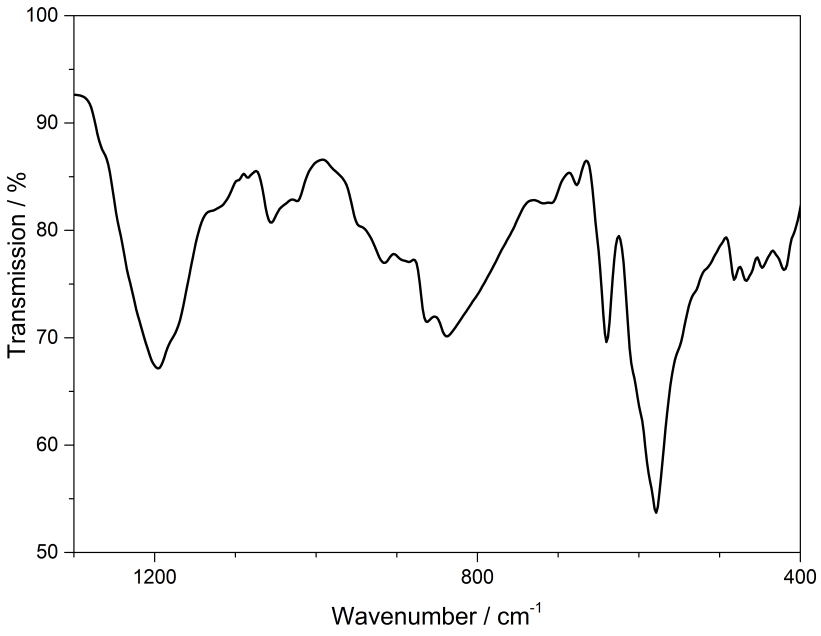

Figure 8.6: Infrared spectrum of $K_5[B(SO_4)_4]$.

Table 8.6: Position / cm^{-1} and assignment of the IR bands in $K_5[B(SO_4)_4]$

Position	Assignment
1196	ν_{as}(SO) [282, 283]
1055, 1024, 947	ν_{as}(BO) [156, 194]
916, 862, 839, 767, 716	ν_{s}(BO) [156, 194]
640	δ_{as}(SO) [282–284]
579	δ(BO) [156]
482, 467, 447, 420	δ_{s}(SO) [282, 283]

Between 1300 and 400 cm^{-1} the characteristic bands of the tetrahedral BO_4 and SO_4 groups are located [156, 283]. With exception of two bands at 3209 and 1412 cm^{-1}, which can be assigned to the stretching and deformation vibrations of the OH groups of the adsorbed water due to the hygroscopicity of the compound, the spectrum between 4000 and 1300 cm^{-1} does not show any considerable vibration bands [194]. The very strong band at 1196 cm^{-1} can be assigned to the ν_{as}(SO) vibrations of the SO_4 tetrahedra [282, 283]. Between 930 and 1090 cm^{-1} the characteristic bands of the ν_{as}(BO) vibrations are located, whereas between 660 and 920 cm^{-1} the ν_{s}(BO) vibrations can be found [156, 194]. The asymmetric SO_4 bending modes appear at 640 cm^{-1} [282–284] and the BO_4 bending modes can be assigned to the strong band at 579 cm^{-1} [156]. Between 400 and 500 cm^{-1} the symmetric SO_4 bending modes are located [282, 283]. Additionally, *Höppe et al.* performed a structural and vibrational study of $K_5[B(SO_4)_4]$ based on quantum chemical calculations. The assignment of the observed bands in the IR spectrum revealed a good correlation compared to the calculated values, exhibiting deviations of less than 50 cm^{-1} [285].

8.6.2 UV-Vis Spectroscopy

The UV–Vis reflection spectrum of $K_5[B(SO_4)_4]$ was recorded between 200–800 nm (Figure 8.7) and shows nearly total reflection between 390–800 nm. At 230 and 299 nm two ligand-to-metal charge transfer bands can be observed. The $[B(SO_4)_4]^{5-}$ anion reveals a weak nephelauxetic effect due to the highly polarised and thus electronegative S^{6+} ion. Hence, the charge transfer band at lower energy can be assigned to the sulphate group, whereas the charge transfer of the borate group appears at higher energy. The calculation of the optical electronegativity by *Klixbüll Jørgensen* [286] leads to values of $\chi(S) = 2.33$ for sulphur and $\chi(B) = 1.99$ for boron, which are very close to the electronegativity values of *Pauling* ($\chi(S) = 2.58$, $\chi(B) = 2.04$) [287].

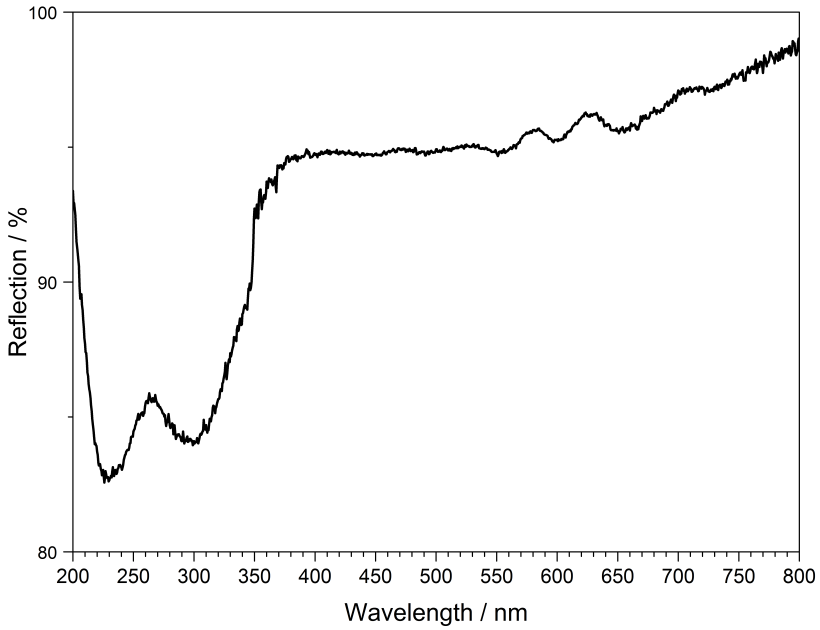

Figure 8.7: UV–Vis spectrum of $K_5[B(SO_4)_4]$.

8.7 Thermal Analysis

The thermal behaviour of $K_5[B(SO_4)_4]$ was investigated between room temperature and 1400 °C (Figure 8.8). The thermogravimetric curve reveals several undefined steps with a total mass loss of 59.7 wt% in the temperature range between 150 and 1300 °C. Assuming that along with 0.5 moles of B_2O_3, 1.5 moles of K_2O and 2 moles of SO_3 evaporate (theor. mass loss: 56.3 wt%) a composition of $K_2S_2O_7$ might be expected (Equation 8.2). Further heating leads to a subsequent mass loss, which is likely due to further evaporation of SO_3. After the thermal treatment the product was glazed and the expected composition could not be confirmed via X-ray powder diffraction.

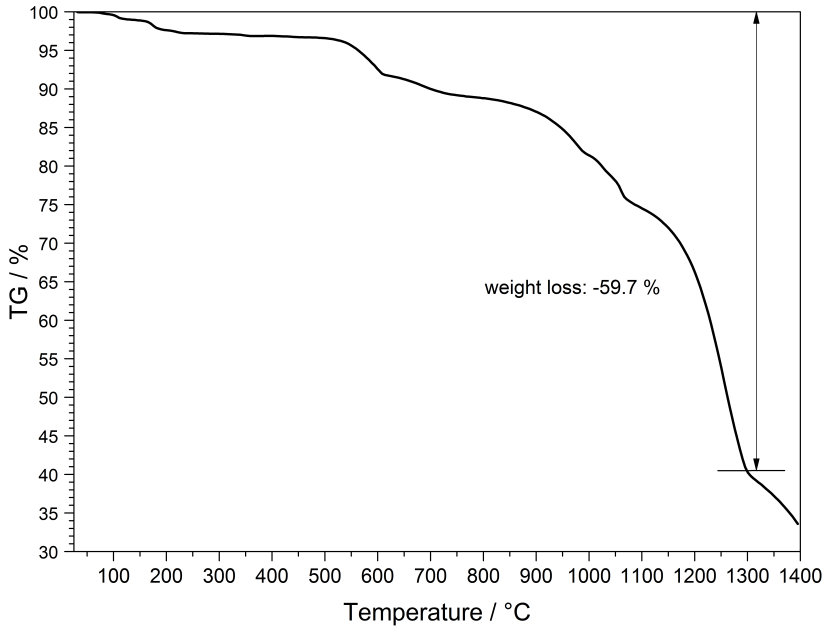

Figure 8.8: Thermogravimetric analysis of $K_5[B(SO_4)_4]$.

$$K_5[B(SO_4)_4] \xrightarrow[N_2]{\Delta} 0.5B_2O_3 + 1.5K_2O + 2SO_3 + K_2S_2O_7 \tag{8.2}$$

In comparison to the very similar compound $Na_5[B(SO_4)_4]$-I [136], which also reveals isolated $[B(SO_4)_4]^{5-}$ units but crystallises in the orthorhombic space group $Pca2_1$, $K_5[B(SO_4)_4]$ exhibits a higher thermal stability. $Na_5[B(SO_4)_4]$-I releases besides 1.5 moles of SO_3 0.5 moles of B_2O_3 in the temperature range between 430–700 °C. In $K_5[B(SO_4)_4]$ this process stretches out until 1300 °C.

8.8 Discussion

$K_5[B(SO_4)_4]$ was synthesised phase-pure comprising a new structure type and a new compound class. The crystal structure was determined and refined via single-crystal structure analysis and by applying a twin law ($0\,1\,0\,1\,0\,0\,0\,0\,\bar{1}$; BASF = 0.373(3). Analogously to borophosphates, $^{0}_{\infty}[B(S\Phi_4)_4]^{5-}$ (Φ = O) anions represent the FBU as an oB pentamer 5□:[□]□|□|□|□| exhibiting a B:S ratio of 1:4. Via MAPLE calculations the electrostatic consistency of the structure model could be proofed. All observed bands in the IR spectrum could be assigned to the corresponding groups. The optical properties of $K_5[B(SO_4)_4]$ show two ligand-to-metal charge transfer bands at 230 and 299 nm. According to the different nephelauxetic effects of the involved groups, the bands can be assigned to the borate and sulphate groups, respectively. Due to the chiral structure without inversion symmetry, $K_5[B(SO_4)_4]$ is a suited host structure for doping with lanthanides. Furthermore, the relatively high electronegativity of sulphur leads to a weak coordination of the cation and thus to a weak nephelauxetic effect to shift the luminescence properties into the blue region of the visible spectrum. Additionally, it shows a higher thermal stability than $Na_5[B(SO_4)_4]$-I [136], whose decomposition proceeds until 700 °C, although both compounds possess the same FBU and very similar crystal structures.

9 General Discussion

9.1 Experience of Synthesis

For the synthesis of the compounds introduced in this work several synthesis routes have been carried out. Besides the hydrated borate $Cs_2[B_{10}O_{14}(OH)_4]\cdot H_2O$ and the phosphates ($Ln[H(PO_3)_4]$ ($Ln =$ Tb, Dy, Ho)), all borophosphates and the borosulphate were synthesised under mild conditions at relatively low temperatures between 180 and 380 °C. Both $Cs_2[B_{10}O_{14}(OH)_4]\cdot H_2O$ and the borophosphates were synthesised in 10 ml teflon autoclaves, which were kept at 195 and 180 °C, respectively, for seven to eight days. This synthesis route was time-consuming but inevitable. Due to reaction temperatures below 200 °C and the presence of predominantly solid starting materials diffusion takes place quite slowly. Reducing the reaction time revealed mixtures of starting materials and side products. The long duration of the reaction time is justified by the relatively high crystallinity of the products in general, which strongly facilitates the analysis of the single-crystal structure.

$Ln[H(PO_3)_4]$ ($Ln =$ Tb, Dy, Ho) were synthesised in a solid state reaction in a silica glass crucible at 380 °C for four hours. The loss of the single proton in $Ln[H(PO_3)_4]$ ($Ln =$ Tb, Dy) was prevented by covering the reaction mixture with H_2O_2, whereas addition of H_2O_2 for the synthesis of $Ho[H(PO_3)_4]$ exhibited $Ho(PO_3)_3$ as side phase. Elevating the synthesis temperature to 400 °C or reducing it to 350 °C had the same effect on all phosphates and lead to $Ln(PO_3)_3$ ($Ln =$ Tb, Dy, Ho). A controlled crystallisation could not be achieved yet. Besides $Dy[H(PO_3)_4]$, which crystallised as polycrystalline powder, $Tb[H(PO_3)_4]$ faced the problem of non-merohedral twin formation. Instead of switching off the furnace a long taking cooling process with cooling rates of 2 °C/h was carried out. However, besides the desired $Ln[H(PO_3)_4]$ also $Ln(PO_3)_3$ was formed as side phase.

In contrast, the non-protonated highly crystalline $Sr_3P_4O_{13}$ was synthesised in an alumina boat at a way higher temperature at 950 °C for several days. Shorter reaction times and a slightly reduced temperature lead to the formation of a polycrystalline powder. The synthesis of $Sr_3P_4O_{13}$:Eu^{2+} in *forming gas* at 850 °C either lead to the formation of $Sr_3P_4O_{13}$:Eu^{2+}/Eu^{3+} due to incomplete reduction, or to

$Sr_3P_4O_{13}:Eu^{2+}/Sr_2P_2O_7:Eu^{2+}$ after a longer reaction time, due to the formation of $Sr_2P_2O_7$ as side phase. The difficulty was to prevent the sample from loosing P_2O_5 in the *forming gas* flow, which is nevertheless favoured in a reducing atmosphere. This could be shown very clearly by a thermal analysis in *forming gas* and synthetic air (Figure 9.1). In a reducing atmosphere mass loss already occurs way below the synthesis temperature of 850 °C.

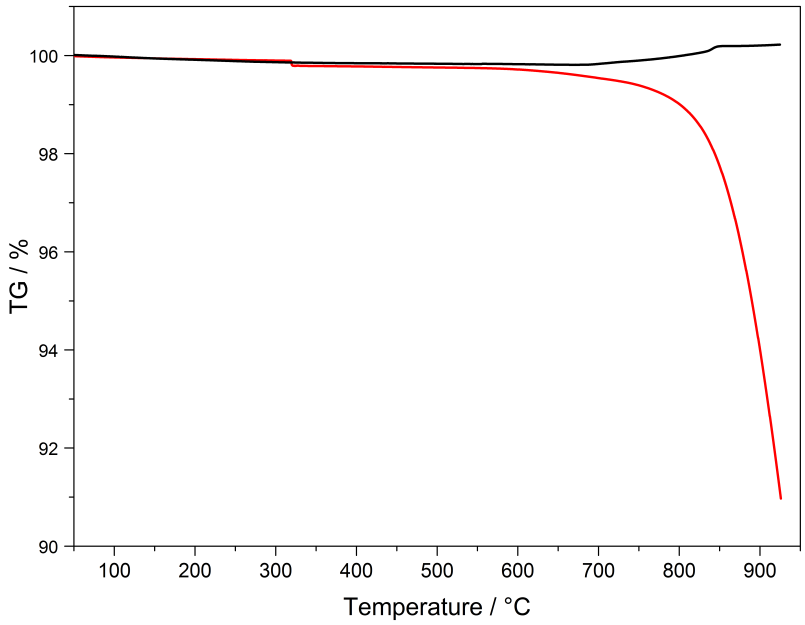

Figure 9.1: Thermogravimetric analysis of β-$Sr(PO_3)_2$ in synthetic air (black) and *forming gas* (red) between 50 and 925 °C with a heating rate of 20 °C·min^{-1}.

Although $K_5[B(SO_4)_4]$ does not exhibit protons the synthesis temperature of 375 °C was still quite low considering solid state reactions. H_3BO_3 as one reaction partner has to be treated carefully due to fast evaporation processes at higher temperatures or rapid heating rates. Thus, heating and cooling processes did not exceed 30 and 20 °C/h, respectively, which also had a positive effect on the crystallinity of the sample. Experiments showed that $KHSO_4$ as starting material instead of $K_2S_2O_7$ did not possess enough reactivity and mixtures of hydrated potassium sulphates and B_2O_3 resulted.

In general, solids served as starting materials, which were ground very carefully to obtain a better homogenisation and smaller particles. H_3BO_3 was used in particular for borates, borophosphates and borosulphates. Both for solid state and hydrothermal reactions it possesses a well suitable reaction behaviour due to the release of water at higher temperatures. Especially in hydrothermal reaction processes small amounts of water originating from crystal water or evaporation favour reactions between solids by serving as solvent and by increasing the pressure in the reaction

vessel. Furthermore, water soluble starting materials, e.g. $MnCl_2$ and $(NH_4)_2HPO_4$, lead to phase pure products by dissolving in the moist reaction mixture.

For doping with $Eu^{2+/3+}$, Ce^{3+} and Tb^{3+}, Eu_2O_3, $Eu(NO_3)_3{\cdot}5H_2O$, $Ce(NO_3)_3{\cdot}6H_2O$ and $Tb(NO_3)_3{\cdot}5H_2O$ were used. Doping levels were between 3.4 and 30 % with regard to the metal content in the starting material. A *forming gas* flow (90 % N_2/10 % H_2) served to reduce Eu^{3+} to Eu^{2+} in the reaction mixture.

9.2 Luminescent Materials and Optical Properties

Both Eu^{3+} and Tb^{3+} play an important role in red and green emitting luminescent materials [3, 4, 49]. Its characteristic f–f transitions are independent on the chemical surrounding [53, 64]. Nevertheless, at higher energies both LMCT and f–d transitions occur, which allow to draw conclusions on the chemical surrounding by means of their energetic position [288] (Figure 9.2).

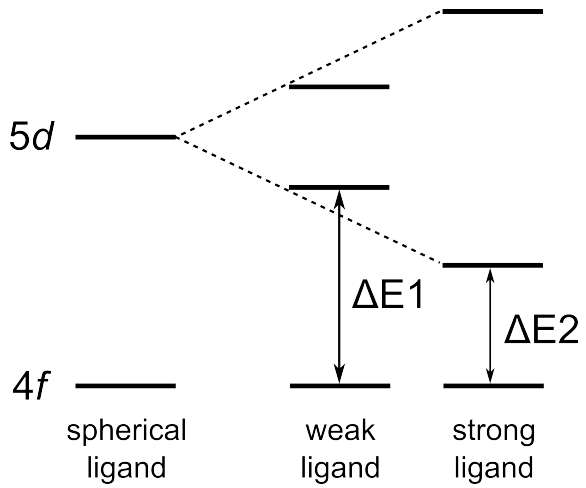

Figure 9.2: Schematic representation of the f–d ligand field splitting in dependence on the ligand strength.

9.2.1 LMCT of Eu^{3+}

Figure 9.3 shows the LMCT (*L*igand-to-*M*etal-*C*harge-*T*ransfer) of Eu^{3+} in $Cs_2[B_{10}O_{14}(OH)_4]{\cdot}H_2O{:}Eu^{3+}$ (black), $(NH_4)_2[B_2P_3O_{11}(OH)]{:}Eu^{3+}$ (red), $Sr_3P_4O_{13}{:}Eu^{3+}$ (green) and $Dy[H(PO_3)_4]{:}Eu^{3+}$ (blue), which are summarised in Table 9.1.

Surprisingly, the excitation wavelengths of the two phosphates, $Sr_3P_4O_{13}{:}Eu^{3+}$ and $Dy[H(PO_3)_4]{:}Eu^{3+}$, occur furthermost from each other, although both compounds

possess an anionic phosphate structure. Nevertheless, besides a varying coordination number also the distances between the central atom and the ligands differ. $Sr_3P_4O_{13}:Eu^{3+}$ exhibits larger distances between Sr and O (2.50–2.81Å), whereas distances d(Dy–O) in $Dy[H(PO_3)_4]:Eu^{3+}$ lie between 2.24–2.47 Å. Hence, due to a stronger coordination in $Dy[H(PO_3)_4]:Eu^{3+}$ a stronger ligand field splitting and thus an excitation at lower energy occurs.

The excitation wavelengths of $Sr_3P_4O_{13}:Eu^{3+}$ and $Cs_2[B_{10}O_{14}(OH)_4]\cdot H_2O:Eu^{3+}$ lie very closely at 264 and 266 nm, respectively. Due to the lower electronegativity of boron and the stronger nephelauxetic effect compared to phosphorus, the coordination sphere in borates reveals a more covalent character than in phosphates. In $Cs_2[B_{10}O_{14}(OH)_4]\cdot H_2O:Eu^{3+}$ ten and fourteen ligands are coordinating to the central atom, whereas in $Sr_3P_4O_{13}:Eu^{3+}$ only eight and nine are present. Hence, the coordination distances in $Cs_2[B_{10}O_{14}(OH)_4]\cdot H_2O:Eu^{3+}$ are larger, than in $Sr_3P_4O_{13}:Eu^{3+}$, which compensates the covalent character of the coordination sphere, and the chemical surrounding of both compounds leads to a very similar influence on the ligand field splitting.

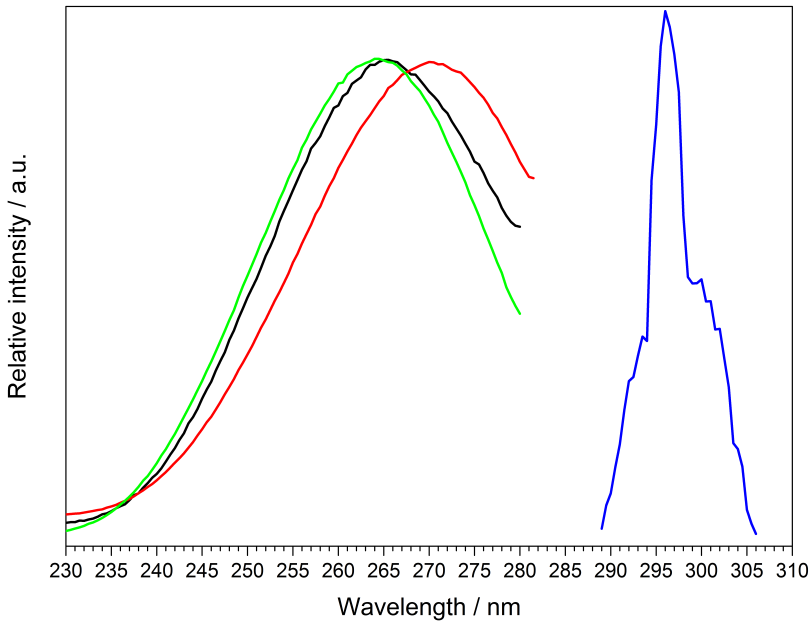

Figure 9.3: Comparison of the LMCT of Eu^{3+} in $Cs_2[B_{10}O_{14}(OH)_4]\cdot H_2O:Eu^{3+}$ (black), $(NH_4)_2[B_2P_3O_{11}(OH)]:Eu^{3+}$ (red), $Sr_3P_4O_{13}:Eu^{3+}$ (green) and $Dy[H(PO_3)_4]:Eu^{3+}$ (blue).

Table 9.1: Comparison of the excitation wavelength λ_{exc} of the LMCT of Eu^{3+} doped compounds

Compound	λ_{exc} / nm	CN	Distance CA–O / Å
$Sr_3P_4O_{13}$:Eu^{3+}	264	8/10	2.50–2.81
$Cs_2[B_{10}O_{14}(OH)_4]\cdot H_2O$:$Eu^{3+}$	266	10/14	2.80–4.00
$(NH_4)_2[B_2P_3O_{11}(OH)]$:$Eu^{3+}$	270	7/8	2.77–3.30
$Dy[H(PO_3)_4]$:Eu^{3+}	299	7	2.24–2.47

CN = Coordination Number, CA = Central Atom

In $(NH_4)_2[B_2P_3O_{11}(OH)]$:$Eu^{3+}$ the excitation wavelength occurs at 270 nm, which lies in close neighbourhood to $Sr_3P_4O_{13}$:Eu^{3+} and $Cs_2[B_{10}O_{14}(OH)_4]\cdot H_2O$:$Eu^{3+}$. According to single-crystal data distances between nitrogen and oxygen atoms are relatively large (2.77–3.30 Å) due to the presence of the hydrogen atoms of the ammonia ions ($r_{NH_4^+} = 1.43$ Å[243], $r_{Eu^{3+}} = 1.07$ Å[60]). In Chapter 7.2.6.3 the fluorescence spectrum of $(NH_4)_2[B_2P_3O_{11}(OH)]$:$Eu^{3+}$ was discussed. Due to the similar intensity of the $^5D_0 \rightarrow {}^7F_1$ and $^5D_0 \rightarrow {}^7F_2$ transition the occupation of more narrow interstitial sites close to centrosymmetry was presumed. Hence, the Eu–O distance should decrease and the coordination becomes more covalent, which leads to a lower transition energy compared to $Sr_3P_4O_{13}$:Eu^{3+} and $Cs_2[B_{10}O_{14}(OH)_4]\cdot H_2O$:$Eu^{3+}$. *Liang et al.* investigated the luminescent properties of $CaBPO_5$:Eu^{3+} [126] and $BaBPO_5$:Eu^{3+} [289]. The non-protonated borophosphates show a LMCT at about 246 nm and 264 nm, respectively. The transition wavelengths are at a slightly higher energy compared to $(NH_4)_2[B_2P_3O_{11}(OH)]$:$Eu^{3+}$. In $AEBPO_5$:Eu^{3+} (AE =Ca, Ba) Eu^{3+} presumably occupies the unique AE^{2+} site, which is coordinated irregularly by ten oxygen atoms. Thus, the coordination distances are relatively large and the coordination becomes weaker. As a consequence the LMCT occurs at a lower wavelength.

9.2.2 FWHM of LMCTs of Eu^{3+}

Due to the overlap of LMCT and f–f transition in $Dy[H(PO_3)_4]$:Eu^{3+} an exact FWHM (*F*ull *W*idth at *H*alf *M*aximum) can not be determined (Figure 9.3). Nevertheless, a trend can be noticed. $Cs_2[B_{10}O_{14}(OH)_4]\cdot H_2O$:$Eu^{3+}$ and $(NH_4)_2[B_2P_3O_{11}(OH)]$:$Eu^{3+}$ show a very similar peak width of the LMCT. According to the single-crystal data both compounds reveal two crystallographic cation sites, which are partially occupied by Eu^{3+}. Various metal sites lead to a band broadening. However, for $(NH_4)_2[B_2P_3O_{11}(OH)]$:$Eu^{3+}$ indications justify the assumption that Eu^{3+} occupies sites close to centrosymmetry, but it is not yet known whether it occupies one or more crystallographic sites. The LMCT of $Cs_2[B_{10}O_{14}(OH)_4]\cdot H_2O$:$Eu^{3+}$

is slightly broader compared to $Sr_3P_4O_{13}$:Eu^{3+}. $Sr_3P_4O_{13}$:Eu^{3+} also possesses two different cation sites. As stated above, the coordination sphere of $Cs_2[B_{10}O_{14}(OH)_4]\cdot H_2O$:$Eu^{3+}$ shows more covalent character due to a stronger nephelauxetic effect. This is accompanied with a stronger interaction between the excited state and the lattice, which results in a broader transition. The LMCT of $Dy[H(PO_3)_4]$:Eu^{3+} is rather half as broad compared to the other transitions. $Dy[H(PO_3)_4]$:Eu^{3+} comprises one unique site of Dy^{3+}, which is partially occupied by Eu^{3+} and thus a more narrow band can be observed.

9.2.3 *f*–*d* Transitions of Tb^{3+}

Figure 9.4 shows the *f*–*d* transitions of Tb^{3+} in $Tb[H(PO_3)_4]$ and $(NH_4)_2[B_2P_3O_{11}(OH)]$:$Tb^{3+}$, which are summarised in Table 9.2.

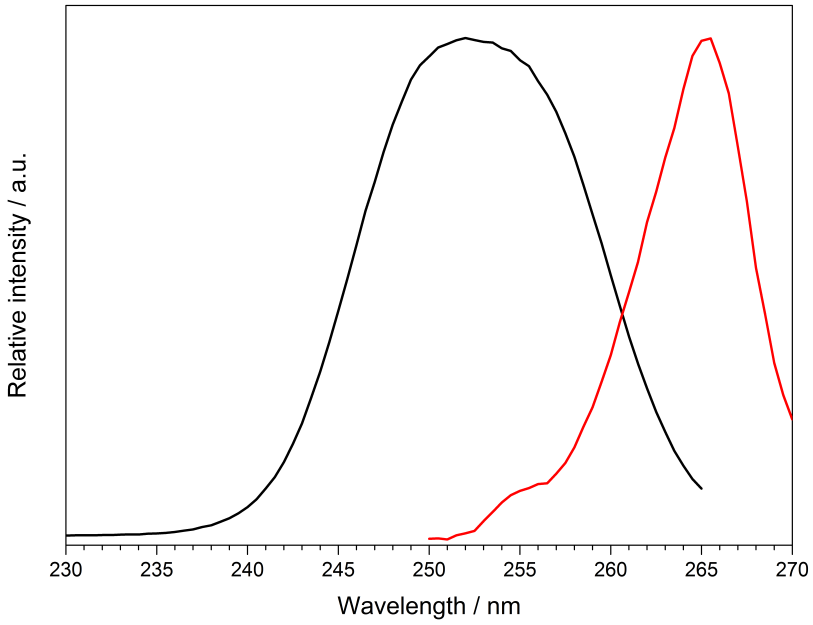

Figure 9.4: Comparison of the *f*–*d* transition of Tb^{3+} in $Tb[H(PO_3)_4]$ (black) and $(NH_4)_2[B_2P_3O_{11}(OH)]$:$Tb^{3+}$ (red).

Both *f*–*d* transitions lie relatively close to each other at 252 and 266 nm for $Tb[H(PO_3)_4]$ and $(NH_4)_2[B_2P_3O_{11}(OH)]$:$Tb^{3+}$, respectively. As mentioned in Chapter 9.2.1 distances *d*(N–O) lie between 2.77 and 3.30 nm and thus are relatively large compared to the distances in $Tb[H(PO_3)_4]$ (2.28–2.45 Å). As a consequence a weaker coordination and a blue shift is expected. However, the opposite occurs. Taking into consideration that in $(NH_4)_2[B_2P_3O_{11}(OH)]$:$Eu^{3+}$ an occupation of interstitial sites close to centrosymmetry of Eu^{3+} ions is presumed, one may expect the same phenomenon for $(NH_4)_2[B_2P_3O_{11}(OH)]$:$Tb^{3+}$ due to the similar ionic radii of the lanthanide ions ($r_{Eu^{3+}} = 1.07$ Å, $r_{Tb^{3+}} = 1.04$ Å) [60]. Borophosphates in contrast

to phosphates exhibit a slightly stronger nephelauxetic effect due to the presence of condensed borate tetrahedra in the structure. Both arguments support the presence of a stronger coordination sphere of Tb^{3+}, which leads to a red shift in the spectrum.

Table 9.2: Comparison of the excitation wavelength λ_{exc} of the f–d transition of Tb^{3+} containing compounds

Compound	λ_{exc} / nm	CN	Distance CA–O / Å
$Tb[H(PO_3)_4]$	252	7	2.28–2.45
$(NH_4)_2[B_2P_3O_{11}(OH)]$:$Tb^{3+}$	266	7/8	2.77–3.30

CN = Coordination Number, CA = Central Atom

9.2.4 FWHM of *f*–*d* Transitions of Tb^{3+}

The peak width of $(NH_4)_2[B_2P_3O_{11}(OH)]$:$Tb^{3+}$ is about half as broad compared to $Tb[H(PO_3)_4]$ (Figure 9.4). Due to only one unique site of Tb^{3+} in $Tb[H(PO_3)_4]$ the opposite is expected. Provided that Tb^{3+} partially occupies one unique interstitial site in $(NH_4)_2[B_2P_3O_{11}(OH)]$:$Tb^{3+}$ a more narrow f–d transition should be observed.

9.3 Structural Properties

9.3.1 Fundamental Building Units

Compounds revealing mixed valent anionic structures, e.g. borophosphates and borosulphates, were named according to the nomenclature suggested by *Ewald* and *Kniep* [13]. The structural classification of the borophosphates and borosulphates was performed by registering the B:P ratios, the FBU and the corresponding dimensionality of the structures.

9.3.1.1 FBUs in Borophosphates

$(NH_4)_2Mn(II)[B_2P_3O_{11}(OH)_2]Cl$ comprises a B:P ratio of 2:3 and an O:OH ratio of 11:2. The FBU as a vierer-single ring 5□:<4□>□ has been observed for the first time (Figure 9.5 right), which builds up a lB vierer-single layer. Up to now for borophosphates with a B:P ratio of 2:3 exclusively oB dreier-single rings 5□:□<3□>□ and olB dreier-single rings 5□:<3□>=<3□>□ have been known as FBU (Figure 9.5 left and middle).

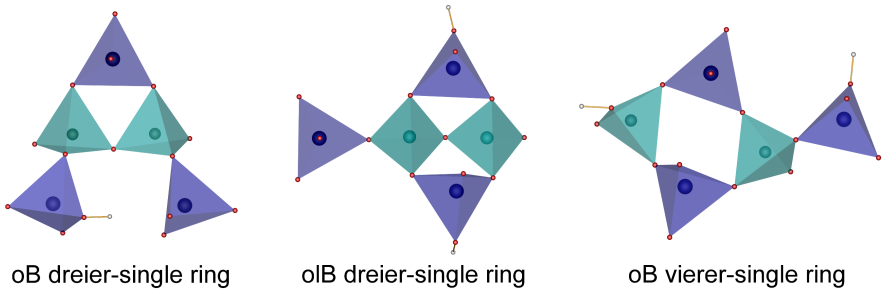

Figure 9.5: FBUs of borophosphates with a B:P ratio of 2:3; phosphate tetrahedra blue, borate tetrahedra turquoise, hydrogen white.

Protonated borophosphates with a B:P ratio of 2:3 either possess an O:OH ratio of 12:1 or 11:2 and can be divided into layer (Figure 9.6) and chain (Figure 9.7) borophosphates. Figure 9.6 shows that $(NH_4)_2Mn(II)[B_2P_3O_{11}(OH)_2]Cl$ is the first representative, which crystallises in a layer structure and exhibits an O:OH ratio of 11:2 at the same time.

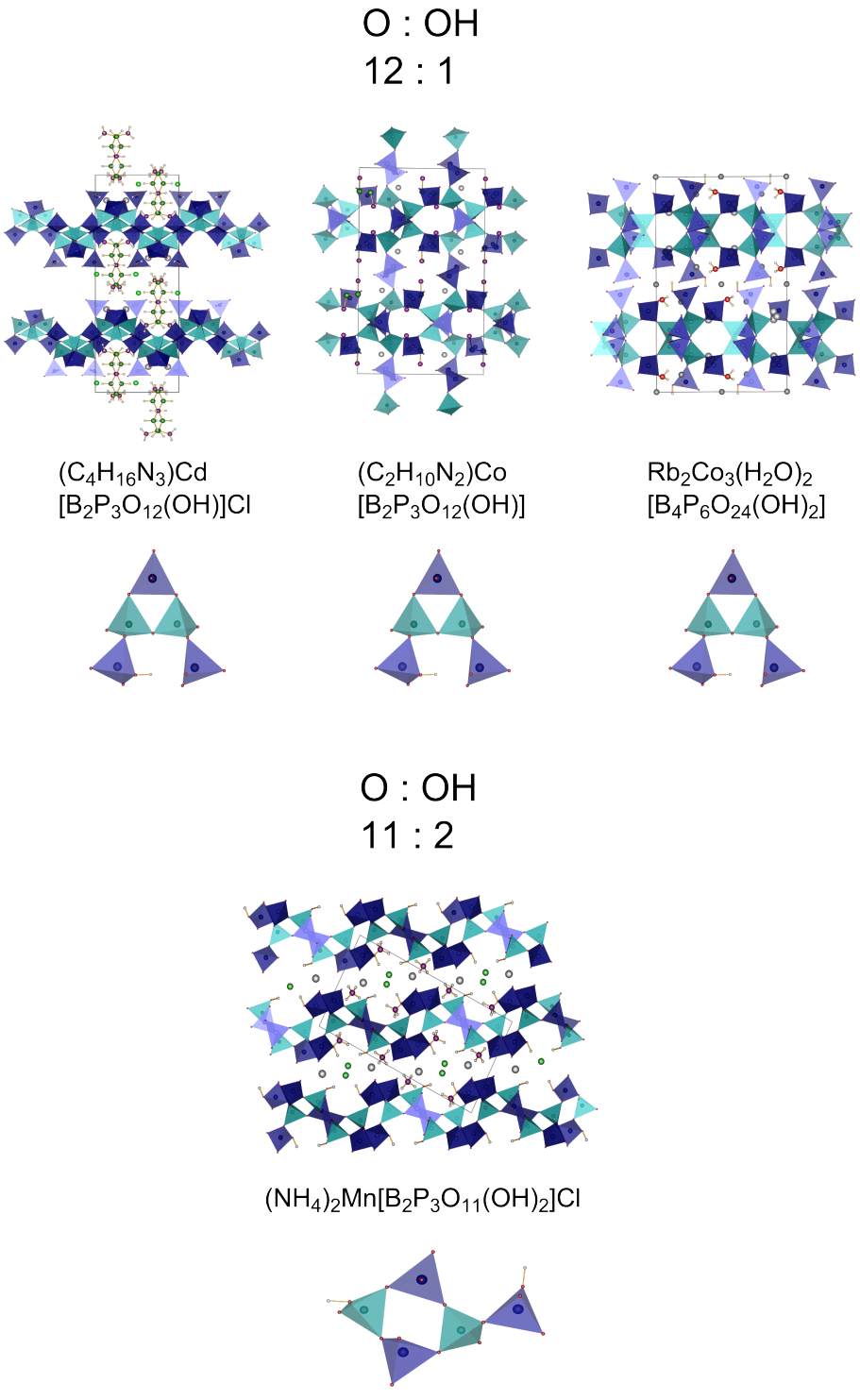

Figure 9.6: Overview of layered borophosphate compounds with an O:OH ratio of 12:1 or 11:2 [124, 224, 225]; phosphate tetrahedra blue, borate tetrahedra turquoise, hydrogen white.

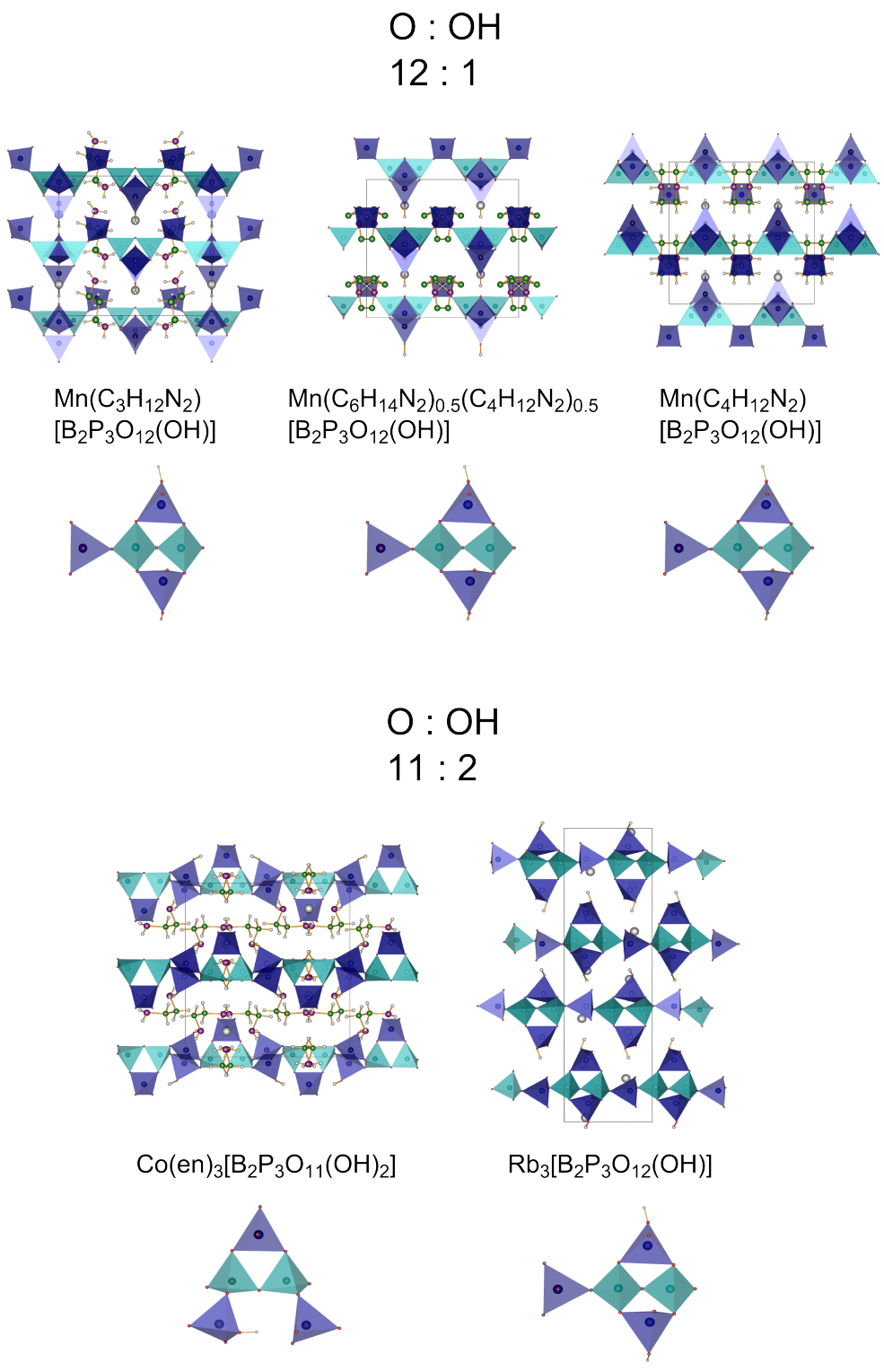

Figure 9.7: Overview of chain structure borophosphate compounds with an O:OH ratio of 12:1 or 11:2 [144, 226, 227]; phosphate tetrahedra blue, borate tetrahedra turquoise, hydrogen white.

$(NH_4)_2[B_2P_3O_{11}(OH)]$ has the same FBU as $(NH_4)_2Mn(II)[B_2P_3O_{11}(OH)_2]Cl$. Besides a lower protonation degree (Figure 9.8) the connection pattern changes as well (Figure 9.9). The hydroxyl group of the borate tetrahedron looses its protonation in favour of a further connection to a phosphate tetrahedron and thus a larger condensation degree in $(NH_4)_2[B_2P_3O_{11}(OH)]$.

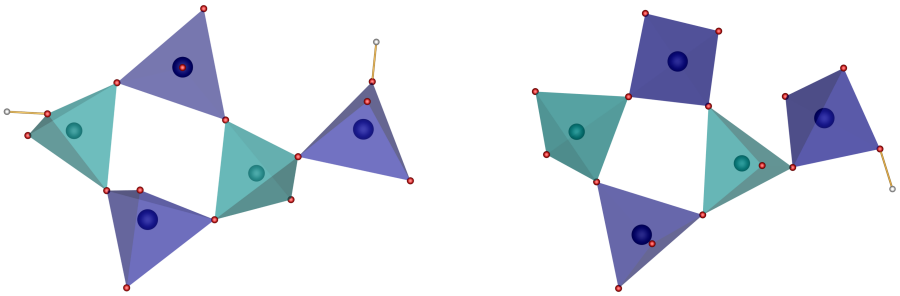

Figure 9.8: OB vierer-single rings as FBUs of $(NH_4)_2Mn(II)[B_2P_3O_{11}(OH)_2]Cl$ (left) and $(NH_4)_2[B_2P_3O_{11}(OH)]$ (right); phosphate tetrahedra blue, borate tetrahedra turquoise, hydrogen white.

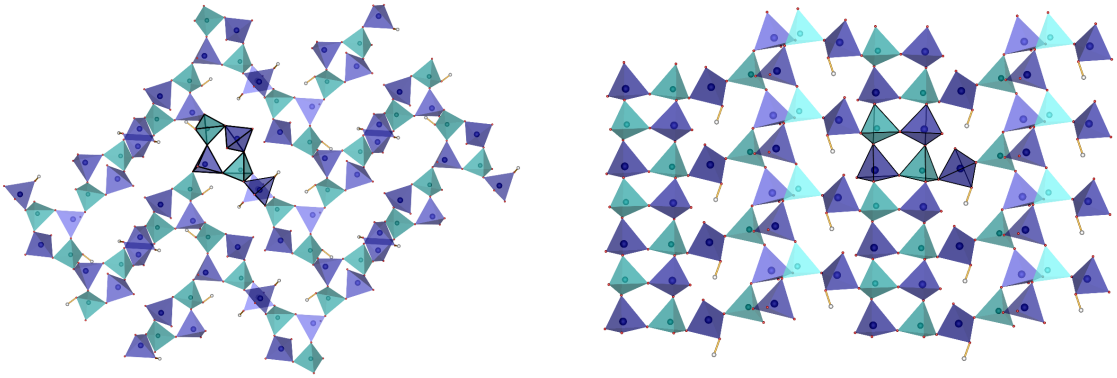

Figure 9.9: Layer structure of $(NH_4)_2Mn(II)[B_2P_3O_{11}(OH)_2]Cl$ (left) and $(NH_4)_2[B_2P_3O_{11}(OH)]$ (right); phosphate tetrahedra blue, borate tetrahedra turquoise, hydrogen white.

In contrast to $(NH_4)_2Mn(II)[B_2P_3O_{11}(OH)_2]Cl$, $(NH_4)_2[B_2P_3O_{11}(OH)]$ represents the first borophosphate with a B:P ratio of 2:3 and an O:OH ratio of 11:1. Up to now borophosphates in this class always revealed a total number of thirteen oxygen atoms including zero, one or two hydroxyl groups [13]. Instead of forming perpendicular intra-layer loops as in $(NH_4)_2Mn(II)[B_2P_3O_{11}(OH)_2]Cl$ (Figures 9.9 left and 9.10), $(NH_4)_2[B_2P_3O_{11}(OH)]$ forms layers of FBUs arranged in sequence (Figure 9.9 right).

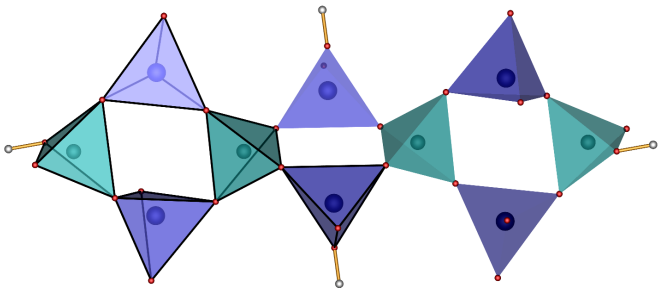

Figure 9.10: Perpendicular intra-layer loops of two FBUs facing each other in $(NH_4)_2Mn(II)[B_2P_3O_{11}(OH)_2]Cl$; phosphate tetrahedra blue, borate tetrahedra turquoise, hydrogen white.

$(NH_4)_2[B_2P_3O_{11}(OH)]$ possesses a strongly corrugated structure as $(NH_4)_2Mn(II)[B_2P_3O_{11}(OH)_2]Cl$ (Figure 9.11). Although $(NH_4)_2[B_2P_3O_{11}(OH)]$ hosts exclusively NH_4^+ ions, the borophosphate layers have the same distance as in $(NH_4)_2Mn(II)[B_2P_3O_{11}(OH)_2]Cl$ (~8 Å), but exhibit a phase shift of a half repetition period.

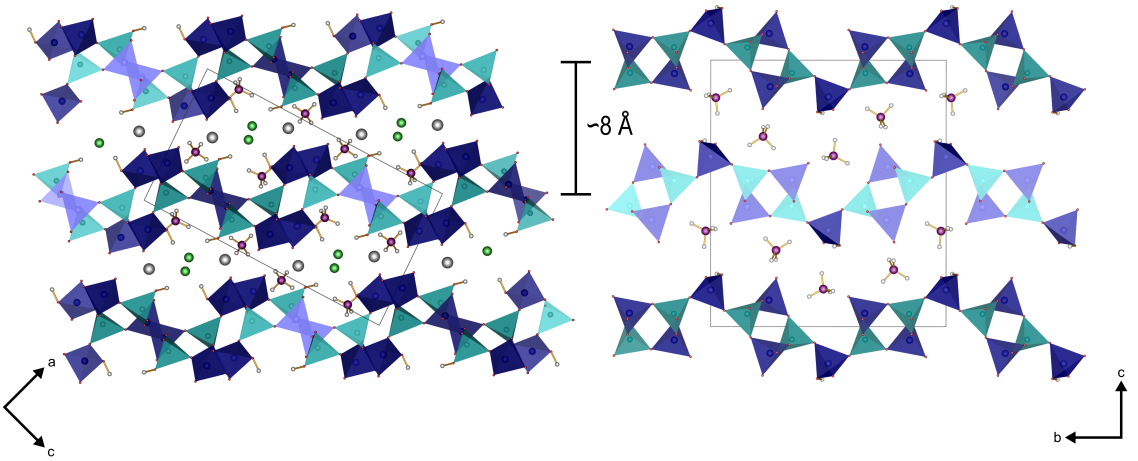

Figure 9.11: Comparison of the corrugated layer structure of $(NH_4)_2Mn(II)[B_2P_3O_{11}(OH)_2]Cl$ (left) and $(NH_4)_2[B_2P_3O_{11}(OH)]$ (right); phosphate tetrahedra blue, borate tetrahedra turquoise, chlorine green, manganese grey, nitrogen violet, hydrogen white.

9.3.1.2 FBUs in Borosulphates

$K_5[B(SO_4)_4]$ is the first representative of the borosulphate family. In analogy to borophosphates nomenclature was adopted from *Ewald* and *Kniep* [13]. The FBU as oB pentamer 5□:[□]□|□|□|□| (Figure 9.12) represents the oligomeric anionic partial structure.

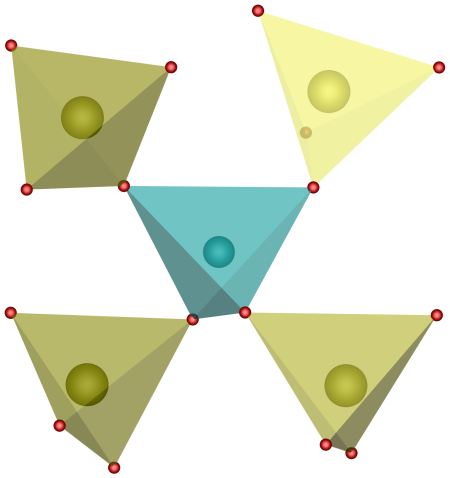

Figure 9.12: OB pentamer as FBU of $K_5[B(SO_4)_4]$; borate tetrahedron turquoise, sulphate tetrahedra yellow.

The B:S ratio is 1:4, hence the central borate tetrahedron is completely surrounded by sulphate tetrahedra and no further connections are observed. In contrast to borophosphates, borosulphates with a B:S ratio of 1:4 already exhibit a large variety in composition revealing besides the oB pentamer a lB dreier-single ring as FBU (Figure 9.13). Compounds are summarised in Table 9.3.

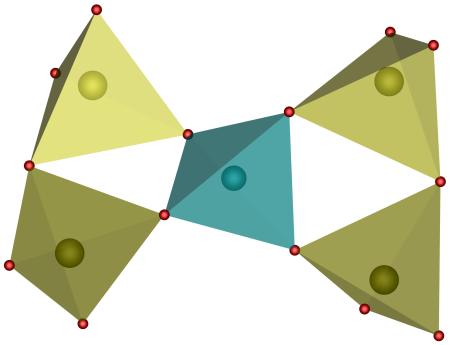

Figure 9.13: LB dreier-single ring as FBU of $A^I[B(S_2O_7)_2]$ (A^I = Li [136], Na, K, NH_4 [137]); borate tetrahedron turquoise, sulphate tetrahedra yellow.

Up to now $K_4[HB(SO_4)_4]$[140] is the only protonated borosulphate representative. In borophosphate chemistry a single protonated compound with a B:P ratio of 1:4 is known. $(C_3N_2H_5)_8[Mo_{12}B_2P_8O_{59}(OH)_3]\cdot 4H_2O$ [277] consists of heteropolyoxoclusters with two protonated borophosphate pentamers. The other known structure is $M^{II}_6[BP_4O_{16}][PO_4]$ (M^{II} = Sr [276], Pb [274, 275]), which possesses besides the oB pentamer isolated PO_4 tetrahedra.

Table 9.3: Borosulphates with a B:S ratio of 1:4 and assignement of the FBU

Compound	FBU
$K_5[B(SO_4)_4]$	oB pentamer
$Li_5[B(SO_4)_4]$ [137]	oB pentamer
I-$Na_5[B(SO_4)_4]$ [136]	oB pentamer
II-$Na_5[B(SO_4)_4]$ [136]	oB pentamer
$K_4[HB(SO_4)_4]$ [140]	oB pentamer
$Li[B(S_2O_7)_2]$ [136]	lB dreier-single ring
$Na[B(S_2O_7)_2]$ [137]	lB dreier-single ring
$K[B(S_2O_7)_2]$ [137]	lB dreier-single ring
$NH_4^+[B(S_2O_7)_2]$ [137]	lB dreier-single ring

9.3.2 Thermal Stability

It is well known that compounds with condensed structures show a higher thermal stability and thus may be well suited as host structures for luminescent materials. Nevertheless, one may not neglect other considerations, e.g. the arrangement of the structural units and the formation of possible decomposition products.

9.3.2.1 Thermal Stability of Chain Structures

The thermal stability of $Cs_2[B_{10}O_{14}(OH)_4]\cdot H_2O$ (black), $Tb[H(PO_3)_4]$ (red) and $NH_4Cr(III)[BP_2O_8(OH)]$ (blue) exhibiting an equal condensation degree (infinite chains) is shown in Figure 9.14.

$Cs_2[B_{10}O_{14}(OH)_4]\cdot H_2O$ possesses the lowest thermal stability with an onset temperature of 240 °C. The behaviour of $Tb[H(PO_3)_4]$ and $NH_4Cr(III)[BP_2O_8(OH)]$ seems to be relatively similar with a stability up to 500 and 430 °C. A closer look on the different chains, which are present in all three structures (Figure 9.15), shows, that $Tb[H(PO_3)_4]$ is the only representative with a helical chain. $Cs_2[B_{10}O_{14}(OH)_4]\cdot H_2O$ reveals zig-zag chains, which are arranged offset, including perpendicular six-membered B_3O_3 rings. $NH_4Cr(III)[BP_2O_8(OH)]$ also comprises zig-zag chains. In contrast to $Cs_2[B_{10}O_{14}(OH)_4]\cdot H_2O$, the borophosphate chains are planar with open branches instead of loops. Both borate tetrahedra in $Cs_2[B_{10}O_{14}(OH)_4]\cdot H_2O$ show a deviation of tetrahedra > 1 %, which is due to the deviation from perpendicular arrangement of the connected B_3O_3 rings (torsion angle: 99°).

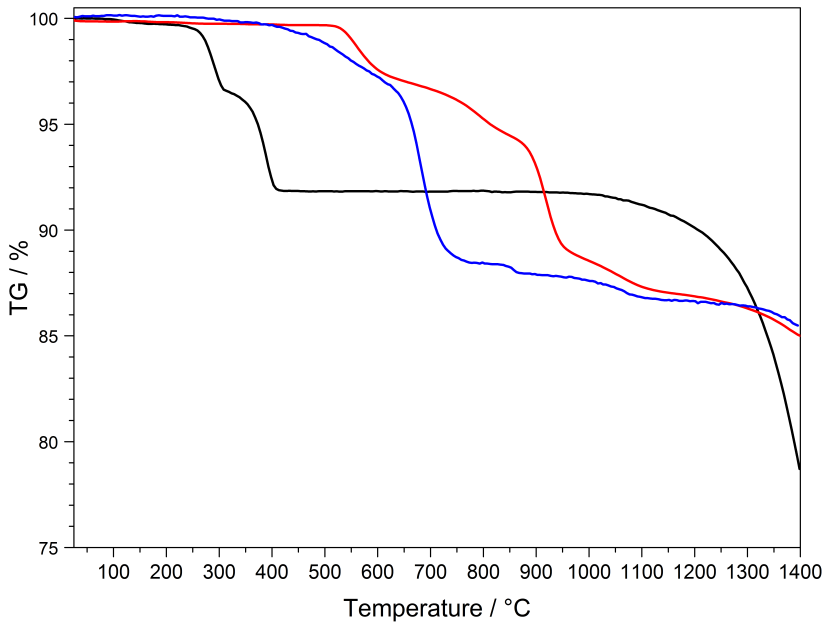

Figure 9.14: Comparison of the thermogravimetric analysis of $Cs_2[B_{10}O_{14}(OH)_4]\cdot H_2O$ (black), $Tb[H(PO_3)_4]$ (red) and $NH_4Cr(III)[BP_2O_8(OH)]$ (blue).

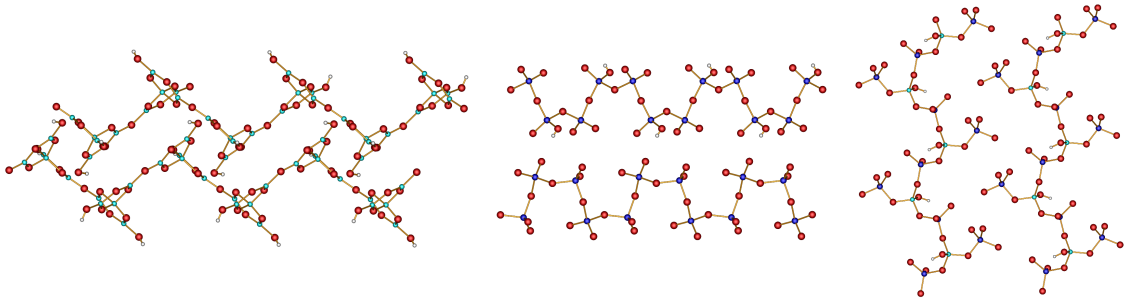

Figure 9.15: Comparison of the chains of $Cs_2[B_{10}O_{14}(OH)_4]\cdot H_2O$ (left), $Tb[H(PO_3)_4]$ (middle) and $NH_4Cr(III)[BP_2O_8(OH)]$ (right); phosphorous blue, boron turquoise, oxygen red, hydrogen white.

Furthermore, the torsion angle between the two different $B_5O_9H_2$ units has a value of 37°, which results in a non-congruent arrangement (Figure 9.16).

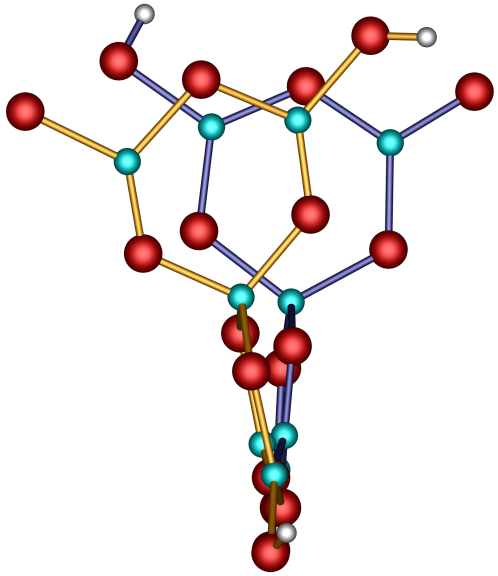

Figure 9.16: Non-congruent arrangement of the two different $B_5O_9H_2$ units in $Cs_2[B_{10}O_{14}(OH)_4]\cdot H_2O$ (front: orange bonds, back: blue bonds); boron turquoise, oxygen red, hydrogen white.

In a congruent, ecliptic arrangement oxygen atoms face each other directly exhibiting a shorter distance. Thus, a stronger repulsion occurs, which leads to a more stable, non-congruent arrangement. Nevertheless, a certain tension is present in $Cs_2[B_{10}O_{14}(OH)_4]\cdot H_2O$. By heating up the compound vibrations quickly lead to bond breaking and H_2O is released.

$Tb[H(PO_3)_4]$ shows a higher thermal stability compared to $NH_4Cr(III)[BP_2O_8(OH)]$. Decomposition of the latter leads to the formation of NH_3, whose vapour pressure is higher compared to H_2O and P_2O_5, which evaporate both when heating up $Tb[H(PO_3)_4]$.

9.3.2.2 Thermal Stability of Layered Structures

Both $(NH_4)_2Mn(II)[B_2P_3O_{11}(OH)_2]Cl$ and $(NH_4)_2[B_2P_3O_{11}(OH)]$ possess layered borophosphate structures and the same FBU. Thus, it does not surprise that their thermal stability is similar (Figure 9.17).

However, the number of decomposition steps deviates strongly. $(NH_4)_2Mn(II)[B_2P_3O_{11}(OH)_2]Cl$ shows a single step of mass loss, whereas $(NH_4)_2[B_2P_3O_{11}(OH)]$ exhibits several steps of mass loss. In both structures the corrugated borophosphate layers reveal a distance of approx. 8 Å(Figure 9.11), but in $(NH_4)_2Mn(II)[B_2P_3O_{11}(OH)_2]Cl$ additional Mn^{2+} and Cl^- ions are accommodated. Due to additional attractive interactions between Mn^{2+}, Cl^- and the borophosphate

layer a higher thermal stability is reached. Furthermore, intra-layer loops, which are exclusively present in $(NH_4)_2Mn(II)[B_2P_3O_{11}(OH)_2]Cl$, give more stability to the structure.

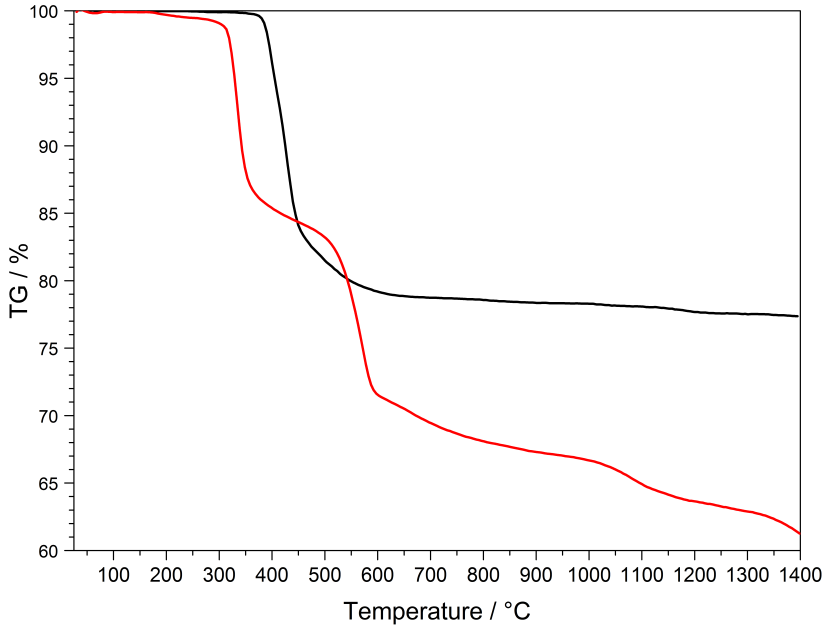

Figure 9.17: Comparison of the thermogravimetric analysis of $(NH_4)_2Mn(II)[B_2P_3O_{11}(OH)_2]Cl$ (black) and $(NH_4)_2[B_2P_3O_{11}(OH)]$ (red).

9.3.3 Deviation of Tetrahedral Symmetry

According to the *octet rule*, in borates, phosphates and sulphates the maximal number of oxygen ligands is four due to the maximum of four binding electron pairs [8, 42] (Table 9.4). The effort of the negatively charged oxygen ligands to arrange as far away as possible from each other leads to a tetrahedral surrounding (Figure 9.18).

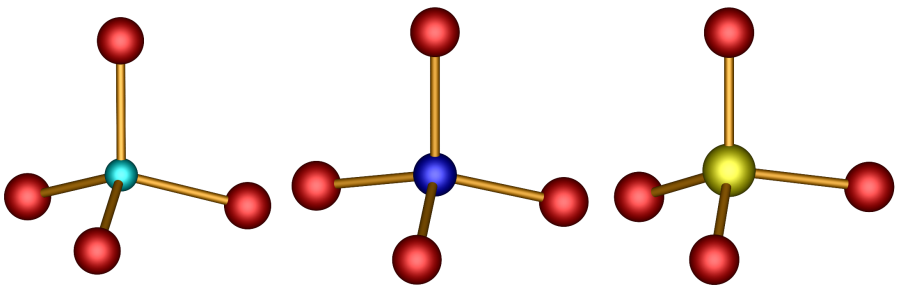

Figure 9.18: Tetrahedral units of BO_4^{5-}, PO_4^{3-} and SO_4^{2-}; boron turquoise, phosphorus blue, sulphur yellow, oxygen red.

Table 9.4: Oxidation states of the central ions in borates, phosphates and sulphates

Tetrahedral unit	BO_4^{5-}	PO_4^{3-}	SO_4^{2-}
Central Ion	B^{3+}	P^{5+}	S^{6+}
Oxidation state	+III	+V	+VI

In this work the deviation of tetrahedra was calculated for compounds belonging to the compound classes of borates, phosphates, borophosphates and borosulphates. The corresponding values are listed in Table 9.5.

In general, tetrahedra with deviations of less than 1% are classified as regular. In $Cs_2[B_{10}O_{14}(OH)_4]{\cdot}H_2O$ and $NH_4Cr(III)[BP_2O_8(OH)]$ deviations larger than 1% occur. In both cases structure data were obtained from *Rietveld* analysis with very good residual values. As structure model compounds crystallising isotypically ($Rb[B_5O_7(OH)_2]{\cdot}0.5H_2O$ and $NH_4V(III)[BP_2O_8(OH)]$) were used, exhibiting deviations of tetrahedra between −0.10 and −0.11% ($Rb[B_5O_7(OH)_2]{\cdot}0.5H_2O$) and −0.15 and −0.32% ($NH_4V(III)[BP_2O_8(OH)]$), respectively. Thus, all tetrahedra are classified as regular.
The question arises why the values of $Cs_2[B_{10}O_{14}(OH)_4]{\cdot}H_2O$ and $NH_4Cr(III)[BP_2O_8(OH)]$ deviate that strongly. In the process of a *Rietveld* refinement besides global also local parameters, e.g. the position of the atoms, are refined. Small shifts of the position of the central atom (e.g. B or P) already lead to a distorted tetrahedron, which can rapidly result in larger values of deviation. Although isotypical structure models used for a *Rietveld* refinement are already very close to the investigated structure, one may not neglect the accuracy of values received by single-crystal structure analysis. Subsequently refining this data via a *Rietveld* refinement gives a very good average of the bulk sample.

In contrast, all the other values of structures solved by single-crystal structure analysis reveal values well below 1%. Nevertheless, a certain distribution is apparent, whereas the sulphate tetrahedra in $K_5[B(SO_4)_4]$ show the smallest spreading width ($\Delta = 0.14\,\%$) followed by the phosphate and borate tetrahedra in the borophosphates $(NH_4)_2Mn(II)[B_2P_3O_{11}(OH)_2]Cl$ and $(NH_4)_2[B_2P_3O_{11}(OH)]$ (B: $\Delta = 0.38\,\%$, P: $\Delta = 0.32\,\%$). The phosphate tetrahedra of the phosphates $Ln[H(PO_3)_4]$ (Ln = Tb, Ho) and $Sr_3P_4O_{13}$ show the largest scattering ($\Delta = 0.5\,\%$).

Table 9.5: Deviation of tetrahedra in borates, phosphates, borophosphates and borosulphates; data either obtained from single-crystal analysis (A) or *Rietveld* refinement (B)

Compound Class	Deviation of Tetrahedra / %		Structure Data obtained from
Borate			
$Cs_2[B_{10}O_{14}(OH)_4]\cdot H_2O$	B1: -2.10		B
	B2: -1.70		
Phosphates			
$Tb[H(PO_3)_4]$		P1: -0.32	A
		P2: -0.29	
		P3: -0.22	
		P4: -0.20	
$Ho[H(PO_3)_4]$		P1: -0.32	A
		P2: -0.29	
		P3: -0.21	
		P4: -0.21	
RT-$Sr_3P_4O_{13}$		P1: -0.06	A
		P2A: -0.56	
		P2B: -0.56	
Borophosphates			
$(NH_4)_2Mn(II)[B_2P_3O_{11}(OH)_2]Cl$	B1: -0.22	P1: -0.19	A
	B2: -0.60	P2: -0.21	
		P3: -0.46	
$(NH_4)_2[B_2P_3O_{11}(OH)]$	B1: -0.36	P1: -0.19	A
	B2: -0.24	P2: -0.32	
		P3: -0.14	
$NH_4Cr(III)[BP_2O_8(OH)]$	B1: -1.12	P1: -0.73	B
		P2: -1.15	
Borosulphate			
$K_5[B(SO_4)_4]$	B1: -0.38	S1: -0.08	A
		S2: -0.15	
		S3: -0.12	
		S4: -0.22	

Despite the small amount of data, a trend becomes visible considering the deviation of different types of tetrahedra derived from single crystal data (A) (Table 9.6). With increasing oxidation state and electronegativity of the central ion (B → P → S) the deviation of tetrahedra decreases.

Table 9.6: Average deviation of tetrahedra of borates, phosphates and sulphates from single crystal data (A)

Compound Class	Average Deviation of Tetrahedra from A / %
$B^{III}O_4$	-0.36
$P^{V}O_4$	-0.28
$S^{VI}O_4$	-0.14

Electronegative elements pull stronger electron density towards themselves, which leads to a stronger coordination of the ligands and the repulsion among themselves also becomes stronger. Additionally, the increased charge of the electronegative element reinforces this phenomenon and the deviation of tetrahedra decreases. Taking into account these considerations a differentiation in the deviation of tetrahedra could be made with respect to the type of the corresponding central atom. The rule of deviation of tetrahedra could still be applied that strictly for phosphates and sulphates, but for borates a stronger deviation of about 2 % could be accepted.

10 Summary

In this work the synthesis and characterisation of silicate-analogous solids, particularly borates, phosphates, borophosphates and borosulphates, were investigated. The focus was on the structural, optical and thermal properties with regard to the suitability as host structures. Several compounds were doped with lanthanide ions to examine the influence of the crystal structure on the optical properties. Besides the examination of a phase transition of a well-known phosphate, novel condensed borophosphate structures and the first representative of the compound class of borosulphates were obtained.

10.1 The Borate $Cs_2[B_{10}O_{14}(OH)_4]\cdot H_2O$

$Cs_2[B_{10}O_{14}(OH)_4]\cdot H_2O$ (Chapter 5) represents a new borate in the group of monovalent pentaborates. The hydrothermally synthesised, colourless and microcrystalline powder was refined via a *Rietveld* analysis ($P\bar{1}$, $Z = 2$, $a = 7.8038(2)$ Å, $b = 9.1840(2)$ Å, $c = 12.3403(3)$ Å, $\alpha = 98.979(2)°$, $\beta = 106.345(1)°$, $\gamma = 91.081(1)°$, R_p =0.013, $R_{wp} = 0.018$, $\chi^2 = 3.28$). The polyanion is constructed by a zig-zag lB sechser-single chain, possessing lB pentamers as FBU. MAPLE calculations confirmed the ninefold coordination of the cations. Besides the determination of one weak and several moderate hydrogen bonds, all bands could be assigned in the IR spectrum. The excitation and emission bands of $Cs_2[B_{10}O_{14}(OH)_4]\cdot H_2O{:}Eu^{3+}$ reveal the typical f–f transitions of Eu^{3+}. The presence of the very intense hypersensitive $^5D_0 \rightarrow {}^7F_2$ transition proves the occupation of Eu^{3+} on Cs^+ sites due its asymmetric surrounding.

10.2 Optical properties of $Ln[H(PO_3)_4]$ (Ln = Tb, Dy, Ho), $Dy[H(PO_3)_4]:Ce^{3+}$ and $Dy[H(PO_3)_4]:Eu^{3+}$

Lanthanide hydrogen-polyphosphates $Ln[H(PO_3)_4]$ (Ln = Tb, Dy, Ho) (Chapter 6.1) were synthesised as colourless (Ln = Tb, Dy) and light pink (Ln = Ho) crystalline powders by reaction of $Tb_4O_7/Dy_2O_3/Ho_2O_3$ with H_3PO_3 at 380 °C. All compounds crystallise isotypically ($P2_1/c$, $Z = 4$, $a_{Tb} = 13.6824(4)$ Å, $b_{Tb} = 7.1042(2)$ Å, $c_{Tb} = 9.6579(3)$ Å, $\beta_{Tb} = 101.200(1)°$, 3112 data, 160 parameters, $R1 = 0.0277$, $wR2 = 0.0622$; $a_{Ho} = 13.6334(5)$ Å, $b_{Ho} = 7.0924(3)$ Å, $c_{Ho} = 9.5907(4)$ Å, $\beta_{Ho} = 101.055(1)°$, 1607 data, 158 parameters, $R1 = 0.0291$, $wR2 = 0.0602$). Whereas the crystal structures of $Tb[H(PO_3)_4]$ and $Ho[H(PO_3)_4]$ were solved from single-crystal data, $Dy[H(PO_3)_4]$ was refined via a *Rietveld* refinement ($P2_1/c$, $Z = 4$, $a_{Dy} = 13.6585(3)$ Å, $b_{Dy} = 7.09739(12)$ Å, $c_{Dy} = 9.6215(2)$ Å, $\beta_{Dy} = 101.116(1)°$, $R_p = 0.009$, $R_{wp} = 0.012$, $\chi^2 = 4.04$). The crystal structure comprises two different infinite helical chains of corner-sharing phosphate tetrahedra running parallel in [010] direction. The cations are coordinated by seven oxygen atoms belonging to four different polyphosphate chains. $Ho[H(PO_3)_4]$ shows the *alexandrite* effect by exhibiting a yellow and pink body colour in ambient day light and artificial light provided by luminescent tubes, respectively. UV-Vis and fluorescence spectra of $Ln[H(PO_3)_4]$ (Ln = Tb, Dy) show the typical absorption, excitation and emission bands. $Dy[H(PO_3)_4]$ was doped with 5, 10 and 30 % Ce^{3+} in order to investigate the effect of Ce^{3+} as sensitiser. Although a slight increase of the emission intensities of Dy^{3+} can be observed, an efficient energy transfer could not be proved. $Dy[H(PO_3)_4]:Eu^{3+}$ (5 mol%) reveals besides two emission bands of Dy^{3+} the typical Eu^{3+} emission lines. The hypersensitive $^5D_0 \rightarrow {}^7F_2$ transition appears very intense due to the asymmetric surrounding of Eu^{3+} and confirms the occupation of Dy^{3+} sites. The magnetic susceptibility measurement confirms the valence state of Tb^{3+} and thus the presence of one proton. $Tb[H(PO_3)_4]$ obeys *Curie's* law over the whole temperature range (1.8–400 K), exhibiting a magnetic moment of $\mu_{eff} = 9.54\,\mu_B$.

10.3 Phase transition of $Sr_3P_4O_{13}$

$Sr_3P_4O_{13}$ (Chapter 6.2) was synthesised via solid-state synthesis at 930 °C as colourless crystalline powder. At room temperature it crystallises in the triclinic space group $P\bar{1}$ ($Z = 1$, $a = 5.5244(2)$ Å, $b = 6.9126(2)$ Å, $c = 7.7199(2)$ Å, $\alpha = 83.316(1)°$, $\beta = 75.788(1)°$, $\gamma = 70.553(1)°$, 1571 data, 89 parameters, $R1 = 0.0179$,

$wR2 = 0.0449$). By slowly cooling the single-crystal to 100 K LT-$Sr_3P_4O_{13}$ undergoes a phase transition yielding a larger unit cell ($P\bar{1}$, $Z = 2$, $a = 7.2636(3)$ Å, $b = 7.7033(3)$ Å, $c = 10.1576(4)$ Å, $\alpha = 102.207(1)°$, $\beta = 103.511(1)°$, $\gamma = 94.448(1)°$, 8999 data, 182 parameters, $R1 = 0.0379$, $wR2 = 0.0686$). S-shaped $[P_4O_{13}]^{6-}$ chains of corner-sharing phosphate tetrahedra separated by layers of edge- and corner-sharing chairs of Sr^{2+} ions are present in both $Sr_3P_4O_{13}$ structures. At room temperature the presence of two individuals in the ratio of 1:1 leads to a splitting of $O_{br}2$. At 100 K all atoms in LT-$Sr_3P_4O_{13}$ are arranged properly. The group-subgroup relation between both structure solutions can be visualised by the *Bärnighausen* formalism [222] by applying an isomorphic transition with the index 2. All atoms on general positions are doubled. The number of crystallographically different sites of strontium atoms increases from two to three (Figure 10.1).

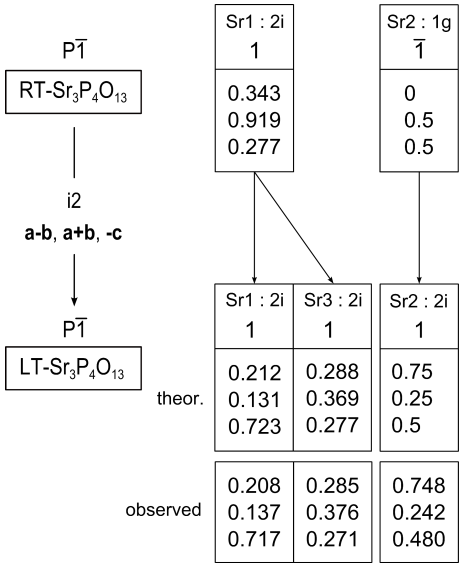

Figure 10.1: *Bärnighausen* formalism [222] showing the group-subgroup relation of the isomorphic transition $i2$ between RT-$Sr_3P_4O_{13}$ and LT-$Sr_3P_4O_{13}$ of the strontium atoms.

$Sr_3P_4O_{13}$ was doped with Eu^{3+} and Eu^{2+}. Whereas $Sr_3P_4O_{13}$:Eu^{3+} could be obtained phase pure showing a red emission, $Sr_3P_4O_{13}$:Eu^{2+} always revealed $Sr_2P_2O_7$:Eu^{2+} as side phase due to evaporation of P_2O_5, or $Sr_3P_4O_{13}$:Eu^{3+} could not be reduced completely to $Sr_3P_4O_{13}$:Eu^{2+} exhibiting a blue ($\lambda_{em} = 404$ nm) or pink emission ($\lambda_{em} = 417$, 594, 612, 652, 699, 754 nm), respectively.

10.4 Layered Structure Borophosphates $(NH_4)_2Mn(II)[B_2P_3O_{11}(OH)_2]Cl$ and $(NH_4)_2[B_2P_3O_{11}(OH)]$

The novel borophosphate $(NH_4)_2Mn(II)[B_2P_3O_{11}(OH)_2]Cl$ (Chapter 7.1) was synthesised as a crystalline colourless powder by reaction of $MnCl_2$, $(NH_4)_2HPO_4$, H_3BO_3 and H_3PO_4 under hydrothermal conditions at 180 °C. According to X-ray single-crystal investigations it crystallises in a new structure type in the monoclinic space group $P2_1/n$ ($Z = 4$, $a = 9.0524(3)$ Å, $b = 8.4729(3)$ Å, $c = 16.5232(5)$ Å, $\beta = 92.303(1)$ °, $R1 = 0.0257$, $wR2 = 0.0632$, 2227 data, 229 parameters). The phase purity of the powder was checked via a *Rietveld* refinement. The lB vierer-single layer reveals an oB vierer-single ring as novel FBU. The layered structure with an O:OH ratio of 11:2 was observed for the first time (Figure 10.2 left).

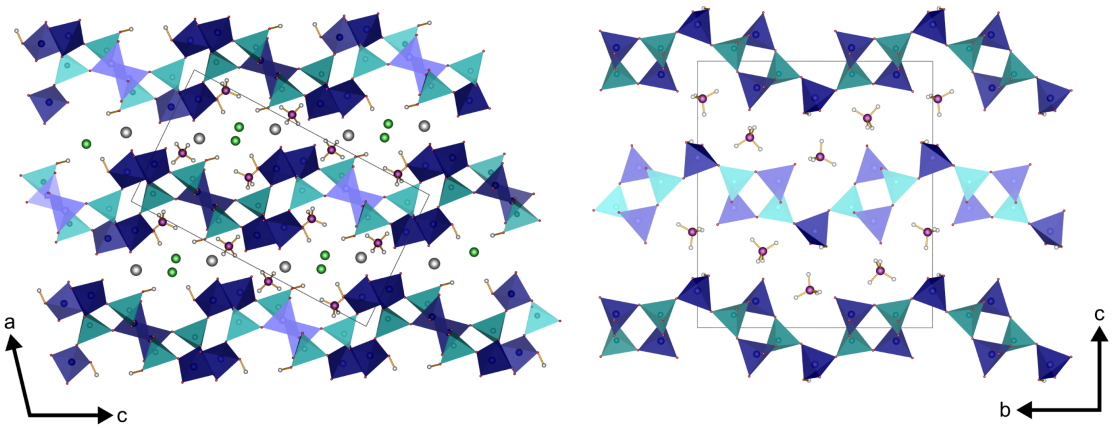

Figure 10.2: Comparison of the corrugated layer structure of $(NH_4)_2Mn(II)[B_2P_3O_{11}(OH)_2]Cl$ (left) and $(NH_4)_2[B_2P_3O_{11}(OH)]$ (right); phosphate tetrahedra blue, borate tetrahedra turquoise, chlorine green, manganese grey, nitrogen violet, hydrogen white.

The electrostatic consistency of the structure model was proved via MAPLE calculations. The magnetic susceptibility obeys *Curie's* law in the whole temperature range (1.8–400 K) and the effective magnetic moment of $\mu_{eff} = 5.79\,\mu_B$ confirms the oxidation state of Mn^{2+} and thus the composition of the compound. $(NH_4)_2Mn(II)[B_2P_3O_{11}(OH)_2]Cl$ is thermally stable up to 340 °C in inert atmosphere before it decomposes to $Mn_2P_2O_7$ and BPO_4.

Diammonium borophosphate $(NH_4)_2[B_2P_3O_{11}(OH)]$ (Chapter 7.2) was synthesised hydrothermally at 180 °C in a *Teflon* autoclave starting from $(NH_4)_2HPO_4$, H_3BO_3 and H_3PO_4. It crystallises in a new structure type in the orthorhombic space group $P2_12_12_1$ ($Z = 4$, $a = 4.509(3)$ Å, $b = 14.490(11)$ Å, $c = 16.401(12)$ Å, $R1 = 0.0457$, $wR2 = 0.0930$, 1682 data, 200 parameters). The phase purity of the powder was

checked via a *Rietveld* refinement. The lB zweier-single layer (Figure 10.2 right) comprises an oB vierer-single ring as FBU, which was also observed in $(NH_4)_2Mn(II)[B_2P_3O_{11}(OH)_2]Cl$. An O:OH ratio of 11:1 in combination with a B:P ratio of 2:3 was observed for the first time. Numerous moderate and weak hydrogen bonds are found between NH_4^+ ions and the parallel corrugated borophosphate layers. In contrast to $(NH_4)_2[B_2P_3O_{11}(OH)]$, $(NH_4)_2Mn(II)[B_2P_3O_{11}(OH)_2]Cl$ exhibits a phase shift of a half in the borophosphate layer (Figure 10.2). At 300 °C the compound decomposes in inert atmosphere.

10.5 The Chain Structure Borophosphate $(NH_4)Cr[BP_2O_8(OH)]$

Ammonium chromium(III) borophosphate $(NH_4)Cr(III)[BP_2O_8(OH)]$ (Chapter 7.3) represents a new borophosphate in the group of mixed monovalent trivalent borophosphates revealing a green body colour. Via a *Rietveld* analysis the structure was refined to very good residuals ($P2_1/c$, $Z = 4$, $a = 9.3389(1)$ Å, $b = 8.2771(1)$ Å, $c = 9.5910(1)$ Å, $\beta = 102.776(1)°$, $R_p = 0.024$, $R_{wp} = 0.035$, $\chi^2 = 4.75$). Layers of oB vierer-single chains exhibit an uB trimer as BBU with a B:P ratio of 1:2. MAPLE calculations indicate that in $(NH_4)Cr(III)[BP_2O_8(OH)]$ exclusively one hydrogen atom is considered as ligand of the ammonia ion, which leads to a relatively large deviation. Hydrogen atoms were not refined in both the *Rietveld* refinement and in $(NH_4)V(III)[BP_2O_8(OH)]$ [248]. Hence, d(N–H) in both compounds possess a large scattering reaching from 0.65–1.08 Å. To compensate this unbalance the *MAPLE values of the hydrogen atoms as ligands in the nearest distance are strongly increased compared to the others. Investigations of the optical properties reveal a *Racah* parameter B' of 731 cm^{-1} and a ligand field splitting Δ_o of 15500 cm^{-1}.

10.6 The Borosulphate $K_5[B(SO_4)_4]$

The very first borosulphate $K_5[B(SO_4)_4]$ (Chapter 8), revealing a covalent B–O–S connection, was synthesised as crystalline colourless powder via a solid state reaction at 375 °C starting from $K_2S_2O_7$ and H_3BO_3. It crystallises in a new structure type ($P4_1$, $Z = 4$, $a = 9.9023(5)$ Å, $c = 16.1871(10)$ Å, 2744 data, 237 parameters, $R1 = 0.0528$, $wR2 = 0.1045$). The crystal structure comprises novel oligomeric borosulphate units as oB pentamers with K^+ ions in-between. Each unit represents a super-tetrahedron BS_4 exhibiting a central borate tetrahedron sharing each corner

with a sulphate tetrahedron. The five crystallographically different K^+ ions are coordinated irregularly by seven (2x), nine (2x) and eleven (1x) oxygen atoms. The UV-Vis spectrum reveals two strong absorption bands in the UV, which could be assigned to a charge transfer between O^{2-} and B^{3+} (230 nm) and S^{6+} (299 nm), respectively. Besides MAPLE calculations, which proved the electrostatic consistency of the structure, investigations of the thermal stability revealed a higher thermal stability compared to the very similar $Na_5[B(SO_4)_4]$-I.

11 Outlook

In this work the focus was on the expansion of the structural diversity and the identification of novel structure types. The obtained results comprise pursuing scientific issues.

$Cs_2[B_{10}O_{14}(OH)_4]\cdot H_2O$ as novel borate was obtained as polycrystalline powder. Optimisation of the synthesis could lead to single-crystals to confirm the structure by single-crystal structure analysis. Further already predicted monovalent pentaborates exhibiting Ag^+ or Tl^+ [147] should be easily accessible. Up to now no crystal structures were solved. Doping with trivalent lanthanides, e.g. Eu^{3+} and Tb^{3+}, leads to possible interesting optical properties, which have to be investigated. The influence of the hydroxyl groups and crystal water in terms of quenching processes could be investigated by heating up the doped compounds carefully until hydroxyl groups and crystal water are removed.

$Ln[H(PO_3)_4]$ ($Ln =$ Tb, Dy, Ho) belong to the binary lanthanide phosphates, which comprise already a great variety in structure and composition [264]. The UV-Vis and fluorescence spectra have been investigated in this work. Furthermore, lifetime measurements and the determination of the quantum yield could demonstrate the qualification as classical luminescent material or as part of a three-colour LED. Nevertheless, $Ln[H(PO_3)_4]$ ($Ln =$ La, Pr, Nd, Tm, Yb) have not been observed up to now. A successful synthesis would open a new field for the investigation of the optical properties of the stoichiometric or doped compounds. Co-doping of the thulium compound with Er^{3+} and Yb^{3+} could result in an effective upconversion phosphor for displays [4]. Moreover, those compounds come into question as magnetic materials. Furthermore, unary phosphates XP_4O_{12} with tetravalent lanthanide ions for X, e.g. Tb^{4+} and Tm^{4+}, might reveal interesting structures, which could thus exhibit interesting magnetic properties. Up to now the crystal structures of the catena-metaphosphates XP_4O_{12} ($X =$ Ce, U) [190] are known, which crystallise isotypic in the monoclinic space group $C2/c$ (no. 15).

Since $Sr_3P_4O_{13}$:Eu^{2+} could not be obtained phase pure, an effective synthesis should be found as the compound possesses great potential as luminescent material [207, 208]. The temperature dependence of the optical properties of the compound was

already investigated by *Zhang et al.* (2013) [110], but $Sr_2P_2O_7$:Eu^{2+} seems to be present as side phase, too. Thus, results have not been unambiguously yet. Co-doping with other divalent lanthanide ions, e.g. Sm^{2+} or transition metal cations, such as Mn^{2+}, could result in a two colour phosphor. Life-time measurements would complete the picture of the potential optical material.

Borophosphates in general and transition metal borophosphates in particular already show a large variety in composition and structure. Nevertheless, this class of compounds seems to represent an everlasting source of novel compounds exhibiting new types of FBUs or structures built of these. Up to now no lanthanide compounds have been obtained yet. $Ln BP_2O_{17}$ (Ln = Pr, Sm) [290] comprise non-condensed borate and phosphate units and are thus not classified as borophosphates, but as borate-phosphates. A number of alkaline earth borophosphates was already doped with lanthanide ions to investigate their optical properties [125–128, 291, 292]. Further borophosphates, especially alkaline earth or lanthanide borophosphates, could be doped with typical activator ions, e.g. Ce^{3+}, Tb^{3+}, Er^{3+} [3, 4], or show as stoichiometric compounds promising properties for optical applications. Additionally, many borophosphates posses a high degree of condensation due to their analogy to silicates [13, 113] and thus reveal high structural and thermal stability, which are important features for luminescent materials. A further step is the partial substitution of alkaline earth ions by others in Eu^{2+} doped compounds, e.g. Sr^{2+} against Ba^{2+} to obtain an expansion of the cationic sites. Thus, the interaction between host lattice and cation decreases followed by a decreased ligand field splitting. A shift towards shorter wavelengths would result and continuous colour tuning would be possible.

Further investigations on $(NH_4)Cr(III)[BP_2O_8(OH)]$ should enable the phase pure synthesis of the compound. The body colour of the compound is intense green and could be intensified by purification. Further investigation of the optical properties and the thermal stability could check its suitability as green pigment. The structure solution of single-crystal data might lead to a much better MAPLE value and thus to a satisfying electrostatic consistency.

In general, the partial substitution of oxygen by fluorine in borophosphates leads to a weaker interaction between host lattice and cation. $NH_4[BPO_4F]$ was the first representative exhibiting a three-dimensional network [293]. In 2013 *Jansen* and *Pilz* published the crystal structures of the polymorphic $Na_3[B_2PO_5F_4]$ comprising isolated dreier-single rings [294]. In both compounds fluorine atoms exclusively occur in the coordination sphere of boron. Doped alkaline earth or lanthanide fluorooxoborophosphates might be used as upconversion phosphors, which could be utilised in solar cells or transparent displays [4].

Concerning the borosulphates in the past years numerous compounds [134–137] were synthesised and characterised. Besides the synthesis and crystal structure of alkaline-earth borosulphates [140, 295] the first lanthanide compound $Gd[B(SO_4)_3]$ [138, 139] was obtained. The family of borosulphates is still rather young and further investigations will bring for sure novel FBUs, structures and compositions. Investigations of doped compounds with Eu^{3+} reveal the luminescence properties of the compounds, as already done in $Ba[B_2S_3O_{13}]:Eu^{3+}$ [140]. A large problem still represents the instability against air or humidity. Except monovalent borosulphates, which are relatively stable, up to now all borosulphates show a strong tendency to decompose when exposed to humid air, which makes an application as luminescent material difficult. However, borosulphates with a high sensitivity to air might be used as very efficient indicators for humidity by decomposition. If the material, which has to be stored in inert atmosphere is insensitive to the aggressive sulphate groups of the compound an application might be imaginable.

12 Appendix

Table 12.1: MAPLE results for $Cs_2[B_{10}O_{14}(OH)_4]\cdot H_2O$

No.	Atom	x	y	z	Distance	ECoN
CA	Cs1	0.4920	0.0576	0.2541		
1	O_H2	0.3050	0.0700	0.0302	275.893	1.507
2	$O_{br}9$	0.4790	−0.2750	0.1960	301.971	0.986
3	$O_{br}12$	0.5130	0.2430	0.4884	307.765	0.872
4	$O_{br}14$	0.7050	0.0600	0.5075	309.730	0.834
5	$O_{br}13$	0.3170	−0.2130	0.3200	313.536	0.763
6	O_W	0.6430	0.3690	0.2330	314.855	0.738
7	$O_{br}3$	0.1250	0.0470	0.3230	321.258	0.625
8	$O_{br}4$	0.8680	0.0420	0.1790	331.571	0.460
9	$O_{br}6$	0.1020	0.2490	0.2280	350.473	0.228
10	$O_{br}1$	0.9450	0.2350	0.3540	365.705	0.111
Next Ligand:						
11	$O_{br}14$	0.2950	−0.0600	0.4925	395.723	0.016
Last Ligand:						
30	$O_{br}1$	−0.0550	0.2350	0.3540	499.929	0.000
CN: 10						

CA = Central Atom

No.	Atom	x	y	z	Distance	ECoN
CA	Cs2	0.8993	0.7064	0.2096		
1	O_H1	1.0490	0.6440	0.4480	299.420	1.466
2	$O_{br}4$	0.8680	1.0420	0.1790	316.886	1.142
3	$O_{br}13$	1.3170	0.7870	0.3200	318.180	1.117
4	$O_{br}9$	0.4790	0.7250	0.1960	324.584	0.998
5	$O_{br}7$	0.8730	0.6420	−0.0650	329.442	0.909
6	$O_{br}10$	1.2690	0.5350	0.2150	330.177	0.896
7	$O_{br}8$	0.7070	0.4540	−0.0349	344.470	0.649
8	$O_{br}3$	1.1250	1.0470	0.3230	344.729	0.645
9	$O_{br}2$	0.8880	0.8550	0.4849	348.393	0.587
10	O_H3	0.4800	0.7210	−0.0081	362.259	0.392
11	O_W	0.6430	0.3690	0.2330	374.916	0.252
12	$O_{br}11$	0.5620	0.6090	0.3563	375.562	0.246
13	O_H2	0.6950	0.9300	−0.0302	385.754	0.161
14	$O_{br}5$	1.0990	0.8420	−0.0250	399.404	0.084
Next Ligand:						
15	$O_{br}7$	1.1270	0.3580	0.0650	409.836	0.047
Last Ligand:						
26	$O_{br}12$	1.4870	0.7570	0.5116	498.973	0.000
CN: 14						

CA = Central Atom

Atom	Charge	Distance	Potential	PMF	MAPLE	*MAPLE
Cs1	+ 1.0000	270.90	-0.59632	0.20560	98.9319	98.9319
Cs2	+ 1.0000	288.03	-0.62684	0.21613	103.9958	103.9958
B1	+ 3.0000	143.01	-2.90906	3.00904	1447.8810	160.8757
B2	+ 3.0000	138.57	-3.00048	3.10360	1493.3833	165.9315
B3	+ 3.0000	135.73	-2.57349	2.66194	1280.8651	142.3183
B4	+ 3.0000	138.53	-2.72602	2.81971	1356.7812	150.7535
B5	+ 3.0000	121.31	-3.12232	3.22962	1554.0235	172.6693
B6	+ 3.0000	136.52	-2.83506	2.93249	1411.0510	156.7834
B7	+ 3.0000	125.76	-2.72489	2.81854	1356.2193	150.6910
B8	+ 3.0000	126.33	-2.81643	2.91323	1401.7798	155.7533
B9	+ 3.0000	137.67	-2.70455	2.79750	1346.0950	149.5661
B10	+ 3.0000	133.15	-2.83919	2.93677	1413.1094	157.0122
$O_{br}1$	- 2.0000	126.33	2.55047	1.75875	846.2710	211.5678
$O_{br}2$	- 2.0000	143.56	2.20475	1.52035	731.5569	182.8892
$O_{br}3$	- 2.0000	125.76	2.43528	1.67931	808.0487	202.0122
$O_{br}4$	- 2.0000	142.75	2.34201	1.61500	777.1029	194.2757
$O_{br}5$	- 2.0000	135.73	2.50298	1.72600	830.5137	207.6284
$O_{br}6$	- 2.0000	148.52	2.06458	1.42369	685.0487	171.2622
$O_{br}7$	- 2.0000	131.88	2.29869	1.58512	762.7270	190.6818
$O_{br}8$	- 2.0000	142.78	2.09566	1.44513	695.3622	173.8406
$O_{br}9$	- 2.0000	136.52	2.26941	1.56494	753.0133	188.2533
$O_{br}10$	- 2.0000	121.31	2.31943	1.59943	769.6113	192.4028
$O_{br}11$	- 2.0000	139.09	2.01020	1.38619	667.0030	166.7507
$O_{br}12$	- 2.0000	135.07	2.49802	1.72258	828.8692	207.2173
$O_{br}13$	- 2.0000	141.99	2.11449	1.45811	701.6084	175.4021
$O_{br}14$	- 2.0000	133.15	2.28160	1.57334	757.0581	189.2645
O_H1	- 2.0000	78.31	2.21173	1.52516	733.8740	183.4685
O_H2	- 2.0000	68.96	2.50311	1.72609	830.5558	207.6389
O_H3	- 2.0000	109.23	2.06294	1.42256	684.5053	171.1263
O_H4	- 2.0000	78.84	2.27180	1.56658	753.8058	188.4514
O_W	- 2.0000	91.74	2.09200	1.44260	694.1475	173.5369
H1	+ 1.0000	78.31	-2.06636	0.71246	342.8188	342.8188
H2	+ 1.0000	68.96	-2.22571	0.76740	369.2557	369.2557
H3	+ 1.0000	109.23	-1.51793	0.52337	251.8324	251.8324
H4	+ 1.0000	78.84	-1.89582	0.65366	314.5260	314.5260
H5	+ 1.0000	91.74	-1.58322	0.54588	262.6640	262.6640
H6	+ 1.0000	107.02	-1.31171	0.45226	217.6195	217.6195
Madelung Constant:				63.0401	± 0.000003	
Coulomb Part of Lattice Energy:				30333.5159	± 0.001261 kcal·mol^{-1}	
Coulomb Part of Lattice Energy:				126976.1285.7541	± 0.005278 kJ·mol^{-1}	

Table 12.2: MAPLE results for $Tb[H(PO_3)_4]$

No.	Atom	x	y	z	Distance	ECoN
CA	Tb1	0.7294	0.0579	0.0590		
1	$O_{term}5$	0.6343	−0.0458	0.2130	228.057	1.103
2	$O_{term}7$	0.6158	0.1415	−0.1374	228.477	1.092
3	$O_{term}3$	0.8414	0.0764	−0.0888	229.169	1.074
4	$O_{term}4$	0.8587	0.2086	0.2048	230.030	1.051
5	O_H1	0.6615	0.3364	0.1191	230.737	1.033
6	$O_{term}2$	0.8343	−0.1895	0.1741	240.125	0.795
7	$O_{term}6$	0.6902	−0.2278	−0.0832	245.093	0.677
Next Ligand:						
8	$O_{br}3$	0.5801	−0.1234	−0.3124	398.123	0.000
Last Ligand:						
33	$O_{br}3$	0.4199	0.3766	−0.1876	498.114	0.000
CN: 7						

CA = Central Atom

Atom	Charge	Distance	Potential	PMF	MAPLE	*MAPLE
Tb1	+ 3.0000	228.06	-2.23560	3.14210	1112.6923	123.6325
P1	+ 5.0000	146.57	-3.94997	9.25271	3276.6030	131.0641
P2	+ 5.0000	146.17	-4.07022	9.53438	3376.3483	135.0539
P3	+ 5.0000	148.04	-3.99612	9.36080	3314.8804	132.5952
P4	+ 5.0000	146.37	-4.02483	9.42806	3338.6996	133.5480
$O_{br}1$	- 2.0000	156.13	2.56676	2.40503	851.6768	212.9192
$O_{br}2$	- 2.0000	157.52	2.48447	2.32792	824.3715	206.0929
$O_{br}3$	- 2.0000	158.26	2.54348	2.38322	843.9533	210.9883
$O_{br}4$	- 2.0000	158.16	2.49563	2.33837	828.0734	207.0183
$O_{term}1$	- 2.0000	93.70	2.29705	2.15231	762.1853	190.5463
$O_{term}2$	- 2.0000	146.57	2.06607	1.93589	685.5427	171.3857
$O_{term}3$	- 2.0000	146.17	2.06933	1.93894	686.6242	171.6561
$O_{term}4$	- 2.0000	147.21	1.97753	1.85293	656.1645	164.0411
$O_{term}5$	- 2.0000	148.04	2.05820	1.92851	682.9300	170.7325
$O_{term}6$	- 2.0000	149.37	2.10980	1.97686	700.0536	175.0134
$O_{term}7$	- 2.0000	148.32	2.06836	1.93803	686.3018	171.5754
O_H1	- 2.0000	146.37	1.99204	1.86652	660.9773	165.2443
H1	+ 1.0000	93.70	-1.59270	0.74617	264.2367	264.2367
Madelung Constant:				66.5088	± 0.000002	
Coulomb Part of Lattice Energy:				23552.3145	± 0.000796 kcal·mol^{-1}	
Coulomb Part of Lattice Energy:				98590.0127	± 0.003333 kJ·mol^{-1}	

Table 12.3: MAPLE results for $Ho[H(PO_3)_4]$

No.	Atom	x	y	z	Distance	ECoN
CA	Ho1	0.7295	0.0566	0.0593		
1	$O_{term}4$	0.6349	−0.0475	0.2120	225.352	1.109
2	$O_{term}2$	0.8395	0.0788	−0.0889	226.060	1.091
3	$O_{term}6$	0.6161	0.1414	−0.1351	226.367	1.083
4	$O_{term}7$	0.6633	0.3331	0.1200	228.084	1.037
5	$O_{term}3$	0.8581	0.2080	0.2034	228.180	1.035
6	$O_{term}1$	0.8334	−0.1891	0.1737	237.676	0.792
7	$O_{term}5$	0.6904	−0.2267	−0.0824	242.694	0.671
Next Ligand:						
8	O_H1	0.8568	−0.4297	−0.0126	397.988	0.000
Last Ligand:						
18	$O_{term}1$	0.8334	−0.3109	−0.3263	494.807	0.000
CN: 7						

CA = Central Atom

Atom	Charge	Distance	Potential	PMF	MAPLE	*MAPLE
Ho1	+ 3.0000	225.35	-2.26810	3.19985	1128.8655	125.4295
P1	+ 5.0000	147.24	-4.00894	9.42642	3325.5141	133.0206
P2	+ 5.0000	146.40	-4.09820	9.63631	3399.5607	135.9824
P3	+ 5.0000	147.90	-3.97454	9.34554	3296.9815	131.8793
P4	+ 5.0000	147.05	-4.00252	9.41132	3320.1886	132.8075
$O_{br}1$	- 2.0000	156.84	2.53961	2.38860	842.6677	210.6669
$O_{br}2$	- 2.0000	157.51	2.44691	2.30141	811.9083	202.9771
$O_{br}3$	- 2.0000	158.04	2.56197	2.40963	850.0864	212.5216
$O_{br}4$	- 2.0000	158.17	2.52780	2.37750	838.7486	209.6871
$O_{term}1$	- 2.0000	147.24	2.01379	1.89405	668.1946	167.0486
$O_{term}2$	- 2.0000	146.40	2.04210	1.92068	677.5893	169.3973
$O_{term}3$	- 2.0000	146.58	1.98252	1.86464	657.8208	164.4552
$O_{term}4$	- 2.0000	147.90	2.09454	1.97000	694.9907	173.7477
$O_{term}5$	- 2.0000	149.45	2.09137	1.96702	693.9372	173.4843
$O_{term}6$	- 2.0000	148.21	2.08974	1.96548	693.3954	173.3489
$O_{term}7$	- 2.0000	147.05	2.00086	1.88189	663.9043	165.9761
O_H1	- 2.0000	94.05	2.28064	2.14504	756.7408	189.1852
H1	+ 1.0000	94.05	-1.71206	0.80513	284.0390	284.0390
Madelung Constant:				66.9105	± 0.000002	
Coulomb Part of Lattice Energy:				23605.1333	± 0.000796 kcal·mol^{-1}	
Coulomb Part of Lattice Energy:				98811.1123	± 0.003333 kJ·mol^{-1}	

Table 12.4: MAPLE results for RT-$Sr_3P_4O_{13}$

No.	Atom	x	y	z	Distance	ECoN
CA	Sr1	0.3432	0.9194	0.2766		
1	$O_{term}5$	0.2546	1.1398	−0.0003	252.779	1.169
2	$O_{term}3$	0.4362	1.2174	0.3777	252.839	1.167
3	$O_{term}1$	0.5753	0.5389	0.3139	253.057	1.162
4	$O_{term}5$	0.7454	0.8602	0.0003	263.142	0.928
5	$O_{term}2$	−0.1121	1.2043	0.3977	265.619	0.872
6	$O_{term}4$	0.0321	0.7231	0.2190	265.731	0.870
7	$O_{term}2$	0.1121	0.7957	0.6023	270.801	0.759
8	$O_{term}3$	0.5638	0.7826	0.6223	312.145	0.136
Next Ligand:						
9	$O_{br}1$	0.2386	0.7476	−0.0994	350.039	0.007
Last Ligand:						
29	$O_{term}2$	0.8879	0.2043	0.3977	497.631	0.000
CN: 8						
CA	Sr2	0.0000	0.5000	0.5000		
1	$O_{term}4$	0.0321	0.7231	0.2190	251.597	1.175
2	$O_{term}4$	−0.0321	0.2769	0.7810	251.597	1.175
3	$O_{term}2$	0.1121	0.7957	0.6023	257.763	1.031
4	$O_{term}2$	−0.1121	0.2043	0.3977	257.763	1.031
5	$O_{term}3$	−0.4362	0.7826	0.6223	258.691	1.009
6	$O_{term}3$	0.4362	0.2174	0.3777	258.691	1.009
7	$O_{term}1$	−0.4247	0.5389	0.3139	296.414	0.289
8	$O_{term}1$	0.4247	0.4611	0.6861	296.414	0.289
9	$O_{term}1$	−0.5753	0.4611	0.6861	323.641	0.061
10	$O_{term}1$	0.5753	0.5389	0.3139	323.641	0.061
Next Ligand:						
11	$O_{br}2$	0.0648	0.4791	0.0352	353.267	0.004
Last Ligand:						
28	$O_{br}1$	0.2386	0.7476	−0.0994	476.891	0.000
CN: 10						

CA = Central Atom

Atom	Charge	Distance	Potential	PMF	MAPLE	*MAPLE
Sr1	+ 2.0000	252.78	-1.53549	2.24916	509.4894	127.3724
Sr2	+ 2.0000	251.60	-1.41283	2.06950	468.7911	117.1978
P1	+ 5.0000	149.87	-4.04668	14.81880	3356.8187	134.2727
P2	+ 5.0000	146.48	-3.95996	14.50124	3284.8839	131.3954
$O_{br}1$	- 2.0000	157.72	2.49888	3.66032	829.1520	207.2880
$O_{br}2$	- 2.0000	154.83	2.56985	3.76429	852.7036	213.1759
$O_{term}1$	- 2.0000	149.87	2.03289	2.97775	674.5323	168.6331
$O_{term}2$	- 2.0000	152.52	1.93661	2.83672	642.5869	160.6467
$O_{term}3$	- 2.0000	151.21	1.86616	2.73352	619.2098	154.8025
$O_{term}4$	- 2.0000	147.83	1.93643	2.83646	642.5264	160.6316
$O_{term}5$	- 2.0000	146.48	1.94864	2.85435	646.5794	161.6449
Madelung Constant:				104.7704	± 0.000004	
Coulomb Part of Lattice Energy:				23733.0525	± 0.000863 kcal·mol^{-1}	
Coulomb Part of Lattice Energy:				99346.5819	± 0.003611 kJ·mol^{-1}	

Table 12.5: MAPLE results for LT-$Sr_3P_4O_{13}$

No.	Atom	x	y	z	Distance	ECoN
CA	Sr1	0.2075	0.7173	0.1369		
1	$O_{term}1$	0.0965	0.6279	0.3322	250.973	1.203
2	$O_{term}6$	0.0446	0.9867	0.2146	254.087	1.130
3	$O_{term}7$	0.1245	0.7804	−0.1074	257.184	1.057
4	$O_{term}8$	0.5063	0.6929	0.0385	259.616	1.001
5	$O_{term}5$	0.4322	0.9864	0.3176	260.684	0.976
6	$O_{term}9$	−0.1627	0.6000	0.0479	264.739	0.884
7	$O_{term}9$	0.1627	0.4000	−0.0479	269.340	0.782
8	$O_{term}10$	0.3785	0.3842	0.1805	300.677	0.244
Next Ligand:						
9	$O_{br}3$	0.2350	1.1014	0.0016	352.728	0.005
Last Ligand:						
30	$O_{term}9$	0.8373	0.6000	0.0479	497.823	0.000
CN: 8						
CA	Sr2	0.7476	0.4795	0.2415		
1	$O_{term}4$	0.6833	0.7795	0.3591	249.915	1.214
2	$O_{term}9$	0.8373	0.6000	0.0479	253.566	1.128
3	$O_{term}7$	0.8755	0.2196	0.1074	254.066	1.116
4	$O_{term}1$	1.0965	0.6279	0.3322	256.784	1.052
5	$O_{term}10$	0.3785	0.3842	0.1805	261.446	0.945
6	$O_{term}2$	0.6528	0.3943	0.4560	262.438	0.922
7	$O_{term}3$	0.9730	0.3195	0.4272	275.808	0.633
8	$O_{term}8$	0.4937	0.3071	−0.0385	297.107	0.279
9	$O_{term}8$	0.5063	0.6929	0.0385	319.635	0.080
Next Ligand:						
10	$O_{br}2$	0.7070	0.0334	0.2266	339.408	0.017
Last Ligand:						
29	$O_{term}10$	1.3785	0.3842	0.1805	485.620	0.000
CN: 9						

CA = Central Atom

Table 12.6: MAPLE results for LT-$Sr_3P_4O_{13}$

No.	Atom	x	y	z	Distance	ECoN
CA	Sr3	0.2852	0.2709	0.3758		
1	$O_{term}3$	−0.0270	0.3195	0.4272	248.154	1.259
2	$O_{term}5$	0.4322	−0.0136	0.3176	253.023	1.145
3	$O_{term}10$	0.3785	0.3842	0.1805	253.442	1.135
4	$O_{term}2$	0.6528	0.3943	0.4560	263.835	0.894
5	$O_{term}6$	0.0446	−0.0133	0.2146	266.068	0.844
6	$O_{term}2$	0.3472	0.6057	0.5440	271.479	0.726
7	$O_{term}4$	0.3167	0.2205	0.6409	276.120	0.631
8	$O_{term}1$	0.0965	0.6279	0.3322	323.295	0.063
Next Ligand:						
9	$O_{br}1$	0.2410	−0.0956	0.5147	343.765	0.012
Last Ligand:						
29	$O_{term}2$	−0.3472	0.3943	0.4560	497.656	0.000
CN: 8						

CA = Central Atom

Atom	Charge	Distance	Potential	PMF	MAPLE	*MAPLE
Sr1	+ 2.0000	250.97	-1.53676	2.28436	509.9128	127.4782
Sr2	+ 2.0000	249.92	-1.41867	2.10883	470.7300	117.6825
Sr3	+ 2.0000	248.15	-1.49894	2.22814	497.3639	124.3410
P1	+ 5.0000	150.68	-4.08337	15.17460	3387.2576	135.4903
P2	+ 5.0000	149.24	-3.97174	14.75975	3294.6547	131.7862
P3	+ 5.0000	148.65	-3.96963	14.75192	3292.9072	131.7163
P4	+ 5.0000	150.41	-4.04238	15.02227	3353.2544	134.1302
$O_{br}1$	- 2.0000	157.86	2.47625	3.68090	821.6461	205.4115
$O_{br}2$	- 2.0000	158.90	2.67113	3.97057	886.3067	221.5767
$O_{br}3$	- 2.0000	158.56	2.50010	3.71634	829.5575	207.3894
$O_{term}1$	- 2.0000	150.68	1.86164	2.76729	617.7115	154.4279
$O_{term}2$	- 2.0000	153.43	1.90564	2.83269	632.3099	158.0775
$O_{term}3$	- 2.0000	150.70	2.04065	3.03339	677.1091	169.2773
$O_{term}4$	- 2.0000	149.38	2.01363	2.99322	668.1426	167.0357
$O_{term}5$	- 2.0000	149.24	1.96045	2.91417	650.4979	162.6245
$O_{term}6$	- 2.0000	148.65	1.97966	2.94272	656.8715	164.2179
$O_{term}7$	- 2.0000	149.69	1.95935	2.91254	650.1331	162.5333
$O_{term}8$	- 2.0000	150.41	2.04463	3.03930	678.4297	169.6074
$O_{term}9$	- 2.0000	152.62	1.90500	2.83175	632.0997	158.0249
$O_{term}10$	- 2.0000	152.15	1.89686	2.81964	629.3965	157.3491
Madelung Constant:				106.7844	± 0.000004	
Coulomb Part of Lattice Energy:				23836.2924	± 0.000863 kcal·mol^{-1}	
Coulomb Part of Lattice Energy:				99778.7446	± 0.003611 kJ·mol^{-1}	

Table 12.7: MAPLE results for $(NH_4)_2Mn(II)[B_2P_3O_{11}(OH)_2]Cl$

No.	Atom	x	y	z	Distance	ECoN
CA	Mn1	0.5995	0.3226	0.1290		
1	Cl1	0.7976	0.3087	0.2450	257.448	1.166
2	$O_{term}3$	0.6903	0.1135	0.0806	212.307	1.088
3	$O_{term}2$	0.7174	0.4962	0.0633	213.875	1.044
4	$O_{term}1$	0.4318	0.3192	0.0309	217.526	0.943
5	O_H1	0.4900	0.5183	0.1875	217.776	0.936
6	$O_{term}4$	0.4266	0.1847	0.1961	227.744	0.674
Next Ligand:						
7	$O_{br}2$	0.3003	0.5587	0.0841	342.438	0.000
Last Ligand:						
28	N2	0.4567	0.8820	0.0956	493.763	0.000
CN: 6						
CA	N1	0.0242	0.4201	0.8597		
1	H4	−0.0070	0.3220	0.8830	96.346	1.016
2	H3	−0.0450	0.5010	0.8742	96.549	1.004
3	H6	0.0160	0.3960	0.8025	96.606	1.000
4	H5	0.1204	0.4480	0.8833	96.933	0.980
Next Ligand:						
5	H2	0.1660	0.1030	0.8294	302.783	
Last Ligand:						
29	P2	−0.1649	0.0426	1.0608	496.652	
CN: 4						
CA	N2	0.4567	0.8820	0.0956		
1	H10	0.4460	0.8350	0.1480	96.098	1.032
2	H8	0.5270	0.9670	0.1020	96.403	1.013
3	H7	0.3660	0.9310	0.0756	96.654	0.998
4	H9	0.4990	0.8070	0.0584	97.355	0.954
Next Ligand:						
5	H2	0.1660	0.1030	0.8294	302.783	0.000
Last Ligand:						
29	P2	−0.1649	0.0426	1.0608	496.652	0.000
CN: 4						

CA = Central Atom

Atom	Charge	Distance	Potential	PMF	MAPLE	*MAPLE
Mn1	+ 2.0000	212.31	-1.61339	1.55043	535.3386	133.8347
P1	+ 5.0000	150.15	-3.93366	9.45042	3263.0726	130.5229
P2	+ 5.0000	149.03	-3.92076	9.41942	3252.3668	130.0947
P3	+ 5.0000	149.37	-3.89386	9.35480	3230.0559	129.2022
B1	+ 3.0000	143.39	-2.91013	4.19487	1448.4168	160.9352
B2	+ 3.0000	145.37	-2.87802	4.14858	1432.4354	159.1595
$O_{br}1$	- 2.0000	146.76	2.37329	2.28068	787.4819	196.8705
$O_{br}2$	- 2.0000	147.46	2.32824	2.23739	772.5332	193.1333
$O_{br}3$	- 2.0000	145.37	2.42999	2.33517	806.2935	201.5734
$O_{br}4$	- 2.0000	147.32	2.49078	2.39359	826.4673	206.6168
$O_{br}5$	- 2.0000	146.96	2.42014	2.32570	803.0262	200.7566
$O_{br}6$	- 2.0000	146.34	2.47153	2.37509	820.0798	205.0200
$O_{br}7$	- 2.0000	148.09	2.49363	2.39633	827.4120	206.8530
$O_{term}1$	- 2.0000	150.42	2.16586	2.08135	718.6555	179.6639
$O_{term}2$	- 2.0000	150.15	2.07962	1.99847	690.0397	172.5099
$O_{term}3$	- 2.0000	149.03	2.10550	2.02334	698.6253	174.6563
$O_{term}4$	- 2.0000	149.37	2.12230	2.03949	704.2015	176.0504
O_H1	- 2.0000	96.37	2.21522	2.12878	735.0308	183.7577
O_H2	- 2.0000	96.96	2.44816	2.35264	812.3254	203.0814
Cl1	- 1.0000	201.47	0.52429	0.25192	86.9827	86.9827
N1	- 3.0000	96.35	3.46574	4.99575	1724.9495	191.6611
N2	- 3.0000	96.10	3.45416	4.97906	1719.1857	191.0206
H1	+ 1.0000	96.37	-1.53266	0.73643	254.2764	254.2764
H2	+ 1.0000	96.96	-1.43996	0.69189	238.8966	238.8966
H3	+ 1.0000	96.55	-1.83655	0.88244	304.6925	304.6925
H4	+ 1.0000	96.35	-1.83336	0.88091	304.1633	304.1633
H5	+ 1.0000	96.93	-1.98425	0.95341	329.1969	329.1969
H6	+ 1.0000	96.61	-1.90254	0.91415	315.6410	315.6410
H7	+ 1.0000	96.65	-1.90131	0.91356	315.4368	315.4368
H8	+ 1.0000	96.40	-1.90126	0.91354	315.4286	315.4286
H9	+ 1.0000	97.35	-1.91150	0.91846	317.1277	317.1277
H10	+ 1.0000	96.10	-1.88468	0.90557	312.6780	312.6780
Madelung Constant:				86.0236	$\pm$ 0.000003	
Coulomb Part of Lattice Energy:				29702.5140	$\pm$ 0.001095 kcal·mol^{-1}	
Coulomb Part of Lattice Energy:				124334.7541	$\pm$ 0.004584 kJ·mol^{-1}	

Table 12.8: MAPLE results for $(NH_4)_2[B_2P_3O_{11}(OH)]$

No.	Atom	x	y	z	Distance	ECoN
CA	N1	0.8881	0.0214	0.6411		
1	H4	0.9080	0.0280	0.7001	97.650	1.018
2	H3	1.0790	−0.0080	0.6300	97.752	1.012
3	H5	0.8790	0.0810	0.6130	97.974	0.998
4	H2	0.7170	−0.0200	0.6340	98.418	0.971
Next Ligand:						
5	H1	1.3310	−0.0260	0.8020	337.991	0.000
Last Ligand:						
30	H8	1.2210	0.2670	0.8300	495.140	0.000
CN: 4						
CA	N2	0.6864	0.2778	0.2137		
1	H6	0.8640	0.2770	0.2480	97.871	1.014
2	H9	0.6960	0.3350	0.1820	97.936	1.010
3	H8	0.7210	0.2330	0.1700	97.951	1.009
4	H7	0.5270	0.2580	0.2510	98.648	0.966
Next Ligand:						
5	H4	0.4080	0.4720	0.2999	339.012	0.000
Last Ligand:						
35	H2	1.2170	0.5200	0.3660	492.745	0.000
CN: 4						

CA = Central Atom

Atom	Charge	Distance	Potential	PMF	MAPLE	*MAPLE
P1	+ 5.0000	148.33	-3.88913	9.49439	3226.1330	129.0453
P2	+ 5.0000	148.76	-3.99693	9.75754	3315.5497	132.6220
P3	+ 5.0000	147.64	-3.89828	9.51671	3233.7167	129.3487
B1	+ 3.0000	145.28	-2.84253	4.16361	1414.7692	157.1966
B2	+ 3.0000	144.96	-2.83096	4.14667	1409.0128	156.5570
$O_{br}1$	- 2.0000	146.30	2.55226	2.49229	846.8638	211.7159
$O_{br}2$	- 2.0000	147.88	2.46533	2.40740	818.0197	204.5049
$O_{br}3$	- 2.0000	145.28	2.53315	2.47363	840.5232	210.1308
$O_{br}4$	- 2.0000	146.14	2.37862	2.32273	789.2495	197.3124
$O_{br}5$	- 2.0000	144.96	2.37128	2.31556	786.8130	196.7032
$O_{br}6$	- 2.0000	148.11	2.52401	2.46471	837.4933	209.3733
$O_{br}7$	- 2.0000	146.43	2.46062	2.40280	816.4569	204.1142
$O_{br}8$	- 2.0000	148.52	2.51130	2.45229	833.2732	208.3183
$O_{term}1$	- 2.0000	148.33	2.04296	1.99496	677.8750	169.4688
$O_{term}2$	- 2.0000	148.76	2.11995	2.07015	703.4221	175.8555
$O_{term}3$	- 2.0000	147.64	2.06573	2.01719	685.4285	171.3571
O_H1	- 2.0000	97.73	2.28924	2.23545	759.5929	189.8982
N1	- 3.0000	97.65	3.33400	4.88350	1659.3804	184.3756
N2	- 3.0000	97.87	3.35544	4.91490	1670.0531	185.5615
H1	+ 1.0000	97.73	-1.74303	0.85104	289.1777	289.1777
H2	+ 1.0000	98.42	-2.03433	0.99327	337.5054	337.5054
H3	+ 1.0000	97.75	-1.94509	0.94969	322.6994	322.6994
H4	+ 1.0000	97.65	-1.92826	0.94148	319.9075	319.9075
H5	+ 1.0000	97.97	-1.92841	0.94155	319.9325	319.9325
H6	+ 1.0000	97.87	-1.94522	0.94976	322.7213	322.7213
H7	+ 1.0000	98.65	-1.97643	0.96500	327.8998	327.8998
H8	+ 1.0000	97.95	-1.78907	0.87352	296.8157	296.8157
H9	+ 1.0000	97.94	-1.93716	0.94582	321.3839	321.3839
Madelung Constant:				82.9376	± 0.000003	
Coulomb Part of Lattice Energy:				28181.6693	± 0.000995 kcal·mol^{-1}	
Coulomb Part of Lattice Energy:				117968.4965	± 0.004167 kJ·mol^{-1}	

Table 12.9: MAPLE results for $NH_4Cr(III)[BP_2O_8(OH)]$

No.	Atom	x	y	z	Distance	ECoN
CA	Cr1	0.2092	0.1497	0.4323		
1	$O_{term}4$	0.1129	0.3371	0.3476	188.458	1.250
2	$O_{term}2$	0.3421	0.1232	0.3095	190.321	1.192
3	O_H1	0.3159	−0.0471	0.5220	200.184	0.891
4	$O_{term}3$	0.0886	0.1680	0.5818	201.535	0.851
5	$O_{term}5$	0.0785	−0.0006	0.2939	202.062	0.835
6	$O_{term}1$	0.3736	0.2927	0.5577	209.476	0.628
Next Ligand:						
7	$O_{term}3$	0.0886	0.3320	0.0818	362.926	0.000
Last Ligand:						
17	$O_{term}2$	0.6579	−0.1232	0.6905	491.982	0.000
CN: 6						
CA	P1	0.0753	0.4323	0.2039		
1	$O_{term}3$	0.0886	0.3320	0.0818	146.300	1.260
2	$O_{term}5$	−0.0785	0.4994	0.2061	154.446	0.938
3	$O_{term}4$	0.1129	0.3371	0.3476	155.875	0.883
4	$O_{br}3$	0.1842	0.5842	0.2234	160.186	0.723
Next Ligand:						
5	$O_{term}3$	−0.0886	0.6680	−0.0818	343.546	0.000
Last Ligand:						
14	$O_{term}5$	0.0785	0.9994	0.2939	477.156	0.000
CN: 4						
CA	P2	0.4157	0.2381	0.2205		
1	$O_{br}1$	0.4078	0.4113	0.2557	147.839	1.221
2	$O_{term}2$	0.3421	0.1232	0.3095	153.787	0.986
3	$O_{term}1$	0.3736	0.2073	0.0577	154.470	0.960
4	$O_{br}2$	0.5941	0.2036	0.2497	165.209	0.572
Next Ligand:						
5	$O_{br}1$	0.5922	−0.0887	0.2443	314.952	0.000
Last Ligand:						
12	$O_{term}1$	0.6264	0.7073	0.4423	465.064	0.000
CN: 4						

CA = Central Atom

No.	Atom	x	y	z	Distance	ECoN
CA	B1	0.3261	0.9370	0.6800		
1	$O_{br}2$	0.4059	0.7964	0.7503	146.359	1.136
2	$O_{br}3$	0.1842	0.9158	0.7234	148.464	1.051
3	$O_{H}1$	0.3159	0.9529	0.5220	150.297	0.977
4	O_{br}	0.4078	1.0887	0.7557	156.234	0.748
Next Ligand:						
5	$O_{br}1$	0.5922	0.5887	0.7443	376.688	0.000
Last Ligand:						
9	$O_{br}2$	0.4059	0.7036	0.2503	475.717	0.000
CN: 4						
CA	N1	0.1791	0.5964	0.5615		
1	H2	0.1320	0.6540	0.5440	64.521	1.031
Next Ligand:						
2	H3	0.1870	0.5200	0.5050	84.656	0.019
Last Ligand:						
9	H4	0.1830	0.9450	0.1680	475.723	0.000
CN: 1						

CA = Central Atom

Atom	Charge	Distance	Potential	PMF	MAPLE	*MAPLE
Cr1	+ 3.0000	188.46	-2.33588	2.26072	1162.6050	129.1783
P1	+ 5.0000	146.30	-3.99855	6.44980	3316.9004	132.6760
P2	+ 5.0000	147.84	-3.89081	6.27600	3227.5206	129.1008
B1	+ 3.0000	146.36	-2.76853	2.67944	1377.9370	153.1041
$O_{br}1$	- 2.0000	147.84	2.53222	1.63382	840.2156	210.0539
$O_{br}2$	- 2.0000	146.36	2.19469	1.41605	728.2208	182.0552
$O_{br}3$	- 2.0000	148.46	2.22538	1.43584	738.4020	184.6005
$O_{term}1$	- 2.0000	154.47	2.07480	1.33869	688.4394	172.1099
$O_{term}2$	- 2.0000	153.79	2.19343	1.41523	727.8023	181.9506
$O_{term}3$	- 2.0000	146.30	2.30676	1.48835	765.4062	191.3516
$O_{term}4$	- 2.0000	155.87	2.03238	1.31132	674.3641	168.5910
$O_{term}5$	- 2.0000	154.45	2.01719	1.30152	669.3247	167.3312
O_H1	- 2.0000	79.08	2.50756	1.61791	832.0343	208.0086
N1	- 3.0000	64.52	3.93601	3.80935	1959.0101	217.6678
H1	+ 1.0000	79.08	-1.83874	0.59319	305.0565	305.0565
H2	+ 1.0000	64.52	-3.23868	1.04482	537.3129	537.3129
H3	+ 1.0000	84.66	-2.18952	0.70635	363.2521	363.2521
H4	+ 1.0000	107.03	-1.76771	0.57027	293.2713	293.2713
H5	+ 1.0000	92.89	-1.78981	0.57741	296.9386	296.9386
Madelung Constant:				37.9261	± 0.000001	
Coulomb Part of Lattice Energy:				19504.0141	± 0.000697 kcal·mol^{-1}	
Coulomb Part of Lattice Energy:				81643.8229	± 0.002917 kJ·mol^{-1}	

Table 12.10: MAPLE results for $NH_4Cr(III)[BP_2O_8(OH)]$ without the protons of the ammonia ion

Atom	Charge	Distance	Potential	PMF	MAPLE	*MAPLE
Cr1	+ 3.0000	188.39	-2.37510	2.81723	1182.1240	131.3471
P1	+ 5.0000	146.30	-3.98620	7.88040	3306.6498	132.2660
P2	+ 5.0000	147.84	-3.97848	7.86514	3300.2476	132.0099
B1	+ 3.0000	146.36	-2.81438	3.33828	1400.7586	155.6398
$O_{br}1$	- 2.0000	147.84	2.44780	1.93564	812.2050	203.0512
$O_{br}2$	- 2.0000	146.36	2.11072	1.66909	700.3594	175.0898
$O_{br}3$	- 2.0000	148.46	2.23826	1.76994	742.6761	185.6690
$O_{term}1$	- 2.0000	154.47	1.99189	1.57512	660.9285	165.2321
$O_{term}2$	- 2.0000	153.79	2.09492	1.65660	695.1170	173.7793
$O_{term}3$	- 2.0000	146.30	2.32820	1.84107	772.5209	193.1302
$O_{term}4$	- 2.0000	155.87	2.04347	1.61592	678.0453	169.5113
$O_{term}5$	- 2.0000	154.45	1.97447	1.56135	655.1503	163.7876
O_H1	- 2.0000	79.08	2.45668	1.94266	815.1506	203.7876
N1	+ 1.0000	272.14	-0.80569	0.31856	133.6683	133.6683
H1	+ 1.0000	79.08	-1.91098	0.75557	317.0409	317.0409
Madelung Constant:				38.5426	$\pm$ 0.000001	
Coulomb Part of Lattice Energy:				16172.6422	$\pm$ 0.000597 kcal·mol^{-1}	
Coulomb Part of Lattice Energy:				67698.6969	$\pm$ 0.002500 kJ·mol^{-1}	

Table 12.11: MAPLE results for $K_5[B(SO_4)_4]$

No.	Atom	x	y	z	Distance	ECoN
CA	K1	0.7550	0.0473	0.2564		
1	$O_{br}1$	0.6561	0.0116	0.1035	268.443	1.188
2	$O_{term}12$	0.5812	−0.0122	0.3789	269.107	1.174
3	$O_{term}10$	0.9351	0.2524	0.2303	273.580	1.076
4	$O_{term}3$	0.8511	−0.2165	0.2588	278.090	0.978
5	$O_{term}9$	0.5237	0.2091	0.2266	283.605	0.860
6	$O_{term}2$	0.8945	−0.0203	0.0892	311.174	0.365
7	$O_{term}2$	1.0203	−0.1055	0.3392	331.500	0.144
Next Ligand:						
8	$O_{term}7$	0.7534	0.3396	0.3885	359.896	0.022
Last Ligand:						
25	$O_{br}3$	0.9769	0.4304	0.4032	498.690	0.000
CN: 7						
CA	K2	0.8545	0.6733	0.0823		
1	$O_{term}5$	0.6165	0.7339	0.1588	272.912	1.410
2	$O_{term}8$	1.1176	0.6894	0.0135	283.782	1.185
3	$O_{term}6$	0.7398	0.6274	−0.0797	289.362	1.069
4	$O_{term}12$	0.9878	0.4188	0.1289	294.320	0.968
5	$O_{term}3$	0.8511	0.7835	0.2588	305.872	0.740
6	$O_{term}2$	0.8945	0.9797	0.0892	306.182	0.734
7	$O_{term}1$	0.7488	0.9146	−0.0225	311.152	0.643
8	$O_{term}11$	0.7607	0.3928	0.1726	327.327	0.385
9	$O_{term}1$	1.0854	0.7488	0.2275	336.340	0.272
10	$O_{br}4$	0.9127	0.4907	0.2621	347.450	0.166
11	$O_{br}3$	1.0231	0.5696	−0.0968	349.960	0.147
Next Ligand:						
12	$O_{term}4$	0.4796	0.6155	0.0603	377.308	0.028
Last Ligand:						
22	$O_{term}7$	1.2466	0.6604	−0.1115	499.326	0.000
CN: 11						

CA = Central Atom

No.	Atom	x	y	z	Distance	ECoN
CA	K3	0.5843	0.3494	0.0489		
1	$O_{term}11$	0.7607	0.3928	0.1726	269.169	1.294
2	$O_{term}5$	0.7339	0.3835	−0.0912	272.989	1.212
3	$O_{br}4$	0.4907	0.0873	0.0121	281.957	1.020
4	$O_{term}4$	0.4796	0.6155	0.0603	283.764	0.981
5	$O_{term}3$	0.7835	0.1489	0.0088	287.271	0.908
6	$O_{term}11$	0.3928	0.2393	−0.0774	299.403	0.666
7	$O_{term}7$	0.3396	0.2466	0.1385	300.186	0.652
8	$O_{term}9$	0.5237	0.2091	0.2266	325.024	0.272
9	$O_{br}1$	0.6561	0.0116	0.1035	353.209	0.061
Next Ligand:						
10	$O_{term}6$	0.7398	0.6274	−0.0797	377.921	0.009
Last Ligand:						
24	$O_{term}8$	0.3106	0.1176	0.2635	496.799	0.000
CN: 9						
CA	K4	0.1704	0.9084	0.1051		
1	$O_{term}1$	0.0854	0.7488	0.2275	267.075	1.183
2	$O_{term}10$	0.2524	1.0649	−0.0197	267.243	1.180
3	$O_{term}8$	0.1176	0.6894	0.0135	267.856	1.166
4	$O_{term}6$	0.3726	0.7398	0.1703	281.250	0.874
5	$O_{term}2$	−0.1055	0.9797	0.0892	283.357	0.830
6	$O_{br}3$	0.4304	1.0231	0.1532	291.980	0.657
7	$O_{br}2$	0.4817	0.8533	0.0560	323.002	0.201
Next Ligand:						
8	$O_{term}8$	0.3106	1.1176	0.2635	357.672	0.022
Last Ligand:						
24	$O_{term}9$	0.5237	1.2091	0.2266	499.736	0.000
CN: 7						

CA = Central Atom

No.	Atom	x	y	z	Distance	ECoN
CA	K5	0.2438	0.5035	0.1489		
1	$O_{term}6$	0.3726	0.7398	0.1703	268.735	1.225
2	$O_{term}12$	−0.0122	0.4188	0.1289	268.969	1.220
3	$O_{term}7$	0.3396	0.2466	0.1385	272.024	1.153
4	$O_{br}2$	0.1467	0.4817	0.3060	272.649	1.139
5	$O_{term}9$	0.2091	0.4763	−0.0234	282.299	0.931
6	$O_{term}4$	0.4796	0.6155	0.0603	295.616	0.662
7	$O_{term}4$	0.3845	0.4796	0.3103	297.031	0.635
8	$O_{term}8$	0.1176	0.6894	0.0135	312.314	0.381
9	$O_{term}1$	0.0854	0.7488	0.2275	315.912	0.332
Next Ligand:						
10	$O_{br}4$	−0.0873	0.4907	0.2621	375.808	0.007
Last Ligand:						
$O_{br}3$	-0.0231	0.4304	0.4032	494.514	0.000	
CN: 9						

CA = Central Atom

Atom	Charge	Distance	Potential	PMF	MAPLE	*MAPLE
K1	+ 1.0000	268.44	-0.78014	0.54403	129.4295	129.4295
K2	+ 1.0000	272.91	-0.73877	0.51518	122.5652	122.5652
K3	+ 1.0000	269.17	-0.84089	0.58639	139.5074	139.5074
K4	+ 1.0000	267.08	-0.78361	0.54644	130.0044	130.0044
K5	+ 1.0000	268.74	-0.83325	0.58106	138.2399	138.2399
S1	+ 6.0000	142.54	-4.76252	19.92668	4740.7520	131.6876
$O_{br}1$	- 2.0000	142.17	2.58694	3.60798	858.3742	214.5936
$O_{term}1$	- 2.0000	144.08	2.24866	3.13619	746.1292	186.5323
$O_{term}2$	- 2.0000	144.77	2.23830	3.12174	742.6917	185.6729
$O_{term}3$	- 2.0000	142.54	2.25918	3.15086	749.6200	187.4050
S2	+ 6.0000	143.47	-4.74211	19.84132	4720.4423	131.1234
$O_{br}2$	- 2.0000	150.89	2.56415	3.57619	850.8114	212.7028
$O_{term}4$	- 2.0000	144.80	2.21412	3.08801	734.6679	183.6670
$O_{term}5$	- 2.0000	143.47	2.26687	3.16157	752.1688	188.0422
$O_{term}6$	- 2.0000	146.02	2.21349	3.08713	734.4588	183.6147
S3	+ 6.0000	139.47	-4.82437	20.18547	4802.3197	133.3978
$O_{br}3$	- 2.0000	142.32	2.68396	3.74329	890.5646	222.6411
$O_{term}7$	- 2.0000	139.47	2.36436	3.29754	784.5179	196.1295
$O_{term}8$	- 2.0000	142.91	2.26332	3.15663	750.9921	187.7480
$O_{term}9$	- 2.0000	146.13	2.09469	2.92145	695.0402	173.7600
S4	+ 6.0000	142.70	-4.81445	20.14397	4792.4457	133.1235
$O_{br}4$	- 2.0000	152.70	2.56343	3.57518	850.5710	212.6428
$O_{term}10$	- 2.0000	143.13	2.31883	3.23405	769.4123	192.3531
$O_{term}11$	- 2.0000	143.16	2.18937	3.05349	726.4540	181.6135
$O_{term}12$	- 2.0000	142.70	2.30176	3.21024	763.7465	190.9366
B	+ 3.0000	142.17	-2.72381	5.69829	1355.6798	150.6311
Madelung Constant:				140.6904	± 0.000004	
Coulomb Part of Lattice Energy:				33471.6064	± 0.001062 kcal·mol^{-1}	
Coulomb Part of Lattice Energy:				140112.1788	± 0.004445 kJ·mol^{-1}	

Bibliography

[1] W. M. Haynes, *CRC Handbook of Chemistry and Physics, Line Spectra of the Elements*, **2012**.

[2] C. Meyer and H. Nienhuis, *Discharge Lamps*, Kluwer, Deventer, **1988**.

[3] T. Jüstel, H. Nikol and C. Ronda, *Angew. Chem. Int. Ed.* **1998**, *37*, 3084.

[4] H. A. Höppe, *Angew. Chem. Int. Ed.* **2009**, *48*, 3572.

[5] S. Nakamura, T. Mukai and M. Senoh, *Appl. Phys. Lett.* **1994**, *64*, 1687.

[6] J. W. D. Callister, *Materials Science and Engineering*, John Wiley & Sons, Inc., **2007**.

[7] U. Kaufmann, M. Kunzer, K. Köhler, H. Obloh, W. Pletschen, P. Schlotter, J. Wagner, A. Ellens, W. Rossner and M. Kobusch, *Phys. Stat. Sol. (a)* **2002**, *192*, 246.

[8] A. Holleman and E. Wiberg, *Lehrbuch der Anorganischen Chemie*, deGruyter Berlin/New York, 102. Ed., **2007**.

[9] C. R. Ronda, T. Jüstel and H. Nikol, *J. Alloys Compd.* **1998**, *275-277*, 669.

[10] L. Ozawa, *Chem. Rev.* **2003**, *103*, 3835.

[11] U. Schubert and N. Hüsing, *Synthesis of Inorganic Materials*, Wiley-VCH Verlag Weinheim, **2005**.

[12] A. Rabenau, *Angew. Chem. Int. Ed.* **1985**, *24*, 1026.

[13] B. Ewald, Y.-X. Huang and R. Kniep, *Z. Anorg. Allg. Chem.* **2007**, *633*, 1517.

[14] T. A. Borisova, E. L. Belokoneva and O. V. Dimitrova, *Russ. J. Inorg. Chem.* **2002**, *47*, 324.

[15] E. L. Belokoneva, T. A. Borisova and O. V. Dimitrova, *Kristallografiya* **2003**, *48*, 634.

[16] W. Massa, *Kristallstrukturbestimmung*, Vieweg+Teubner Studienbücher Chemie Wiesbaden, 5. Ed., **2011**.

[17] R. Allmann, *Röntgenpulverdiffraktometrie*, Springer Verlag Berlin Heidelberg, **2003**.

[18] L. Spieß, R. Schwarzer, H. Behnken and G. Teichert, *Moderne Röntgenbeugung, Röntgendiffraktometrie für Materialwissenschaftler, Physiker und Chemiker*, B. G. Teubner Verlag Wiesbaden, **2005**.

[19] R. E. Dinnebier and S. J. L. Billinge, *Powder Diffraction Theory and Practice*, The Royal Society of Chemistry, **2008**.

[20] Bruker, *SADABS*, Bruker AXS Inc., Madison, Wisconsin, USA, **2001**.

[21] G. Sheldrick, *SHELXTL*, Version 6.14, Bruker AXS, **2003**.

[22] G. M. Sheldrick, *Acta Crystallogr., Sect. A* **2008**, *A64*, 112.

[23] K. Brandenburg, *Diamond*, Version 3.2i, Crystal Impact GbR, Bonn, **2012**.

[24] *POV-Ray for Windows*, Version 3.6.2, Persistence of Vision Raytracer Pty. Ltd., **2009**.

[25] H. M. Rietveld, *Acta Crystallogr.* **1967**, *22*, 151.

[26] H. M. Rietveld, *J. Appl. Cryst.* **1969**, *2*, 65.

[27] J. Rodríguez-Carvajal, *Physica B* **1993**, *192*, 55.

[28] *OriginPro*, Version 8.6.0G, OriginLab Corporation, Northampton, **2011**.

[29] G. Reimer, L. Pfefferkorn, *Rasterelektronenmikroskopie*, Springer Berlin, **1977**.

[30] P. J. Goodhew, *Electron Microscopy and Analysis*, Taylor & Francis, London/New York, **2001**.

[31] *Genesis Spectrum*, Version 5.21, EDAX Inc., Mahwah (USA), **2007**.

[32] R. Hoppe, *Angew. Chem. Int. Ed.* **1966**, *5*, 95.

[33] R. Hoppe, *Angew. Chem. Int. Ed.* **1970**, *9*, 25.

[34] M. Binnewies, M. Jäckel, H. Willner and G. Rayner-Canham, *Allgemeine und Anorganische Chemie*, Spektrum Akademischer Verlag Heidelberg, **2011**.

[35] T. Balić-Žunić and E. Makovicky, *Acta Crystallogr., Sect. B* **1996**, *52*, 78.

[36] E. Makovicky and T. Balić-Žunić, *Acta Crystallogr., Sect. B* **1998**, *54*, 766.

[37] P. Skrabal, *Spektroskopie*, vdf Hochschulverlag AG an der ETH Zürich, Zürich, **2009**.

[38] H. Günzler and H.-U. Gremlich, *IR Spectroscopy*, Wiley-VCH Verlag Weinheim, **2002**.

[39] *OPUS*, Version 5.0, Bruker Optik GmbH, Karlsruhe, **1997**.

[40] J. R. Lakowicz, *Principles of Fluorescence Spectroscopy*, Springer Science+Business Media, LLC, 3. Ed., **2006**.

[41] C. Janiak, H.-J. Meyer, D. Gudat and R. Alsfasser, *Riedel Moderne Anorganische Chemie*, de Gruyter Berlin/Boston, **2012**.

[42] J. E. Huheey, E. A. Keiter and R. L. Keiter, *Anorganische Chemie*, de Gruyter Berlin/Boston, **2014**.

[43] Y. Tanabe and S. Sugano, *J. Phys. Soc. Jpn.* **1954**, *9*, 753.

[44] *Varian UV Scan Application*, Version 3.0, **2007**.

[45] G. H. Dieke and H. M. Crosswhite, *Appl. Opt.* **1963**, *2*, 675.

[46] K. Ogasawara, S. Watanabe, H. Toyoshima and M. G. Brik, *Handbook on the Physics and Chemistry of Rare Earths*, Band 37, Elsevier, **2007**.

[47] *FluorEssence*, Version 3.1.5.11, HORIBA Ltd., Kyoto, **2009**.

[48] D. J. Robbins, *J. Electrochem. Soc.* **1979**, *126*, 1550.

[49] C. Feldmann, T. Jüstel, C. Ronda and P. Schmidt, *Adv. Funct. Mater.* **2003**, *13*, 511.

[50] M. Born and T. Jüstel, *Physik Journal* **2003**, *2*, 294.

[51] T. Jüstel, J.-C. Krupa and D. U. Wiechert, *J. Lumin.* **2001**, *93*, 179.

[52] M. Born and T. Jüstel, *Chemie in unserer Zeit* **2006**, *40*, 294.

[53] W. T. Carnall, P. R. Fields and K. Rajnak, *J. Chem. Phys.* **1968**, *49*, 4450.

[54] Y.-C. Li, Y.-H. Changa, Y.-F. Lin, Y.-S. Changb and Y.-J. Lin, *J. Alloys Compd.* **2007**, *439*, 367.

[55] G. Blasse, A. Bril and W. Nieuwpoort, *J. Phys. Chem. Solids* **1966**, *27*, 1587.

[56] G. Blasse and A. Bril, *J. Chem. Phys.* **1967**, *47*, 5442.

[57] M. Koedam and J. J. Opstelten, *Lighting Research and Technology* **1971**, *3*, 205.

[58] H. A. Höppe, H. Lutz, P. Morys, W. Schnick and A. Seilmeier, *J. Phys. Chem. Solids* **2000**, *61*, 2001.

[59] F. Stadler, O. Oeckler, H. A. Höppe, M. H. Möller, R. Pöttgen, B. D. Mosel, P. Schmidt, V. Duppel, A. Simon and W. Schnick, *Chem. Eur. J.* **2006**, *12*, 6984.

[60] R. D. Shannon, *Acta Crystallogr., Sect. A* **1976**, *32*, 751.

[61] F. D. S. Butement, *Trans. Faraday Soc.* **1948**, *44*, 617.

[62] M. Thoms, H. von Seggern and A. Winnacker, *Phys. Rev. B* **1991**, *44*, 9240.

[63] P. Dorenbos, *J. Lumin.* **2003**, *104*, 239.

[64] W. T. Carnall, P. R. Fields and K. Rajnak, *J. Chem. Phys.* **1968**, *49*, 4447.

[65] S. Colak and W. K. Zwicker, *J. Appl. Phys.* **1983**, *54*, 2156.

[66] G. Blasse and B. Grabmeier, *Luminescent Materials*, Springer, Berlin, **1994**.

[67] W. T. Carnall, P. R. Fields and K. Rajnak, *J. Chem. Phys.* **1968**, *49*, 4424.

[68] W. T. Carnall, *J. Phys. Chem.* **1963**, *67*, 1206.

[69] C. Klixbüll Jørgensen and B. Judd, *Molecular Physics* **1964**, *8*, 281.

[70] Z.-J. Zhang, J.-L. Yuan, H.-H. Chen, X.-X. Yang and J.-T. Zhao, *Solid State Sci.* **2009**, *11*, 549.

[71] H. A. Höppe, *Dissertation*, Ludwig-Maximilians-Universität München, **2003**.

[72] W. B. White, R. Roy and J. McKay Crichton, *Amer. Mineral.* **1967**, *52*, 867.

[73] M. Taran, A. Lebedev and A. Platonov, *Phys. Chem. Miner.* **1993**, *20*, 209.

[74] K. Schmetzer, *Naturwissenschaften* **1978**, *65*, 592.

[75] M. Malinowski, Z. Frukacza, M. Szuflinskaa, A. Wnuka and M. Kaczkana, *J. Alloys Compd.* **2000**, *300-301*, 389.

[76] A. Guhur and S. Jackson, *Opt. Express* **2010**, *18*, 20164.

[77] S. Rai, *Spectrochim. Acta, Part A* **2002**, *58*, 1559.

[78] S. Rai, A. Singh and S. Singh, *Spectrochim. Acta, Part A* **2003**, *59*, 3221.

[79] E. Rukmini and C. Jayasankar, *Opt. Mater.* **1995**, *4*, 529.

[80] H. Lueken, *Magnetochemie*, B. G. Teubner Stuttgart Leipzig, **1999**.

[81] *Netzsch STA*, Version 4.8.5, Selb, **2009**.

[82] P. C. Burns, J. D. Grice and F. C. Hawthorne, *Can. Mineral.* **1995**, *33*, 1131.

[83] J. D. Grice, P. C. Burns and F. C. Hawthorne, *Can. Mineral.* **1999**, *37*, 731.

[84] J. Krogh-Moe, *Acta Crystallogr.* **1992**, *38*, 127.

[85] H. Huppertz and B. von der Eltz, *J. Am. Chem. Soc.* **2002**, *124*, 9376.

[86] F. C. Hawthorne, *Amer. Mineral.* **1985**, *70*, 455.

[87] F. C. Hawthorne, *Can. Mineral.* **1986**, *24*, 625.

[88] F. C. Hawthorne, *Z. Kristallogr.* **1990**, *192*, 1.

[89] F. C. Hawthorne, *Acta Crystallogr., Sect. B* **1994**, *50*, 481.

[90] C. L. Christ and J. R. Clark, *Phys. Chem. Miner.* **1977**, *2*, 59.

[91] P. Burns, *Can. Mineral.* **1995**, *33*, 1167.

[92] A. Durif, *Bull. Soc. Fr. Mineral. Crystallogr.* **1971**, *94*, 314.

[93] M. Bagieu-Beucher, I. Tordjman and A. Durif, *Rev. Chim. Miner.* **1971**, *8*, 753.

[94] M. Bagieu-Beucher and A. Durif, *Z. Kristallogr.* **1987**, *178*, 239.

[95] H. Assaaoudi, M. Ijjaali, A. Ennaciri, I. Butler and J. Kozinski, *J. Chem. Crystallogr.* **2007**, *37*, 601.

[96] F. Chehimi-Moumen and M. Férid, *Mater. Res. Bull.* **2007**, *42*, 1.

[97] M. Daub, K. Kazmierczak and H. A. Höppe, *Z. Anorg. Allg. Chem.* **2014**, *640*, 46.

[98] H. Höppe, K. Kazmierczak and M. Daub, *Z. Anorg. Allg. Chem.* **2010**, *636*, 1106.

[99] A. Mbarek, M. Fourati, D. Zambon and D. Avignant, *Acta Crystallogr., Sect. E* **2010**, *66*, i46.

[100] M. Weil, *Acta Crystallogr., Sect. E* **2010**, *66*, i75.

[101] R. Glaum, H. Thauern, A. Schmidt and M. Gerk, *Z. Anorg. Allg. Chem.* **2002**, *628*, 2800.

[102] D. Tranqui, M. Bagieu and A. Durif, *Acta Crystallogr., Sect. B* **1974**, *30*, 1751.

[103] M. Bagieu, I. Tordjman, A. Durif and G. Bassi, *Crystallogr. Struct. Commun.* **1973**, *3*, 387.

[104] D. Tranqui, M. Bagieu-Beucher and A. Durif, *Bull. Soc. Fr. Mineral. Crystallogr.* **1972**, *95*, 437.

[105] M. Rzaigui, N. Kbir-Ariguib, M. T. Averbuch-Pouchot and A. Durif, *J. Solid State Chem.* **1984**, *52*, 61.

[106] Y.-C. Zhang, W.-D. Cheng, D.-S. Wu, H. Zhang, D.-G. Chen, Y.-J. Gong and Z.-G. Kan, *J. Solid State Chem.* **2004**, *177*, 2610.

[107] J. M. Millet, H. S. Parker and R. S. Roth, *J. Am. Ceram. Soc.* **1986**, *69*, C103.

[108] B. M. Gatehouse, S. N. Platts and R. S. Roth, *Acta Crystallogr., Sect. C* **1991**, *47*, 2285.

[109] J. Bennazha, A. Boukhari and E. M. Holt, *Acta Crystallogr., Sect. C* **2002**, *58*, i29.

[110] X. Zhang, F. Meng, C. Yang and H. J. Seo, *J. Lumin.* **2013**, *140*, 74.

[111] X. Zhang, F. Meng, W. Li and H. J. Seo, *Ceram. Int.* **2013**, *39*, 8975.

[112] R. Kniep, G. Gözel, B. Eisenmann, C. Röhr, M. Asbrand and M. Kizilyalli, *Angew. Chem. Int. Ed.* **1994**, *33*, 749.

[113] F. Liebau, *Structural Chemistry of Silicates*, Springer Verlag, Berlin Heidelberg, **1985**.

[114] H. Bauer, *Z. Anorg. Allg. Chem.* **1965**, *337*, 183.

[115] H. Bauer, *Z. Anorg. Allg. Chem.* **1966**, *345*, 225.

[116] R. Kniep, H. Engelhardt and C. Hauf, *Chem. Mater.* **1998**, *10*, 2930 .

[117] L. Pauling, *J. Am. Chem. Soc.* **1929**, *51*, 1010.

[118] W. Loewenstein and M. Loewenstein, *Am. Mineral.* **1954**, *39*, 92.

[119] R. Kniep, G. Gözel, B. Eisenmann, C. Röhr, M. Asbrand and M. Kizilyalli, *Angew. Chem.* **1994**, *106*, 791.

[120] Y.-X. Huang, G. Schäfer, W. Carrillo-Cabrera, R. Cardoso, W. Schnelle, J.-T. Zhao and R. Kniep, *Chem. Mater.* **2001**, *13*, 4348.

[121] Y.-X. Huang, B. Ewald, W. Schnelle, Y. Prots and R. Kniep, *Inorg. Chem.* **2006**, *45*, 7578.

[122] K. Förg and H. A. Höppe, *Z. Anorg. Allg. Chem.* **2015**, *641*, 1009.

[123] I. Boy, F. Stowasser, G. Schäfer and R. Kniep, *Chem. Eur. J.* **2001**, *7*, 834.

[124] W. Liu, G. M., X. Yang, H. Chen, M. Li and J. Zhao, *Inorg. Chem.* **2004**, *43*, 3910.

[125] P. F. J. Van den Boom and A. M. J. H. Seuter, *Luminescent Bivalent Europium-Activated Barium Borophosphate And Discharge Lamp Containing The Same*, **1980**.

[126] H. Liang, Q. Zeng, Y. Tao, S. Wang and Q. Su, *Mat. Sci. Eng. B* **2003**, *98*, 213.

[127] S. Laubach, *Dissertation*, Technische Universität Darmstadt, **2008**.

[128] G. Wang, M. Valldor, C. Lorbeer and A.-V. Mudring, *Eur. J. Inorg. Chem.* **2012**, 3032.

[129] H. A. Höppe, K. Kazmierczak, M. Daub, K. Förg, F. Fuchs and H. Hillebrecht, *Angew. Chem. Int. Ed.* **2012**, *51*, 6255.

[130] U. Betke, W. Dononelli, T. Klüner and M. S. Wickleder, *Angew. Chem.* **2011**, *123*, 12569.

[131] C. Logemann and M. S. Wickleder, *Inorg. Chem.* **2011**, *50*, 11111.

[132] C. Logemann, T. Klüner and M. S. Wickleder, *Angew. Chem. Int. Ed.* **2012**, *51*, 4997 .

[133] J. Bruns, C. Logemann, A. Weiz, C. Kolb and M. S. Wickleder, *Z. Naturforsch. B* **2014**, *70*, 3.

[134] C. Logemann and M. S. Wickleder, *Angew. Chem.* **2013**, *125*, 14479.

[135] M. Daub, K. Kazmierczak, H. A. Höppe and H. Hillebrecht, *Chem. Eur. J.* **2013**, *19*, 16954.

[136] M. Daub, K. Kazmierczak, P. Gross, H. A. Höppe and H. Hillebrecht, *Inorg. Chem.* **2013**, *52*, 6011.

[137] M. Daub, H. A. Höppe and H. Hillebrecht, *Z. Anorg. Allg. Chem.* **2014**, *640*, 2914.

[138] P. Gross, A. Kirchhain and H. A. Höppe, *Angew. Chem. Int. Ed.* **2016**, *55*, 4353.

[139] P. Gross, A. Kirchhain and H. A. Höppe, *Angew. Chem.* **2016**, *128*, 4426.

[140] P. Gross, *M. Sc. Thesis*, Universität Augsburg, **2014**.

[141] R. Kniep and G. Schäfer, *Z. Anorg. Allg. Chem.* **2000**, *626*, 141.

[142] G. Schäfer, H. Borrmann and R. Kniep, *Z. Anorg. Allg. Chem.* **2001**, *627*, 61.

[143] B. Ewald, P. Menezes, Y. Prots and R. Kniep, *Z. Anorg. Allg. Chem.* **2004**, *630*, 1721.

[144] B. Ewald, Y. Prots, P. Menezes, S. Natarajan, H. Zhang and R. Kniep, *Inorg. Chem.* **2005**, *44*, 6431.

[145] J. Kocher, *Rev. Chim. Miner.* **1966**, *3*, 209.

[146] A. Benhassaine, *C. R. Acad. Sc.* **1972**, *C 274*, 1933.

[147] M. Touboul, *Rev. Chim. Miner.* **1971**, *8*, 347.

[148] L.-Y. Li, G.-B. Li, M. Xiong, Y.-X. Wang and J.-H. Lin, *Acta Crystallogr., Sect. C* **2003**, *59*, i115.

[149] Y.-H. Gao, *Acta Crystallogr., Sect. E* **2011**, *67*, i57.

[150] T. Steiner, *Angew. Chem. Int. Ed.* **2002**, *41*, 48.

[151] N. Penin, L. Seguin, B. Gérand, M. Touboul and G. Nowogrocki, *J. Alloys Compd.* **2002**, *334*, 97.

[152] R. Hübenthal, *MAPLE*, MAPLE, Program for the Calculation of the Madelung Part of Lattice Energy, University of Gießen, Germany, **1993**.

[153] K. R. Tsai, P. M. Harris and E. N. Lassettre, *Z. Anorg. Allg. Chem.* **1950**, *242*, 33.

[154] G. E. Gurr, P. W. Montgomery, C. D. Knutson and B. T. Gorres, *Acta Crystallogr., Sect. B* **1970**, *26*, 906.

[155] A. Goto, T. Hondoh and S. Mae, *J. Chem. Phys.* **1994**, *93*, 1412.

[156] L. Jun, X. Shuping and G. Shiyang, *Spectrochim. Acta, Part A* **1995**, *51*, 519.

[157] P. Broadhead and G. Newman, *Spectrochim. Acta, Part A* **1972**, *28*, 1915.

[158] H. Yu, H. Wu, S. Pan, Z. Yang, X. Hou, X. Su, Q. Jing, K. R. Poeppelmeier and J. M. Rondinelli, *J. Am. Chem. Soc.* **2014**, *136*, 1264.

[159] N. Penin, L. Seguin, M. Touboul and G. Nowogrocki, *J. Solid State Chem.* **2001**, *161*, 205.

[160] S. Merlino and F. Sartori, *Acta Crystallogr., Sect. B* **1972**, *28*, 3559.

[161] H. Behm, *Acta Crystallogr., Sect. C* **1984**, *40*, 217.

[162] K. H. Woller and G. Heller, *Z. Kristallogr.* **1981**, *156*, 159.

[163] W. Yongjiang, P. Shilie, T. Xuelin, Z. Zhongxiang, W. Jide and J. Dianzeng, *Acta Crystallogr., Sect. B* **2009**, *48*, 7800.

[164] M. Marezio, *Acta Crystallogr., Sect. B* **1969**, *25*, 1787.

[165] S. Menchetti and S. Sabelli, *Acta Crystallogr., Sect. B* **1977**, *33*, 3730.

[166] E. Corazza, S. Menchetti and S. Sabelli, *Amer. Mineral.* **1974**, *59*, 1005.

[167] J. Krogh-Moe, *Acta Crystallogr., Sect. B* **1972**, *28*, 172.

[168] M. G. Krzhizhanovskaya, R. S. Bubnova, R. S. Filatov and S. K. Belger, *Z. Kristallogr.* **2000**, *215*, 740.

[169] M. Touboul and G. Novogorocki, *J. Solid State Chem.* **1998**, *136*, 220.

[170] W. H. Zachariasen and H. A. Plettinger, *Acta Crystallogr.* **1963**, *16*, 376.

[171] K. Palkina and K. H. Jost, *Acta Crystallogr., Sect. B* **1975**, *31*, 2285.

[172] K. Palkina, N. Kuzmina, A. Selevich and A. Lesnikovich, *Russ. J. Inorg. Chem.* **2003**, *48*, 161.

[173] K. Palkina, N. Chudinova and G. Balagina, *Izves. Akad. Nauk SSSR* **1982**, *18*, 1337.

[174] D. T. Palumbo and J. J. Brown Jr., *J. Electrochem. Soc.* **1970**, *117*, 1184.

[175] D. T. Palumbo and J. J. Brown Jr., *J. Electrochem. Soc.* **1971**, *118*, 1159.

[176] B. Smets, *Mater. Chem. Phys.* **1987**, *16*, 283.

[177] C. Ronda, *J. Lumin.* **1997**, *72-74*, 49.

[178] S. P. Puppalwar, S. J. Dhoble and A. Kumar, *Indian J. Pure Appl. Phys.* **2011**, *49*, 239.

[179] X. Zhang and M. Gong, *Dalton Trans.* **2013**, *43*, 2465.

[180] K. Förg and H. A. Höppe, *Dalton Trans.* **2015**, *44*, 19163.

[181] G. M. Sheldrick, *Twinabs*, Universität Göttingen, **1996**.

[182] K. H. Jost, *Z. Kristallogr.* **1963**, *16*, 623.

[183] M. Rzaigui and K. Arigiub, *J. Solid State Chem.* **1983**, *50*, 240.

[184] M. Graia, A. Driss and T. Jouini, *Solid State Sci.* **2003**, *5*, 393.

[185] H. A. Höppe, *Solid State Sci.* **2005**, *7*, 1209.

[186] M. Weil, M. Puchberger, J. Schmedt auf der Günne and J. Weber, *Chem. Mater.* **2007**, *19*, 5067.

[187] H. A. Höppe, *J. Solid State Chem.* **2009**, *182*, 1786.

[188] S. J. Sedlmaier and W. Schnick, *Z. Anorg. Allg. Chem.* **2008**, *634*, 1501.

[189] H. A. Höppe, M. Daub and O. Oeckler, *Solid State Sci.* **2009**, *11*, 1484.

[190] H. A. Höppe and M. Daub, *Z. Kristallogr.* **2012**, *227*, 535.

[191] M. Daub, A. J. Lehner and H. A. Höppe, *Dalton Trans.* **2012**, *41*, 12121.

[192] A. Goto, T. Hondoh and S. Mae, *J. Chem. Phys.* **1990**, *93*, 1412.

[193] C. H. MacGillavry, H. C. J. de Decker and L. M. Nijland, *Nature* **1949**, *164*, 448.

[194] J. Weidlein, U. Müller and K. Dehnicke, *Schwingungsfrequenzen I Hauptgruppenelemente*, Georg Thieme Verlag Stuttgart/New York, **1981**.

[195] A. Rulmont, R. Cahay, M. Liegeois-Duyckaerts and P. Tarte, *Eur. J. Solid State Inorg. Chem.* **1991**, *28*, 207.

[196] H. A. Höppe and J. M. U. Panzer, *Eur. J. Inorg. Chem.* **2009**, 3127.

[197] O. Y. Miroshnichenko and V. V. Mombelli, *Russ. J. Inorg. Chem. Engl. Transl.* **1979**, *24*, 1631.

[198] H. A. Höppe, G. Kotzyba, R. Pöttgen and W. Schnick, *J. Mater. Chem.* **2001**, *11*, 3300.

[199] K. Kazmierczak and H. A. Höppe, *J. Solid State Chem.* **2011**, *184*, 1221.

[200] W. Lü, H. Zhou, G. Chen, J. Li, Z. Zhu, Z. You and C. Tu, *J. Phys. Chem. C* **2009**, *113*, 3844.

[201] C. Yang, Y. Pan and Q. Zhang, *Mater. Sci. Eng.: B* **2007**, *137*, 195.

[202] Q. Luo, X. Qiao, X. Fan, H. Yang, X. Zhang, S. Cui, L. Wang and G. Wang, *J. Appl. Phys.* **2009**, *105*, 043506.

[203] H. Yu, W. Zi, S. Lan, S. Gan, H. Zou, X. Xu and G. Hong, *Luminescence* **2013**, *28*, 679.

[204] A. Mbarek, M. Graia, G. Chadeyron, D. Zambon, J. Bouaziz and M. Fourati, *J. Solid State Chem.* **2009**, *182*, 509.

[205] A. Selevich, A. Lyakhov and A. I. Lesnikovich, *Phosphorus Res. Bull.* **1999**, *10*, 171.

[206] S. B. Moussa, I. Sobrados, J. E. Iglesias, M. Trabelsi-Ayedi and J. Sanz, *J. Mater. Chem.* **2000**, *10*, 1973.

[207] A. H. McKeag and E. G. Steward, *Br. J. Appl. Phys.* **1955**, *6*, S26.

[208] A. H. McKeag, *Improvements in or relating to luminescent materials*, **1958**.

[209] E. R. Kreidler and F. A. Hummel, *Inorg. Chem.* **1967**, *6*, 884.

[210] Y. Okonek, *M. Sc. Thesis*, Universität Freiburg, **2008**.

[211] M. Graia, A. Driss and T. Jouini, *Acta Crystallogr., Sect. C* **1999**, *55*, 1395.

[212] H. A. Höppe, *Z. Anorg. Allg. Chem.* **2005**, *631*, 1272.

[213] W. Primak, H. Kaufman and R. Ward, *J. Am. Chem. Soc.* **1948**, *70*, 2043.

[214] D. Stachel, I. Svoboda and H. Fuess, *Acta Crystallogr., Sect. C* **1995**, *51*, 1049.

[215] M. Hesse, H. Meier and B. Zeeh, *Spektroskopische Methoden in der Organischen Chemie*, Georg Thieme Verlag Stuttgart, New York, 8. Ed., **2011**.

[216] D. E. C. Corbridge and E. J. Lowe, *J. Chem. Soc.* **1954**, 493–502.

[217] K. Horchani, M. Ferid, J.-C. Gacon, S. Lecocq, M. Trabelsi-Ayedi and I. Gregora, *Mater. Res. Bull.* **2002**, *37*, 1259.

[218] Y. Moustafa and K. El-Egili, *J. Non-Cryst. Solids* **1998**, *240*, 144.

[219] M. Gjikaj, P. Wu and W. Brockner, *Z. Anorg. Allg. Chem.* **2014**, *640*, 379.

[220] V. Natarajan, M. Bhide, A. Dhobale, S. Godbole, T. Seshagiri, A. Page and C.-H. Lu, *Mater. Res. Bull.* **2004**, *39*, 2065.

[221] H. A. Höppe, M. Daub and M. C. Bröhmer, *Chem. Mater.* **2007**, *19*, 6358.

[222] H. Bärnighausen, *MATCH, Communications in Mathematical Chemistry* **1980**, *9*, 139.

[223] V. Petricek, M. Dusek and L. Palatinus, *Jana2006*, Version 14/05/2012, Institute of Physics, Czech Academy of Sciences, Prague, Czech Republic, **2006**.

[224] S. C. Sevov, *Angew. Chem.* **1996**, *108*, 2814.

[225] H. Engelhardt, W. Schnelle and R. Kniep, *Z. Anorg. Allg. Chem.* **2000**, *626*, 1380.

[226] G.-Y. Yang and S. C. Sevov, *Inorg. Chem.* **2001**, *40*, 2214.

[227] Y.-X. Huang, O. Hochrein, D. Zahn, Y. Prots, H. Borrmann and R. Kniep, *Chem. Eur. J.* **2007**, *13*, 1737.

[228] T. Yang, J. Ju, F. Liao, J. Sasaki, N. Toyota and J. Lin, *J. Solid State Chem.* **2008**, *181*, 1110.

[229] S. Sasaki, K. Fujino and Y. Takeuchi, *Proc. Jpn. Acad.* **1979**, *55*, 43.

[230] K. Mansikka and J. Poyhonen, *Ann. Acad. Sci. Fenn.* **1962**, *Ser. A6*, 118.

[231] A. Khan and W. Baur, *Acta Crystallogr., Sect. B* **1973**, *29*, 2721.

[232] A. Yilmaz, L. Tatar Yildirim, X. Bu, M. Kizilyalli and G. D. Stucky, *Cryst. Res. Technol.* **2005**, *40*, 579.

[233] W. Yang, J. Li, T. Na, J. Xu, L. Wang, J. Yu and R. Xu, *Dalton Trans.* **2011**, *40*, 2549.

[234] H. Shi, Y. Feng, Q. Huang, D. Qiu, M. Li and K. Liu, *Cryst. Eng. Comm* **2011**, *13*, 7185.

[235] A. Baykal, M. Kizilyalli and R. Kniep, *J. Mater. Sci.* **2000**, *35*, 4621.

[236] A. Baykal, A., G. Gözel, M. Kizilyalli and R. Kniep, *Turk. J. Chem.* **2000**, *24*, 381.

[237] L. E. Orgel, *J. Chem. Phys.* **1955**, *23*, 1824.

[238] T. Stefanidis and A. G. Nord, *Acta Crystallogr., Sect. B* **1984**, *40*, 1995.

[239] M. Schmidt, B. Ewald, Y. Prots, R. Cardoso-Gil, M. Armbrüster, I. Loa, L. Zhang, Y.-X. Huang, U. Schwarz and R. Kniep, *Z. Anorg. Allg. Chem.* **2004**, *630*, 655.

[240] K. Förg and H. A. Höppe, *in preparation* **2016**.

[241] A. A. Khan, J. P. Roux and W. J. James, *Acta Crystallogr., Sect. B* **1972**, *28*, 2065.

[242] H. Arnold, *Z. Kristallogr.* **1986**, *177*, 139.

[243] W. L. Masterton, D. Bolocofsky and T. P. Lee, *J. Phys. Chem.* **1971**, *75*, 2809.

[244] Y. Huang, Q. Li, A. H. Jensen, M. Yin, J. O. Jensen, E. Christensen, C. Pan, N. J. Bjerruma and W. Xing, *J. Mater. Chem.* **2012**, *22*, 22452.

[245] H. Engelhardt and R. Kniep, *Z. Kristallogr. NCS* **1999**, *214*, 443.

[246] R. Kniep, I. Boy and H. Engelhardt, *Z. Anorg. Allg. Chem.* **1999**, *625*, 1512.

[247] H. Engelhardt, H. Borrmann and R. Kniep, *Z. Kristallogr. NCS* **2000**, *215*, 203.

[248] M. Kritikos, E. Wikstad and K. Walldén, *Solid State Sci.* **2001**, *3*, 649.

[249] M.-R. Li, S. Y. Mao, Y.-X. Huang, J. X. Mi, Z.-B. Wei, J.-T. Zhao and R. Kniep, *Z. Kristallogr. NCS* **2002**, *217*, 165.

[250] J.-X. Mi, J.-T. Zhao, Y.-X. Huang, J.-F. Deng, H. Borrmann and R. Kniep, *Z. Kristallogr. NCS* **2002**, *217*, 171.

[251] J. X. Mi, Y.-X. Huang, J.-F. Deng, H. Borrmann, J.-T. Zhao and R. Kniep, *Z. Kristallogr. NCS* **2002**, *217*, 169.

[252] J. X. Mi, H. Borrmann, Y.-X. Huang, S. Y. Mao, J.-T. Zhao and R. Kniep, *Z. Kristallogr. NCS* **2003**, *218*, 171.

[253] A. H. Hill, A. Harrison, C. Dickinson, W. Zhou and W. Kockelmann, *Microporous Mesoporous Mater.* **2010**, *130*, 280.

[254] I. Olovsson and D. H. Templeton, *Am. Crystallogr. Assoc.* **1959**, 35.

[255] C. E. Rice and W. R. Robinson, *Acta Crystallogr., Sect. B* **1977**, *21*, 145.

[256] W. Yang, J. Li, Q. Pan, Z. Jin, J. Yu and R. Xu, *Chem. Mater.* **2008**, *20*, 4900.

[257] A. Adamczyk and M. Handke, *J. Mol. Struct.* **2000**, *555*, 159.

[258] A. Adamczyk, M. Handke and W. Mozgawa, *J. Mol. Struct.* **1999**, *511-512*, 141.

[259] M. Lenglet, F. Petit and J. Malvault, *Phys. Stat. Sol. (a)* **1994**, *143*, 361.

[260] E. Sarina, *Tanabe-Sugano Diagrams*, University of California, Davis, **2015**, http://chemwiki.ucdavis.edu/Core/Inorganic_Chemistry/Crystal_Field_Theory/Tanabe-Sugano_Diagrams, accessed on 20.10.2015.

[261] Ö. F. Öztürk, B. Zümreoglu-Karan and M. M. Can, *Z. Anorg. Allg. Chem.* **2008**, *634*, 1127.

[262] H. Thauern and R. Glaum, *Inorg. Chem.* **2007**, *46*, 2057.

[263] R. Kniep, H. G. Will, I. Boy and C. Röhr, *Angew. Chem. Int. Ed.* **1997**, *36*, 1013.

[264] A. Durif, *Crystal Chemistry of Condensed Phosphates*, Plenum Press New York, **1995**.

[265] J. P. Gamondes, F. D'Yvoire and A. Boullé, *C. R. Acad. Sc. Paris Ser. C* **1969**, *269*, 1532.

[266] I. Grunze and H. Grunze, *Z. Anorg. Allg. Chem.* **1984**, *512*, 39.

[267] G. Schott and H. U. Kibbel, *Z. Anorg. Allg. Chem.* **1962**, *314*, 104.

[268] R. J. Gillespie, *Can. J. Chem.* **1962**, *40*, 1009.

[269] G. Blasse and A. Bril, *J. Chem. Phys.* **1966**, *45*, 2350.

[270] J. A. Duffy and M. D. Ingram, *J. Chem. Soc., Chem. Commun.* **1973**, 635.

[271] M. Daub, H. A. Höppe and H. Hillebrecht, *Z. Anorg. Allg. Chem.* **2012**, *638*, 1637.

[272] H. A. Höppe, K. Kazmierczak, M. Daub, K. Förg, F. Fuchs and H. Hillebrecht, *Angew. Chem.* **2012**, *124*, 6359.

[273] *X-Area*, Version 1.6.10, STOE & Cie GmbH, Darmstadt, **2005**.

[274] E. L. Belokoneva, O. V. Ruchkina, O. V. Dimitrova and S. Y. Stefanovich, *Russ. J. Inorg. Chem.* **2001**, *46*, 179.

[275] H. Ehrenberg, S. Laubach, P. Schmidt, R. McSweeney, M. Knapp and K. K.C. Mishra, *J. Solid State Chem.* **2006**, *179*, 968.

[276] N. Shin, J. Kim, D. Ahn and K.-S. Sohn, *Acta Crystallogr., Sect. C* **2005**, *61*, i54.

[277] E. Dumas, C. Debiemme-Chouvy and S. C. Sevov, *J. Am. Chem. Soc.* **2002**, *124*, 908.

[278] J. Barbier and H. Park, *Can. Mineral.* **2001**, *39*, 129.

[279] C. Logemann, T. Klüner and M. S. Wickleder, *Z. Anorg. Allg. Chem.* **2012**, *638*, 758.

[280] K. Ståhl, T. Balić-Žunić, F. da Silva, K. Michael Eriksen, R. W. Berg and R. Fehrmann, *J. Solid State Chem.* **2005**, *178*, 1697.

[281] P. Touzain, F. Brisse and M. Caillet, *Can. J. Chem.* **1970**, *48*, 3358.

[282] A. Periasamy, S. Muruganand and M. Palaniswamy, *Rasayan J. Chem.* **2009**, *2*, 981.

[283] J. T. Kloprogge, L. V. Ruan, H. Duong and R. L. Frost, *Neth. J. Geosci.* **2001**, *80*, 41.

[284] C. Postmus and J. R. Ferraro, *J. Chem. Phys.* **1968**, *48*, 3605.

[285] H. A. Höppe, K. Kazmierczak, E. Romano and S. A. Brandán, *J. Mol. Struct.* **2013**, *1037*, 294.

[286] C. Klixbüll Jørgensen, *Orbitals in Atoms and Molecules*, Academic Press, **1962**.

[287] L. Pauling, *The Nature of the Chemical Bond*, Cornell Univ. Press, 3. Ed., **1960**.

[288] E. Nakazawa and F. Shiga, *Jpn. J. Appl. Phys.* **2003**, *42*, 1642.

[289] H. Liang, Y. Tao, W. Chen, X. Ju, S. Wang and Q. Su, *J. Phys. Chem. Solids* **2004**, *65*, 1071.

[290] B. Ewald, Y. Prots and R. Kniep, *Z. Kristallogr. NCS* **2004**, *219*, 213.

[291] R. Ternane, M. Cohen-Adad, G. Panczer, C. Goutaudier, C. Dujardin, G. Boulon, N. Kbir-Ariguib and M. Trabelsi-Ayedi, *Solid State Sci.* **2002**, *4*, 53.

[292] C.-H. Lu and V. Godbole, S.and Natajaran, *J. Mater. Sci.* **2006**, *41*, 2471.

[293] M.-R. Li, W. Liu, M.-H. Ge, H.-H. Chen, X.-X. Yang and J.-T. Zhao, *Chem. Commun.* **2004**, 1272.

[294] M. Jansen and T. Pilz, *Z. Kristallogr.* **2013**, *228*, 476.

[295] R. Erdmann, *M. Sc. Thesis*, Universität Augsburg, **2015**.

Publications

The First Borosulfate $K_5[B(SO_4)_4]$
H. A. Höppe, K. Kazmierczak, M. Daub, K. Förg, F. Fuchs, *Angew. Chem. Int. Ed.* **2012**, *51*, 6255–6257.

Das erste Borosulfat $K_5[B(SO_4)_4]$
H. A. Höppe, K. Kazmierczak, M. Daub, K. Förg, F. Fuchs, *Angew. Chem.* **2012**, *124*, 6359–6362.

Synthesis, Crystal Structure, Optical, Magnetic and Thermal Properties of $(NH_4)_2Mn[B_2P_3O_{11}(OH)_2]Cl$
K. Förg, H. A. Höppe, *Z. Anorg. Allg. Chem.* **2015**, *641*, 1009–1015.

Synthesis, Crystal Structure, Optical and Thermal Properties of Lanthanide Hydrogen-Polyphosphates $Ln[H(PO_3)_4]$ (Ln = Tb, Dy, Ho)
K. Förg, H. A. Höppe, *Dalton Trans.*, **2015**, *44*, 19163–19174.

Synthesis and Crystal Structure of $(NH_4)_2[B_2P_3O_{11}(OH)]$
K. Förg, H. A. Höppe, *in preparation.*

Synthesis and Crystal Structure of $(NH_4)Cr(III)[BP_2O_8(OH)]$
K. Förg, H. A. Höppe, *in preparation.*

Synthesis and Crystal Structure of $Cs_2[B_{10}O_{14}(OH)_4]\cdot H_2O$
K. Förg, H. A. Höppe, *in preparation.*